Durham E-Theses

Relaxation in epitaxial layers of III-V compounds

Turnbull, Aidan Gerard

How to cite:

Turnbull, Aidan Gerard (1992) *Relaxation in epitaxial layers of III-V compounds*, Durham theses, Durham University. Available at Durham E-Theses Online: http://etheses.dur.ac.uk/5709/

Use policy

The full-text may be used and/or reproduced, and given to third parties in any format or medium, without prior permission or charge, for personal research or study, educational, or not-for-profit purposes provided that:

- a full bibliographic reference is made to the original source
- a link is made to the metadata record in Durham E-Theses
- the full-text is not changed in any way

The full-text must not be sold in any format or medium without the formal permission of the copyright holders.

Please consult the full Durham E-Theses policy for further details.

Academic Support Office, The Palatine Centre, Durham University, Stockton Road, Durham, DH1 3LE
e-mail: e-theses.admin@durham.ac.uk Tel: +44 0191 334 6107
http://etheses.dur.ac.uk

Relaxation in Epitaxial Layers of III-V Compounds

by

Aidan Gerard Turnbull B.Sc.
Physics Department, University of Durham

The copyright of this thesis rests with the author.
No quotation from it should be published without
his prior written consent and information derived
from it should be acknowledged.

Thesis submitted to the University of Durham in
canditure for the degree of Doctor of Philosophy,

February, 1992.

2 6 AUG 1992

Dedicated to my Parents

Abstract

Semiconductor devices can be fabricated by growing III-V heteroepitaxial layers which are coherently strained to a III-V substrate. The relaxation of layer lattice strain through the nucleation of misfit dislocations near the interface causes a drop in performance for these devices. This thesis uses two non destructive x-ray techniques to examine relaxation in III-V epitaxial layers; double crystal diffractometry and x-ray topography. The dynamical and kinematical theories of x-ray diffraction are discussed in chapter 2. The apparatus used for double crystal diffractometry and x-ray topography and the theory of operation of these techniques is discussed in chapter 3. The properties of misfit dislocations in III-V epitaxial layers and the critical layer thickness at which relaxation occurs are discussed in chapter 4.

Double crystal diffractometry and x-ray topography have been used to examine relaxation in epitaxial layers of AlAs on GaAs, InGaAs on GaAs, GaAsSb on GaAs, InGaAs on InP and an InGaAs superlattice on InP. All layers were deposited on 001 orientated substrates. Asymmetric double crystal rocking curves have been analysed using a novel technique which allows deduction of the position of an *hhl* layer reflection in reciprocal space. The layer unit cell parameters in the [110] and $[1\bar{1}0]$ directions are determined from this. Individual misfit dislocation lines can be resolved by topography for dislocation line densities less than 0.2 μm^{-1}. In each of these samples the layer relaxation was found to be asymmetric about the $\langle 110 \rangle$ directions. The sensitivity of diffractometry and topography to the detection of layer relaxation has been compared for samples with different thicknesses and dislocation line densities. The resolution of these techniques to the determination of layer relaxation has been shown to meet for a 1 μm layer of AlAs on GaAs.

Tilt between the epitaxial layer lattice and the substrate has been measured for coherently strained and partially relaxed epitaxial layers grown on 001 orientated substrates. The lattice tilt in $\langle 110 \rangle$ directions was found to increase with misfit dislocation line density in these directions. Two theoretical models have been developed describing the relationship between lattice tilt and misfit dislocation line density and the tilts predicted by these compared with experiment.

At high dislocation densities measurements of layer relaxation by diffractometry indicate that the images recorded by topography represent bundles of misfit dislocations and not individual dislocation lines. The number of dislocation lines per

bundle was found to decrease with decreasing layer relaxation. Bunching of misfit dislocations into dislocation bundles is also observed on topographs from a low dislocation density sample where the individual dislocation lines are resolved. Screw dislocations in a strained layer and an interaction between two 60° dislocations to form a mixed dislocation have been characterised using Burgers vector analysis.

Interference fringes have been observed on 004 double crystal rocking curves recorded from an ultra thin InGaAs layer sandwiched between a GaAs substrate and a GaAs cap. The position and intensity of these fringes was found to be sensitive to the composition and thickness of the InGaAs layer. Comparison between simulated and experimental rocking curve data allowed determination of the layer thickness to within a single monolayer and layer composition to within 0.5%. Topography of this sample showed that the dislocation line density varied from zero to 0.12 μm^{-1} across the wafer. The critical layer thickness and Indium concentration at which the first few misfit dislocation lines were observed was measured as 162 $\pm$ 2 Å and 17 $\pm$ 0.5 %.

Acknowledgements

Financial support for this work from the Science and Engineering Research Council and British Telecommunications p.l.c through the provision of a CASE award is gratefully acknowledged.

I am grateful to Professors A. W. Wolfendale and A . D. Martin for allowing me use of the facilities of the Physics Department at the University of Durham and the S.E.R.C for the use of facilities at the Daresbury Laboratory Synchrotron Radiation Source.

I would like to thank Professor B. K. Tanner for his supervision of this project, particularly in the later stages of writing up, and Mrs. M. A. G. Halliwell of the British Telecom Research Laboratories for her supervision and many useful discussions. Thanks to Dr. E. G. Scott, Dr. J. Wilkie and Dr. A. K. Chatterjee of British Telecom for the MBE, MOVPE and LPE samples provided and also to Dr. C. Stanley of Glasgow University, Dr. S. Barnett of RSRE, and Dr. M. S. Goorsky of the IBM Research Division, New York, for allowing me to present results on their samples. I am also grateful to Dr. G. S. Green and Dr. S. Cockerton for their help and advice during experiments at the Daresbury Laboratory.

My thanks to Mr. T. Jackson and the staff from the Electronics Workshop for their patience in effecting seemingly endless repairs and Mr. D. Jobling and the staff of the Student Workshop for precision engineering. Mr. M. Lee and Miss V. Greener for their friendly advice and help with photography and reprographics. Mrs. N. Bingham for her encouragement and secretarial skills. Also to the members of the Solid State Group past and present for their companionship and support.

Finally, I would like to thank my parents for their support and guidance over the years.

Preface

This thesis describes work undertaken in the Solid State Group of the Physics Department, University of Durham and the S.E.R.C synchrotron radiation source at Daresbury laboratory during the period October 1988 to September 1991. All of the work contained herein is the author's own and is previously unpublished with the exception of material contained in the list of publications. All collaborative work and material from other sources is duly referenced where appropriate. Finally, it should be noted that diagrams have been numbered sequentially by chapter. They have been placed in the thesis immediately subsequently to the page on which reference to them is made.

List of Publications

Turnbull, A. G., Green, G. S., Tanner, B. K., and Halliwell, M. A. G., "Asymmetric Relaxation in Epitaxial Layers of III-V Compounds", Mater. Res. Soc. Proc. **202** 513 (1991)

Green, G. S., Tanner, B. K., Turnbull, A. G., Barnett, S. J., Emeny, M., and Whitehouse, C. R., "Misfit Dislocations at the Critical Thickness for InGaAs/GaAs Strained Layers", Mater. Res. Soc. Proc. **202** 507 (1991)

Tanner, B. K., Turnbull, A. G., Stanley, C. R., Kean, A. H., and McElhinney, M., "Measurement of Aluminium Concentration In Epitaxial Layers of $Al_xGa_{1-x}As$ on GaAs by Double Axis X-ray Diffractometry", Appl. Phys. Lett. **59** 2272 (1991)

Contents

1 Epitaxial Layers and Their Application to Semiconductor Devices **1**

1.1 Semiconductor Compounds 1

1.2 Semiconductor Devices 3

1.3 Epitaxial Layer Growth 7

1.2.1 Liquid Phase Epitaxy 8

1.2.2 Metal-Organic Vapour Phase Epitaxy 9

1.2.3 Molecular Beam Epitaxy 10

1.4 Epitaxial Layer Growth Modes 11

1.5 Critical Parameters for Epitaxial Layer Growth 12

2 Kinematical and Dynamical Theory **15**

2.0 Introduction 15

2.1 Interaction between X-rays and Matter 17

2.2 Kinematical X-ray Diffraction 18

2.3 Dynamical X-ray Diffraction 21

2.4 Simulation by the Takagi-Taupin Equations 27

3 Diffraction Instruments and Theory of their Operation **30**

3.1 Double Crystal Diffractometry 30

3.1.1 The Double Crystal Diffractometer 30

3.1.2 DuMond Diagrams for Successive Reflections 33

3.1.3 The Effect of Diffractometer Misalignment and X-ray Divergence 35

3.2 Techniques in X-ray Topography 39

3.2.0 Introduction 39

3.2.1 Single Crystal Topography Employing a Characteristic Line Source 42

3.2.1.1 Berg Barrett Topography 43

3.2.1.2 Hirst Topography 43

3.2.1.3 Section Topography 44

3.2.1.4 Lang Topography 44

3.2.2 Topographic Techniques Employing a Synchrotron Radiation Source 45
3.2.3 Single Crystal White Beam Topography 46
3.2.4 Double Crystal Synchrotron Radiation Topography 47

4 The Relief of Epitaxial Layer Strain by Misfit Dislocations 51

4.1 Dislocations in the Zinc Blende Lattice 51
4.2 The Peierls-Nabarro Force 53
4.3 Misfit Dislocation Generation 54
4.4 The Critical Epitaxial Layer Thickness 55
4.4.1 The Matthews Model 55
4.4.2 The Frank-van der Merwe Model 56
4.5 The Origins of Asymmetric Relaxation 57

5 Analysis of Double Crystal Rocking Curve Data 59

5.0 Introduction 59
5.1 Determination of the Composition of a Strained Epitaxial Layer 59
5.1.1 Symmetric Bragg Geometry 59
5.1.2 Calibration of the Double Crystal Diffractometer 60
5.1.3 The Effect of Tilt between the Epitaxial Layer and the Substrate 62
5.1.4 Precise Determination of the Aluminium Concentration in a Layer of AlGaAs 63
5.2 Determination of Epitaxial Layer Relaxation by Diffractometry 64
5.2.1 Asymmetric Bragg Geometry 65
5.2.2 Geometric Construction for Deduction of Layer Parameters for the case of Asymmetric Relaxation 66
5.2.3 Asymmetric Relaxation on a Layer of AlAs grown by MBE 67
5.3 Factors Affecting the Accuracy of the Determination of Layer Relaxation 69
5.4 Relationship between Layer Relaxation and Misfit Dislocation Density 72
5.5 Relationship between Layer Lattice Tilt and Misfit Dislocation Density 72
5.5.1 The Edge Component of a Burgers Vector 74
5.5.2 Model 1 75
5.5.3 Model 2 75
5.5.4 Comparison with Experiment 78

6 Epitaxial Layers with High Dislocation Densities **80**

6.0 Introduction 80

6.1 The Samples 80

6.2 Determination of Layer Relaxation by Diffractometry 80

6.2.1 Sample InP1 81

6.2.2 Sample GaAs3 81

6.2.3 Comments 82

6.3 Double Crystal SRS Topography 82

6.3.1 Sample InP1 83

6.3.2 Sample GaAs3 83

6.4 Conclusions 84

7 Epitaxial Layers with Low Dislocation Densities **85**

7.0 Introduction 85

7.1 Asymmetric Relaxation in a Thin InGaAs Layer 85

7.1.1 Precision of the Strained Layer Thickness Measurement 89

7.2 Asymmetric Relaxation in a Superlattice 90

7.3 Asymmetric Relaxation in Epitaxial Layers of AlAs 92

7.4 Conclusions 95

8 Characterisation of Misfit Dislocations by Topography **97**

8.0 Introduction 97

8.1 Determination of the Burgers Vector of a Dislocation Line 97

8.2 Identification of Screw Dislocations in a Strained Layer 99

8.3 Interactions between 60° Dislocations at Low Dislocation Density 100

8.4 Conclusions 102

Conclusions and Suggestions for Future Work **103**

References **106**

Chapter 1 106

Chapter 2 108

Chapter 3 109

Chapter 4 111
Chapter 5 113
Chapter 6 115
Chapter 7 115
Chapter 8 118

Chapter 1

Epitaxial Layers and Their Application to Semiconductor Devices.

1.1 Semiconductor Compounds

Epitaxial layer technology centres on the growth of highly ordered crystalline layers which are coherent with a crystalline substrate. Deposition of material onto a substrate of the same material is known as homoepitaxy whereas deposition of material onto a substrate of a different material is known as heteroepitaxy. In general the application of homoepitaxial layer technology to III-V materials is restricted to substrate surface preparation prior to heteroepitaxial layer growth through the deposition of 'buffer' layers.

III-V compounds are materials created from the combination of elements in group III of the periodic table with elements in group V of the periodic table following the classification developed by Mendeleev. The six elements which are commonly employed in the production of semiconducting III-V epitaxial layers are listed below.

Table 1.1. Group III and Group V Semiconductor Elements.

Group III	Group V
Al	P
Ga	As
In	Sb

The elements in Table 1.1 can combine to form nine binary compounds which are listed in Table 1.2 together with the values of bulk lattice parameter and Poisson ratio employed in this thesis, where these are known. The material parameters for two group IV elements, silicon and germanium, are included for completeness.

Table 1.2. Nine Binary Semiconductor Compounds

Binary	Bulk Lattice Parameter in Angstroms	Poisson Ratio
AlP	5.4625	—
AlAs	5.6628	0.28
AlSb	6.1355	—
GaP	5.4495	0.307
GaAs	5.65375	0.311
GaSb	6.0940	0.313
InP	5.8687	0.360
InAs	6.0584	0.352
InSb	6.4788	0.353
Si	5.4308	0.271
Ge	5.6575	0.278

These III-V binary compounds crystallise in the sphalerite structure. This is also known as the zinc blende structure and, following the convention developed by Gatos and Lavine [1], consists of a face centred cubic lattice with a basis of two atoms; a group III atom at the origin and a group V atom at coordinate position (1/4,1/4,1/4). The structure can also be thought of as a face centred cubic lattice of group III atoms interpenetrated by a face centred cubic lattice of group V atoms where the group V lattice is displaced by the vector [1/4,1/4,1/4] with respect to the group III lattice. The epitaxial layers examined in this thesis were grown on 001 substrate surfaces. Hence if the layer/substrate structure is viewed along the $[00\bar{1}]$ direction then the advancing (111) planes contain group III atoms whereas the advancing $(\bar{1}\bar{1}1)$ planes contain group V atoms. Silicon and germanium crystallise in the diamond structure which is equivalent to a zinc blende structure incorporating atoms of only one type.

Perhaps the most important property of III-V materials in relation to heteroepitaxial layer technology is the ease with which they form ternary and quaternary compounds e.g. $Al_xGa_{1-x}As$ and $In_xGa_{1-x}As_{1-y}P_y$ respectively. Ternary and quaternary compounds have physical properties which are limited by the extrema

of the constituent binary compounds and can be deduced from the relative concentrations of the binary compounds. The lattice parameter of a ternary or quaternary compound follows Vegard's Law to a good approximation. Vegard's Law simply states that the bulk lattice parameter of a ternary or quaternary compound can be deduced by taking a linear combination of the lattice parameters of the basic binary constituents; i.e a ternary bulk lattice parameter is deduced by linearly interpolating between the two binary bulk lattice parameters. Approximations for the Poisson ratios of ternary and quaternary compounds can be determined in a similar fashion.

The epitaxial layer samples examined in this thesis consist of ternary compounds grown on thick (200-300 μm) substrate crystals of binary III-V compounds, namely GaAs and InP. In all cases the composition of the ternary layer is such that its lattice parameter is not equal to the lattice parameter of the substrate. Hence the epitaxial layer lattice is strained with respect to the substrate lattice at the interface. The degree to which the layer lattice is coherent with the substrate lattice across the interface is governed by the lattice parameter difference and layer thickness. The difference between the bulk layer lattice parameter, a_r, and the substrate lattice parameter, a_0, is characterised by the lattice mismatch, m, which is defined by equation 1.1

$$m = \frac{(a_r - a_0)}{a_0} \qquad 1.1$$

The lattice mismatch also defines the strain between the layer lattice and the substrate lattice at the interface.

1.2. Semiconductor Devices

A brief overview of the basic properties of semiconductor materials and their application to device production via heteroepitaxial layer technology is presented here. The physics of semiconductor devices is discussed in detail by Sze [2], Streetman [3], and Zanger [4].

The energy gap, E_g, between the highest valence band and the lowest conduction band in a ternary compound is related to the energy gaps of the component binary compounds by equation 1.2

$$E_g = E_{g1} + bx + cx^2 \qquad 1.2$$

where E_{g1} is the smaller energy gap and x is the fractional composition of the larger energy gap binary material [5]. The constants b and c can be determined through a theoretical treatment of the band structure and are unique for each ternary. The expressions relating energy gap with composition for quaternary compounds are in general far more complicated. The extreme energy gap values for ternary compounds are 0.24 eV (InSb) and 2.48 eV (AlP). III-V ternary heteroepitaxy allows selection of any energy gap between these extrema.

The energy of the band gap between the valence and conduction bands in semiconductor materials is comparable to the thermal energy of an electron at room temperature. Electrons are fermions and so the distribution of electrons between these bands is governed by Fermi-Dirac statistics and depends on the number of energy levels in the conduction band (density of states), the energy of the band gap, the temperature of the material and the Fermi energy of the material. The Fermi energy level is the energy of the quantised state whose probability of occupation by an electron is exactly equal to a half. The action of an applied field accelerates the electrons in the conduction band causing the electrons to carry charge through the semiconductor. Each electron that is thermally excited into the conduction band leaves behind a vacant energy level in the valence band. The electrons in the valence band move to occupy the vacancy and the net effect is that the vacancy moves through the material. From consideration of the electrical neutrality of the crystal, the vacancy, which is known as a hole, is equivalent to a positively charged electron and indeed when the mobility of these holes is investigated it is found that their effective mass is often of the same order of magnitude as the effective mass of an electron in the semiconductor.

In practice semiconductor materials are often doped with impurity atoms to create extra energy levels within the energy gap. Donor impurities are atoms which, when present in the semiconductor crystal, have more valence electrons than are required to complete the bonds with neighbouring atoms, e.g group V or group VI atoms in a group IV crystal. The extra electrons are readily released into the conduction band whereas the donor atoms remain as positively charged ions within the crystal lattice. Hence the presence of donor impurities creates an excess of mobile negative charge carriers and so the doping is described as n-type. Acceptor impurities are atoms that have fewer valence electrons than are required to complete the bonds with neighbouring atoms and therefore accept electrons from surrounding atoms e.g. group II or group III atoms in a group IV crystal. The accepted electrons are tightly bound to the impurity atom creating a sessile negative ion in the crystal and leaving a hole which is loosely bound to a neighbouring atom in the crystal

lattice. Hence the presence of acceptor impurities leads to an excess of mobile positive charge carriers and the doping is referred to as p-type.

Junctions between semiconductors of different types, such as those created by the deposition of a heteroepitaxial layer on a substrate, play a fundamental part in modern electronic components. If an n-type semiconductor and a p-type semiconductor are brought into contact with no external applied field, thermal equilibrium will be established between the two, and the condition of zero net current requires the Fermi level to be constant throughout the sample. The n-type semiconductor contains an excess of mobile electrons whereas the p-type semiconductor contains an excess of mobile holes, hence electrons and holes will diffuse across the junction in an attempt to distribute the mobile charge carriers evenly between the two semiconductors. This diffusion is counteracted by space charge regions which reside on both sides of the junction and result from the sessile ionized impurity atoms. Hence a dynamic equilibrium is reached which is characterised by a potential difference across the junction known as the diffusion potential. Application of an electric field causes the junction to act as a diode. Conduction across the junction is allowed if the polarity of the applied voltage opposes the diffusion potential. In this case the junction acts as forward biased diode. If the polarity of the applied voltage is in the same sense as the diffusion potential then no current flows and the junction acts as a reverse biased diode.

The semiconductor laser and heavily doped light emiting diode (LED) essentially consist of a forward biased diode formed from the junction between two direct band gap semiconductors. Electrons flow from the n-type material conduction band across the junction to the p-type material conduction band and combine with a hole in that region resulting in the emission of a photon which has an energy approximately equal to the band gap energy. This process is called electron injection. As the injection current is increased above a threshold current, the majority of photon emissions from electron-hole recombination events are stimulated by photons produced from previous electron-hole recombination events and leads to laser action. The diode is constructed so that two opposite ends of the crystal perpendicular to the interface between the epitaxial layer and the substrate are flat and polished. These flat ends act as partially reflecting mirrors which reflect light back across the p-type material causing amplification of the stimulated emission. An intense laser beam emerges from the flat ends of the crystal. The output power is tens of milliwatts at wavelengths just longer than visible light wavelengths and the laser efficiency can be as high as 10 %.

The energy gap for a III-V semiconductor is typically of the order of 1 eV which corresponds to a photon wavelength of about 1 μm. Kao and Hockham [6] first proposed the use of an optical fibre communication system in 1961 and since then research has demonstrated that loss in fused silica fibres is remarkably reduced in the 1 μm wavelength region [7]. In this region there are two wavelength ranges that are attractive for long haul optical fibre communication systems, such as optical submarine cable systems. One is the 1.3 μm wavelength range where chromatic dispersion in a single mode fibre goes through zero [8]. This wavelength is suitable for broadband optical communication systems. The other is the 1.55 μm wavelength range where fused silica fibre shows an ultimate minimum loss of 0.2 dB/km [9]. Yamamoto achieved continuous wave operation of InGaAsP/InP laser diodes at room temperature with emission wavelengths of 1.3 μm and 1.55 μm in 1977 [10] and 1979 [11] respectively.

In recent years considerable interest has been shown in low dimensional structures. Charge carriers confined within ultra-thin (100 Å or less) epitaxial layers exhibit two dimensional quantised energy levels as a result of the quantum size effect and band bending at the layer/substrate interface. This can be visualised as a two dimensional electron gas (2DEG) or a quantum well and has novel electronic properties such as the quantum Hall effect. Superlattices, also known as multi quantum wells (MQWs), can be produced by stacking several quantum well structures on top of each other. The separation between quantum wells is precisely controlled, leading to a periodic variation in band structure throughout the stack. Charge carriers confined within this periodic band structure exhibit quantised energy levels which can be engineered through alteration of the repeat period and selection of different layer materials. This is equivalent to the creation of a new one dimensional material.

To meet the needs of information processing in the 1990's, the need for ultra-high speed computers (supercomputers) with a far superior performance to that of existing computers has been widely recognised. This necessitates the development of ultra-fast, low dimensional device components for integrated circuits. However the physical limits of silicon as a device material has retarded progress in some areas of device performance, e.g. switching speed. In order to break through these performance limitations other materials such as GaAs and InP, which have superior electronic properties compared to silicon, have been investigated and applied to the production of high-speed, low-power dissipation integrated circuits. The high electron mobility transistor (HEMT) has attracted great interest as one of the most promising candidates for post-silicon devices as it demonstrates excellent high-speed

performance at low temperatures. Hall measurements on an n-type AlGaAs/GaAs HEMT at 77k and 5k have been reported [12] which demonstrate electron mobilities in excess of an order of magnitude greater than those obtained in conventional GaAs field effect transistors operating at room remperature.

1.3 Epitaxial Layer Growth

There are three main techniques for the production of epitaxial layers, liquid phase epitaxy (LPE), vapour phase epitaxy (VPE) and molecular beam epitaxy (MBE). Liquid phase epitaxy involves bringing molten material into contact with the substrate and allowing the melt to cool for a specified time enabling the required epitaxial layer thickness to crystallise. In vapour phase epitaxy carrier gasses containing the correct relative concentrations of the alloy elements contact with a heated substrate which causes pyrolytic cracking of the carrier gases and deposition of the epitaxial layer material. Molecular beam epitaxy involves directing molecular or atomic beams from elemental sources onto a heated substrate in an ultra-high vacuum environment. LPE and VPE operate in regimes which are far from equilibrium and rely on the production of supersaturated media. In essence they resemble the attempts made by most high school students to grow crystals by introducing a seed crystal or other growth surface into a supersaturated aqueous solution. In contrast, MBE resembles graffiti spray painting with an aerosol can.

VPE is most usually practised as metal-organic vapour phase epitaxy (MOVPE) [13] which is also known in a more general context as metal-organic chemical vapour deposition (MOCVD). Several other techniques have been developed by combining particular aspects from MBE and MOVPE. With Gas-Source MBE (GSMBE) the group III elements derive from elemental sources but the arsenic and phosphorous fluxes result from the decomposition of AsH_3 and PH_3 [14]. Metal organic MBE (MOMBE) can utilise the group III organometallics with either the conventional condensed group V sources [15], the decomposed hydrides [16] or group V organometallics [17]. Conventional MOCVD relies on the decomposition of group III alkyls whereas recent techniques have been developed which employ metalorganic halides [18]. The samples examined in this thesis were grown by LPE, MOVPE and MBE.

1.3.1 Liquid Phase Epitaxy

LPE is based on creating a supersaturated melt of the desired layer material and placing this in contact with the substrate crystal. Various methods are used to achieve this, the most versatile of which is the multibin furnace [19] illustrated in Figure 1.1 [20]. The substrate is positioned in an indented holder so that the substrate surface is flush with the carbon tray. Quantities of the materials to be used in the epitaxial growth are loaded into carbon silos which are aligned sequentially and adjacent to the substrate. The entire growth chamber is heated inside a gold furnace until all materials are molten and have reached a state of "liquidness". In this state the molten materials are supersaturated and will preferentially crystallise if a suitable surface is provided. As the liquid state is approached the substrate materials often appear slightly transparent and this is used as an indicator that the correct growth temperature has been reached. The silos are then slid over the substrate in turn. Layer thickness is simply controlled by regulating the time for which this contact occurs. The chamber is continuously flushed with pure hydrogen during growth.

LPE techniques require great care to avoid outdiffusion from the substrate (many LPE processes involve allowing the melts to equilibrate for a few hours) and this is particularly problematic when growing epitaxial layers on InP substrates. At temperatures below $365°C$ indium and phosphorus evaporate at the same rate. However at temperatures above $350°C$ phosphorous evaporates at a much faster rate causing the formation of indium rich InP droplets on the substrate surface which decrease the quality and morphology of subsequent epitaxial layers [21]. One possible solution to this problem is to carry out LPE growth in a phosphine (PH_3) rich environment [22]. Whilst this arrests the net phosphorus outdiffusion it also contaminates the epitaxial layer materials in adjacent silos, restricts sample access and is expensive to incorporate. At present the problem is resolved by closing off certain silos with carbon caps and pellets of a tin, indium and InP mixture [23]. The pellet undergoes thermal decomposition and produces an overpressure of phosphine. However this only works efficiently at low vapour pressures and so LPE is not attempted at temperatures higher than $700°C$ for InP substrates. Similar considerations limit growth on Gallium Arsenide substrates by LPE to temperatures below $750°C$.

The rate of deposition of the epitaxial layer is typically around 1 μm per minute and so this technique is particularly suitable for growing relatively thick layers of between 2 and 10 μm [24]. It is used mainly for the fabrication of LED's and

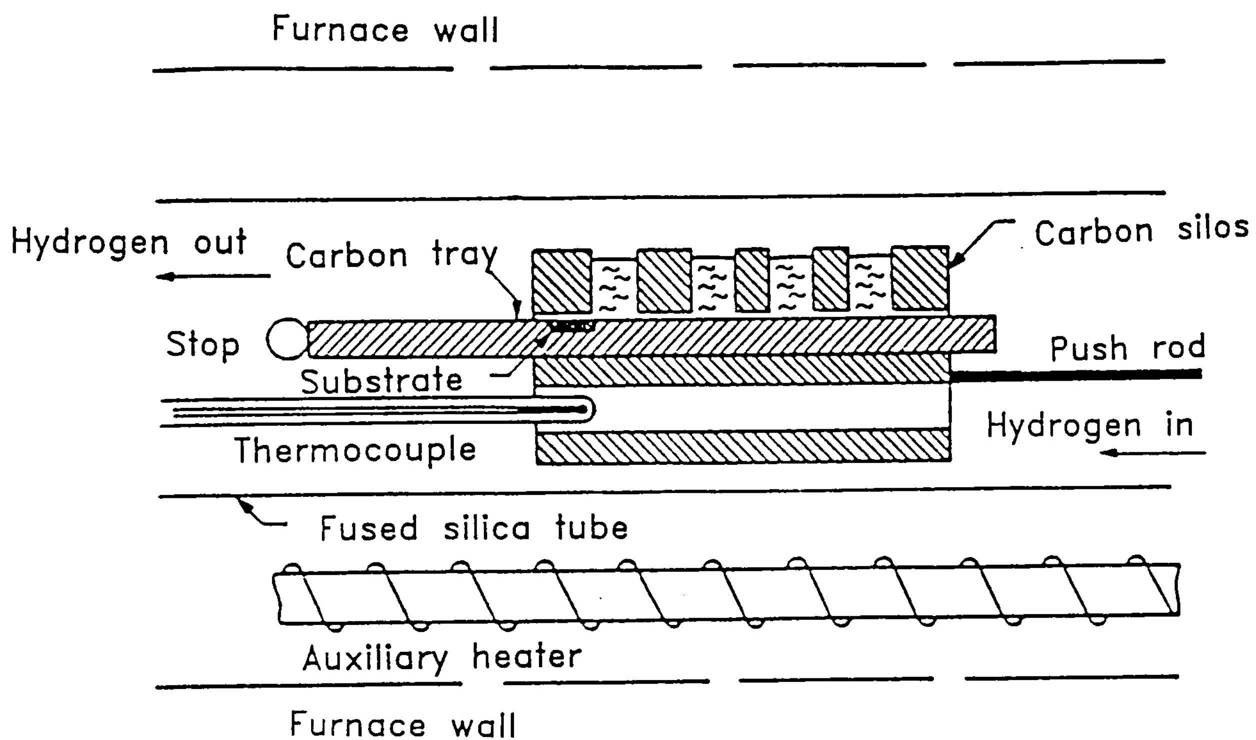

Figure 1.1: Schematic illustration of the LPE multibin furnace. After Agrawal and Dutta [20].

growing experimental samples of novel compounds. An LPE kit is at least an order of magnitude cheaper than MBE and MOVPE kits which can cost upwards of £500,000. However MBE and MOVPE allow much higher control of epitaxial layer composition, thickness and uniformity.

1.3.2 Metal-Organic Vapour Phase Epitaxy

Metal-organic vapour phase epitaxy is illustrated schematically in Figure 1.2 [31] and consists of three distinct sections: the mass/flow analyser and gas delivery system; the reactor; and the waste disposal system.

The Mass Flow Analyser

The mass/flow analyser controls the composition and rate at which the gas is supplied to the reactor. Group III elements are supplied to the reactor as covalent alkyls e.g. trimethyl indium ($In(CH_3)_3$) and trimethyl gallium ($Ga(CH_3)_3$) whereas group V elements are supplied as trihydrides e.g. arsine (AsH_3) and phosphine (PH_3). Dimethyl zinc or hydrogen sulphide may also be present to provide p-type or n-type doping respectively. Each of these gases is supplied to the reactor separately. Group III alkanes have low boiling points and high vapour pressures and so are difficult to regulate. To ease this problem, helium gas is bubbled through the liquified alkyl and becomes saturated. The saturated helium gas transports the group III alkyl to the reactor but remains unreactive during growth.

The final composition of the gas as it enters the reactor is computer controlled and is calculated from the temperatures and pressures of the individual components. In epitaxial growth it is assumed that the deposited phase has the same composition as the gas phase above the substrate.

The Reactor

The substrate is positioned on a carbon table called the susceptor which is orientated at about 2 degrees to the incoming gases. The susceptor is heated by infra-red halogen lamps or rf coils to about $500°C$ which induces pyrolytic cracking of the gas phase. This generates a stagnant boundary layer of free radicals above the substrate. The free radicals combine on the substrate to form the epitaxial layer.

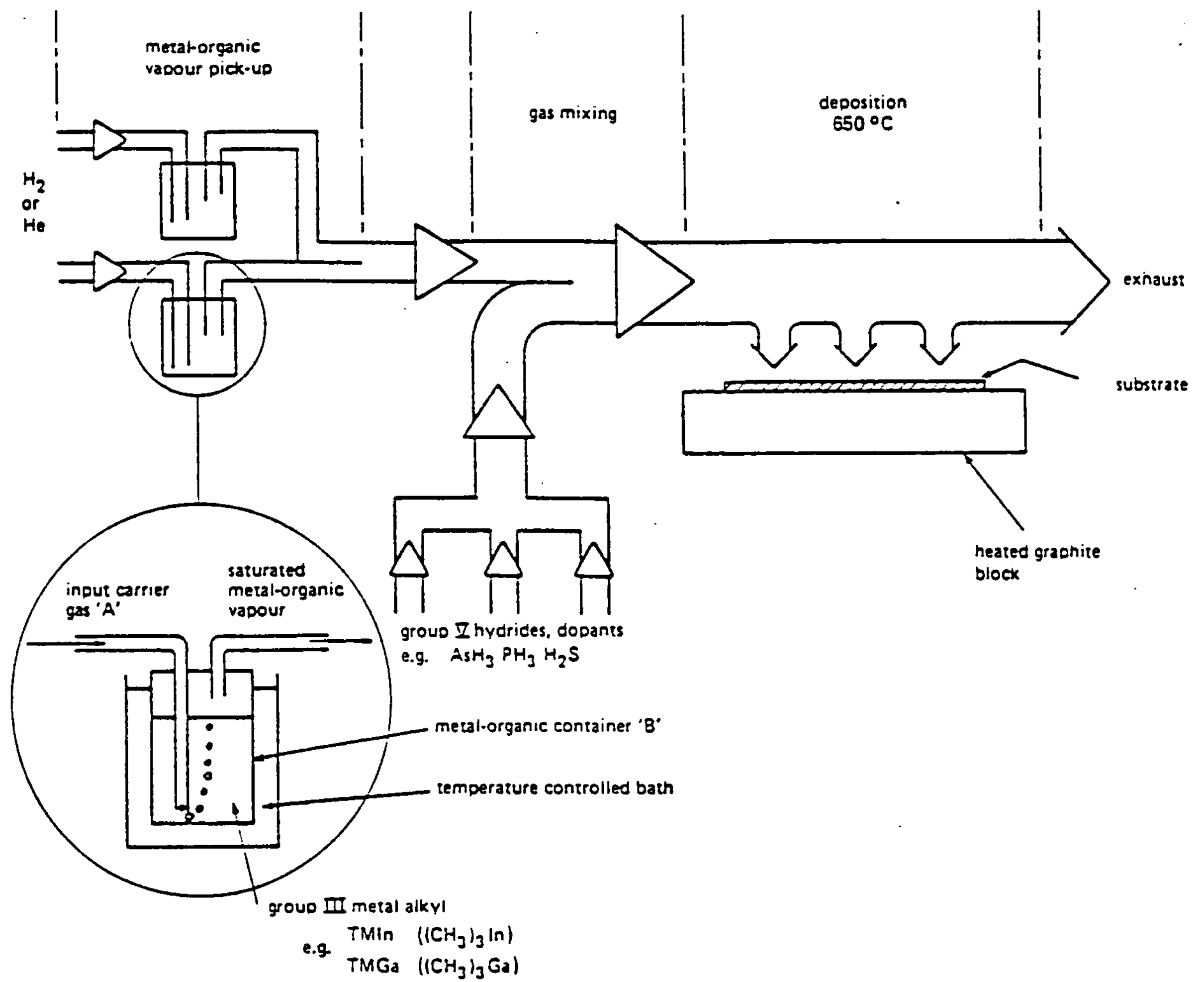

Figure 1.2: Schematic illustration of the MOVPE growth process. After Nelson et al [25].

The flow of the incoming gasses must be laminar and this is achieved by the geometry of the quartz vessel surrounding the susceptor. Laminar flow is more easily achieved at low pressures though some kits succeed in operating at atmospheric pressure. Contrary to expectations low pressure operation requires larger quantities of the component gasses. Typical gas flow velocities are in the range of 1 to 15 cms^{-1} for working pressures between 0.1 and 0.5 atm.

The surface chemistry of the deposition reactions is not fully understood though it is known empirically that the growth rate is solely dependent upon the amount of group III material present.

Waste Disposal

The compounds used in MOVPE are in general highly toxic and the safe disposal of unused gases is of paramount importance. The gases are cracked in a high temperature pyrolytic chamber so that, as far as possible, the toxic waste is in solid form. The waste arsenic is collected by a particulate filter and the remaining vapour is passed through several carbon filters.

1.3.3 Molecular Beam Epitaxy

Molecular beam epitaxy was originally developed by Günther in 1958 [26] who grew III-V binary and ternary polycrystalline layers on glass slides. Monocrystalline epitaxial layer growth had to await the arrival of commercial ultra-high vacuum systems in the middle 1960's and was first achieved by Davey and Pankey in 1968 [27] who produced the first single crystal layers of GaAs. The historical background of MBE and its development up to the end of 1974 has been reviewed by Cho and Arthur [28] whereas the growth of both II-VI and III-V compounds by MBE has been reviewed by Chang and Ludeke [29] and Smith [30]. Compared to MOVPE, the most distinguishing characteristics of MBE are a low growth rate (between 1 and 3 $\AA s^{-1}$ for GaAs), a low growth temperature (less than $630°C$ for GaAs), the ability abruptly to cease or initiate growth, smoother surfaces during growth and the facility for insitu analysis via reflection high energy electron diffraction (RHEED).

Molecular beam epitaxy involves directing molecular or atomic beams onto a heated substrate in an ultra-high vacuum environment, Figure 1.3 [31]. The molecular beams are generated by Knudsen effusion cells operating at temperatures be-

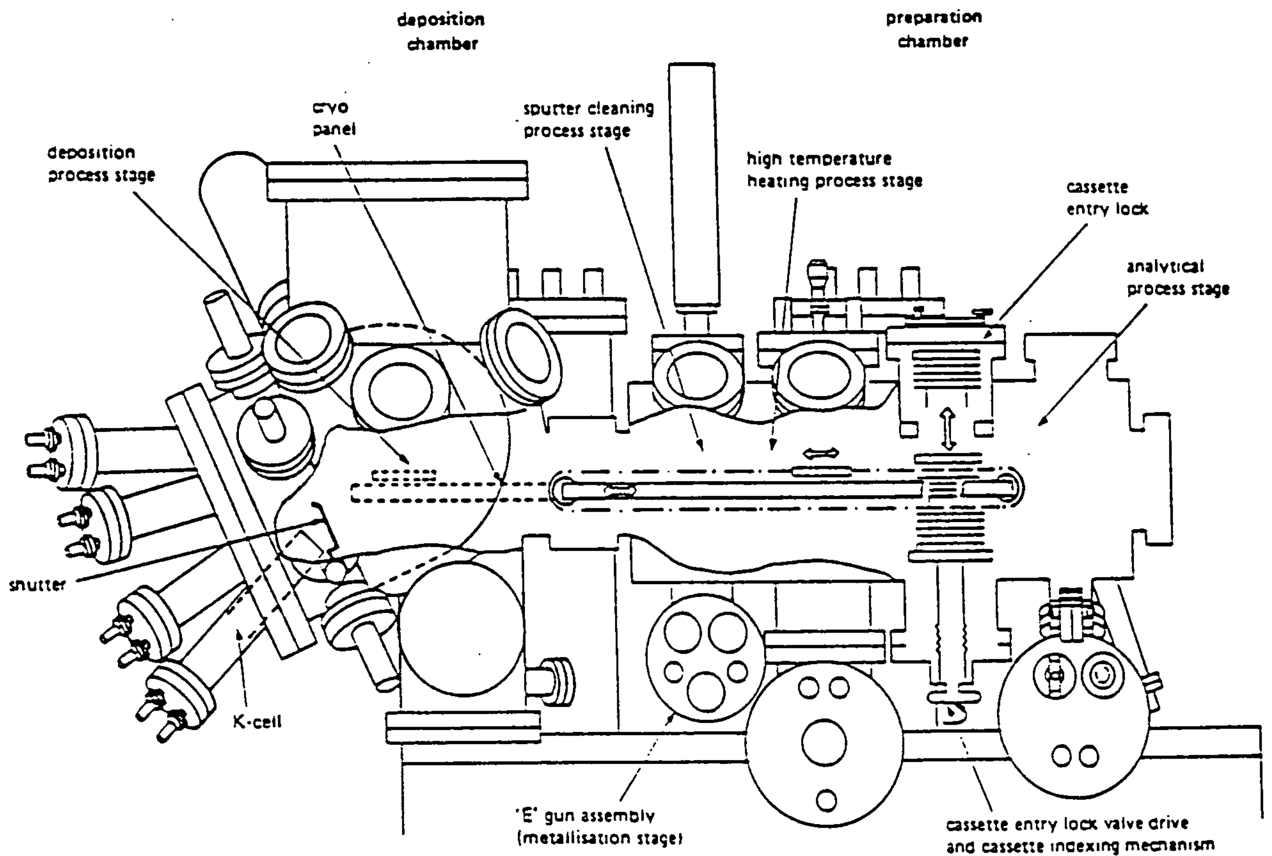

Figure 1.3: Cross-sectional view of an MBE system illustrating the major components. After Davies and Andrews [31].

tween $250°C$ and $1400°C$ with temperature stability to within $\pm 0.002°C$. When the effusion cells are heated the vapour pressure of the elements they contain increases and beams of atoms or molecules are emitted. Their mean free path is long relative to the cell to substrate distance and so they impinge on the heated substrate surface without having undergone collisions. The relative beam intensities are adjusted by altering individual effusion cell temperatures and aperture sizes to allow for the difference in sticking coefficients between the various materials of the epitaxial layers. In a similar fashion to MOVPE, the growth rate of the epitaxial layer is determined by the group III material flux rate provided that an excess flux of group V atoms is present.

The substrate is mounted on a molybdenum block and an arrangement of airlocks and tracks allows sample positioning in line with the molecular beams. Layer thickness and alloy composition varies across the area of the substrate with the local variation in the angle subtended between the molecular beam and the substrate. This effect is counteracted by rotating the sample about the centre of the wafer. Hence epitaxial layers grown by MBE often show a slight radial variation in layer thickness and composition.

1.4 Epitaxial Layer Growth Modes

The deposition of a heteroepitaxial layer commences with the formation of a stable cluster of a few atoms at the substrate surface. The subsequent growth and morphology of the epitaxial layer is strongly dependent on the interatomic properties of the layer/substrate system and the thermodynamics of the growth environment [32]. This leads to a subdivision of the subsequent nucleation processes into three main classes [33].

If the substrate-vacuum interfacial energy is greater than the sum of the energies of the substrate-layer and layer-vacuum interfaces then the formation of the interface between the layer and the substrate is exo-energetic and layer formation is essentially planar. If the bond enthalpies of the deposit material decrease with increasing layer thickness towards the bulk epitaxial layer values then continued growth is also planar. This is referred to as the Frank-van der Merwe growth mode. Systems which exhibit this growth mode are characterised by strong substrate to layer bonding and generally have small lattice misfits and identical crystal structures (e.g. metal-metal and semiconductor-semiconductor systems).

The second growth mode, in contrast with the Frank-van der Merwe mode, is

exhibited by layers which are highly mismatched relative to the substrate (⟩10%) or have a different crystal structure to the substrate. In this scenario formation of the interface is endo-energetic and the layer will preferentially grow in a three dimensional fashion producing ' islands' of layer material which eventually coalesce together. This layer formation process is called the Volmer-Weber or island mode. Bond strengths between atomic species within the layer are much greater than bonds across the interface and layer growth is only possible if a large overpressure of the layer material is sustained. Examples of layer/substrate systems which are deposited by this process include GaAs/Si and CdTe/GaAs. The islands of material can be tilted with respect to each other and are separated by dislocation-rich boundaries. Thin layers of these systems are highly dislocated and imperfect. However as the layer thickness increases the trailing screw sections from dislocation half-loops nucleated at the epitaxial layer surface tend to pin each other and layer perfection increases.

The third layer growth mode, known as the Stranski-Krastanov mode, is an intermediate case of the two modes already discussed. Growth by this process commences with the formation of successive monolayers. Subsequent growth transfers to the formation of three dimensional islands which coalesce to form the layer. The transition from two dimensional to three dimensional growth occurs because of a perturbation in the decrease of layer material bond enthalpies with increasing layer thickness.

The samples examined in this thesis consist of III-V semiconductor layers on III-V semiconductor substrates with a maximum lattice parameter mismatch of 2%. Hence all these samples exhibit the characteristics of Frank-van der Merwe layer growth.

1.5 Critical Parameters for Coherent Epitaxial Layer Growth

For coherent epitaxial layer growth the lattice mismatch is accommodated by elastic strain in the epitaxial layer. Hence for non-zero lattice mismatch, the epitaxial layer is tetragonally distorted to enable lattice coherency across the interface. This is illustrated in Figure 1.4. The degree of tetragonal distortion increases with the magnitude of the lattice mismatch whereas the state of distortion (compression or tension) depends upon the sign of the lattice mismatch.

The epitaxial layer strain can be approximated to a problem in classical elasticity

on the assumption of sharply defined interfaces, a rigid substrate and an elastically isotropic layer subjected to a state of plane stress. Following Davidenkov [34] Chu et al. [35] and Hill [36] have extended this treatment to describe the tetragonal distortion in coherent epitaxial layers. Hornstra and Bartels [37] have demonstrated that for growth on 001 substrates the strained layer lattice parameter perpendicular to the interface, c, is related to the Poisson ration of the epitaxial layer by

$$(c - a_0) = \frac{(1+\nu)}{(1-\nu)} \times (c_0 - a_0) \qquad 1.3$$

where c_0 and a_0 are the bulk lattice parameters of the layer and substrate respectively. Similar expressions are easily developed for growth on substrate surfaces other than 001 [37]. The Poisson ratio is related to the elastic constants C_{12} and C_{11} through equation 1.4 [37].

$$\nu = \frac{C_{12}}{C_{11} + C_{12}} \qquad 1.4$$

Equation 1.3 is more usually expressed in terms of lattice mismatch, m, and an effective lattice mismatch, m^*, as in equation 1.5 [38].

$$m^* = m \times \frac{(1+\nu)}{(1-\nu)} \qquad 1.5$$

Clearly if the mismatch is non-zero then the total strain energy in the layer increases with layer thickness. At a critical layer thickness, h_c, the strain energy in the epitaxial layer reaches a value for which coherent epitaxial growth is no longer favourable. Critical thickness can also be described in Hookean terms as the elastic limit of the layer/substrate system. If the epitaxial layer critical thickness is exceeded then misfit dislocations are formed near the interface which reduce the strain energy in the epitaxial layer. The proportion of the misfit strain which is relaxed by this process is the known as the layer relaxation, R, and is defined by equation 1.6 [40]

$$R = \frac{(a_l - a_0)}{(a_r - a_0)} \qquad 1.6$$

where a_0, a_l and a_r are the lattice parameters parallel to the interface of the substrate, partially strained epitaxial layer and totally unstrained epitaxial layer

respectively. The layer unit cell for a coherent, partially relaxed and fully relaxed epitaxial layer was drawn in Figure 1.4.

The presence of misfit dislocations can have a major effect on device performance. For example, in the quantum well laser the dislocations act as centres for non-radiative recombination of electron-hole pairs and this strongly reduces the luminescence quantum efficiency. The quantum efficiency can drop by more than two orders of magnitude for only a 10 % increase in thickness at the critical thickness for an InGaAs/GaAs quantum well laser [41].

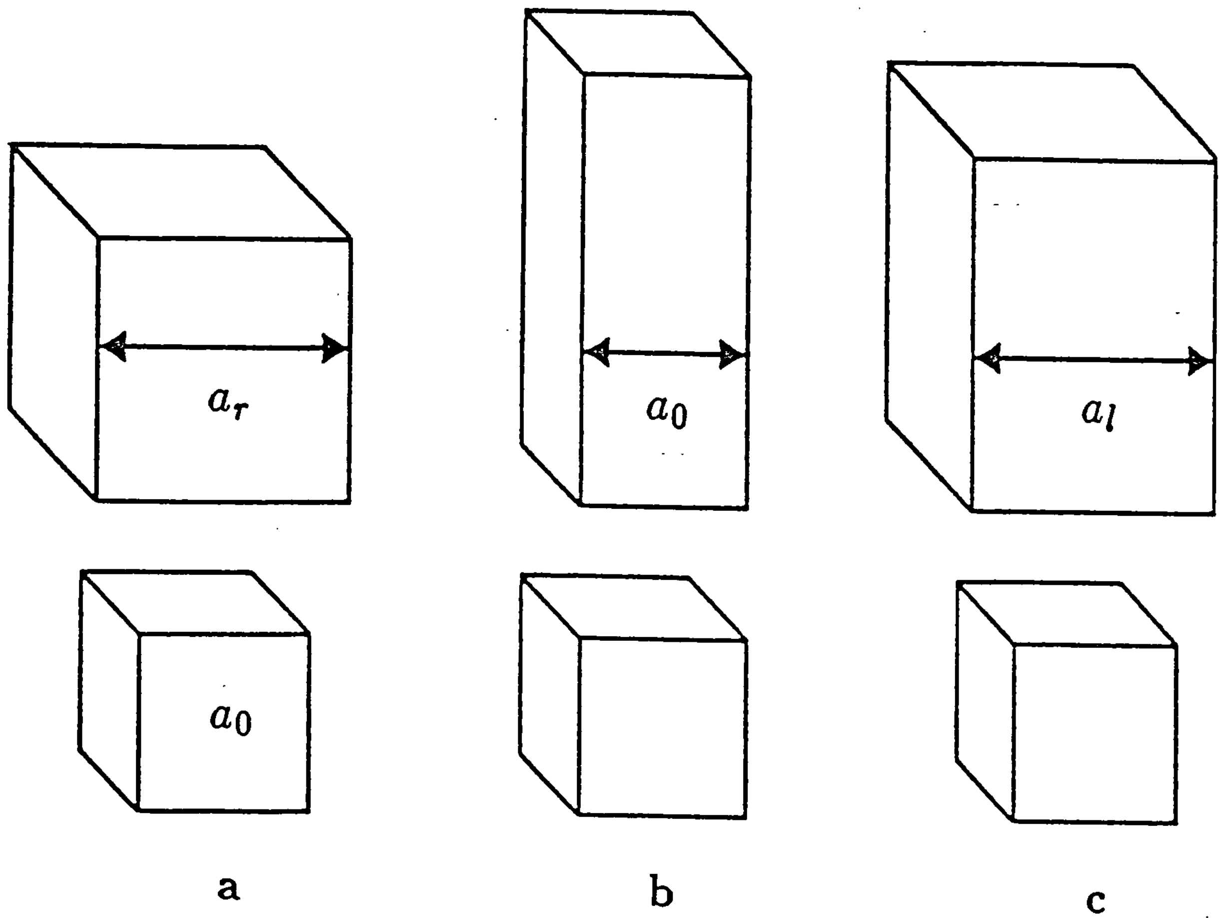

Figure 1.4: Epitaxial layer unit cell; (a) Bulk or fully relaxed, (b) Coherently strained, (c) Partially relaxed. After Halliwell [40]

Chapter 2

Kinematical and Dynamical Diffraction Theory

2.0 Introduction

In essence, X-ray diffractometry examines the diffraction patterns produced when x-rays are scattered by planes of atoms in a crystalline lattice. Analagous to the more familiar optics of visible light, the x-ray wavelength (usually between 0.7 Å and 2 Å) is of the same order of magnitude as the interplanar spacing and so the crystal lattice can be treated as a three dimensional diffraction grating. The condition for constructive interference is given by Bragg's Law, equation 2.1, and is illustrated in Figure 2.1.

$$2dsin\theta_B = n\lambda \qquad 2.1$$

The differential of the Bragg condition for fixed wavelength, equation 2.2, relates the change in Bragg angle, $\delta\theta_B$, required to accommodate a change in interplanar spacing, δd, and is the central equation in double crystal diffractometry. A double crystal rocking curve records the x-ray intensity reflected by a crystalline sample as the sample is 'rocked' through the Bragg condition for a fixed x-ray wavelength.

$$\frac{\delta d}{d} = -cot\theta_B\delta\theta_B \qquad 2.2$$

Crystallographic lattice planes are described in terms of the axial directions defined by the lattice unit cell. In an orthorhombic unit cell with dimensions a, b and c in the [100], [010] and [001] directions respectively The interplanar separation for an *hkl* reflection is given by

$$d_{hkl} = \left(\sqrt{\frac{h^2}{a^2} + \frac{k^2}{b^2} + \frac{l^2}{c^2}}\right)^{-1} \qquad 2.3$$

III-V compounds crystallise in the zinc blende structure which consists of a face

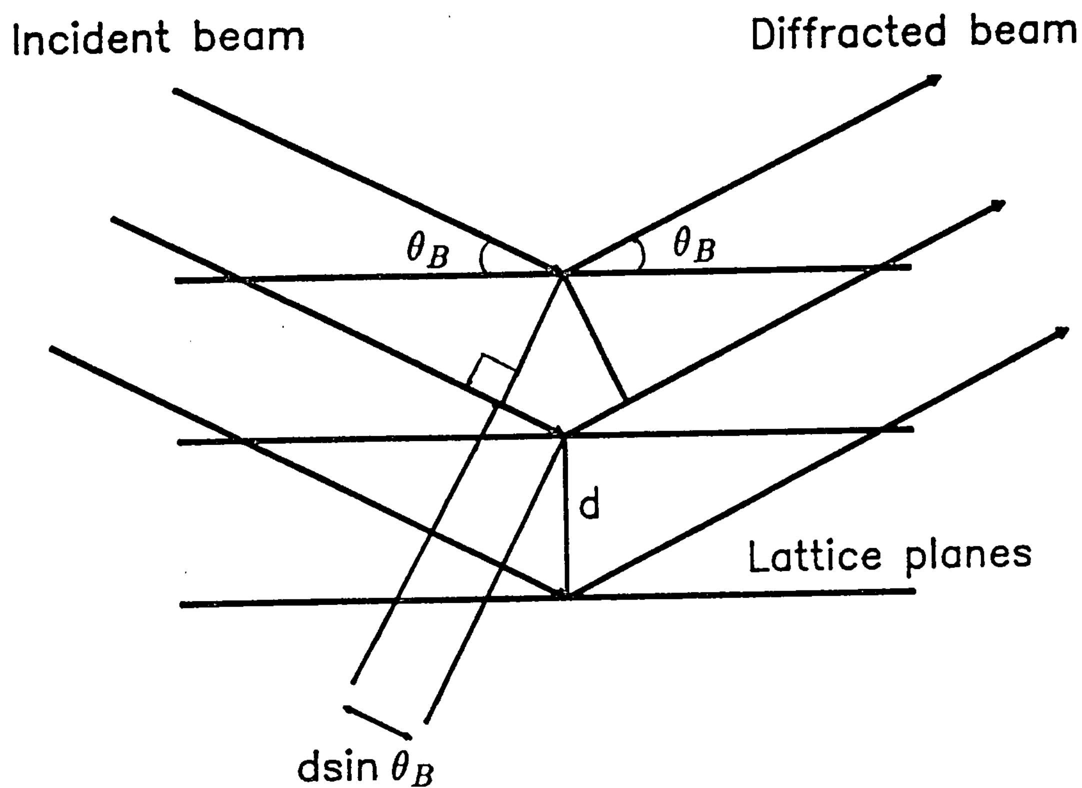

Figure 2.1: Diagram showing that the path difference for beams diffracted by planes d apart is $2dsin\theta_B$. The Bragg condition for constructive interference is $\lambda = 2dsin\theta_B$.

centred cubic lattice with a basis of two atoms. Hence a = b = c and equation 2.3 reduces to equation 2.4.

$$d_{hkl} = \frac{a}{\sqrt{h^2 + k^2 + l^2}} \qquad 2.4$$

Lattice planes which are not parallel to the surface of the crystal are termed asymmetric and in order to find the condition for Bragg diffraction from asymmetric lattice planes (h,k,l) the angle ϕ subtended between these planes and the crystal surface (u,v,w) must be known. Cos ϕ is equal to the dot product of the lattice planes and crystal surface unit normals and is given by equation 2.5

$$cos\phi = \frac{(u, v, w).(h, k, l)}{\sqrt{u^2 + v^2 + w^2}\sqrt{h^2 + k^2 + l^2}} \qquad 2.5$$

In order to maximise the Bragg diffraction profile from a set of crystal lattice planes, the vector normal to the lattice planes should be contained within the diffraction plane. Hence strong Bragg diffraction from asymmetric lattice planes requires that the x-ray beam path is coincident with the projection of the lattice plane normal in the surface of the crystal. For example, a 115 reflection requires that the diffraction plane contains the $[\bar{1}\bar{1}0]$ direction in the crystal whereas a 404 reflection requires that the diffraction plane contains the $[\bar{1}00]$ direction. This criterion groups the crystal lattice planes into diffraction zones. The diffraction zones for a cubic lattice viewed along the $[00\bar{1}]$ direction are illustrated in Figure 2.2 where the diffraction zones lie on the solid outer circle and the crystal lattice planes lie within. In this projection the hkl zone contains all reflections which lie on a straight line from the outer circle to, but not including, the 001 reflection. The symmetric reflections are superimposed upon the 001 reflection.

Thus far the geometry of the Bragg condition has been presented without investigation into the relative intensities of the various possible reflections. Calculation of these diffracted intensities relies on the kinematical and dynamical theories of x-ray scattering which are discussed in sections 2.2 and 2.3.

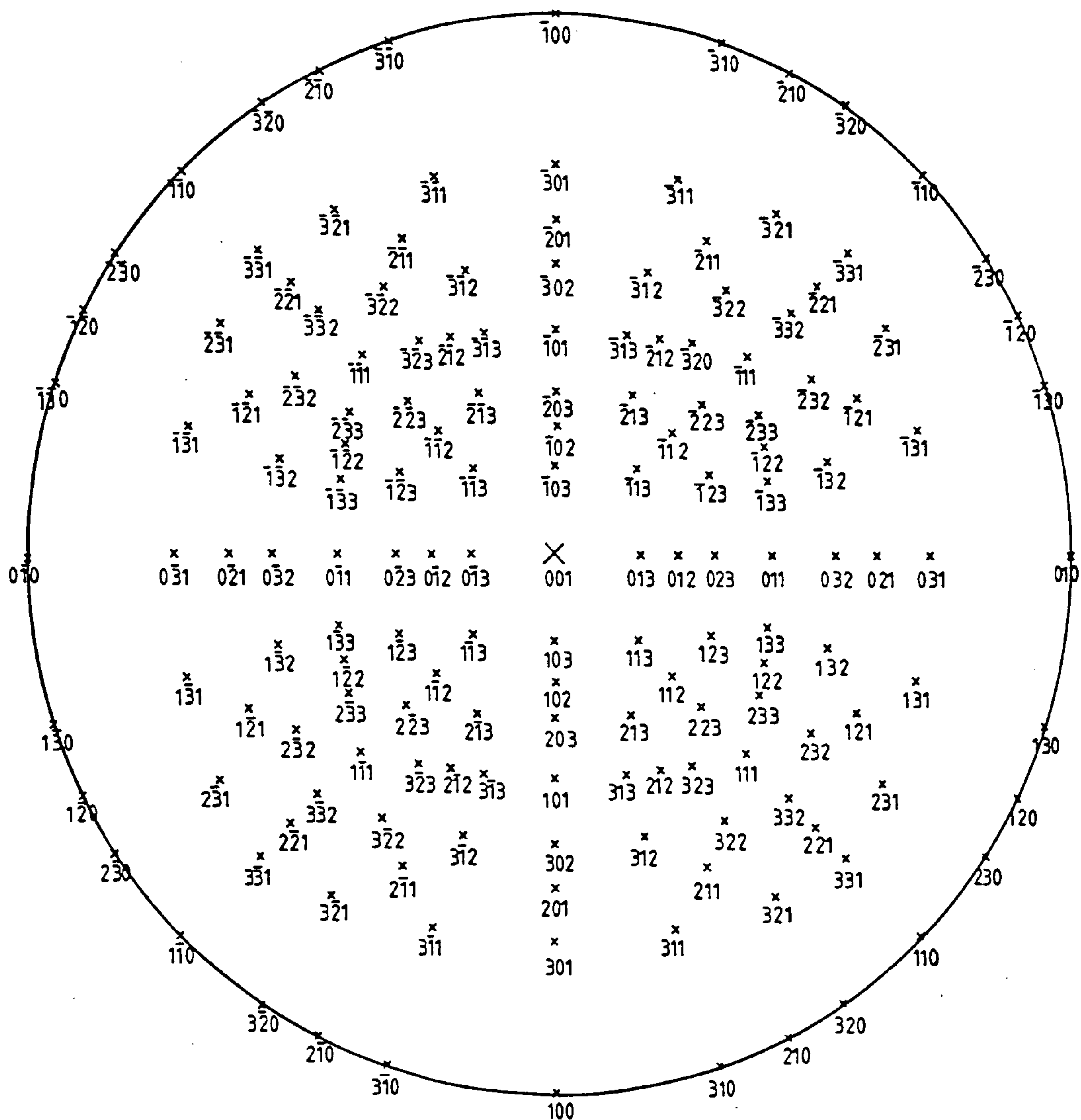

Figure 2.2: The reflections within each diffraction zone for a cubic lattice viewed along the $[00\bar{1}]$ direction

2.1. Interaction between X-rays and Matter

When an x-ray beam passes through a material medium its intensity is reduced by a variety of interaction processes which may be grouped under two general headings *absorption* and *scattering.*

The *absorption* of x-ray photons by atoms leads, among other effects, to the ejection of electrons from inner atomic shells and consequently transitions between electrons in higher energy levels to fill the vacancies so created. These electronic transitions are accompanied by the emission of x-rays of definite wavelength which is determined from the difference in energy between the initial and final state of the electron transition. The flourescent x-rays so produced may be reabsorbed by another atom leading to the ejection of electrons from shells of even higher energy and emission of flourescent x-rays of lower energy and therefore of longer wavelength. Absorption phenomena are utilized in x-ray flourescence analysis (EXAFS) which, among other applications, can be employed to detect individual elements within a material of unknown composition.

The *scattering* of x-rays by an atom may occur in either of two ways, both of which again involve interaction between x-radiation and electrons in the medium. An x-ray photon passing close to a loosely bound or free electron will be deflected by the electromagnetic field of the electron and will impart some of its energy to the electron as kinetic energy. Radiation so scattered is called Compton modified radiation and is not coherent with the incident x-ray beam. Hence this radiation cannot take part in a diffraction process.

The second scattering interaction occurs between x-ray radiation and tightly bound atomic electrons. An x-ray photon is an electromagnetic wave characterised by an electric field whose strength varies sinusoidally with time. The x-ray photon's oscillating electric field will force any tightly bound electron it encounters into oscillatory motion about its mean position. In turn, the oscillating electron radiates x-radiation which is coherent with the incident x-ray photon i.e. there is a definite relationship between the phase of the scattered radiation and the phase of the incident x-ray photon.

The diffraction profile of the coherently scattered x-radiation can be described in terms of two theories, kinematical diffraction and dynamical diffraction. Kinematical diffraction theory is based on the assumption that the loss of intensity in the incident x-ray beam as it propagates through the material is negligible and hence multiple scattering processes do not occur. Dynamical theory is not restricted by this

assumption and is based on the solution of Maxwell's equations for the propagation of an electromagnetic wave in a dielectric medium. Hence kinematical theory can be employed to describe the intensity of Bragg diffraction profiles from thin epitaxial layers and polycrystalline samples whereas dynamical theory must be employed to describe Bragg diffraction from thick perfect epitaxial layers. Kinematical theory enables a qualitative understanding of the diffraction process and for this reason is often invoked as a first approximation. Dynamical theory, although more accurate, is cumbersome and does not facilitate a physical interpretation of the diffraction process.

2.2 Kinematical X-ray Diffraction

The theory of the kinematical diffraction of x-rays from a crystal lattice has been discussed in detail by many authors [1,2,3]. In order to develop the kinematical theory, the x-ray wavelength is assumed to be far from an absorption edge. Hence the refractive index of the material can be approximated to unity and the scattered x-rays have a phase difference relative to the incident x-ray radiation which includes a phase change of π. Since the phase change of π is the same for all the scattering centres in the crystal, it can be ignored. The incident x-ray beam is assumed to be a plane wave and the scattered x-radiation is observed at a distance $|\underline{R}|$, from the origin of the unit cell, which is much larger than the x-ray wavelength; i.e. kinematical diffraction is an example of Fraunhofer, as distinct from Fresnel, diffraction.

In an analagous fashion to Fraunhofer diffraction from an aperture, the amplitude and the phase of the x-radiation scattered by a crystal, $G(\underline{h})$, is related to the Fourier transform of the electron density in the reciprocal space of the crystal through equation 2.6

$$G(\underline{h}) = A \int^{V} g(\underline{r})\, exp(2\pi i \underline{r}.\underline{h})\, d\underline{r} \qquad 2.6$$

$g(\underline{r})$ represents the electron density at a position vector, $\underline{r}$, within the volume of the crystal, V and $\underline{h}$ is a vector in the reciprocal space of the crystal. A is a constant which is derived from the Thompson model.

If unpolarised radiation of amplitude E_0 and wavelength λ is incident on a free classical electron of charge e and mass m at the origin, it can be shown that the amplitude, A, of the scattered radiation at a displacement $\underline{R}$ from the electron, where $|\underline{R}| >> \lambda$, is

$$A = \frac{E_0}{R}\frac{e^2}{mc^2}\left(\frac{1 + cos^2\, 2\theta}{2}\right)^{\frac{1}{2}} \qquad 2.7$$

where c is the velocity of light and 2θ is the angle between the scattered beam and the forward direction of the incident beam. The factor $\{(1 + cos^2\, 2\theta)/2\}^{\frac{1}{2}}$ arises from the partial polarisation of the scattered beam.

The Fourier transform of the electron density in the cystal, $g(\underline{r})$ for a reciprocal lattice vector $\underline{h}$ is known as the Structure Factor, $F_{\underline{h}}$. The crystal consists of a basis which is repeated N times at lattice positions $\underline{r_j}$ and so $F_{\underline{h}}$ can be written as

$$F_{\underline{h}} = \sum_{j=1}^{N} F_B\, exp(2\pi i \underline{r}_j.\underline{h}) \qquad 2.8$$

where F_B is the Fourier transform of the electron density of the basis. The vector $\underline{r}_j$ is expressed as (x_j, y_j, z_j), the coordinate position of the jth lattice point in terms of the unit cell dimensions. It can be shown that the integral in equation 2.6 is zero for reciprocal lattice vectors $\underline{h}$ which do not represent a lattice plane in the crystal, hkl. Hence equation 2.8 reduces to equation 2.9

$$F_{hkl} = \sum_{j=1}^{N} F_B\, exp\,[2\pi i\,(hx_j + ky_j + lz_j)] \qquad 2.9$$

The basis consists of n atoms where the coordinate position of the pth atom in the basis is (X_p, Y_p, Z_p). Hence equation 2.9 is expanded as equation 2.10

$$F_{hkl} = \sum_{j=1}^{N} exp\,[2\pi i\,(hx_j + ky_j + lz_j)] \times \sum_{p=1}^{n} f_p exp\,[2\pi i\,(hX_p + kY_p + lZ_p)] \qquad 2.10$$

where f_p is the Atomic Scattering Factor of the pth atom in the basis.

The scattered intensity from the crystal, $I(\underline{h})$, is related to $G(\underline{h})$ by equation 2.11

$$I(\underline{h}) = G(\underline{h}) \; . \; G(\underline{h})^* \qquad 2.11$$

where $G(\underline{h})^*$ is the complex conjugate. Hence the intensity of a reflection (h,k,l) is proportional to F^2_{hkl}.

Group III-V compounds crystallise in the zinc blende structure. The lattice is face centred cubic and the basis consists of two atoms; a group III atom at the origin and a group V atom at fractional coordinate position (1/4, 1/4, 1/4). Hence the relative intensities of the hkl reflections are given by equations 2.12

$$F^2_{hkl} = 16(f_{III} + f_V)^2 \qquad hkl \quad even \qquad h+k+l = 4n$$
$$F^2_{hkl} = 16(f_{III} - f_V)^2 \qquad hkl \quad even \qquad h+k+l = 4n+2$$
$$F^2_{hkl} = 16(f^2_{III} + f^2_V) \qquad hkl \quad odd$$
$$F^2_{hkl} = 0 \qquad hkl \quad mixed \qquad 2.12$$

Silicon and germanium crystallise in the diamond structure wherein the lattice is face centred cubic and the basis consists of a group IV atom at the origin and a group IV atom at fractional coordinate position (1/4,1/4,1/4). Hence the relative intensities of the hkl reflections, obtained from equations 2.12, are given by equations 2.13.

$$F^2_{hkl} = 64\, f^2_{IV} \qquad hkl \quad even \qquad h+k+l = 4n$$
$$F^2_{hkl} = 0 \qquad hkl \quad even \qquad h+k+l = 4n+2.$$
$$F^2_{hkl} = 32\, f^2_{IV} \qquad hkl \quad odd$$
$$F^2_{hkl} = 0 \qquad hkl \quad mixed \qquad 2.13.$$

2.3 Dynamical X-ray Diffraction

Dynamical theory is not restricted by the assumptions necessary for kinematical theory. In other words, absorption as a function of penetration depth in the crystal sample and the existence of multiple scattering within the crystal are incorporated in the theory. If the angle subtended between the incident x-ray beam, $\underline{I}_0$, and the crystal lattice planes satisfies the Bragg condition for the wavelength of the radiation then we expect to observe a reflected x-ray beam, $\underline{I}_1$ Figure 2.3. However the angle subtended between the reflected x-ray beam and these crystal lattice planes also satisfies the Bragg condition and hence leads to a second Bragg reflected x-ray beam $\underline{I}_2$ which is parallel to the incident x-ray beam. The kinematical theory neglects this second reflected x-ray beam whereas dynamical theory, a more rigorous theory of x-ray diffraction, makes proper allowance for multiple Bragg diffraction in the crystal. Since the magnitude of the second reflected x-ray beam from a single layer is very small, the effect is only of importance when it can build up over a large number of layers in a perfect crystal. Hence kinematical theory is still a good approximation when applied to thin layers of perfect crystal or highly imperfect crystals consisting of very small mosaic blocks.

The first dynamical theory of x-ray diffraction was given by Darwin in 1914 [4] while a completely different treatment was presented independently by Ewald in 1916 [5] and it is from the terminology in these papers that the name *dynamical theory* has come into use. In 1931 Von Laue [6] reformulated the Ewald treatment as a problem involving the solution of Maxwell's equations for a medium with a periodic complex dielectric constant. General introductions to the different forms of the dynamical theory can be found in books by James [7], Zachariasen [8] and Pinsker [9] whereas reviews of dynamical theory have been written by Batterman and Cole [10], Authier [11] Hart [12] and Tanner [13].

In Bragg reflection we are, by definition, interested in the elastic scattering of photons by a periodic medium: the crystal. The incident wave and the diffracted waves inside the crystal have their wavevectors, $\underline{K}_0$ and $\underline{K}_h$; restricted by the conservation of energy and momentum. Thus

$$\hbar\omega_0 = \hbar\omega_h \qquad 2.14$$

where $\hbar$ is Planck's constant divided by 2π. Outside the crystal this implies that the wavevectors of the incident and diffracted waves are linked by $|\underline{K}_0^i| = |\underline{K}_h^i| = k$.

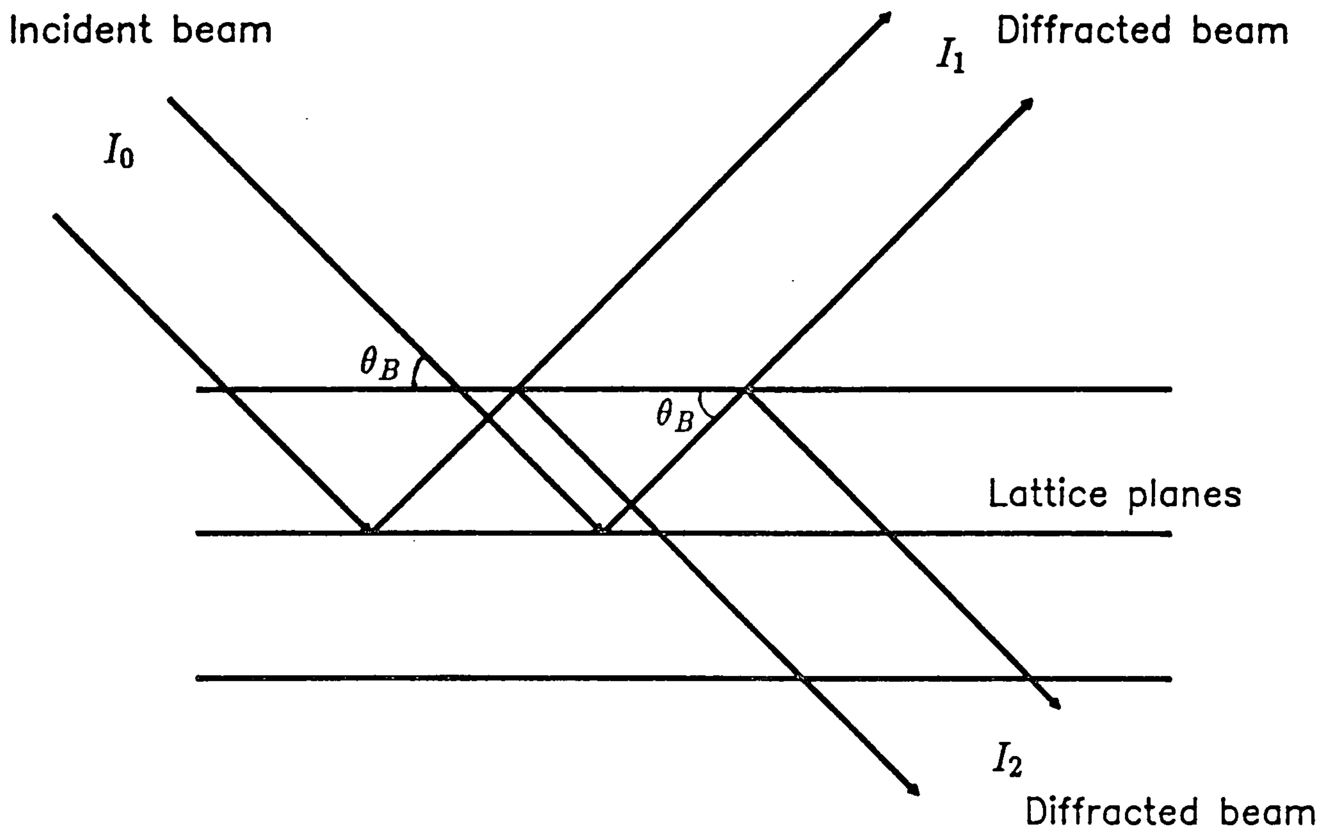

Figure 2.3: Diagram showing incident and diffracted beams at the Bragg condition. The intensity of diffracted beam I_2 must be considered when examining diffraction from thick perfect crystals.

Inside the crystal the Laue condition must be satisfied

$$\underline{K}_0 + \underline{h} = \underline{K}_h \qquad 2.15$$

where $\underline{h}$ is a vector in the reciprocal lattice of the crystal. If the x-ray wavelength is far from an absorption edge then the refractive index of the dielectric medium is approximately unity and so

$$|\underline{K}_0| \simeq |\underline{K}_h| \simeq |\underline{K}_0^i| = |\underline{K}_h^i| = \frac{1}{\lambda} \qquad 2.16$$

Hence when the Bragg condition is approximately satisfied inside the crystal there are two x-ray waves whose difference in wavevector is exactly equal to a reciprocal lattice vector, $\underline{h}$, and this sets up a standing wavefield whose spacing and orientation are exactly those of the diffracting atomic planes. Two electromagnetic waves thus constrained must be related by a constant phase factor and so all that remains is to determine the amplitudes and phases of the two waves. This is achieved in three stages: first a set of waves is found which can exist in dynamical equilibrium in an infinite perfect crystal; then the solutions in this set which are excited by the incident wave are determined; and finally the effects of absorption in the crystal, apertures or other experimental conditions, are investigated. The relative phases and amplitudes of the participating waves are determined from the boundary conditions at the surface of the crystal.

The relative magnetic permeability, μ, is assumed to be unity and Maxwell's equations are manipulated to form equation 2.17

$$\nabla \times \nabla \times (1-\chi)\underline{D} = -\frac{1}{c^2}\frac{\partial^2 \underline{D}}{\partial t^2} \qquad 2.17$$

In order to find solutions of Maxwell's equations in a complex periodic medium, a convenient expression for the susceptibility, χ, of the medium must be found. Through the inverse Fourier transform of equation 2.6, the electron density in the scattering volume V can be expanded as a Fourier sum over the reciprocal lattice, equation 2.18.

$$g(r) = \frac{1}{V}\sum_{\forall\, \underline{h}} F_{\underline{h}} exp(-2\pi i \underline{h}.\underline{r}) \qquad 2.18$$

It can be shown [12] that if $\varepsilon \simeq 1$, where ε is the relative permittivity, then χ is given by

$$\chi = -\frac{e^2\lambda^2}{\pi mc^2} g(\underline{r}) \qquad 2.19$$

The susceptibility is expanded as a Fourier sum over the reciprocal lattice,

$$\chi = \sum_{\forall\ \underline{h}} \chi_{\underline{h}} exp(-2\pi i \underline{h}.\underline{r}) \qquad 2.20$$

so that, by comparing terms,

$$\chi_{\underline{h}} = -\frac{e^2\lambda^2}{\pi mc^2 V} F_{\underline{h}} \qquad 2.21$$

We are now in a position to look for solutions to equation 2.17. These solutions are known as Bloch waves, even though they were first proposed by Ewald, and are given in equation 2.22

$$\underline{D} = \sum_{\forall\ \underline{h}} \underline{D}_{\underline{h}} exp(-2\pi i \underline{K}_h.\underline{r}) \qquad 2.22$$

where the $\underline{K}_h$ are linked by the Laue condition, equation 2.15. The Bloch solutions, equation 2.22, and the Fourier series representing the susceptibility, equation 2.20, are substituted into equation 2.17 to form equation 2.23.

$$\sum_{\forall\ \underline{h}'} \{\chi_{\underline{h}-\underline{h}'} \left(\underline{K}_{\underline{h}}.\underline{D}_{\underline{h}'}\right) \underline{K}_{\underline{h}} - \chi_{\underline{h}-\underline{h}'} \left(\underline{K}_{\underline{h}}.\underline{K}_{\underline{h}}\right) \underline{D}_{\underline{h}'}\} = \{k^2 - \underline{K}_{\underline{h}}.\underline{K}_{\underline{h}}\}\underline{D}_{\underline{h}} \qquad 2.23$$

where h' ranges over all the wavevectors in the reciprocal space of the crystal lattice and $k = \omega/c$ is the vacuum wavevector. The components $\underline{D}_h$, the Fourier coefficient of each solution, are obtained by imposing the two beam approximation.

The Laue condition, equation 2.15, is often represented by the Ewald sphere construction. This consists of a sphere of radius $|\underline{K}_0|$ whose surface contains the origin and the position of the Bragg reflection in reciprocal space. For x-ray diffraction the radius of the Ewald sphere is of the order of $1\AA^{-1}$ and so the curvature of the sphere is large compared to the spacing between adjacent reflection points

in reciprocal space. Hence the probability of two or more reflection points being contained within the surface of the sphere is very small and this occurence can be neglected. This assumption is not true for the diffraction of 10 Kev electrons or γ rays where the radius of the Ewald sphere is of the order of $30\mathring{A}^{-1}$ and it is quite possible to excite several reflections at once.

Hence, on the assumption that the Ewald sphere cannot be orientated within the crystal reciprocal space to intersect more than one lattice point other than the origin, then x-rays of the correct wavelength to satisfy the Bragg condition will have wavevectors which are either parallel to the incident x-ray beam, $\underline{K}_0$, or parallel to the diffracted beam, $\underline{K}_h$ and so equation 2.23 reduces to equations 2.24.

$$\chi_{\underline{h}}\left(\underline{K}_h.\underline{D}_0\right)\underline{K}_h - \chi_{\underline{h}}\left(\underline{K}_h.\underline{K}_h\right)\underline{D}_0 + \chi_{\underline{0}}\left(\underline{K}_h.\underline{D}_h\right)\underline{K}_h - \chi_{\underline{0}}\left(\underline{K}_h.\underline{K}_h\right)\underline{D}_h = \left(k^2 - \underline{K}_h.\underline{K}_h\right)\underline{D}_h \qquad 2.24a$$

$$\chi_{\underline{\bar{h}}}\left(\underline{K}_0.\underline{D}_h\right)\underline{K}_0 - \chi_{\underline{\bar{h}}}\left(\underline{K}_0.\underline{K}_0\right)\underline{D}_h + \chi_{\underline{0}}\left(\underline{K}_0.\underline{D}_0\right)\underline{K}_0 - \chi_{\underline{0}}\left(\underline{K}_0.\underline{K}_0\right)\underline{D}_0 = \left(k^2 - \underline{K}_0.\underline{K}_0\right)\underline{D}_0 \qquad 2.24b$$

Equation 2.24a represents the interaction between the diffracted x-ray beam $\underline{K}_h$ and the incident x-ray beam $\underline{K}_0$ and equation 24b represents the interaction between x-rays which have been multiply scattered back into the incident x-ray beam. The scalar product of equation 2.24a with $\underline{D}_h$ and the scalar product of equation 2.24b with $\underline{D}_0$ are taken and, remembering that electromagnetic waves are transverse i.e. $\underline{K}_0.\underline{D}_0 = \underline{K}_h.\underline{D}_h = 0$, equations 2.25 are formed.

$$k^2\, C\, \chi_{\underline{\bar{h}}}\underline{D}_h + \left[k^2\left(1 + \chi_{\underline{0}}\right) - \underline{K}_0.\underline{K}_0\right]\underline{D}_0 = 0 \qquad 2.25a$$

$$\left[k^2\left(1 + \chi_{\underline{0}}\right) - \underline{K}_h.\underline{K}_h\right]\underline{D}_h + k^2\, C\, \chi_{\underline{h}}\underline{D}_0 = 0 \qquad 2.25b$$

where

$$C = \widehat{\underline{D}_0}.\widehat{\underline{D}_h} = 1 \qquad for\ \sigma\ polarization$$

$$C = cos2\theta_B \qquad for\ \pi\ polarization \qquad 2.26$$

For a non trivial solution,

$$\begin{vmatrix} k^2\, C\, \chi_{\bar{\underline{h}}} & k^2\left(1+\chi_{\underline{0}}\right) - \underline{K}_{\underline{0}}.\underline{K}_{\cdot\underline{0}} \\ k^2\left(1+\chi_{\underline{0}}\right) - \underline{K}_{\underline{h}}.\underline{K}_{\underline{h}} & k^2\, C\, \chi_{\underline{h}} \end{vmatrix} = 0 \qquad 2.27$$

It is convenient to write

$$\alpha_0 = \frac{k}{2}\left[\underline{K}_{\underline{0}}.\underline{K}_{\underline{0}} - k^2\left(1+\chi_0\right)\right] \qquad 2.28$$

and

$$\alpha_h = \frac{k}{2}\left[\underline{K}_{\underline{h}}.\underline{K}_{\underline{h}} - k^2\left(1+\chi_0\right)\right] \qquad 2.29$$

which lead to the fundamental equation in dynamical theory, the equation of the dispersion surface, equation 2.30. The dispersion surface is the surface in the reciprocal space of the crystal which describes the values of the wavevectors $\underline{K}_{\underline{0}}$ and $\underline{K}_{\underline{h}}$ which are allowed to exist within the crystal.

$$\alpha_0 \alpha_h = \frac{k^2}{4}\, C^2\, \chi_{\underline{h}}\, \chi_{\bar{\underline{h}}} \qquad 2.30$$

Each point on the dispersion surface determines a pair of allowed wavevectors in the crystal and the corresponding amplitude ratio of these Bloch waves. The dispersion surface is best understood by constructing the surface geometrically in reciprocal space. A sphere of radius nk, where $n = \left(1 + \chi_{\underline{0}}/2\right)$ is drawn within a sphere of radius k at two points in reciprocal space of the crystal; the origin and the position of the crystal reflection $\underline{h}$, Figure 2.4. The region surrounding the intersection of the spheres contains points representing pairs of wavevectors which satisfy equation 2.30. When equation 2.30 is investigated graphically, Figure 2.5, it can be seen that surfaces containing points representing allowed pairs of wavevectors can be drawn which are asymptotic to the surfaces of the spheres near the region of intersection. As this region is very small compared to the radii of the spheres, then the curvature of the spheres can be approximated by tangents and the equation of the dispersion surface, equation 2.30, becomes a hyperboloid of revolution. Generally there are four dispersion surface branches, two each for the two polarisation states.

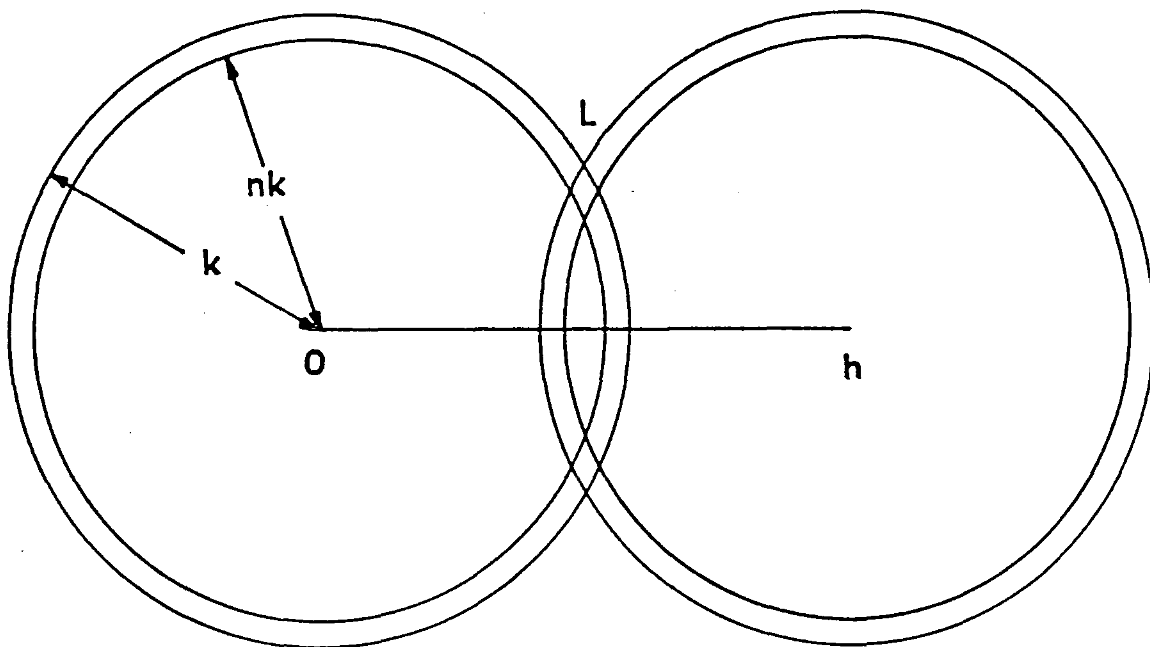

Figure 2.4: Spheres in reciprocal space about the lattice points O and h. After Tanner [13]

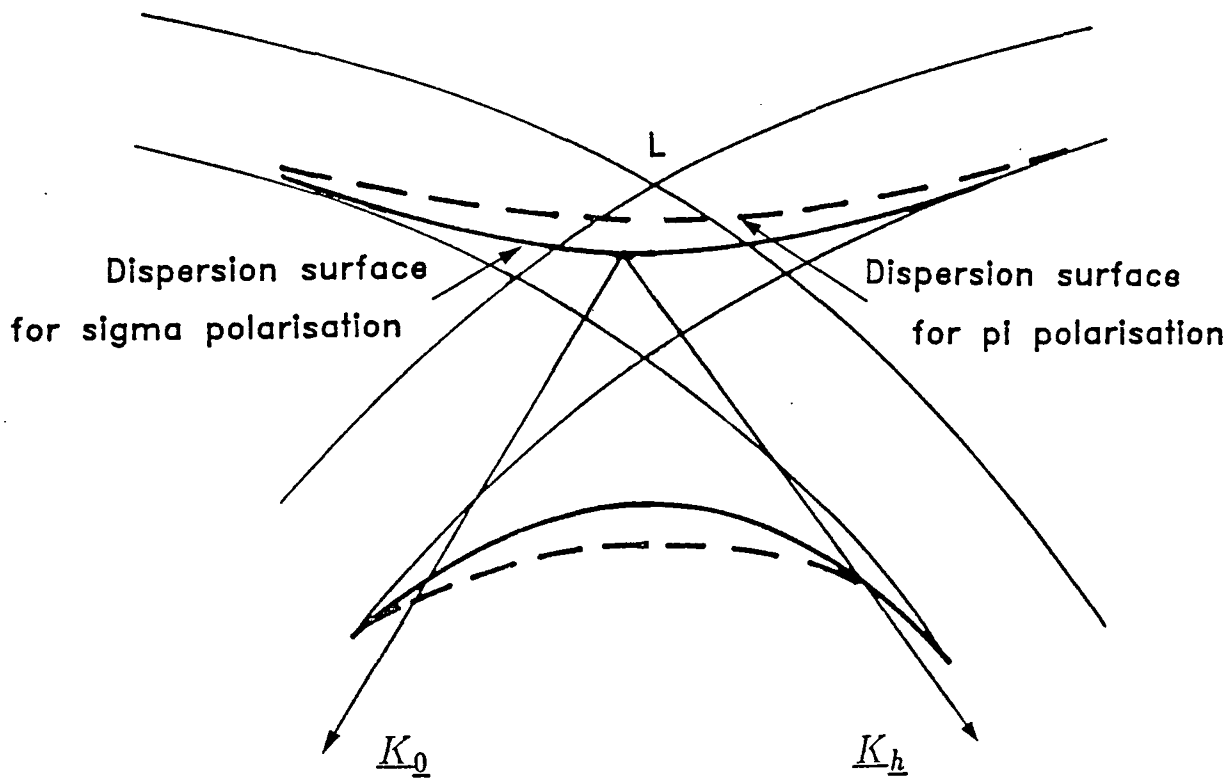

Figure 2.5: The dispersion surface construction. This is a magnified drawing of the region around L on figure 2.4. After Tanner [13]

The amplitudes and wavevectors of a pair of waves which satisfy the Bragg condition in the crystal, $\underline{K}_0$ and $\underline{K}_h$ are determined from the corresponding position on the dispersion surface, which is known as a tie point. Application of the boundary conditions, some of which are specific to the particular experiment, determines the number of tie points excited on the dispersion surface by enabling the wave-vector and the amplitude to be matched across the crystal surface. The first of these results from the transverse nature of an electromagnetic wave; the tangential components of both $\underline{E}$ and $\underline{H}$ must remain continuous across the crystal surface. Hence the wavevectors inside the crystal can only differ from those outside the crystal by a vector perpendicular to the crystal surface. This condition determines which tie points are excited in the dispersion surface and this allows calculation of several important relations which are summarised here.

The full width at half maximum intensity of a Bragg reflection profile is given by

$$\Delta\theta_{\frac{1}{2}} = \frac{2\,C\,\left(\chi_{\underline{h}}\,\chi_{\overline{\underline{h}}}\right)^{\frac{1}{2}}}{sin\ 2\theta_B}\sqrt{\frac{|\gamma_{\underline{h}}|}{\gamma_{\underline{0}}}} \qquad 2.31$$

where $\gamma_{\underline{h}}$ and $\gamma_{\underline{0}}$ are the direction cosines of the incident and diffracted beams respectively.

The integrated intensity, as a fraction of the incident intensity, $\delta I/I_0$, of the diffraction profile for Bragg reflection from a crystal is given by

$$\frac{\delta I}{I_0} = \frac{8}{3}|C|\frac{\chi_{\underline{h}}}{sin\ 2\theta_B}\sqrt{\frac{|\gamma_{\underline{h}}|}{\gamma_{\underline{0}}}} \qquad 2.32$$

Hence in the case where the diffraction profile must be described by the dynamical theory of x-ray scattering then the intensity of a Bragg reflection is found to be directly proportional to the structure factor. This is in contrast to the case where the diffraction profile can be closely described by the kinematical theory and the scattered intensity is proportional to the square of the structure factor.

Dynamical theory predicts interference oscillations, called Pendellösung fringes, in the wings of the rocking curve for a thin crystal. This is illustrated in Figure 2.6, an 004 copper $K_{\alpha 1}$ double crystal rocking curve of sample GaAs1, which is discussed in detail later. In order to observe Pendellösung fringes the the interface must appear to be uniform across the width of the x-ray beam. The thickness of

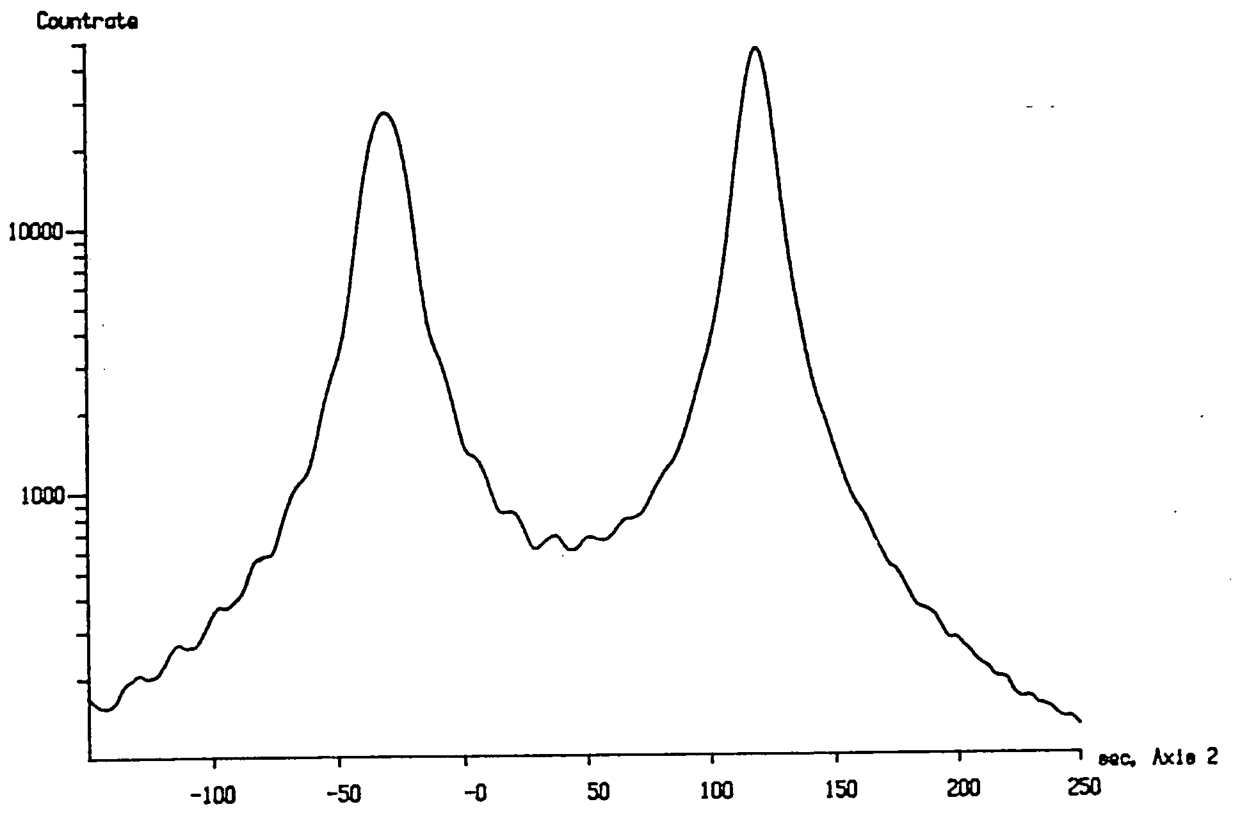

Figure 2.6: 004 double crystal rocking curve of sample GaAs1 showing Pendellösung fringes

the epitaxial layer, t, is related to the period of the fringes observed on the rocking curve,P (in radians), by equation 2.33 [14].

$$t = \frac{\lambda \; sin\vartheta}{P sin 2\theta_B} \qquad 2.33$$

where ϑ is the angle subtended between the diffracted beam and the sample surface. The period of the interference fringes in figure 2.6 is (15.6 ± 0.7) seconds which implies an epitaxial layer thickness of (1.21 ± 0.05) μm.

2.4 Simulation by the Takagi-Taupin Equations

Kinematical diffraction theory has been successfully applied to the simulation of double crystal diffraction profiles from a variety of thin epitaxial layers which incorporate depth (z) dependent variations in lattice parameter and structure factor. Segmüller [15] has considered a plane wave with unit amplitude incident on a planar structure with a structure factor distribution F(z). On the assumption that the scattering is weak and absorption can be neglected then the diffracted amplitude as a function of the angle subtended between the x-ray beam and the lattice planes, $E(\theta - \theta_B)$, is given by the Fourier transform of the structure factor distribution, equation 2.34

$$E(\theta - \theta_B) = \int_{-\infty}^{+\infty} F(z) \, exp \; - i\alpha(\theta - \theta_B) z \, dz \qquad 2.34$$

where α is a geometric term related to the phases of the incident and reflected x-radiation at a depth z. Clearly the above assumption cannot be applied to the substrate and so the relative integrated intensities of the substrate and epitaxial layer Bragg diffraction profiles predicted by a simulation program based on kinematical theory will be incorrect. Instead a simulation program based on the dynamical theory of x-ray diffraction must be employed in order to obtain the correct relative integrated intensities. However simulations of double crystal x-ray diffraction rocking curves based on kinematical theory can be up to three orders of magnitude faster than the equivalent simulation from a program based on dynamical theory [16] and for this reason are useful as a first approximation in understanding complicated double crystal rocking curve profiles. The semi-kinematical approximation represents a good compromise wherein the epitaxial layer structure is treated kinematically and the substrate is treated dynamically [17].

In order to develop a simulation program based on the dynamical theory of diffraction, the generalised diffraction theory, which was developed independently by Takagi [18,19] and Taupin [20], is employed. The wavefield inside the crystal is described in a similar form to that presented in section 2.3, with the exception that $\underline{D}_0$ and $\underline{D}_h$ now are the total amplitudes of the wavefield in the forward and diffracted beam directions, which may also be slowly varying functions of position across the x-ray beam. Also, $|\underline{K}_0| = nk$ where n is the refractive index far from the Bragg condition. These conditions, in addition to the two-beam approximation, reduce the analysis presented in section 2.3 to two coupled partial differential equations expressed along the forward and diffracted beam directions $\underline{s}_0$ and $\underline{s}_g$, equations 2.35

$$\frac{i\lambda}{\pi}\frac{\partial \underline{D}_0}{\partial \underline{s}_0} = \chi_0 \underline{D}_0 + C\ \chi_{\bar{\underline{h}}} \underline{D}_h$$

$$\frac{i\lambda}{\pi}\frac{\partial \underline{D}_h}{\partial \underline{s}_h} = (\chi_0 - \delta_h)\, \underline{D}_h + C\ \chi_h \underline{D}_0 \qquad 2.35$$

where δ_h, which represents the deviation of the incident wave from the exact Bragg condition, is given by equation 2.36

$$\delta_h = -2\Delta\theta_h\ sin2\theta_B \qquad 2.36$$

The parameter $\Delta\theta_h$ is the local deviation from the exact Bragg angle, taking account of lattice strains, and θ_B is the local exact (vacuum) Bragg angle. The epitaxial layer is subdivided into a series of laminae parallel to the interface of constant composition, structure and thickness wherein the Takagi-Taupin equations can be solved analytically. Hence the reflectivity at the top of a lamina can be calculated in terms of the reflectivity at the bottom of a lamina. The reflectivity of the substrate is calculated first and this is employed iteratively to calculate the reflectivities of the laminae through the thickness of the epitaxial layer and hence the total reflectivity of the epitaxial layer. The calculation is repeated for a series of angles across the reflectivity profile and the final double crystal rocking curve is derived by correlating the reflectivity profile from the sample crystal with the reflectivity profile from the Bragg reflection at the first crystal. As a characteristic line x-ray source produces randomly polarised x-rays, the calculation is repeated for both states of polarisation.

The core of the simulation program employed in this thesis was written by Capano [21] and is marketed by Bede Scientific Instruments Ltd. as the Rocking Curve Analysis by Dynamical Simulation (RADS) software package. Many other authors have developed equivalent simulation programs [22,23,24,25,26].

Chapter 3

Diffraction Instruments and Theory of their Operation

3.1 Double Crystal Diffractometry

3.1.1 The Double Crystal Diffractometer

The concept of double crystal diffractometry was first developed in the 1920's and is presented in several classic papers including Schwarzschild [1], Allison and Williams [2], Allison [3] and Compton and Allison [4]. Double crystal diffractometers were first constructed in the early 1930's [5,6] although it is only with the development of highly perfect monocrystalline epitaxial layers in the past 30 years that their use has become more widespread. The technique is now widely used in industry to provide detailed structural analysis of epitaxial layer samples. It is used by crystal growers to obtain information on the crystalline perfection of novel epitaxial layer systems and can also be introduced into a production line to provide on-line quality control of composition, layer thickness and uniformity.

The basic design of the double crystal diffractometer used to examine the samples presented in this thesis was developed in 1969 by Hart [7]. Many further refinements were provided by Tanner and Bowen through their company, Bede Scientific Instruments of Bowburn, Durham. The double crystal diffractometer used to collect data for this thesis is illustrated in Figures 3.1 and 3.2 and is similar to those of the model 150 double crystal diffractometer commercially available from Bede Scientific Instruments, Ltd. The term model 150 relates to the separation between the first and second crystals which in this case is 150 mm.

A beam of x-rays from an x-ray source is reflected consecutively from two crystals. The first crystal reflection, in conjunction with the collimation system, conditions the x-ray beam and directs it onto the sample crystal. Further collimation of the x-ray beam may be obtained by positioning a set of slits between the first and second crystals. The sample crystal is then rotated through the Bragg conditions for the substrate and epitaxial layer(s) and the variation in reflected x-ray intensity with

Figure 3.1: Experimental arrangement of the double crystal diffractometry at Durham University. The photograph shows the collimator (A), first crystal axis (B), slits (C), second crystal axis (D) and detector (E).

Figure 3.2: Photograph of the mechanics of the diffractometer in figure 3.1 showing the first axis (A), second axis (B), tangent arms (C), micrometers (D) and stepper motors (E).

the angle subtended between the incident x-ray beam and the epitaxial layer sample is recorded to produce a 'rocking curve'. Information on the thickness, composition and crystalline perfection of the epitaxial layer sample can be deduced from the angular separation between the substrate Bragg reflection peak and the epitaxial layer reflection peak(s) and the relative intensities and shapes of these peaks. Further details concerning the extraction of this information are presented in chapter 5.

The first crystal and sample crystal are positioned so that a central ray in the incident beam subtends angles at the crystal surfaces allowing Bragg reflection at a specific x-ray wavelength. These angles must take into account the slight difference between the refractive index for x-ray propagation in air and the refractive index for x-ray propagation in semiconductor material. This effect, predicted by Snell's law, causes bending of the x-ray beam as it enters and exits a crystal [8]. For an x-ray wavelength which is far from an absorption edge of a semiconductor material, the refractive index effect is described by equation 3.1

$$n_a sin I_a = n_s sin I_s \qquad 3.1$$

where the angles I_a and I_s describe the directions of the x-ray beams relative to the surface of a crystal before and after refraction and n_a and n_s are the refractive indices in air and the semiconductor material respectively. For an x-ray wavelength of 1.54051 $\mathring{A}$, the angular correction varies between 3 and 35 seconds for the 004, 115, 224, 335 and 404 reflections from a GaAs crystal with an 001 surface. The largest refractive index correction of 35 seconds occurs for the 404 grazing incidence reflection which, of those mentioned, has the lowest angle of incidence to the (001) crystal surface of 5.44°. The electron density, and hence refractive index, does not vary dramatically within the various III-V compounds. Hence, for the epitaxial layer samples examined in this thesis, the angular correction only serves to alter the rocking curve data set by a minute constant amount and does not significantly affect difference measurements. The refractive index correction is only really noticed when comparing simulated and experimental data wherein the simulated Bragg reflection peak from the substrate is always slightly offset from the expected position. However in some epitaxial layer systems the change in electron density across the interface is large and the refractive index effect allows resolution of the Bragg reflections from the layer and the substrate on the double crystal rocking curve even when the layer is lattice matched. This method has been exploited by Pietsch and Borchard [9] for the study of lattice matched $Ca_xSr_{1-x}F_2$ grown on GaAs. Although the Bragg peaks for the layer and substrate on the rocking curve overlap for reflections which

involve a high angle of incidence to the sample surface, the refractive index effect is sufficiently large to resolve these Bragg peaks individually for reflections which involve very low angles of incidence to the sample surface.

In order to facilitate the alignment of the second crystal with respect to the first crystal, the axis of the first crystal is coaxial with the main diffractometer axis. Thus setting the angle subtended by the incident x-ray beam and the diffractometer at twice the Bragg angle for the first crystal reflection ensures that the reflected beam passes over the centre of the second axis. The detector is on an arm which is coaxial with the second axis so that, as before, setting the angle between the detector arm and the diffractometer at twice the Bragg angle for the sample reflection ensures that the reflected beam is in line with the detector.

The first and second axes are driven by tangent arms connected to micrometer screws which in turn are driven by 4 phase stepper motors through gearboxes. The arrangement of stepper motors, gearbox ratios and tangent arm lengths allows reproducible movement of the first and second axes. The axes stepper motors, sample position and sample tilt stepper motors as well as data collection from the scintillation counter are controlled through an IEEE board in a MINICAM interface using an Opus PC III computer and Bede Scientific Instruments DCC control software. Data collection was facilitated by using a wide-area Nuclear Enterprises DM1-1 sodium iodide scintillation counter. Double crystal diffractometry data was taken using the copper $K_{\alpha 1}$ characteristic radiation from a Philips fixed-anode copper x-ray tube which is located in a Hilton Brooks model DG2 x-ray generator. The wavelength of the copper $K_{\alpha 1}$ characteristic line is 1.54051 $\pm$ 0.00004 $\mathring{A}$ [10].

All experiments were run in a safely interlocked X-ray enclosure to avoid radiation hazards. Although the x-ray tube has a maximum power rating of 1.5 kW, the tube was operated at a voltage of 40 Kv and an anode current of 30 mA in order to prolong its lifetime. In contrast to the topography techniques discussed in section 3.4 of this chapter, the saving in data collection time for the double crystal diffractometry technique does not warrant the use of higher power x-ray generators for many applications of DCD to the analysis of epitaxial layer samples. For the x-ray source described above, counting times of between 0.5 and 2 seconds per data point provide ample statistical resolution for the majority of features observed on the double crystal rocking curves discussed in this thesis. In exceptional cases, counting times of between 10 and 20 seconds per data point were employed (chapter 7). However in these cases the stability of the x-ray generator and diffractometer was sufficient to allow overnight data collection.

3.1.2. DuMond Diagrams for Successive Reflections

The simplest method of presenting the diffraction conditions central to double crystal diffraction is by way of the Du Mond diagrams for successive diffraction from two perfect crystals [11]. A DuMond diagram is a graphical representation of Bragg's law and displays the variation in angular range for which diffraction occurs with x-ray wavelength for a particular reflection. In Figure 3.3 the Bragg equation is drawn for the first three orders, n, of a reflection. The DuMond curve has a finite width; the perfect crystal reflecting range. This is equal to the intrinsic width of a reflection and represents the full width at half maximum intensity of the single crystal rocking curve for an incident plane wave. The perfect crystal reflecting range is dependent on the crystal material, the x-ray wavelength and the choice of reflection. It is most easily determined from the dynamical simulation programs discussed in chapter 2.

The diffraction condition for successive Bragg reflection from two crystals is obtained by drawing the DuMond diagrams for both crystal reflections on the same graph and examining the degree of overlap between these curves as the DuMond curve for the second crystal is moved across the DuMond curve for the first crystal. This procedure models the physical process of setting the first crystal at a particular angle and rocking the sample crystal through its Bragg condition. The area of overlap between the DuMond curves at a particular wavelength repesents the correlation function for the x-ray reflectivity profiles from the first crystal reflection and the sample crystal reflection at this wavelength. Figures 3.4, 3.5 and 3.6 present the Du Mond diagrams for three diffraction geometries of the double crystal diffractometer. The degree of angular divergence in an x-ray beam can be reduced by collimating the x-ray beam before it is incident on the first crystal and also by positioning a set of slits between the first crystal and the sample crystal. Hence the collimator and slits are represented in Figure 3.4 as pairs of upper and lower angular bounds centered on the condition for successive Bragg diffraction from the two crystals and limit the area of overlap for these reflections.

Figure 3.4.The Parallel Non-Dispersive Setting

This mode requires that both crystals have the same lattice parameter and undergo Bragg reflection from the same set of lattice planes. When the first crystal and sample crystal are precisely orientated with respect to each other, the DuMond curves for the two crystals overlap completely enabling diffraction from both crys-

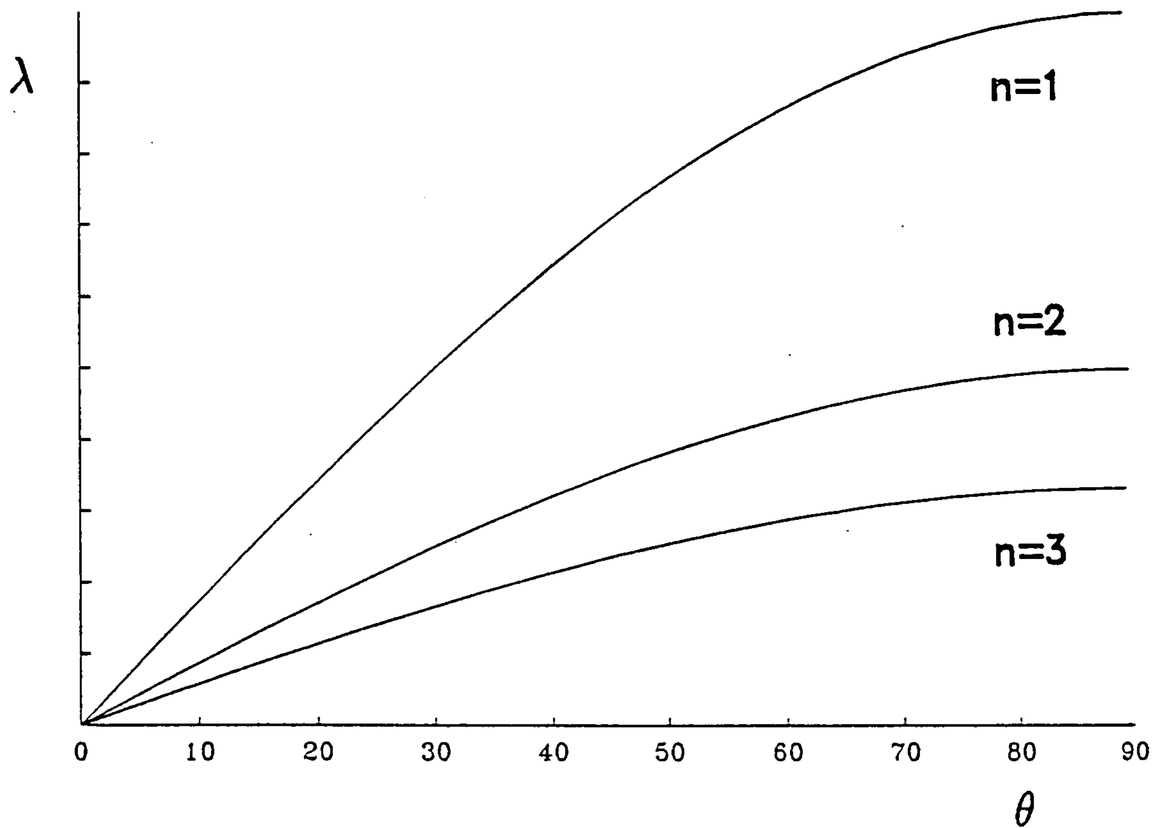

Figure 3.3: A plot of the Bragg equation for the first three orders of reflection.

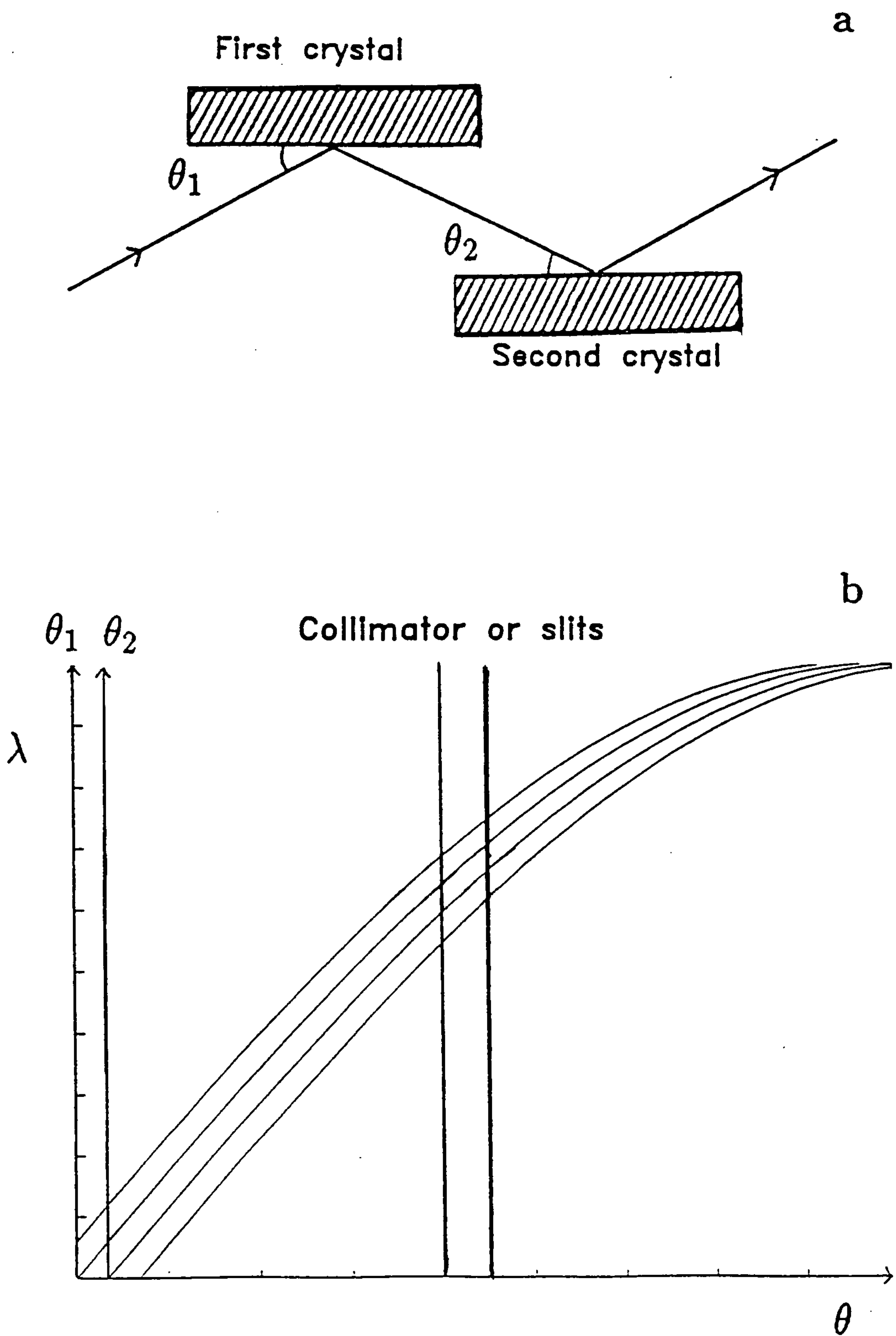

Figure 3.4: The parallel non-dispersive setting; (a) arrangement of crystals, (b) DuMond diagram.

tals to occur for all combinations of wavelength and Bragg angle allowed by the x-ray source and the geometry of the collimator and the slits. Hence this diffraction geometry is termed non-dispersive. The minimum full width at half maximum of a rocking curve recorded in this geometry is limited by the perfect crystal reflecting range of the first crystal, which is equal to the perfect crystal reflecting range of the substrate in the sample crystal. In practice, however, sample curvature, diffractometer misalignment, interfacial dislocations and impurity scattering will broaden the actual width of the Bragg reflection from the substrate. The epitaxial layer is generally less perfect than the substrate and so the width of the Bragg reflection from the layer rarely approaches the perfect crystal reflecting range.

Figure 3.5. The Parallel Dispersive Setting

This geometry is often employed when examining epitaxial layers of II-VI compounds or epitaxial layers grown on novel III-V substrates. In these cases it may not be possible to obtain crystals of sufficiently high quality and uniformity to act as first crystals. Instead it is usual to select a silicon or GaAs crystal to act as the first crystal which results in a diffracted beam with a high intensity and a narrow width. As the DuMond curve for the second crystal is moved across the DuMond curve for the first crystal, the area of intersection, which corresponds to the condition of Bragg reflection from both the first and second crystals, is seen to vary with wavelength. Hence this arrangement is described as wavelength dispersive. The presence of angular divergence in the x-ray beam allows Bragg reflection at the first and second crystals for a range of wavelengths. Each wavelength component within this range will produce a separate rocking curve at a specific Bragg angle. These component rocking curves are superimposed at the detector and this can lead to confusion in the data set. With care, this situation is easily avoided. A copper characteristic line source produces intense x-radiation at specific wavelengths, viz. the $K_{\alpha 1}$, $K_{\alpha 2}$ and K_{β} characteristic lines. The $K_{\alpha 1}$ characteristic line is the most intense of these and so the diffractometer is aligned for Bragg diffraction at this wavelength. The collimation system reduces the angular divergence of the x-ray beam sufficiently to prevent simultaneous diffraction from the K_{α} and K_{β} components at the first crystal. Careful positioning of a slit between the first and second crystals can remove any copper $K_{\alpha 2}$ radiation diffracted at the first crystal, leaving a single rocking curve from the copper $K_{\alpha 1}$ component. However in dispersive geometries the correlation which produces the double crystal rocking curve profile also contains a contribution from the natural width of the copper $K_{\alpha 1}$ characteristic line. The full width at

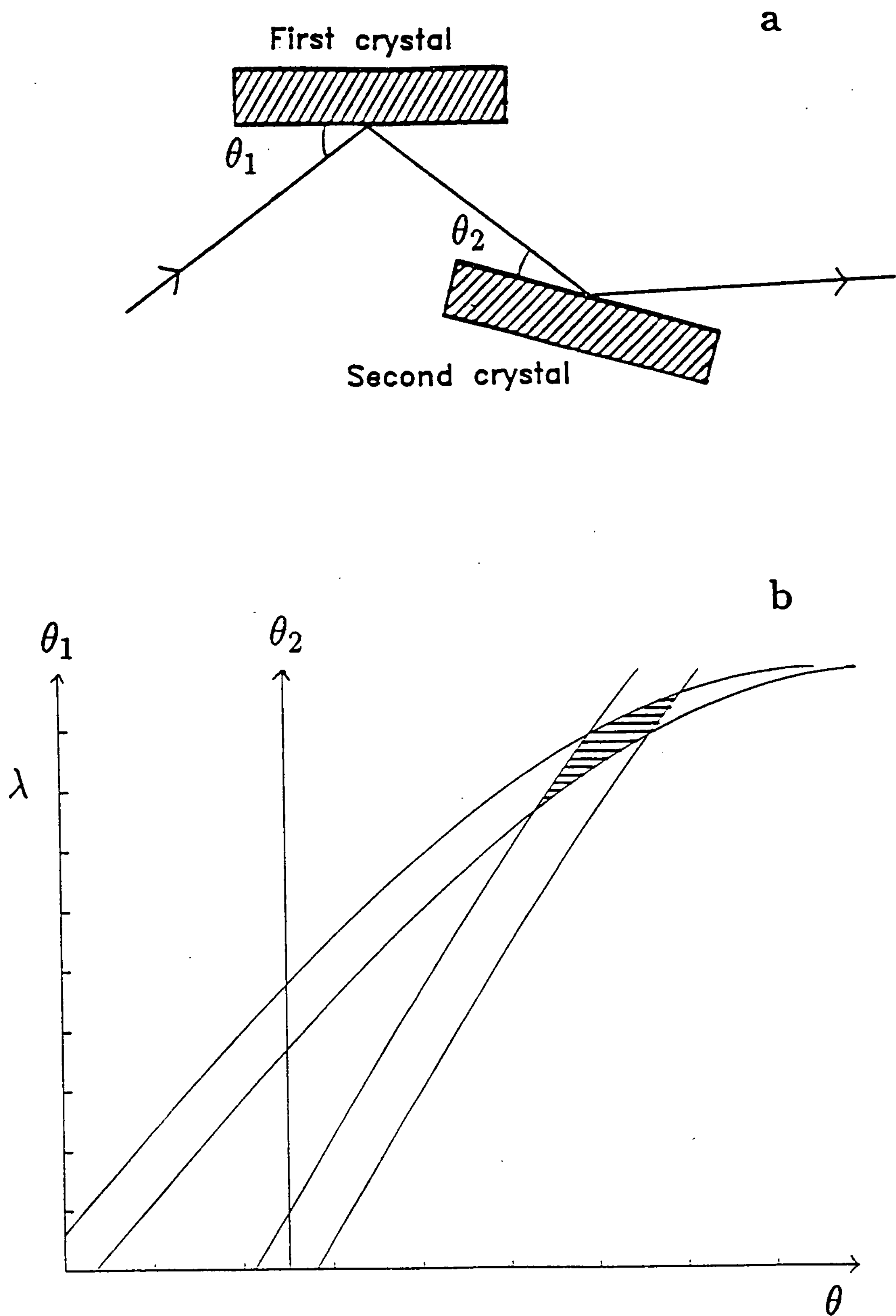

Figure 3.5: The dispersive setting; (a) arrangement of crystals, (b) DuMond diagram.

half maximum intensity of the x-ray reflectivity profile from the first crystal, $\delta\phi_1$, is related to the natural width of the copper $K_{\alpha 1}$ line, $\delta\lambda$, through equation 3.2, which is the differential of the Bragg condition for fixed lattice plane spacing

$$\delta\phi_1 = \frac{\delta\lambda}{\lambda} tan\theta_1 \qquad 3.2$$

where θ_1 is the Bragg angle at the first crystal. A similar expression is readily developed for the second crystal. Hence the effective rocking curve width of the apparatus is increased by δR where δR is given by equation 3.3.

$$\delta R = |\delta\phi_1 - \delta\phi_2| = \frac{\delta\lambda}{\lambda}|tan\theta_2 - tan\theta_1| \qquad 3.3$$

Figure 3.6. The Anti-Parallel Dispersive Setting

In this geometry the DuMond curve for the second crystal is reversed with respect to the DuMond curve for the first crystal and movement of the former across the latter reveals that this geometry is highly wavelength dispersive. Following a similar analysis to that outlined above in the parallel dispersive geometry, the effective rocking curve width is again increased by δR where δR is given by equation 3.4

$$\delta R = |\delta\phi_1 + \delta\phi_2| = \frac{\delta\lambda}{\lambda}|tan\theta_2 + tan\theta_1| \qquad 3.4$$

3.1.3. The Effect of Diffractometer Misalignment and X-ray Divergence on the Rocking Curve

Thus far double crystal diffractometry has been discussed for the case where the diffractometer is ideally aligned with respect to the x-ray beam. In this case the diffraction plane defined by the x-ray beam is normal to both the first crystal reflecting planes and the second crystal reflecting planes. In reality the reflecting plane normals are often slightly out of coincidence with the diffraction plane. The combination of diffractometer misalignment and x-ray divergence normal to the diffraction plane causes a broadening of the Bragg reflection peaks in the rocking curve recorded at the detector, i.e. the full widths at half maxima are increased and the peak heights are decreased. However the integrated intensities of the substrate and epitaxial layer Bragg reflections remain constant.

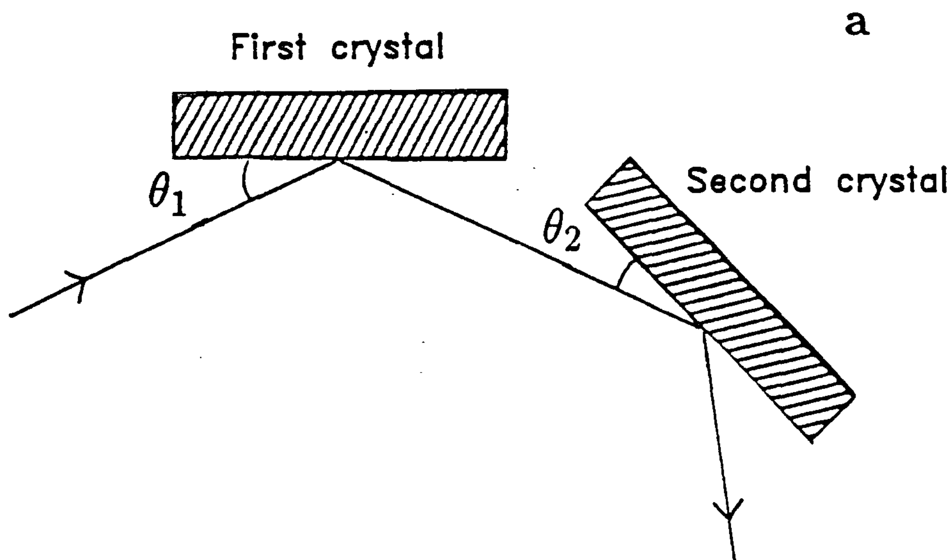

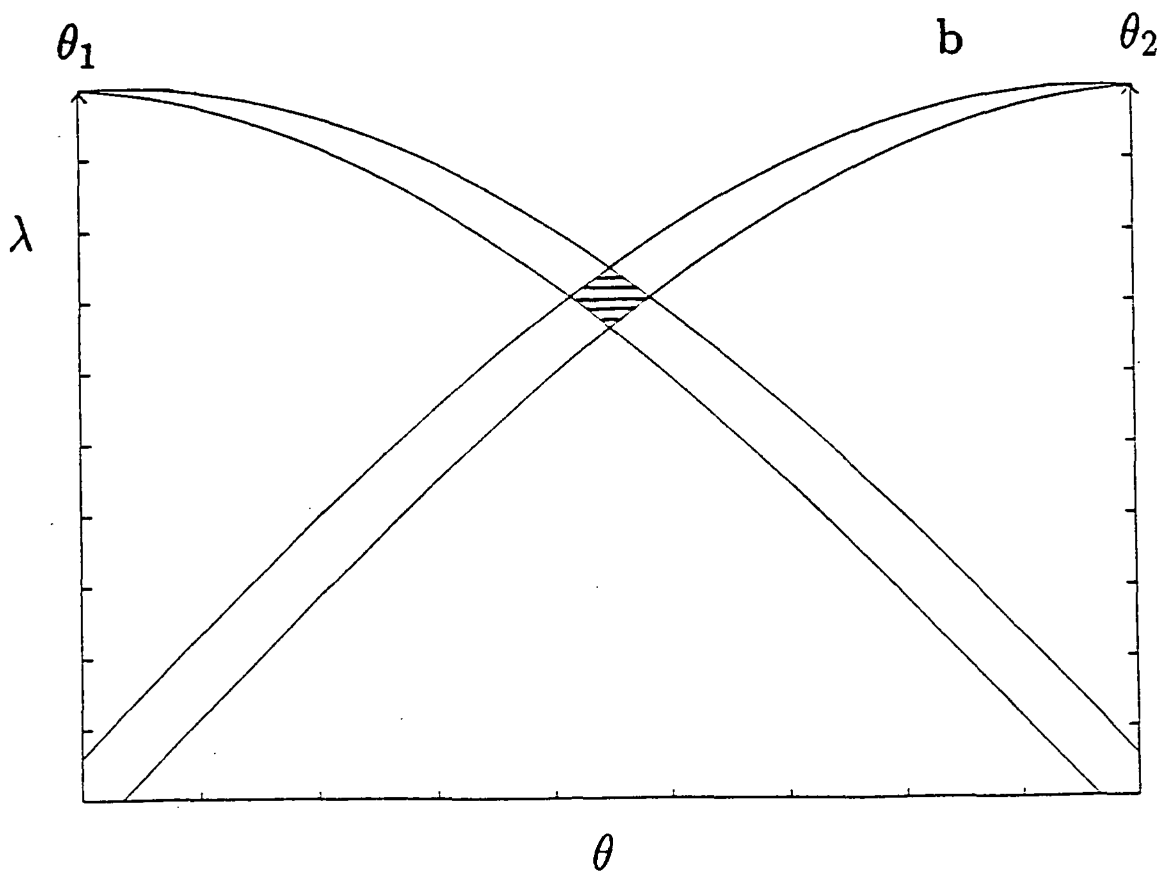

Figure 3.6: The anti-parallel dispersive setting; (a) arrangement of crystals, (b) DuMond diagram.

The angular divergence of the x-ray beam can be reduced by an effective collimator system and also by positioning a set of slits between the first and second crystals. The remaining angular divergence can be resolved into a component in the diffraction plane and a component normal to the diffraction plane. The discussion of DuMond diagrams presented above has already demonstrated that the component of angular divergence in the diffraction plane gives rise to a broadening of the double crystal rocking curve in the dispersive geometries but has no affect on the width of a Bragg reflection profile in the non-dispersive geometry. However if the diffractometer is misaligned then the divergence component normal to the diffraction plane causes a broadening of a Bragg reflection on a double crystal rocking curve in all three geometries. These components of angular divergence can be treated analytically by extending the DuMond diagram into three dimensions where the third axis, ψ, represents the component of the angle subtended by the x-ray beam at the sample surface that is normal to the diffraction plane. Hence the Bragg condition is now represented as a DuMond volume where dimensions along the θ and ψ axes represent the components of the angular divergence in the diffraction plane and normal to the diffraction plane respectively. This formalism was presented by Yoshimura in 1984 [12] and later developed by Xu and Li in 1988 [13] who used three dimensional DuMond diagrams to analyse successive diffraction from several crystals. This enabled Xu and Li to determine graphically the effect of x-ray divergence on double crystal diffractometers and led to the derivation of an expression for the resolution of a double crystal diffractometer.

In essence, the component of divergence normal to the diffraction plane causes the Bragg angles at the first and second crystals to vary across the width of the x-ray beam Figure 3.7. This variation is convoluted with the diffractometer misalignment and results in a broadening of the Bragg reflections recorded at the second crystal. In 1928 Schwarzschild [1] developed a purely geometric model which, although it ignores refraction and dynamical effects, is sufficient to obtain an order of magnitude estimate of the Bragg reflection broadening.

The collimation system usually consists of a pin hole slit of width, W, a distance Y away from the x-ray source. Hence if the x-ray source can be treated as a point source then the maximum component of divergence normal to the diffraction plane ψ_n, is given by equation 3.5

$$2 \times \psi_n = \frac{W}{Y} \qquad 3.5$$

Schwarzschild assumed that the diffractometer misalignment, γ, can be approx-

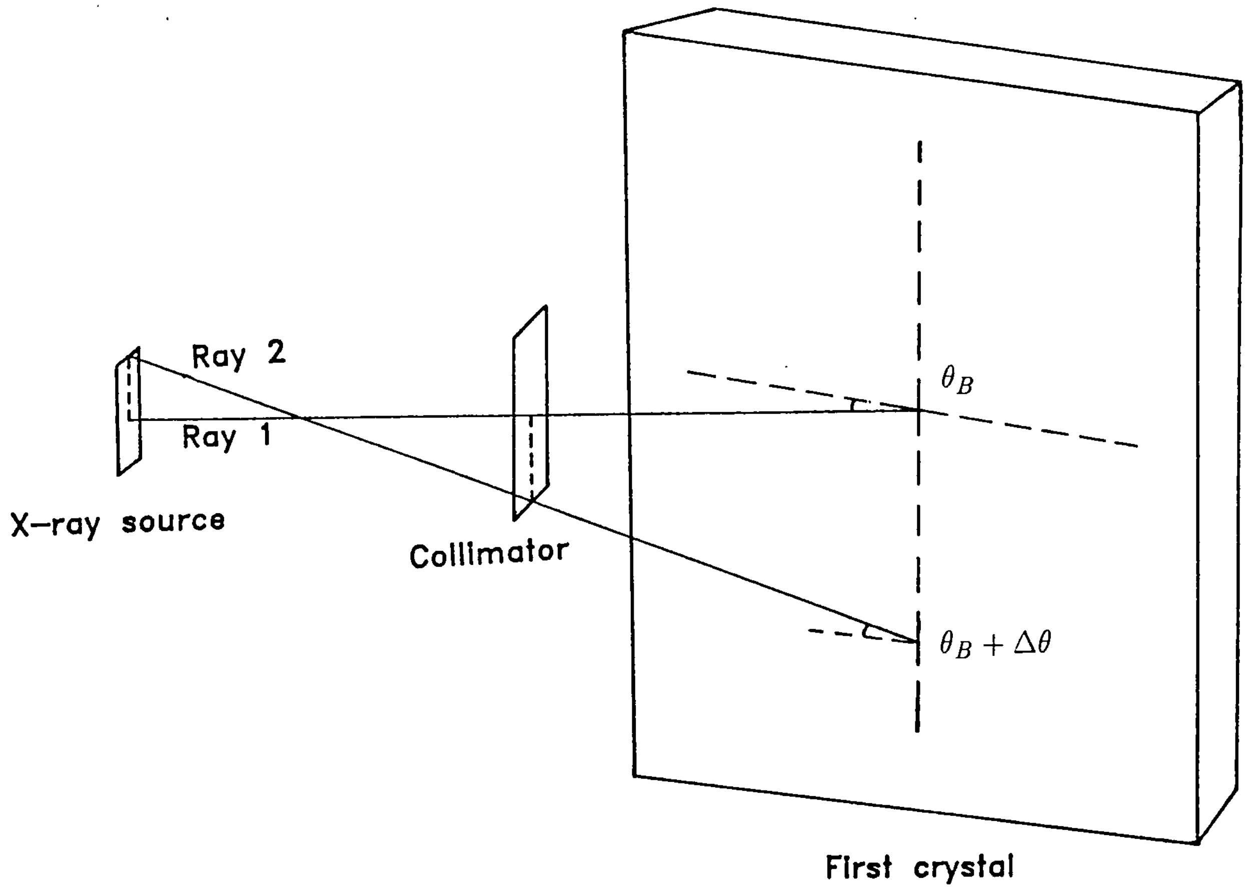

Figure 3.7: The maximum deviation of a ray (2) from the central ray (1) due to divergence normal to the diffraction plane. The diagram shows the difference in angle of incidence, $\Delta\theta$, for these rays at the Bragg condition for ray 1.

imated by $\gamma = \delta_1 + \delta_2$ which represents the sum or difference of the angles of inclination of the first and second crystals to the diffraction plane normal. He then developed relationships which describe the increase in the full width at half maximum intensity of a Bragg reflection, ϵ, caused by a diffractometer misalignment, γ, and a component of divergence normal to the diffraction plane, ψ_n, which are presented in equations 3.6.

$$\epsilon = 2\gamma\psi_n \qquad for \quad \gamma > \psi_n\{tan\theta_1 \pm tan\theta_2\}$$

$$\epsilon = M\psi_n^2 + \gamma\psi_n + \frac{\gamma^2}{4M} \qquad for \quad \gamma < 2M\psi_n \qquad 3.6$$

$M = \frac{1}{2}\{tan\theta_1 \pm tan\theta_2\}$ with the upper sign for the anti-parallel setting and the lower for the parallel settings. Hence $M = 0$ in the non-dispersive setting and so the Bragg reflection broadening varies linearly with γ. In the dispersive geometry ϵ is usually small compared to δR.

The collimation system for the double crystal diffractometer at Durham University consists of a brass channel with a diameter of 8mm and a length of 16cm terminated by a pin hole with a diameter of 0.5mm. Double crystal experiments at Durham employ radiation from a Philips PW2053/65 normal focus fixed anode copper x-ray tube which has an effective source size of 1mm $\times$ 1mm. Hence by trigonometry the angular divergence which remains in the x-ray beam as it is incident on the first axis is about 4.7×10^{-3} rads. The average uncertainty in diffractometer alignment for the apparatus at Durham is estimated at 0.25° which results in a broadening of the FWHM of a Bragg reflection in the non-dispresive geometry of about 8 seconds. This does not have a significant effect on the location of the centroids of the rocking curve features examined in this thesis and upon which the analysis of the rocking curve data presented in this thesis is based.

Fewster [14] has examined the effect of diffractometer misalignment on the diffraction condition and demonstrates that the difference between the effective Bragg angle and the true Bragg angle is a small second order correction. In Chapter 7 double crystal rocking curve data recorded with radiation from the copper $K_{\alpha 1}$ characteristic line is presented for the 004 reflection from sample GaAs2 which consists of a 1 μm layer of AlAs grown on a GaAs substrate. The measured separation between the Bragg reflections from the layer and the substrate is -(375 $\pm$ 0.5) seconds. Following the analysis presented by Fewster [14], the correction to the separation between these Bragg refelections incurred for a diffractometer misalignment

of 0.25° is 0.03 seconds. In view of the above factors it was normally unnecessary to align the diffractometer to better than 0.25° when determining asymmetric relaxation.

The component of the angular divergence in the diffraction plane of the x-ray beam allows Bragg reflection at the first crystal for a range of wavelengths, $\delta\lambda$, where $\delta\lambda$ can be calculated from equation 3.2. Assuming that $\tan\theta_B$ is approximately equal to 1 then for copper $K_{\alpha 1}$ characteristic radiation, which has a wavelength of 1.54051 $\pm$ 0.00004 Å, $\delta\lambda$ is roughly equal to 0.01 Å. Copper $K_{\alpha 2}$ characteristic radiation has a wavelength of 1.54433 Å [10] and so this component is also Bragg reflected by the first crystal. However the wavelengths of the copper $K_{\beta 1}$ and $K_{\beta 2}$ characteristic lines are 1.39217 $\pm$ 0.00004 Å and 1.38102 $\pm$ 0.00004 Å respectively and so these are not Bragg reflected at the first crystal. A piece of film placed after the first crystal clearly distinguishes the $K_{\alpha 1}$ diffraction spot from the $K_{\alpha 2}$ diffraction spot. If the diffraction geometry is wavelength dispersive then the rocking curves recorded at the detector from the $K_{\alpha 2}$ radiation and the $K_{\alpha 1}$ radiation are angularly separated and represent diffraction from adjacent regions across the sample surface. The $K_{\alpha 2}$ rocking curve is easily distinguished from the $K_{\alpha 1}$ rocking curve because the characteristic line for copper $K_{\alpha 1}$ radiation is roughly twice as intense as the characteristic line for copper $K_{\alpha 2}$ radiation. Recording two distinct rocking curves can be avoided by either employing a non-dispersive diffraction geometry, in which case the two rocking curves are integrated at the window of the detector, or by physically removing the $K_{\alpha 2}$ radiation by placing a slit after the first crystal. Employing a slit after the first crystal reduces the intensity of the Bragg reflections in the rocking curve with respect to the non-dispersive geometry but has the advantage that it allows selection of Bragg reflections from the sample crystal which are dispersive with respect to the first crystal. Placing a slit after the first crystal may also be required if the sample perfection varies rapidly with position or if the sample is highly curved because in these cases superimposing diffraction information from adjacent areas across the sample is undesirable.

3.2 Techniques in X-ray Topography

3.2.0 Introduction

X-ray topography is based upon employing a photographic medium to record the diffraction pattern produced by x-rays which are scattered from a sample crystal. Strong diffraction occurs when the angle subtended by the x-ray beam at the sample crystal satisfies the Bragg condition for a particular wavelength in the x-ray beam. The change in x-ray intensity across the Bragg diffraction spot, which is recorded as regions of varying contrast on the photographic medium, contains information on the crystalline perfection and defect distribution across the epitaxial layer sample. Photographic media consist of a thin layer of emulsion which contains closely packed grains of light sensitive material. Each grain requires at least one x-ray photon to be incident on it for the grain to become photochemically activated. Therefore for a given flux of x-ray photons the exposure time for a photographic film is inversely proportional to the grain size, and hence resolution, of the film.

Since x-rays are uncharged and have a refractive index which is only very slightly greater than 1 for all materials, it is very difficult to produce an x-ray lens with a sensible focal length. Hence the resolution of x-ray topography techniques is dictated by the effective grain size of the photographic medium. Ilford L4 nuclear emulsion plates have an undeveloped grain size of 0.14 μm which is the smallest grain size of any commercially available x-ray-sensitive photographic film. On developing, the grain size swells slightly and this effect in conjunction with the degree of overlap between grains through the thickness of the emulsion (usually 25 μm, 50 μm or 100 μm) leads to an effective resolution of 1 μm for x-ray beams incident normally to L4 Nuclear Emulsion plates. Occasionally x-ray photons cascade within the nuclear emulsion in which case each photon can lead to the activation of several grains in the film and hence the effective resolution is decreased.

X-ray topography detects defects and dislocations in a crystal sample because the strain field surrounding a defect in the sample causes a local distortion of the crystal lattice which changes the Bragg diffraction conditions in this region. This region is then imaged on the photographic medium as a region of different contrast within the uniform diffraction conditions of the surrounding crystal. The degree of lattice distortion which creates a change in the Bragg diffraction conditions depends upon the width of the Bragg reflection at the sample. To a first approximation the

sensitivity of x-ray topographic techniques to the detection of defect strain fields within a sample crystal is inversely dependent on the width of the Bragg reflection.

X-ray topographic techniques divide into two distinct types, single crystal x-ray topography and multiple crystal x-ray topography. Multiple crystal x-ray topography uses one or more perfect crystals to condition the x-ray beam before it is incident on the sample. In practice this technique is usually reduced to double crystal topography and is performed with a very similar experimental arrangement as double crystal diffractometry. Hence, if the x-ray beam is non divergent, then the spectrum of wavelengths incident on the sample crystal is defined by the perfect crystal reflecting range of the reference crystal. In single crystal topography, the wavelength spectrum incident on the crystal is solely determined by the x-ray source. In single crystal synchrotron topography the spectrum is polychromatic whereas if a laboratory x-ray generator is employed as the x-ray source then the wavelength spectrum consists of characteristic emission lines which have relatively large natural widths. As a result of the angular divergence of the x-ray beam from a characteristic line source and the polychromatic x-ray spectrum from a synchrotron source, single crystal topography is only sensitive to short range strain fields such as those in the immediate vicinity of a crystal defect whereas double crystal topography can be sensitive to long range strain fields and tilt boundaries as well as short range strain fields.

Until about 15 years ago, available x-ray sources were limited to fixed-anode x-ray tubes which have power ratings of the order of 1.5 kW. The advent of reliable rotating anode generators which produce order of magnitude greater photon fluxes went some way to reducing x-ray topograph exposure times. Major advances in x-ray topography had to await the arrival of synchrotron radiation sources producing highly collimated x-ray beams with usable fluxes which can be up to three orders of magnitude larger than those produced by standard cooled target sources. The cross sectional area of the x-ray beam at a synchrotron radiation source can be up to 20 cm^2. Synchrotron radiation reduces single crystal and double crystal topograph exposure times for Ilford L4 Nuclear Emulsion plates to the order of seconds and minutes respectively.

Single crystal and double crystal x-ray topographic techniques are briefly presented in sections 3.2.1, 3.2.2 and 3.2.3. For a more detailed discussion of these techniques see references [15] to [21].

In many respects x-ray topography is a complementary technique to transmission electron microscopy (TEM). TEM images a very small volume of the sample,

typically 0.1 micron thick and a few microns wide, with a resolution of less than a nanometer whereas x-ray topography images a much larger volume of the sample with a resolution limit of 1 μm. The degree of sample coverage depends on the specific x-ray topographic technique and in most of these, the extent to which the sample is curved. The Lang topography technique described in section 3.2.1 enables full coverage of samples which are up to 1mm thick and in excess of 10cm wide by incorporating a feedback mechanism to cope with sample curvature in the diffraction plane. TEM is ideally suited to examining samples containing a high density of defects, greater than 10^5 dislocations cm^{-1}, whereas x-ray topography is best suited to imaging defect densities of less than $10^3 cm^{-1}$. The mechanisms by which x-ray topography and TEM produce images of dislocation lines and other crystal defects are similar. In essence, the sensitivity of x-ray topography and TEM to strain in the crystal lattice is inversely dependent on the width of the Bragg reflection from the sample crystal. In x-ray topography this can be as low as 10 seconds whereas in TEM the width of the Bragg reflection from the sample crystal for 100 keV electrons is about 0.5°. Hence TEM images short range strain fields whereas x-ray topography can also be sensitive to long range strain fields and tilt boundaries. The width of a dislocation image in TEM can be several orders of magnitude smaller than in x-ray topography. However the electron microscope employs electrostatic lenses to focus the electron beams and magnify the images enabling resolution of the dislocation images. TEM requires intricate and time-consuming sample preparation whereas x-ray topography is a relatively easy technique to operate and, most importantly, is nondestructive. Hence x-ray topography more easily lends itself to quality control in an industrial environment. Sample analysis by x-ray topography is particularly appropriate in III-V heteroepitaxial layer technology which is well established and routinely produces epitaxial layers of excellent morphology and crystalline perfection.

3.2.1 Single Crystal Topography Employing a Characteristic Line X-ray Source

Characteristic line sources radiate almost isotropically and have effective source dimensions which are typically about 1mm × 1mm. Hence for topography techniques which utilise an effectively uncollimated x-ray beam the angular width of the x-ray beam at a point on the sample is, to a first approximation, simply calculated from the source dimensions and the separation between the x-ray source and the sample. Points on the sample satisfying the Bragg condition allow Bragg diffraction from a cone of radiation in the incident beam with apex angle equal to twice the angular width of the x-ray beam at the sample. The apex angle of the incident cone is given by q/u, where q is the effective size of the x-ray source and u is the separation between the x-ray source and the sample. Since the diffracted cone has the same apex angle as the incident cone, the geometric resolution, GR, for single crystal topographic techniques is given by equation 3.7

$$GR = (q/u) \times Y \qquad 3.7$$

where Y is the separation between the specimen and the photographic film. To optimise resolution, a minimum separation between the sample and the photographic film is desired. However, excessively small values of Y lead to overlapping diffracted x-ray beams and must be avoided. A compromise therefore becomes necessary.

A typical separation between the x-ray source and the sample crystal is of the order of 1m which results in an angular width at any point on the sample of 100 seconds. In the case of a point on a GaAs sample which satisfies the Bragg diffraction condition for a 404 Bragg reflection when illuminated with radiation from the copper $K_{\alpha 1}$ characteristic line, the angular width of the x-ray beam at this point allows a spectrum of Bragg diffracted wavelengths which has a width of 0.002 Å. Therefore an x-ray source to sample separation of 1m ensures that the angular divergence of the x-ray beam at this point on the sample is sufficiently low to prevent Bragg diffraction from more than one characteristic line wavelength. In fact the minimum source to sample separation in this geometry which still prevents simultaneous Bragg diffraction at the same point on the sample from both the $K_{\alpha 1}$ and $K_{\alpha 2}$ characteristic lines is 17cm and corresponds to an angular width of the x-ray beam at the sample of 600 seconds.

3.2.1.1 Berg-Barrett Topography

Berg-Barrett topography was first introduced by Berg in 1931 [22] and later refined by Barrett in 1945 [23]. The technique is illustrated schematically in Figure 3.8. In the Berg-Barrett technique the sample crystal is set at an angle to the incident x-ray beam so that the Bragg diffraction conditions are satisfied for one of the characteristic emission wavelengths produced by the x-ray source. The photographic film must be positioned close to the sample so that the separate images produced from the $K_{\alpha 1}$ and $K_{\alpha 2}$ charateristic lines do not diverge significantly. However due to the small specimen to film distance this technique is relatively insensitive to misorientations in the crystal though large misorientations of the order of a degree will result in no diffracted intensity reaching the film. The Bragg reflection is chosen to be asymmetric with respect to the sample surface so that the x-ray beam enters the sample at a shallow angle and exits the crystal surface at an angle as near to the surface normal as possible. A shallow incidence angle increases the degree of sample coverage by the x-ray beam whereas a near-normal exit angle allows a small sample to photographic film separation.

3.2.1.2 Hirst Topography

This technique was designed to reduce the exposure time necessary to produce large area topographs from a characteristic line x-ray source. The geometry of the transmission technique is shown in Figure 3.9 [24]. The sample is cylindrically bent until its radius of curvature is equal to the diameter of a circle whose circumference contains the x-ray source and is also tangential to the sample surface at a point on the sample. This is known as the Rowland circle [25] and, provided the circle is sufficiently large, has the property that all rays that emanate from the x-ray source have the same angle of incidence with the surface of the sample. Hence this technique allows all points across the sample to Bragg diffract simultaneously.

An oscillating Soller slit arrangement is employed to shield the photographic plate from the undiffracted beam and background scattered radiation, and also allows the photographic plate to be placed close to the sample. Despite the low x-ray intensity at the sample resulting from a source to sample separation which is typically about 2m, Hirst topography can completely image samples with diameters of up to several inches for exposure times of about one hour using Ilford L4 Nuclear Emulsion plates.

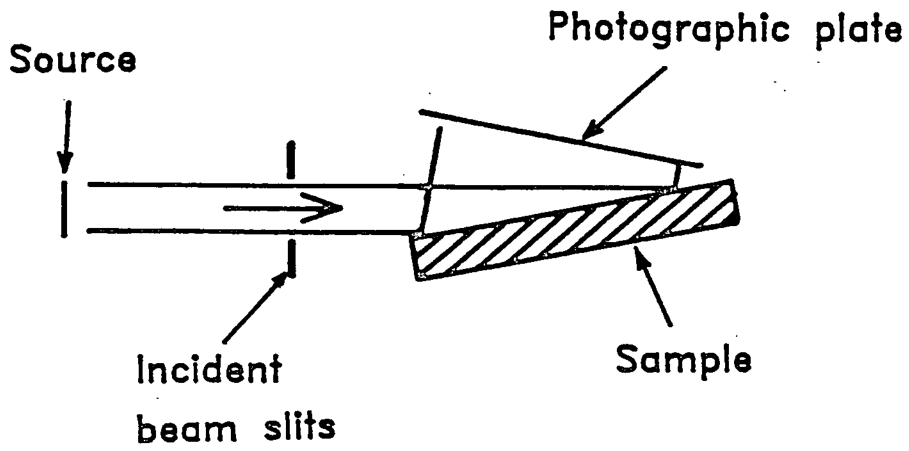

Figure 3.8: Line diagram showing the geometry of Berg-Barrett topography.

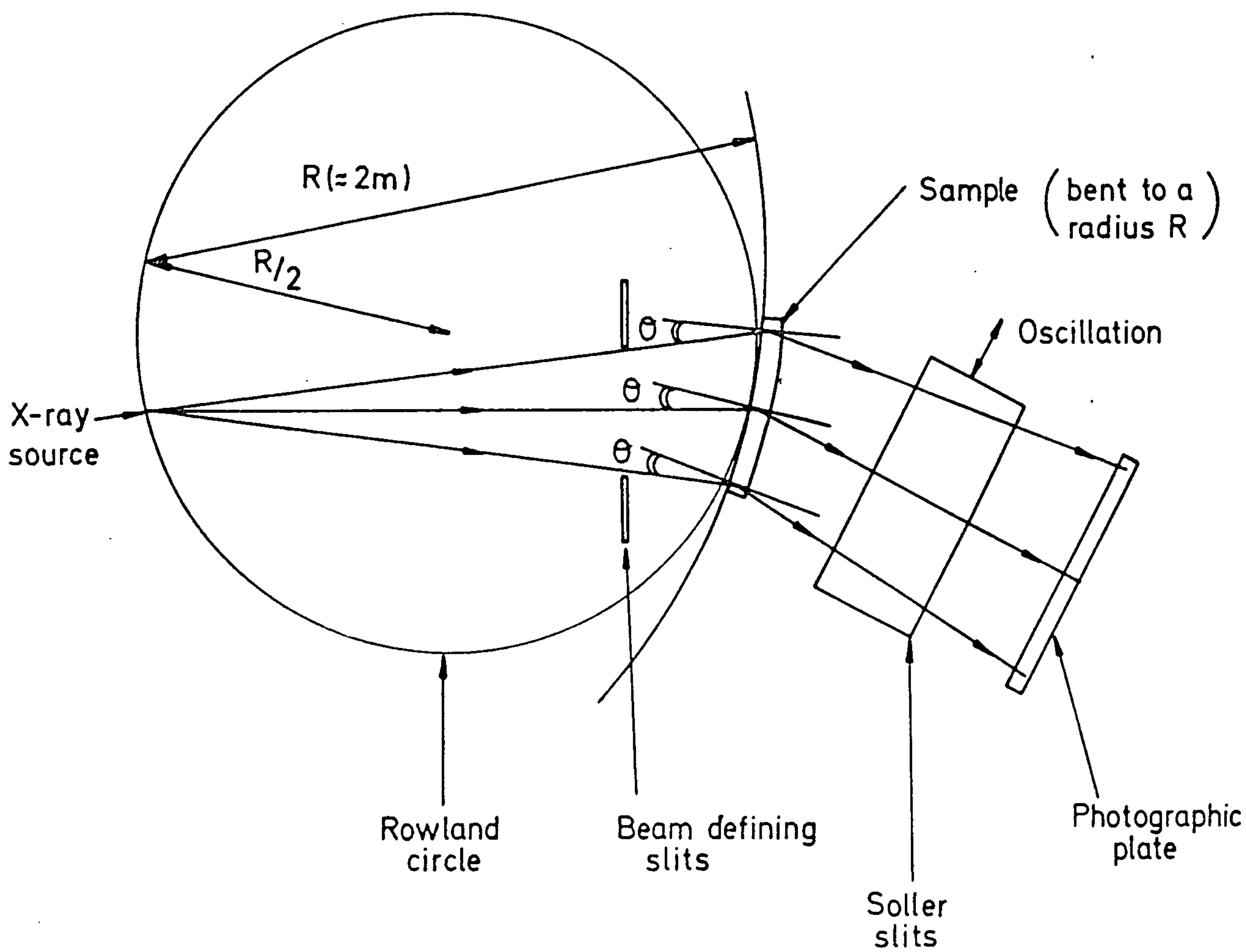

Figure 3.9: Line diagram showing the geometry of Hirst topography.

3.2.1.3 Section Topography

The geometry of section topography [18,26] is illustrated in Figure 3.10. The x-ray beam is collimated normal to the plane of diffraction by a set of slits 10-15 μm wide and at a distance of the order of 1m from the source thus reducing the angular divergence of the x-ray beam in the plane of diffraction to about 100 seconds and ensuring that the width of the x-ray beam is significantly smaller than the width of the base of the Borrmann fan for the chosen sample reflection. The reflection from the sample crystal is selected so that the diffracted beam is transmitted through the width of the sample crystal, e.g a 220 reflection is commonly employed for samples which have 001 surfaces. In general a characteristic line source providing harder radiation is preferred, such as Molybdenum $K_{\alpha 1}$ at 0.71 Å or Silver $K_{\alpha 1}$ at 0.559 Å. The x-ray beam is so well collimated that the $K_{\alpha 1}$ and $K_{\alpha 2}$ characteristic lines are clearly separated on a single crystal rocking curve from the sample crystal. A photographic plate is placed behind the sample and is shielded from the residual undiffracted x-ray beam by a set of scatter slits. This technique images defects within the Borrmann triangle and is unique in that it allows direct determination of the depth of a defect within a crystal. The diffraction patterns obtained can contain complex interference patterns and interpretation of these requires the use of an image simulation program based on the dynamical theory of x-ray scattering [27].

3.2.1.4 Lang Topography

Lang topography employs a similar experimental arrangement as the section topography technique but in order to obtain full sample coverage the sample and photographic film are traversed across the incident beam, figure 3.11. Hence a Lang topograph can be considered as the spatial integration of many section topographs which results in a topograph of the whole sample. A control program ensures that the Bragg diffraction condition is maintained at the sample and the sample and photographic film are traversed across the x-ray beam [18]. This is required in order to cope with crystal curvature which is present in strained epitaxial layer samples. The width of the collimating slit is increased to between 100 and 200 microns in order to increase the x-ray intensity incident on the sample crystal but this is still sufficiently narrow to clearly resolve the $K_{\alpha 1}$ and $K_{\alpha 2}$ characteristic emission lines on a single crystal rocking curve from the sample. Lang topography can also be operated in reflection mode.

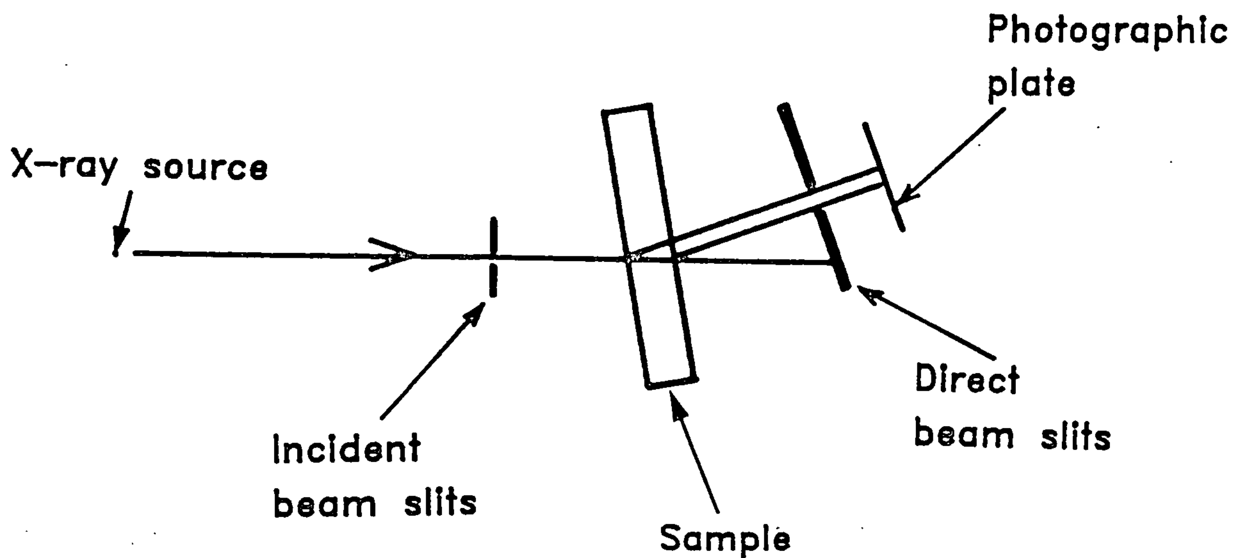

Figure 3.10 Line diagram showing the geometry of section topography.

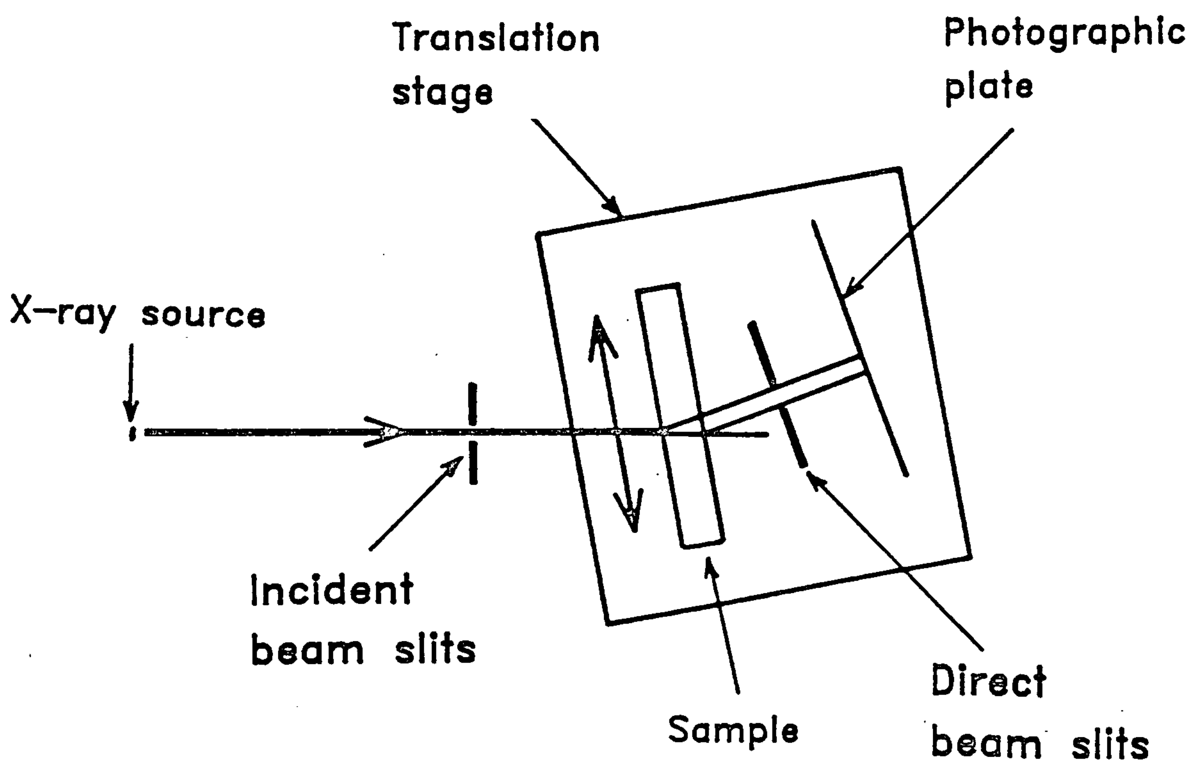

Figure 3.11: Line diagram showing the geometry of Lang topography.

3.2.2 Topographic Techniques Employing a Synchrotron Radiation Source

It is well known that an accelerating charged particle emits electromagnetic radiation. This phenomenon is exploited to produce cyclotron and synchrotron radiation which is emitted by electrons when they are forced to move in a circular orbit through their interaction with electric and magnetic fields. Cyclotron radiation is emitted when the electron energies are non-relativistic and this radiation is monoenergetic. However if the electron energies become relativistic then the resulting radiation spectrum is continuous and is called synchrotron radiation. The synchrotron radiation spectrum extends from the infrared to a minimum wavelength, λ_c, which is calculated from the electron energy, E, in GeV and the magnetic field strength causing the centripetal acceleration, B, in Tesla through equation 3.8 [28]

$$\lambda_c = \frac{1.86}{BE^2} \quad nm \tag{3.8}$$

Due to the relativistic Lorentz transformation from the rest frame of the electron to the laboratory frame, the radiation in the laboratory frame is confined to a forward directed cone. The apex angle for a single electron, δS, emitting radiation at the minimum wavelength, λ_c, is given by equation 3.9 [28]

$$\delta S = \frac{5.12 \times 10^{-4}}{E} \tag{3.9}$$

An integration over the full wavelength spectrum and for all electron velocities in the storage ring leads to the calculation of the effective source dimensions for the synchrotron radiation source. Beam lines are positioned at tangents to the electron orbit which allow the emitted radiation to escape safely from the synchrotron ring and reach interlocked experimental areas. At all points across the spectrum, the radiation is extremely intense and has a very low angular divergence and so is ideal for the study of diffraction phenomena.

The synchrotron source at Daresbury consists of a 30m diameter storage ring which is fed by a linear accelerator and in turn supplies radiation to thirteen beam lines. Intense x-radiation is emitted by the electrons in the storage ring when their trajectory is forced into an arc by a 'bending' magnet. Each of the thirteen beamlines is associated with a particular bending magnet, most of which produce magnetic fields of 1.2 Tesla. However one of the beamlines (line 9) is positioned directly after a 5 Tesla superconducting wiggler magnet and so this beamline carries particularly

intense radiation. The storage ring operates at an electron energy of 2 GeV and a current of typically 200 mA when running in multiple electron bunch mode. The lifetime of the electrons in the storage ring is in excess of 24 hours and in optimum operating conditions a new beam of electrons is injected into the storage ring on a daily basis. The 1.2 tesla bending magnets produce a radiation spectrum which extends from the infra-red to a minimum x-ray wavelength of 0.6-0.7 Å. However the beryllium beam pipe windows absorb radiation with wavelengths greater than 4 Å. The spectrum is shown in Figure 3.12 along with the fluxes available from sealed tube sources.

3.2.3 Single Crystal White Beam Synchrotron Topography

The practice of single crystal synchrotron radiation x-ray topography is very straightforward, requiring only a simple goniometer to orientate the sample [29]. If the sample is thin enough to allow transmission of the x-ray beam and has a strain-free back surface then white beam transmission topography is preferred to white beam reflection topography as less background noise from the main x-ray beam reaches the photographic plate in this geometry and the defect contrast recorded on the topographic plate is intrinsically higher [30]. In white beam transmission topography, where in general the sample is orientated with respect to the incident beam to favour a particular reflection zone, the photographic medium is displaced from the incident beam axes and so records an elliptical pattern of diffraction spots. As before, the Bragg condition describes the relationship between the angle subtended by the x-ray beam at the Bragg reflecting planes and the wavelength of the diffracted x-rays for each diffraction spot. Each diffraction spot recorded on the photographic plate consists of a single crystal topographic image of the sample. Hence this technique provides a rapid means of analysing the Burgers vectors of dislocation lines and the directional components of other lattice distortions. Although the synchrotron radiation source x-ray beam has a very low intrinsic angular divergence it is also polychromatic and so this technique is not sensitive to crystal tilts and long range strain fields. However abrupt tilt boundaries do show either enhanced or diminished intensity because portions of the x-ray beam reflected from each side of the boundary will either converge or diverge.

White beam synchrotron topography has two main technical problems; harmonic contamination and a high background of scattered radiation. The continuous spectral range may lead to the superposition of several harmonic reflections onto one

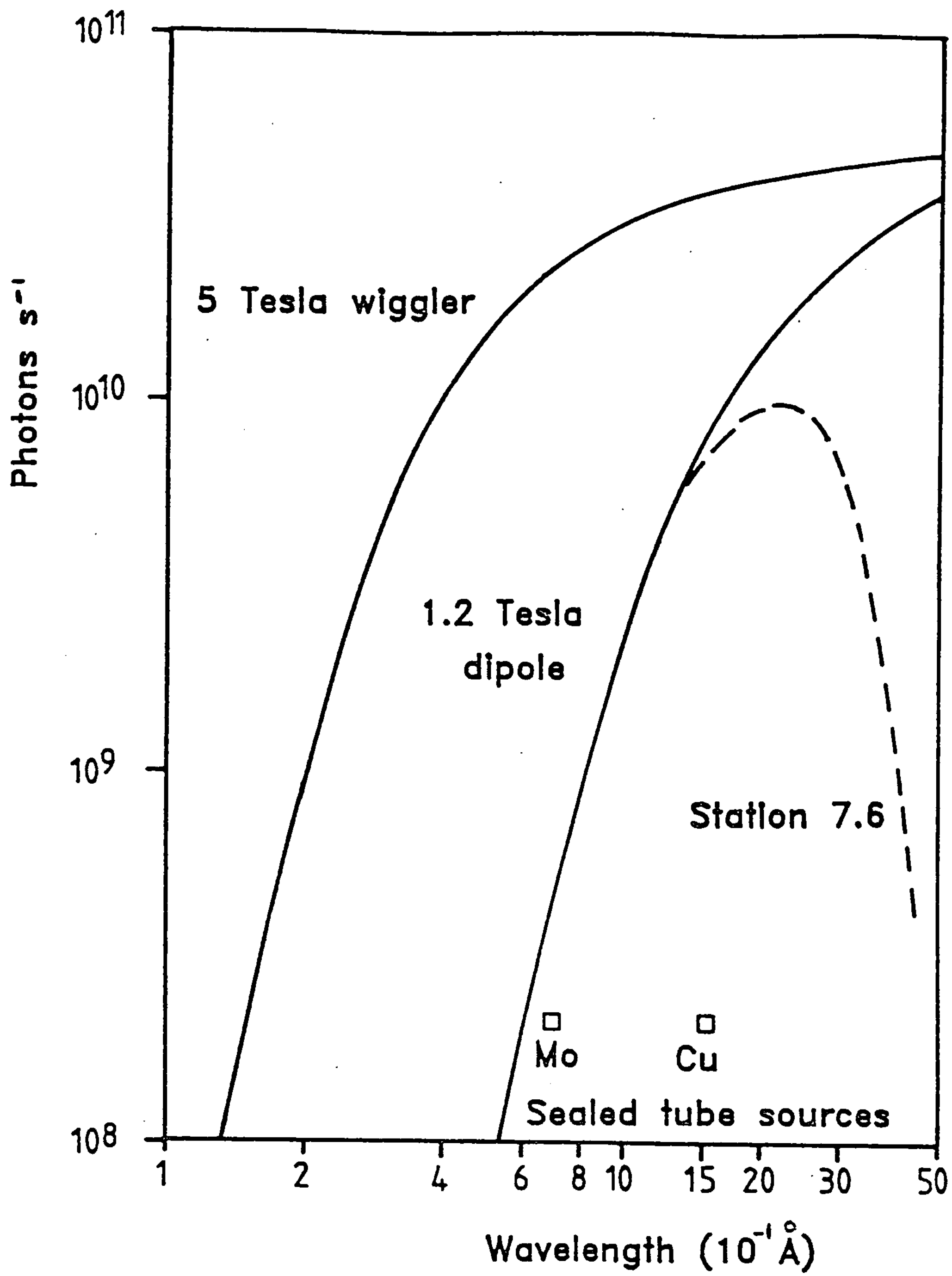

Figure 3.12: The radiation spectra on the Daresbury synchrotron radiation source shown relative to the output from two sealed tube sources.

diffraction spot thus convoluting the structural information contained within the spot. Harmonic contamination can be avoided by orientating the sample to favour specific reflections where unwanted higher or lower order reflections are forbidden or of very low intensity. The problem of high background can be reduced by careful shielding, the use of filters to absorb unwanted long wavelength components of the spectrum and an increased sample to photographic film separation. A high percentage of the background radiation on the photographic film results from scattering at the sample and hence decreases as a function of the square of the film to sample separation. The low angular divergence and small effective source size associated with synchrotron radiation allows an increased sample to photographic plate separation without significant loss of spatial resolution. Hence the signal to noise ratio on the photographic film increases with film to sample separation. However this technique is best applied to small samples because the background scatter becomes prohibitively high for samples in excess of a few cm^2.

3.2.4 Double Crystal Synchrotron Radiation Topography

Double crystal x-ray topography was first reported by Bond and Andrus in 1952 [31] and later developed by Bonse and Klapper in 1958 [32] who used the parallel non-dispersive setting to detect long range strain variations. Since then the technique has been developed and extended to the study of long range and short range strain variations in a diverse range of materials but with particular reference to semiconductors and quartz [33]. The double crystal topographic technique is illustrated schematically in Figure 3.13 and essentially consists of a double crystal diffractometer with the detector replaced by a photographic plate and a spatially large incident x-ray beam. Double crystal topography can be performed with a characteristic line source but produces poor sample coverage and involves exposure times of the order of ten hours during which time the relative position of the sample on the second axis must remain stable to within a few seconds of arc. Bragg diffraction at the first crystal reduces the angular divergence of the x-ray beam to the perfect crystal reflecting range of this reflection, typically less than 10 seconds, and enables double crystal topography to be sensitive to long range strain fields and local crystal misorientations. The particular choice of x-ray optics selects the rocking curve width of the Bragg reflection from the second crystal and hence the degree of sensitivity of the technique to the detection of long range strain fields in the sample. The parallel non-dispersive crystal setting has the narrowest effective rocking curve width and

GEOMETRIC SCALING FACTOR $= \frac{1}{\sin \Phi}$

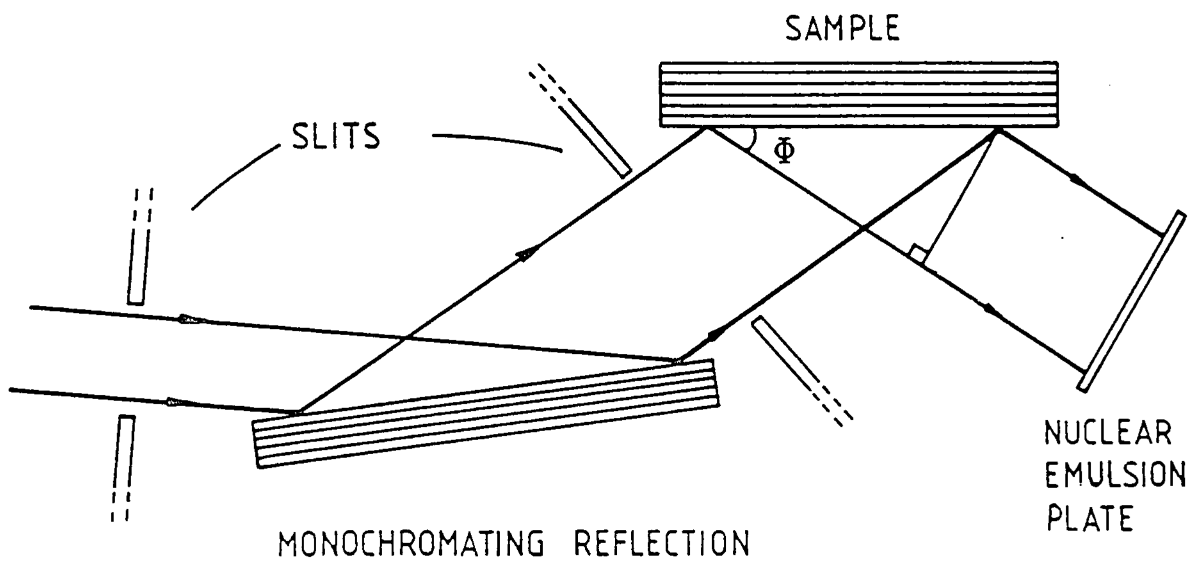

Figure 3.13: Schematic illustration of the double crystal topography technique.

Figure 3.14: Experimental arrangement for double crystal topography on station 7.6 at the Daresbury laboratory synchrotron radiation source. The photograph shows the first axis with beam conditioner in place (a), second axis with sample in place (b), position of the photographic plate (c), detector (d), beam defining slits (e) and shielding (f).

hence the highest sensitivity to long range strain fields in the sample whereas the non-parallel dispersive crystal setting has the largest effective rocking curve width and hence the lowest sensitivity to these strain fields. It also follows that the defect image widths are largest in the non-parallel dispersive geometry and smallest in the parallel non-dispersive geometry. The parallel dispersive crystal setting represents a compromise between these two. The parallel dispersive crystal setting is most often employed when recording a double crystal topograph in the laboratory with x-radiation from a characteristic line source because this geometry does not allow simultaneous Bragg reflection from the $K_{\alpha 1}$ and $K_{\alpha 2}$ emission lines unless the sample is curved in which case the reflected x-ray beams are divergent and form separate distinct images on the topographic plate.

Double crystal topography can be thought of as the convolution of a single crystal topograph from the reference crystal with a single crystal topograph from the sample crystal to form a composite topograph containing information about both crystals. Hence defects in the reference crystal can be imaged on the composite topograph. If one assumes that the single crystal topograph from the first crystal is essentially unchanged upon Bragg reflection at the sample then the image resolution of defects in the reference crystal on the topographic plate can be modelled by equation 3.7, where Y, is now defined as the sum of the sample to photographic film separation and the separation between the reference crystal and the sample crystal. The separation between the x-ray source and the first axis at the synchrotron ring in Daresbury is 80m whereas the separation between the first axis and the photographic film is less than 2m. Hence the geometric resolution on the composite topograph of defects in the reference crystal is only slightly less than the geometric resolution of defects in the sample crystal. Consequently the reference crystal employed for double crystal topography at a synchrotron x-ray radiation source must be uniform and defect free. In contrast, consider the corresponding dimensions for double crystal topography in the laboratory incorporating a characteristic line x-ray source. In this case the separation between the x-ray source and the first crystal is roughly half the separation between the x-ray source and the sample crystal. Hence the geometric resolution of lattice defects in the sample crystal is about twice as high as the geometric resolution of lattice defects in the first crystal. As a result, the crystalline perfection of the first crystal is less critical to the composite topograph.

Employing successive reflections from 'perfect' crystals may reduce the spectral width of the x-ray beam and increase the collimation whilst also eliminating harmonic contamination. Several multiple reflection monochromator systems have been developed [34 to 38] which can reduce the angular divergence of the x-ray

beam to 0.01 seconds. However the beam intensity rapidly decreases as the number of monochromating reflections increases resulting in very long exposure times.

Double crystal X-ray topographs were taken on station 7.6 at the Daresbury laboratory SRS, Figure 3.14, using 25 μm thick Ilford L4 nuclear emulsion plates. For comprehensive descriptions of the double crystal camera and associated alignment procedures the reader is referred to Bowen and Davis [39] and Barnett [40] respectively. For details of the photographic processes the reader is referred Tanner [15] and Lang [17]. Best dislocation images were obtained using the substrate reflection in the dispersive parallel crystal setting and imaging the long range dislocation strain fields extending from the interface into the substrate. The topograph plates were mounted normal to the X-ray beam Bragg reflected from the sample. Hence sample dimensions perpendicular to the X-ray beam are reproduced exactly on the topograph plate whereas sample dimensions parallel to the X-ray beam are reduced by a geometric scaling factor, GSF, given by equation 3.10

$$GSF = \frac{1}{sin\Phi} \qquad 3.10$$

where Φ is the angle subtended between the diffracted X-ray beam and the sample surface, Figure 3.13. If the topographic plate is mounted parallel to the sample surface then the image magnification is unity in both directions. However this arrangement is usually undesirable since the diffracted beam now passes through the nuclear emulsion at an angle to its surface normal, leading to a significant broadening of the image for all but the thinnest emulsions. This problem can be circumvented by employing an asymmetric reflection at the sample and selecting the x-ray wavelength Bragg diffracted at the monochromator so that the x-ray exit beam is normal to the sample surface [41].

In the vicinity of a dislocation line the lattice planes are distorted and hence the Bragg condition varies as a function of the distance from the core of the dislocation line. Hence if the Bragg condition is exactly satisfied for surrounding regions of perfect crystal then the dislocation line is recorded on the topograph as a light image surrounded by a dark background. The size of the dislocation line image is equal to the region around the dislocation line in which the lattice planes are misorientated by more than the width of the Bragg reflection rocking curve at this region of the sample. The Durham group condition the x-ray beam with a 111 surface symmetric reflection from a thick silicon crystal which has a perfect crystal reflecting range of 7 seconds [42]. Station 7.6 at Daresbury is 80m away from the x-ray source which has an effective width of 0.25 mm [43]. Hence the angular divergence of the x-ray beam in

the diffraction plane is 0.6 seconds. This is negligibly small compared to the perfect crystal reflecting range of the reference crystal reflection. Therefore the rocking curve width at a point on the sample is effectively independent of the diffraction geometry and is simply obtained by convoluting the x-ray reflectivity profile from the reference crystal with the x-ray reflectivity profile from the sample crystal. For the sample reflections employed in this thesis this convolution produces an effective rocking curve width at a point on the sample of less than 30 seconds. Halliwell et al [44] have calculated the lattice distortion at dislocation cores in terms of deviation from the Bragg condition. This work suggests that the dislocation image widths will be about 5 μm for isolated 60° dislocation lines. Thus if dislocation interactions are assumed to be weak then the linear dislocation line density must be less than $0.2\mu m^{-1}$ for individual dislocations to be resolved by topography.

Chapter 4

The Relief of Epitaxial Layer Strain by Misfit Dislocations

4.1 Dislocations in the Zinc Blende Lattice

A dislocation line is a localised variation in crystal perfection which surrounds a core region that extends along a particular direction in the crystal lattice. Hence a dislocation line is characterised by two parameters; that describing the localised disruption in the crystal lattice and the direction of the dislocation line. The direction of the dislocation line is characterised simply by a vector which is parallel to the dislocation core, $\underline{l}$. The magnitude and direction of the lattice disruption surrounding the dislocation core is described by the Burgers vector, $\underline{b}$ [1]. The Burgers vector is obtained by drawing a circuit in a perfect region of the crystal lattice and comparing this to an equivalent circuit which encloses the dislocation line. Following the convention adopted by [1,2], the Burgers vector is defined as the vector required to close the latter circuit from start to finish. Since the sense of the circuit is that of a right-handed screw with respect to the dislocation line direction, this convention for $\underline{b}$ is called the **SF**/*RH* convention. The reader is referred to Hirth and Lothe [1] and Hull [3] for detailed descriptions of the properties of the various types of dislocation lines which exist in different crystal structures.

The Burgers vector of a screw dislocation is parallel to the dislocation line whereas the Burgers vector of an edge dislocation is normal to the dislocation line. These dislocations are illustrated in Figures 4.1 and 4.2. There are two criteria which predict the allowed glide planes for a particular dislocation line, the first arises from the nature of the dislocation and the second arises from the crystal structure in which the crystal is located. Both these criteria must be applied to each specific dislocation line in order to determine the allowed glide plane(s) for this dislocation. The restriction on dislocation glide which arises from the nature of the dislocation line is simply that the glide plane must contain both the dislocation line direction and also the Burgers vector. The crystal structure in which the dislocation line is located also restricts the allowed glide plane(s) which are associated with the dislocation, viz. the dislocation core can only contain one type of atom.

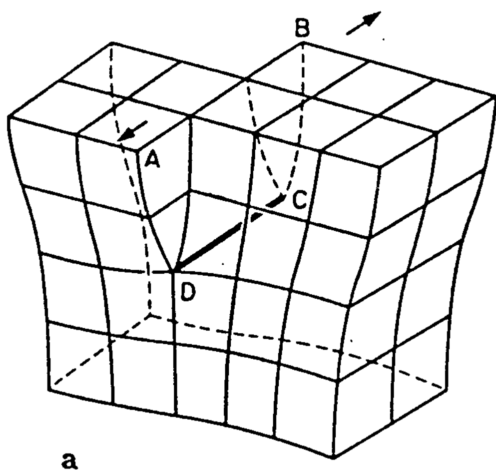

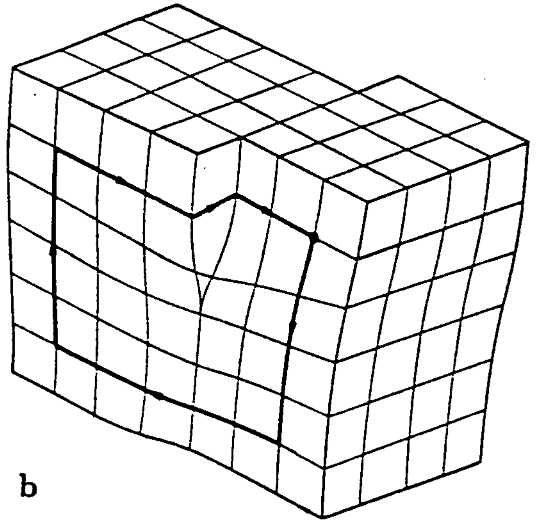

Figure 4.1:(a) Screw dislocation DC formed by displacing the faces ABCD relative to each other in direction AB, (b) Burgers circuit around the screw dislocation. After Hull [3]

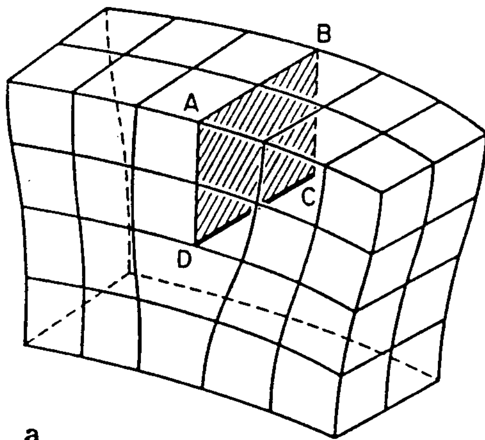

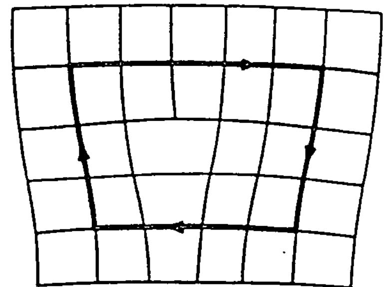

Figure 4.2:(a) Edge dislocation DC formed by insertion of an extra half plane of atoms ABCD, (b) Burgers circuit around the edge dislocation. After Hull [3]

An individual screw dislocation does not relieve misfit strain between an epitaxial layer and a substrate and so this dislocation is not discussed further here. It is sufficient to note that most of the dislocations in the substrate, caused by small thermal gradients in the substrate melt or other bulk crystal growth effects, have Burgers vectors with large screw components and hence extend into the epitaxial layer with ease and essentially unchanged during the initial stages of epitaxial layer deposition. These dislocations are popularly known as threading dislocations.

A strain relieving edge dislocation relaxes the epitaxial layer strain by a length a_o in the interface. However the (001) plane contains both group III and group V atoms and hence a pure edge misfit dislocation is sessile in the zinc blende lattice. This was first identified by Lomer [4] who suggested that it could be responsible for work hardening.

Transmission electron microscopy studies show that at low dislocation densities the mismatch dislocations which cause epitaxial layer relaxation at interfaces in zincblende structures are predominantly of the 60° type [5,6,7,8,9,10,11,12] although some evidence of misfit dislocation of pure edge character is reported [8,10,12]. Edge dislocations as well as a slight variant, the Lomer-Cottrell or stair rod dislocation, can be formed by two 60° dislocations gliding on intersecting {111} glide planes and combining along the line of intersection. However this process is only observed at high dislocation densities where the probability that two 60° dislocation lines are close enough to interact is significant.

A 60° dislocation is a hybrid between a screw dislocation and an edge dislocation and as its name implies, the angle between the Burgers vector and the dislocation line is 60°, Figure 4.3. A 60° dislocation line near an (001) interface has a Burgers vector of $a_0/2\langle 110\rangle$ inclined at 45° to the (001) plane and can glide on {111} planes. The edge component of the Burgers vector for a 60° dislocation has a magnitude $a_0\sqrt{3}/2\sqrt{2}$ in a $\langle 112\rangle$ direction (Figure 4.3). The projection of the edge component in the (001) plane relaxes the epitaxial layer misfit strain by a length $a_0/2\sqrt{2}$ in a $\langle 110\rangle$ direction normal to the dislocation line, i.e. half the {110} interplanar separation.

The lack of symmetry in the zinc blende structure leads to the creation of two types of 60° dislocation lines in the glide set. These are illustrated in Figure 4.4, a schematic diagram of the zinc blende structure, which represents the stacking sequence for the {111}-type planes. If the Volterra cut terminates on a plane of group III atoms then the dislocation is A-type whereas if the Volterra cut terminates on a plane of group V atoms then the dislocation is B-type. Evidence has been presented

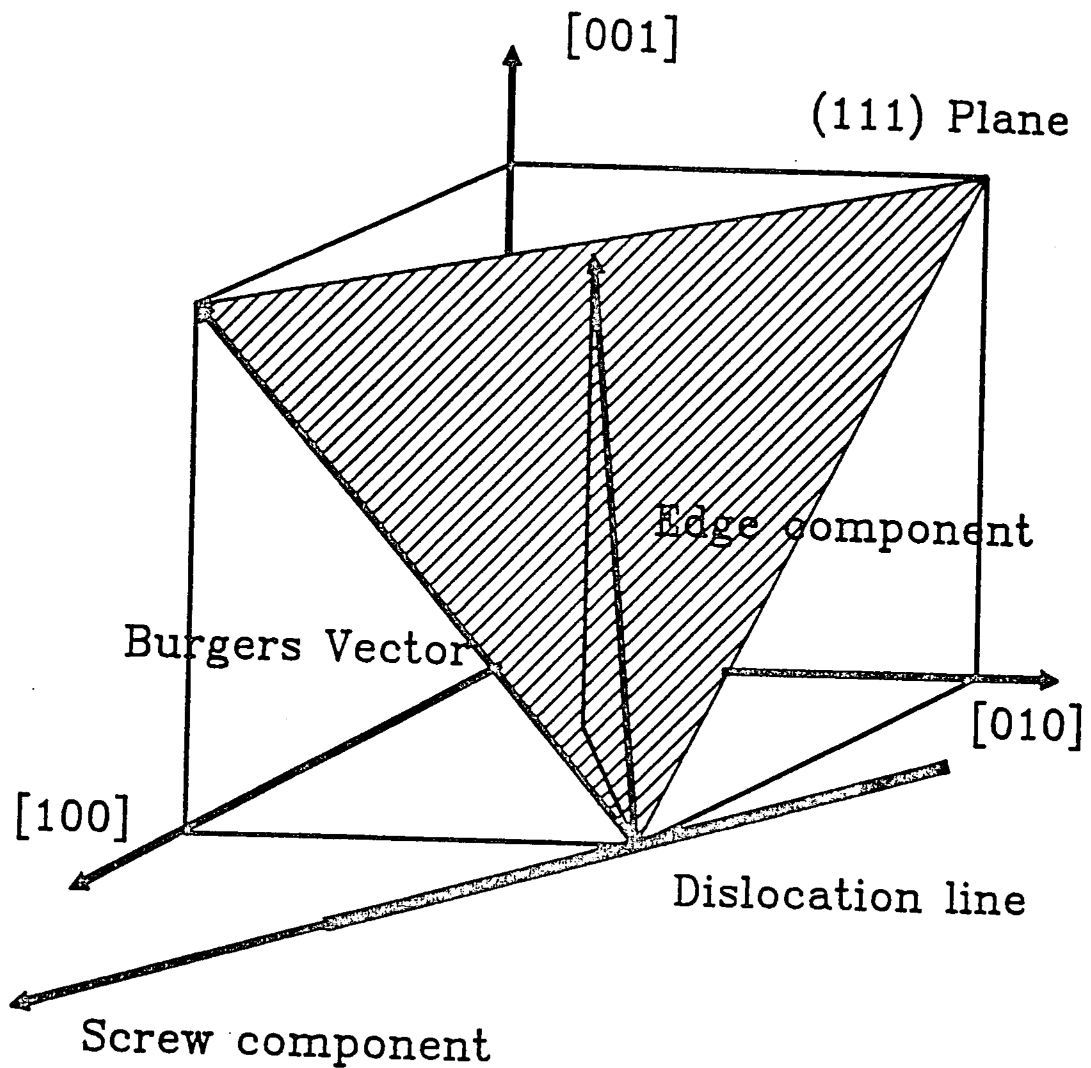

Figure 4.3: A $[1\bar{1}0]$ 60° dislocation line with a Burgers vector of $(a_0/2)$ [101]. The projection of the edge component in the (001) plane is $(a_0/2\sqrt{2})$ $[\bar{1}\ \bar{1}0]$.

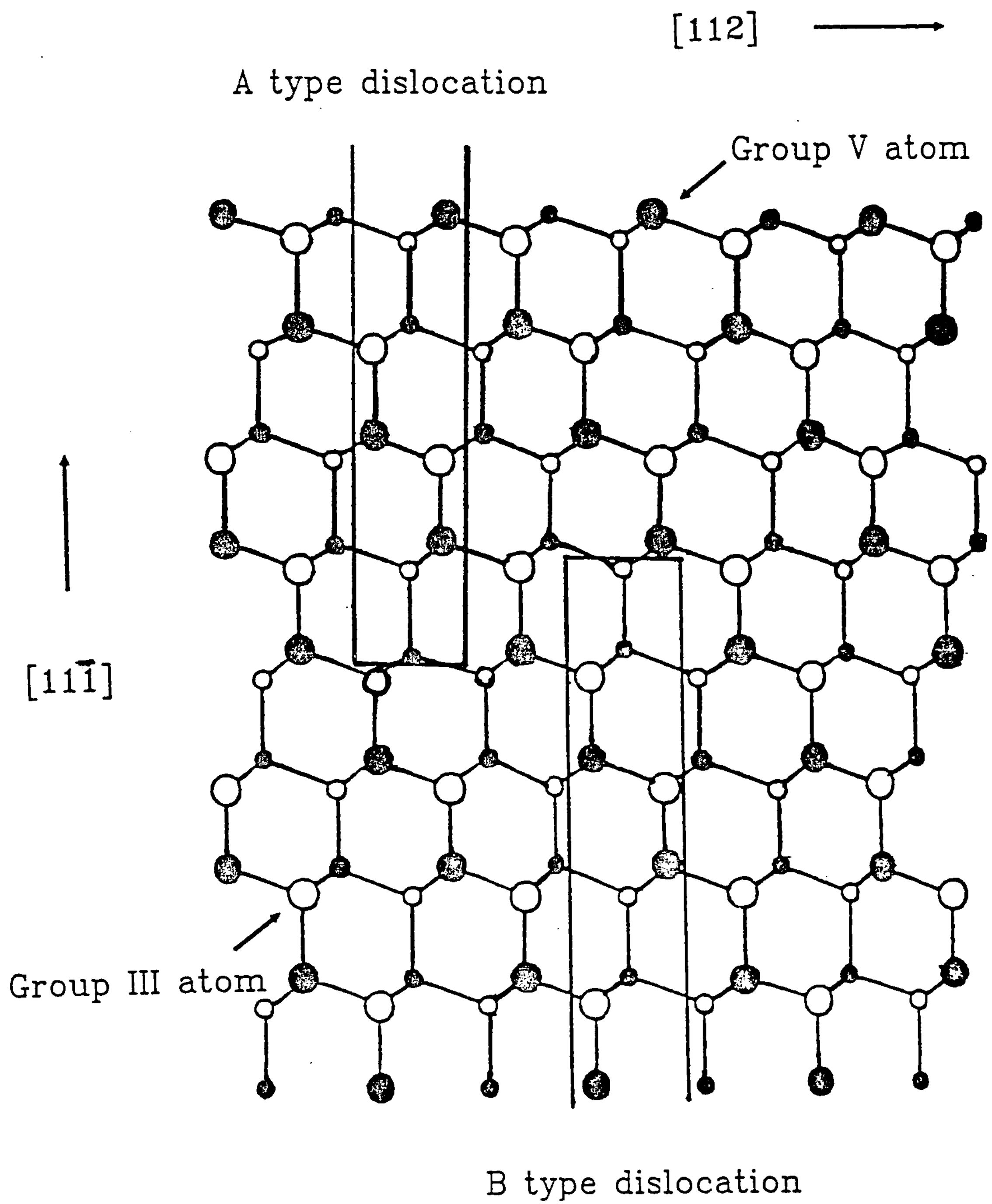

Figure 4.4: Definition of A type and B type dislocations in III-V compounds. After Hirth and Lothe [1].

which indicates that dislocations in III-V compounds are dissociated [13] over a few nanometres. Nonetheless, since the dissociation of a dislocation line requires the insertion or removal of pairs of layers of the same index, the polarity of the A-type or B-type dislocation is preserved. Hence we continue to consider perfect dislocations. Alexander [14] observed the motion of 60° dislocations in the dissociated state. Dissociation implies motion on the glide set due to the unfavourable stacking configuration which results from motion of a partial dislocation on the shuffle set and hence dislocations are taken to be the glide set rather than the shuffle set.

4.2 The Peierls-Nabarro Force

Examination of the propagation of an interfacial misfit dislocation line requires an atomistic study of the elastic forces across the interface. The Peierls-Nabarro [15,16] model approaches the problem of examining interfacial edge dislocations by assuming that the substrate and epitaxial layer system can be treated as two lattices separated by an interface and that the plane of the interface coincides with the glide plane of the edge dislocation Figure 4.5. The interface is represented as a non-hookean slab of roughly a lattice parameter width. If the radial extent of the strains associated with the dislocation line is large compared with the lattice parameters then the horizontal and vertical displacement of atoms in the plane directly above and the plane directly below the glide plane will vary slowly from atom to atom. The relative displacements of neighbouring atoms within each lattice is then much smaller than the lattice parameters and so each lattice is treated as an elastic continuum. For the sake of simplicity the lattices are assumed to be elastically isotropic.

The total energy of the P-N model consists of two parts

(i) the elastic strain energy of the two lattices and

(ii) the potential energy of attraction within the non-hookean slab

The first contribution can be calculated by using standard elasticity theory whereas the second contribution is more involved.

Consider the force on the atoms in plane **A** from the atoms in the lattice below and in particular from the atoms in plane **B**. It is assumed that the vertical component of force depends only on the relative vertical displacement of atoms in **A** with respect to atoms in **B** and that from symmetry these cancel. The horizontal component of the force is assumed to be dependant only on the horizontal displacement of atoms in **A** relative to atoms in **B**. and is treated as a continuous sinusoidal

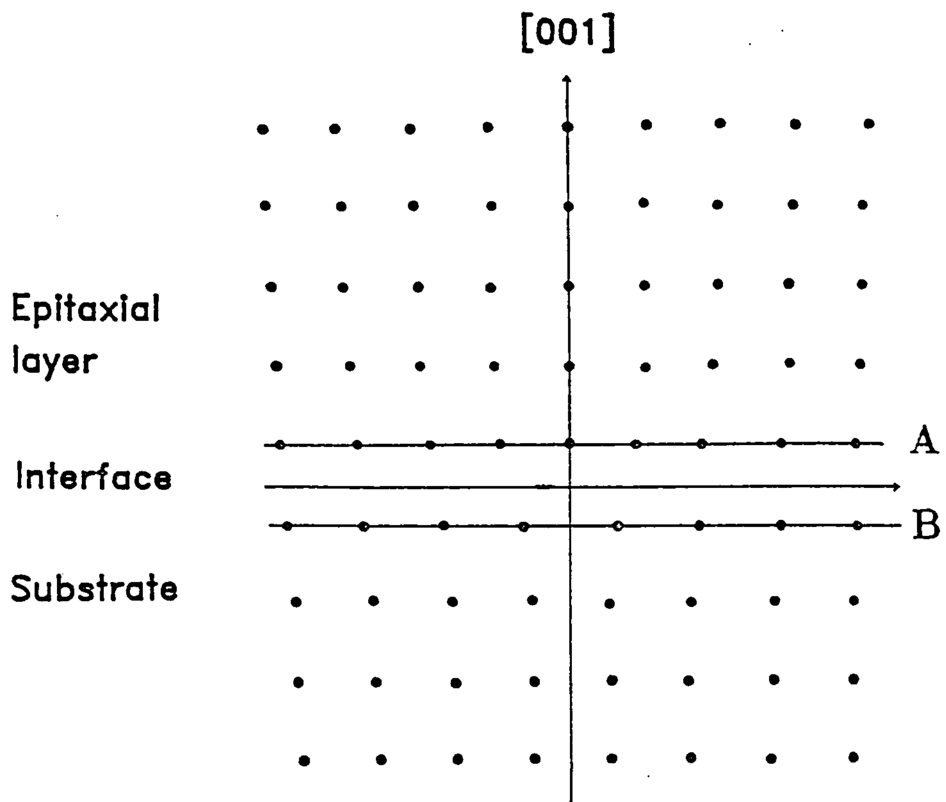

Figure 4.5: Atomistic diagram of a pure edge dislocation in the interface between two lattices.

function. Hence the potential energy of a dislocation, obtained by integrating over the interface, is independant of its position. Thus the dislocation is always in neutral equilibrium and will glide under any applied force.

However if the atomic structure is taken into account, the energy of a dislocation must, in the absence of stress, depend upon its exact position i.e. whether the plane of symmetry (i.e. the plane orthogonal to the glide plane and containing the dislocation line) passes through a row of atoms. The potential energy of the dislocation is better expressed as a sum of terms involving the displacements of the atoms in the plane directly above and the plane directly below the interface. The summation extends from $-\infty$ to $+\infty$ and is smoothly varying. The difference between the sum and the integral is small and is inversely proportional to the size of the dislocation strain field. This difference is manifest as a critical stress for dislocation glide and is known as the Peierls stress. For simplicity, the model only considers misfit in one direction. However the equations discussed above are linear within the approximations used and so solutions can be superimposed and the treatment extended to cover misfit in two orthogonal directions [17]. Further refinements to the model have been made by Van der Merwe [18,19,20].

4.3 Misfit Dislocation Generation

III-V epitaxial layer systems often contain dislocation lines which extend from the substrate, through the interface and into the layer. Under stress, these threading dislocations can bend over at the interface to form lengths of misfit dislocations. This process is considered in detail by Matthews and Blakeslee [21,22]. The early work of Petroff and Sauvage [23] on the AlGaAs/GaAs system showed conclusively that, in this system, the misfit dislocations were nucleated at either threading dislocations from the substrate or from scratches. This nucleation mechanism has been observed to operate in the highly mismatched InGaAs/GaAs system and also thin layers of AlAs on GaAs and is reported in detail in this thesis.

Matthews and Blakeslee also considered the surface nucleation of dislocation half-loops and their subsequent glide down to the interface. Below a critical radius, R_c, dislocation half-loops will contract under their own line tension and so a nucleation process must be present to form a half-loop large enough to grow under the influence of the misfit stress. Hence formation of a half-loop at a nucleation site requires an activation energy which depends upon the amount of misfit stress in the layer. If the layer is thinner than R_c then loop nucleation will not occur.

Other mechanisms for the generation of misfit dislocations include dislocation multiplication at Frank-Read sources [24], nucleation at the junction of 'islands' formed in the initial stages of epitaxial layer growth and nucleation at the base of cracks.

4.4 The Critical Epitaxial Layer Thickness

The first evidence that thin films strain elastically to accommodate misfit strain was provided not by films grown epitaxially on substrates but by layers doped by diffusion. In 1961 Queisser studied changes associated with diffusion of boron and phosphorus into silicon [25]. He found that dislocations were generated to accommodate lattice strain but did not appear until a critical quantity of dopant had diffused into the silicon lattice. This showed that in the early stages of the process the change in the surface lattice parameter of the silicon caused by dopant diffusion was wholly accommodated by elastic strain.

The critical thickness, h_c, of a mismatched epitaxial layer can be modelled by either considering the total stress in the system or the total energy in the system.

4.4.1 The Matthews Model

The conditions under which a grown-in threading dislocation in the layer might bow and glide under the influence of misfit stress to generate a misfit dislocation are examined in conjunction with the conditions necessary for the nucleation and expansion of half-loops [26,27,28,29]. The model developed by Matthews and co-workers determines h_c as the film thickness at which a pre-existing threading dislocation is in mechanical equilibrium. In mechanical equilibrium the force exerted by the misfit strain is balanced by the tension in the dislocation line, the tension of the surface step and the Peierls stress. The surface tension and the Peierls stress were shown to have little significance, [27]. The critical thickness obtained by the Matthews model for the generation of 60° misfit dislocations in an epitaxial layer is

$$h_c = \frac{b(1 - 0.25 \times \nu)}{4\pi m(1 + \nu)} \left(ln \left[\frac{h_c}{b} \right] + 1 \right) \qquad 4.1$$

where b is the magnitude of the Burgers vector and m is the mismatch [28].

This model is best applied to metallic systems and group III-V semiconductor

sytems which contain a high density of threading dislocations. Advances in group IV semiconductor epitaxy ensure that the threading dislocation density in this sytem is rarely high enough for the Matthews model to apply. This model is important as it was the first model to incorporate a physical description of the mechanism by which misfit dislocation lines are generated.

4.4.2 The Frank-van der Merwe Model

This model determines h_c as the thickness at which the strain energy density in the layer coincides with the energy density required by the most favourable dislocation generating mechanism. At this point it is assumed that pseudomorphic growth becomes unstable and misfit dislocations are generated. This model assumes that the layer is initially dislocation-free and hence that misfit dislocation generation occurs via the nucleation of half-loops at the sample surface. This approach was first adopted by Frank and van der Merwe in 1949 [30]. Their study was concerned with the stability of a single monolayer on a substrate so that a critical misfit was the more appropriate quantity to establish. The model was extended to include epitaxial layers of finite thickness [17] and further developed in a rigorous form by van der Merwe [19,20,31]. The Frank-van der Merwe model calculates the interfacial energy required to produce an array of misfit dislocations. This is determined from the strain fields of the misfit dislocations and the residual elastic misfit. The interfacial energy is compared with the areal strain energy density in the layer and leads to an expression for critical thickness, h_c,

$$h_c = \frac{a_0(1-\nu)}{8\pi^2(1+\nu)m} \qquad 4.2$$

where m is again the lattice mismatch. Although this model does not reliably predict the critical layer thickness for most semiconductors, it laid the foundations for the People and Bean model [32,33]. The People and Bean model accurately predicts the critical thickness in the SiGe/Si system and can be applied to group III-V systems where the threading dislocation density in the substrate is very low.

4.5 The Origins of Asymmetric Relaxation

There is considerable experimental evidence that the relief of misfit stress in III-V epitaxial layers grown on 001 substrates is asymmetric about the [110] and $[1\bar{1}0]$ directions although no such effects are observed in epitaxial layers of SiGe on Si. Asymmetric relaxation in epitaxial layers of III-V compounds has been observed by Fitzgerald and co-workers [34,35] using cathodoluminescence whereas Nagai [36] observed asymmetric stress relief to manifest itself as asymmetric curvature of the epitaxial layer. The most conclusive demonstration of asymmetric relaxation was performed by Rozgonyi *et al* [37] who inverted a piece of a GaAs wafer to grow a quaternary layer on both the (001) and $(00\bar{1})$ planes. They used x-ray topography to show that a 90° rotation in the dislocation asymmetry occurred and concluded that not all 60° dislocation slip systems were equivalent. In this thesis and elsewhere [39], the present author has measured asymmetric relaxation in epitaxial layers by double crystal x-ray diffractometry and double crystal x-ray topography, comparing and contrasting both techniques.

At low dislocation densities the relief of misfit stress is accommodated by the nucleation and propagation of 60° dislocations which glide on {111} planes. The lack of centro-symmetry in a III-V zincblende lattice results in the classification of two chemically distinct types of 60° dislocation; if the Volterra cut terminates on a group III atom then the 60° dislocation is of type A whereas if the Volterra cut terminates on a group V atom then the 60° dislocation is of type B, figure 4.4. The III-V zinc blende structure consists of a face centred cubic lattice with a basis of two atoms. In the Gatos and Lavine convention [39] the basis consists of a group III atom at the origin and a group V atom at coordinate position (1/4,1/4,1/4). Thus for an 001 orientated epitaxial layer sample viewed along the $[00\bar{1}]$ direction the advancing (111) planes contain group III atoms whereas the advancing $(\bar{1}\bar{1}1)$ planes contain group V atoms. Therefore A-type 60° dislocations glide on (111) planes and have a dislocation line direction of $[1\bar{1}0]$ whereas B-type 60° dislocations glide on $(\bar{1}\bar{1}1)$ planes and have a dislocation line direction of $[\bar{1}10]$. The Peierls stress for dislocation glide across (111) planes of group III atoms is different to the Peierls stress for dislocation glide across $(\bar{1}\bar{1}1)$ planes of group V atoms. It is not surprising, therefore, that the mobilities of the A-type and B-type dislocations are also different. Recently Fox and Jesser [40] have presented a thorough investigation into the source of asymmetric misfit dislocation morphology which confirms that a definitive correlation can be made between the relaxation asymmetry and the differences in the Peierls stresses for A-type and B-type 60° dislocations. Furthermore they

conclude that there is a separate critical thickness for each dislocation type. Prior to this, measurements on bulk crystals carried out by Erofeeva [41] and Steinhard and Haasen [42] demonstrated that the mobilities of A-type and B-type dislocations are indeed different. This accounts for the marked asymmetry in dislocation rosettes punched out from indention sites reported by Warren [43] and Surowiec [44].

Chapter 5

Analysis of Double Crystal Rocking Curve Data

5.0 Introduction

Sections 5.1 to 5.4 illustrate how rocking curves can be analysed using rocking curve data collected during the course of this thesis. Section 5.5 uses this to examine how epitaxial layer tilt is related to misfit dislocation line density in four samples.

5.1 Determination of the Composition of a Strained Epitaxial Layer

5.1.1 Symmetric Bragg Geometry

A double crystal rocking curve records the variation in the x-ray intensity diffracted by a sample crystal as a set of lattice planes within the crystal is rotated through the Bragg diffraction condition. The x-ray wavelength is defined by the Bragg diffraction condition at the first crystal. All the rocking curve data presented in this thesis were taken at an x-ray wavelength of 1.54051 ± 0.00004 Å (section 3.1.1). The samples examined in this thesis consist of a substrate, usually about 0.25mm thick, upon which is deposited a relatively thin epitaxial layer, of between 100 Å and 10 μm, which has a slightly different bulk lattice parameter to the substrate. Bragg planes which are parallel to the epitaxial layer interface are termed symmetric. The samples examined in this thesis were grown on 001 orientated substrates and hence the lowest order symmetric reflection which is permitted in the zinc blende structure is the 004 (section 2.2). The difference between the Bragg condition for diffraction from the epitaxial layer and the Bragg condition for diffraction from the substrate, $\delta\theta_B$, is defined by $\delta\theta_B = \theta_{BS} - \theta_{BL}$. The angle $\delta\theta_B$ is small compared to θ_{BS} and so the differential of the Bragg equation for fixed x-ray wavelength, which was introduced in section 2.0 as equation 2.2 and is repeated here as equation 5.1, can be applied to calculate the difference, δd, between

the interplanar separation of the Bragg reflecting planes in the substrate, d, and the epitaxial layer.

$$\delta d = -d \; cot\theta_B \; \delta\theta_B \qquad 5.1$$

Equation 5.1 is usually written in terms of the effective mismatch m^*, equation 5.2, and allows calculation of the real mismatch, m, through equation 1.5

$$m^* = - \; cot\theta_B \; \delta\theta_B \qquad 5.2$$

5.1.2 Calibration of the Double Crystal Diffractometer

Clearly the limitation on the accuracy of m^* depends on the accuracy of calibration. Thus the number of stepper motor steps corresponding to an axis rotation of one second in the software must be investigated. Bede Scientific DCC control software enables the user to calibrate his/her own diffractometer through a configuration file which contains relations describing the number of stepper motor steps corresponding to a rotation of the first and second axes by 1 second. The Durham diffractometer can be calibrated approximately from the mechanics of the arrangement of motors, gearboxes and tangent arms which is used to rotate the diffractometer axes. The first and second axes are driven by 4 phase stepper motors which complete one revolution in 200 steps. Each stepper motor is down geared through a 100:1 gearbox which in turn drives a tangent arm connected to an axis. The tangent arm has a length of 113.1 mm and so a movement of the arm by 1mm rotates the axis by about 30.4 arc minutes. The Bede Scientific Instruments DCC control software is accurately calibrated for a model 150 diffractometer incorporating metric micrometer screws in which case a complete revolution of the micrometer moves the tangent arm by 0.5 mm and so an axis rotation of 1 second requires 9.804 motor steps. However the apparatus at Durham incorporates imperial micrometers and a complete revolution of one of these micrometer screws moves the tangent arm by $\frac{1}{40}$" which is equivalent to 0.6356 mm.

An effective method of calibrating the double crystal diffractometer at Durham involves positioning thick, perfect crystals on the first and second crystal axes in a parallel dispersive geometry and comparing the angular separation of the copper $K_{\alpha 1}$ and $K_{\alpha 2}$ characteristic lines on the rocking curve recorded at the detector with

the corresponding angular separation predicted from consideration of the parallel dispersive geometry. The separation, ΔK, between the $K_{\alpha 1}$ and $K_{\alpha 2}$ Bragg reflections is given by equation 5.3 which is derived in a similar fashion to equation 3.3.

$$\Delta K = \frac{\delta \lambda_k}{\lambda}\{tan\theta_2 - tan\theta_1\} \qquad 5.3$$

$\delta\lambda_k$ represents the difference in wavelength between the $K_{\alpha 1}$ and $K_{\alpha 2}$ characteristic lines i.e. $(3.82 \pm 0.05) \times 10^{-3}\mathring{A}$. The second axis of the Durham diffractometer was accurately calibrated by measuring ΔK for the parallel dispersive geometries listed in Table 5.1. In Table 5.1 $\Delta K_{exp.}$ corresponds to the measured separation assuming a calibration constant of 9.804 steps for 1 arc second whereas $\Delta K_{th.}$ is the peak separation calculated from equation 5.3. The experimental error associated with the values of $\Delta K_{exp.}$ in Table 5.1 arises from the uncertainty in locating the centroids of the Bragg reflections on the rocking curves.

Table 5.1. Parallel Dispersive Geometries Employed in the Calibration of the Durham Double Crystal Diffractometer

1st Crystal			2nd Crystal			$\lvert\Delta K_{th.}\rvert$ (seconds)	$\lvert\Delta K_{exp.}\rvert$ (seconds)	Calibration Ratio
Mat.	Surf.	Refln.	Mat.	Surf.	Refln.			
GaAs	001	004	Si	111	333	226	170 ± 1	1.33 ± 0.01
InP	001	004	Si	111	111	186	150 ± 1	1.24 ± 0.01
InP	001	004	Si	111	333	243	193 ± 1	1.26 ± 0.01
InP	001	004	InP	110	220	111	90 ± 1	1.24 ± 0.01
InP	001	004	InP	110	440	252	196 ± 1	1.29 ± 0.01
GaAs	001	004	Si	111	111	203	150 ± 1	1.35 ± 0.01
GaAs	001	004	Si	111	333	226	176 ± 1	1.28 ± 0.01
GaAs	001	004	InP	110	220	128	96 ± 1	1.33 ± 0.01
GaAs	001	004	InP	110	440	235	180 ± 1	1.30 ± 0.01

The average calibration ratio was calculated as (1.292 ± 0.038) which implies that the calibration entry in the configuration file for the second axis should be (7.59 ± 0.22) stepper motor steps for a 1 arc second rotation.

5.1.3 The Effect of Tilt between the Epitaxial Layer and the Substrate

The epitaxial layer lattice is often tilted with respect to the substrate lattice, Figure 5.1, which precludes the measurement of $\delta\theta_B$ from only one double crystal rocking curve.

The component of tilt between the substrate and epitaxial layer lattices in the diffraction plane, β, is decoupled from the separation between the diffraction peaks on the rocking curve, $\delta\theta$, by repeating the rocking curve with the sample rotated through 180° wherein $\delta\theta_B$ is equal to the mean value of $\delta\theta$ measured on the rocking curve pair. A pair of anti-parallel rocking curves is obtained most easily by employing a rotating sample stage aligned so that the incident x-ray beam strikes the axis of rotation [1]. The rocking curve data presented in this thesis were taken with the aid of a rotation stage similar to the product commercially available from Bede Scientific Instruments. The accuracy associated with the alignment of the axis of rotation of the sample stage with the x-ray beam is estimated at 0.5 mm.

The absolute tilt between the lattices can be measured from two orthogonal pairs of rocking curves [2]. The tilt components parallel and perpendicular to a reference direction in the sample surface, β_1 and β_2 respectively, result from an absolute tilt, B, given by

$$tan^2 B = tan^2\beta_1 + tan^2\beta_2 \qquad 5.4$$

The direction of maximum tilt is at an angle α to the reference direction where α is given by

$$tan\alpha = \frac{tan\beta_1}{tan\beta_2} \qquad 5.5$$

If the epitaxial layer is coherent with the substrate then the composition of the epitaxial layer can be determined from equation 5.2, equation 1.3 and a pair of anti-parallel 004 double crystal rocking curves.

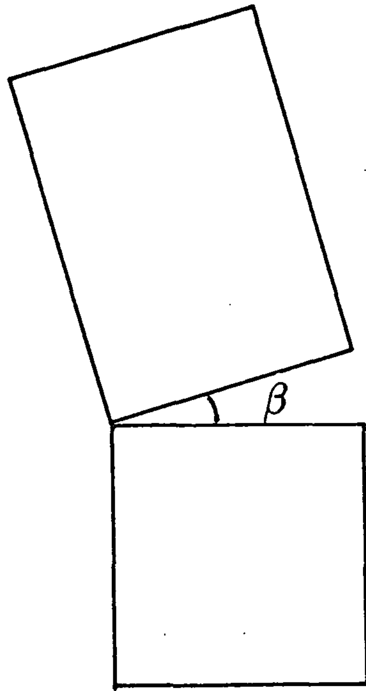

Figure 5.1: Tilt between the substrate and epitaxial layer unit cells.

5.1.4 Precise Determination of the Aluminium Concentration in a Layer of AlGaAs

Sample GaAs1 consists of a layer of AlGaAs which was deposited by MBE on an 001 GaAs substrate at Glasgow University by C. Stanley. Expecting a layer composition of $Al_{0.35}Ga_{0.65}As$, Stanley allowed a nominal layer thickness of 1.2 μm which is well below the critical layer thickness for this system. Simon Miles [3] had examined samples cut from different positions on the same wafer and found that the aluminium concentration in the epitaxial layer varied from $(35.9 \pm 1)\%$ for a sample taken at a distance of 2mm from the centre of the wafer to $(39.8 \pm 1)\%$ for a sample taken at a distance of 14mm from the centre of the wafer. This demonstrates the importance of point by point sample mapping, but here an uncertainty existed as to the calibration in the independent experiments. The Glasgow group were experiencing problems of discrepency between x-ray and reflection high energy electron diffractometry (RHEED) data. A very careful measurement was undertaken to determine the composition at a further position on the wafer. In the case of GaAs1 the sample was taken at a distance of 18 mm from the centre of the wafer.

The diffractometer was aligned in the parallel non-dispersive geometry employing Bragg diffraction from the 004 lattice planes in the sample crystal. A pair of antiparallel rocking curves was recorded in order to calculate β. Data were collected at arc second steps along the rocking curve with a counting time of four seconds per data point. The rocking curves are presented in Figure 5.2 and the reduced diffractometry data is summarised in Table 5.2. The error in the separation between the substrate and epitaxial layer peaks, $\delta\theta$, was deduced from accuracy to which these can be located on the rocking curves.

Table 5.2. 004 Diffractometry Data from Sample GaAs1

	$\delta\theta$ (seconds)	Substrate Peak FWHM (seconds)	Layer Peak FWHM (seconds)
Parallel Rocking Curve	-(153 $\pm$ 0.5)	20	21
Anti-Parallel Rocking Curve	-(153 $\pm$ 0.5)	20	24

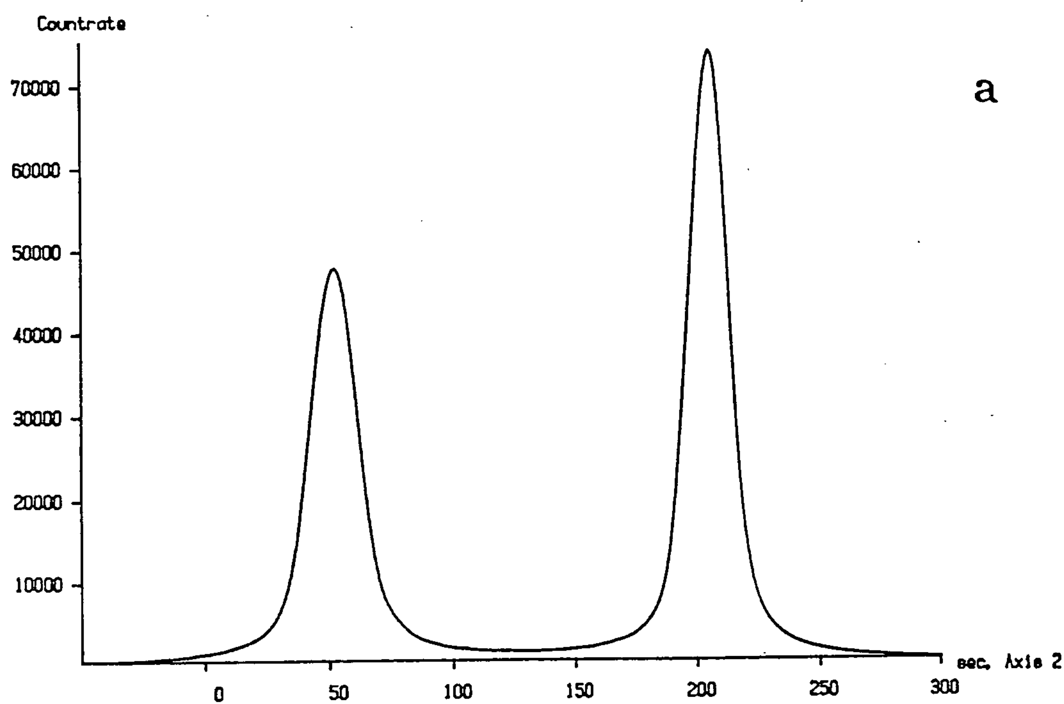

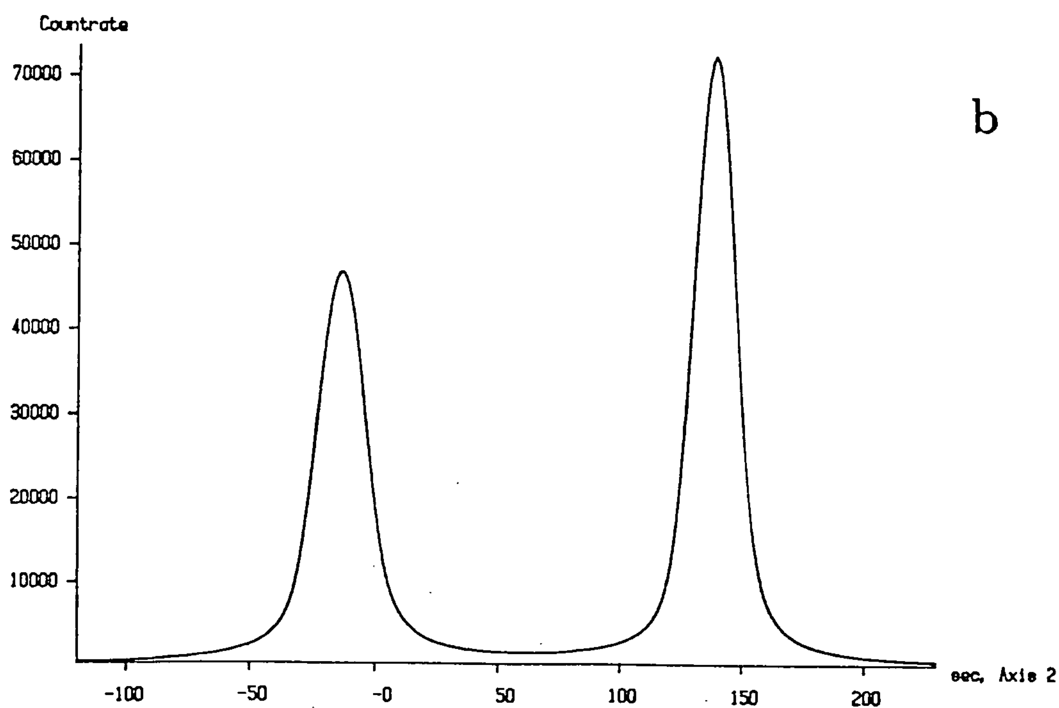

Figure 5.2: 004 experimental rocking curves of GaAs1: (a) 0° rotation, (b) 180° rotation.

The diffractometry data demonstrate that $\beta = 0 \pm 0.5$ arc seconds for this sample. The lack of tilt between the epitaxial layer lattice and substrate lattice (section 5.5) and the narrow full width at half maximum intensity (FWHM) of the Bragg reflections [4] are strong indications of crystalline perfection at the interface.

The AlAs Poisson ratio has recently been extablished definitively [5,6] and the Bragg peak splitting for the 004 reflection at 1.54051 Å for an AlGaAs layer on an 001 GaAs substrate, $\delta\theta_B$ in arc seconds, as a function of Al concentration, x, given by the equation

$$|\delta\theta_B| = 409x - 29.5x^2 \qquad 5.6$$

Thus the Al concentration in the epitaxial layer is determined as (38.5 ± 1)%. Comparison of the Al concentration for this sample, taken at a distance of 18mm from the wafer centre, with the values of Al concentration determined by Miles [3] demonstrates that the Al concentration does increase with distance from the centre of the wafer.

The variation in Al concentration arises as a result of the position of the wafer in the MBE chamber. In general, the Knudsen effusion cells in an MBE chamber are focussed on the centre of the substrate wafer and epitaxial layer deposition in this region is accurately controlled. However the angles subtended between the molecular beams and the substrate vary with the distance from the focal point. The effusion cells are spatially separated and so the individual molecular beams are not co-axial. Hence the compositon of the epitaxial layer varies with the distance from the centre of the wafer. In this case the variation in Al concentration with distance from the centre of the wafer is considerable. Usually the variation in layer composition is reduced to a radial effect by rotating the wafer about the focal point.

5.2 Determination of Epitaxial Layer Relaxation by Diffractometry

The methodology presented thus far enables deduction of the epitaxial layer unit cell lattice parameters from double crystal diffractometry data on the assumption that the layer is coherent with the substrate across the interface. However if the critical thickness of the epitaxial layer is exceeded then misfit dislocations are nucleated which propagate near the interface in order to reduce the strain energy in the epitaxial layer. In this case the epitaxial layer is said to be incoherent or relaxed.

The epitaxial layer relaxation, R, is defined by equation 1.6, which is reproduced here as equation 5.7.

$$R = \frac{(a_l - a_o)}{(a_r - a_o)} \qquad 5.7$$

5.2.1 Asymmetric Bragg Geometry

The value of $\delta\theta_B$ obtained from symmetric double crystal rocking curves enables deduction of the epitaxial layer lattice parameter perpendicular to the interface. Information on the epitaxial layer lattice parameters parallel to the interface is obtained by recording the Bragg diffraction profiles from lattice planes which are asymmetric with the interface. If the mismatch is non-zero then the epitaxial layer unit cell will be strained to fit the substrate unit cell across the interface and the layer unit cell will not be cubic. Hence asymmetric lattice planes in the layer are not parallel to the equivalent asymmetric lattice planes in the substrate, Figure 5.3. The angles subtended between these planes and the sample surface are referred to as ϕ_L and ϕ_S for the layer and substrate respectively, where ϕ_S can be calculated from equation 2.5. Asymmetric reflections allow two possible incident X-ray beam paths Figure 5.3. The separation between the Bragg diffraction peaks from the substrate and the epitaxial layer on the rocking curve, $\delta\theta$, is then $(\delta\theta_B + \delta\phi)$ for the high angle of incidence and $(\delta\theta_B - \delta\phi)$ for the low angle of incidence, where $\delta\phi = \phi_S - \phi_L$. If rocking curves are recorded using both beam paths then $\delta\theta_B$ and $\delta\phi$ can be found independently, since $\delta\theta_B$ is half the sum of the two separations whilst $\delta\phi$ is half the difference. As the epitaxial layer lattice may be tilted with respect to the substrate lattice, a minimum of four asymmetric rocking curves is required in order to determine the values of ϕ_L and θ_L.

In the case where the epitaxial layer is coherently strained to the substrate across the interface, and so a = b in the epitaxial layer unit cell, then equations 5.8 and 5.9 can be deduced from equation 2.5, equation 5.1 and the Bragg condition [3].

$$cos\phi_L = cos(\phi_S + \delta\phi) = \frac{l}{c}\left(\sqrt{\frac{h^2+k^2}{a^2} + \frac{l^2}{c^2}}\right)^{-1} \qquad 5.8$$

$$sin\theta_L = sin(\theta_S - \delta\theta) = \frac{\lambda}{2}\sqrt{\frac{h^2+k^2}{a^2} + \frac{l^2}{c^2}} \qquad 5.9$$

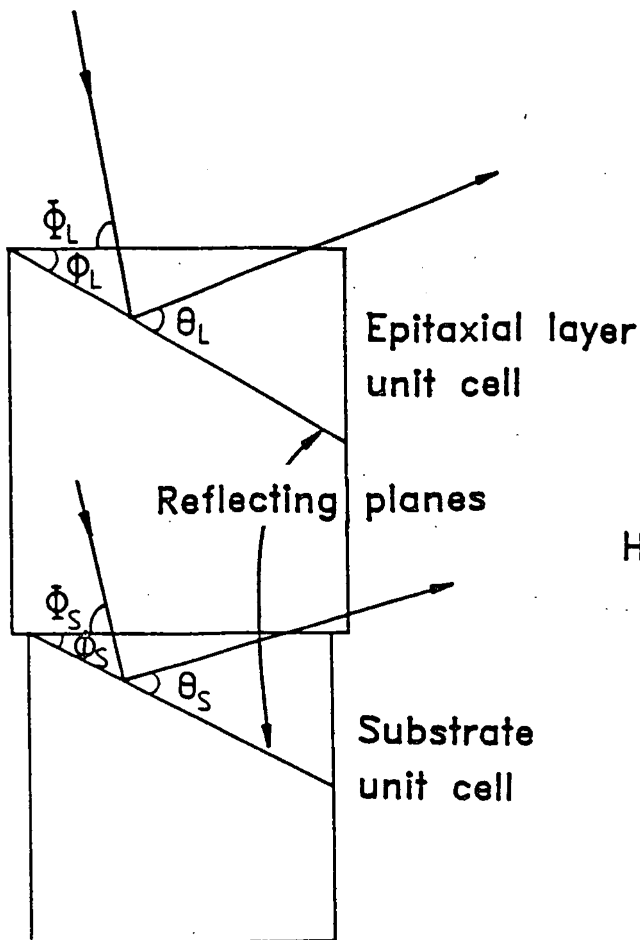

High Angle of incidence

$$\begin{aligned}\delta\theta &= \Phi_S - \Phi_L \\ &= \theta_{BS} + \phi_S - (\theta_{BL} + \phi_L) \\ &= \delta\theta_B + \delta\phi\end{aligned}$$

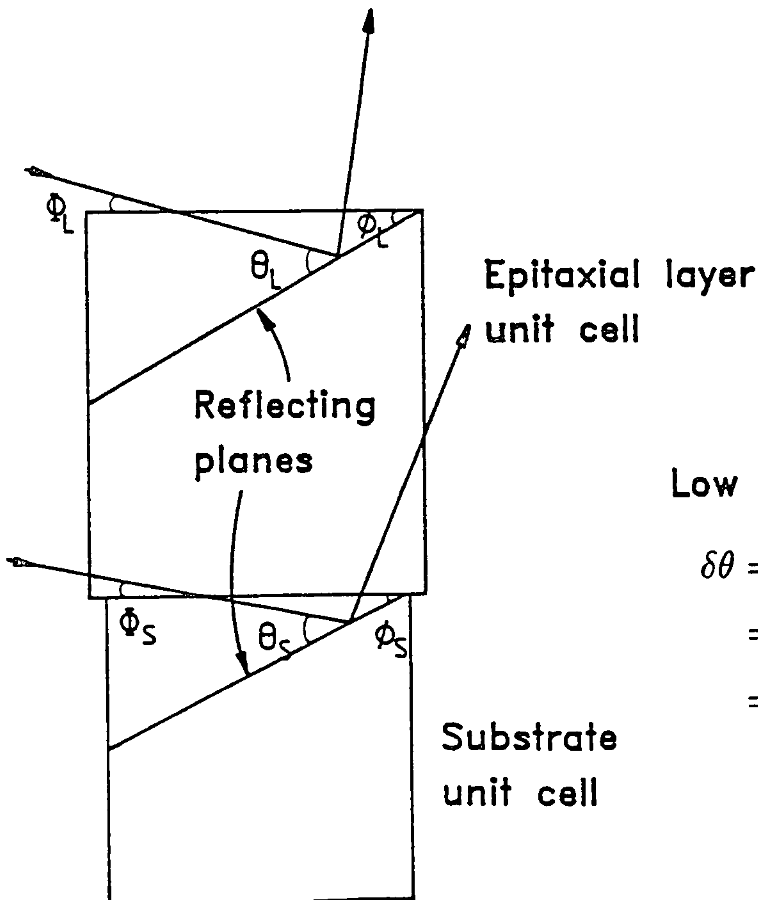

Low angle of incidence

$$\begin{aligned}\delta\theta &= \Phi_S - \Phi_L \\ &= \theta_{BS} - \phi_S - (\theta_{BL} - \phi_L) \\ &= \delta\theta_B - \delta\phi\end{aligned}$$

Figure 5.3: X-ray beam paths for an asymmetric reflection

5.2.2 Geometric Construction for Deduction of Layer Parameters for the case of Asymmetric Relaxation

The experimental evidence discussed in chapter 4 demonstrates that the relief of misfit strain in epitaxial layers of III-V compounds grown on 001 substrates is often asymmetric with respect to the [110] and $[1\bar{1}0]$ directions. In this case the [110] and $[1\bar{1}0]$ vectors in the layer will have different lengths and so the [100] and [010] vectors in the layer will no longer be orthogonal. Hence it is inaccurate simply to extend the analysis developed in section 5.2.1 and formulate equations similar to equations 5.8 and 5.9. However to a first approximation, the [110] and $[1\bar{1}0]$ vectors in the layer will remain orthogonal and this assumption, in conjunction with the Ewald sphere construction, can be used to develop a general method for deriving the relaxed layer unit cell dimensions from double crystal diffractometry data [7,8].

The Ewald sphere construction is essentially a statement of Bragg's law in reciprocal space. The separation between the Bragg reflections from the epitaxial layer and the substrate on a double crystal rocking curve represents the change in the angle of incidence subtended between the X-ray beam and the sample which is required to move the Ewald sphere from a position in reciprocal space where it intercepts the substrate reflection to a position where it intercepts the layer reflection. The substrate lattice parameter is known and hence the absolute position of the layer reflection in reciprocal space can be deduced. Asymmetric reflections in the four $\langle 110 \rangle$ zones are used so that the calculation reduces to a two dimensional problem in reciprocal space. In Figure 5.4 the position of the layer reflection in reciprocal space (x,z) is expressed in terms of the angle subtended between the incident x-ray beam and the sample surface for the high angle of incidence beam path, i_H, and the x-ray wavelength, λ, through equation 5.10

$$\left(x + \frac{\cos i_H}{\lambda}\right)^2 + \left(z - \frac{\sin i_H}{\lambda}\right)^2 = \frac{1}{\lambda^2} \qquad 5.10$$

A similar expression is developed for the low angle of incidence beam path.

$$\left(\frac{\cos i_L}{\lambda} - x\right)^2 + \left(z - \frac{\sin i_L}{\lambda}\right)^2 = \frac{1}{\lambda^2} \qquad 5.11$$

These equations are combined to form equation 5.12.

$$\frac{z}{x} = \frac{\cos i_H + \cos i_L}{\sin i_H - \sin i_L} \qquad 5.12$$

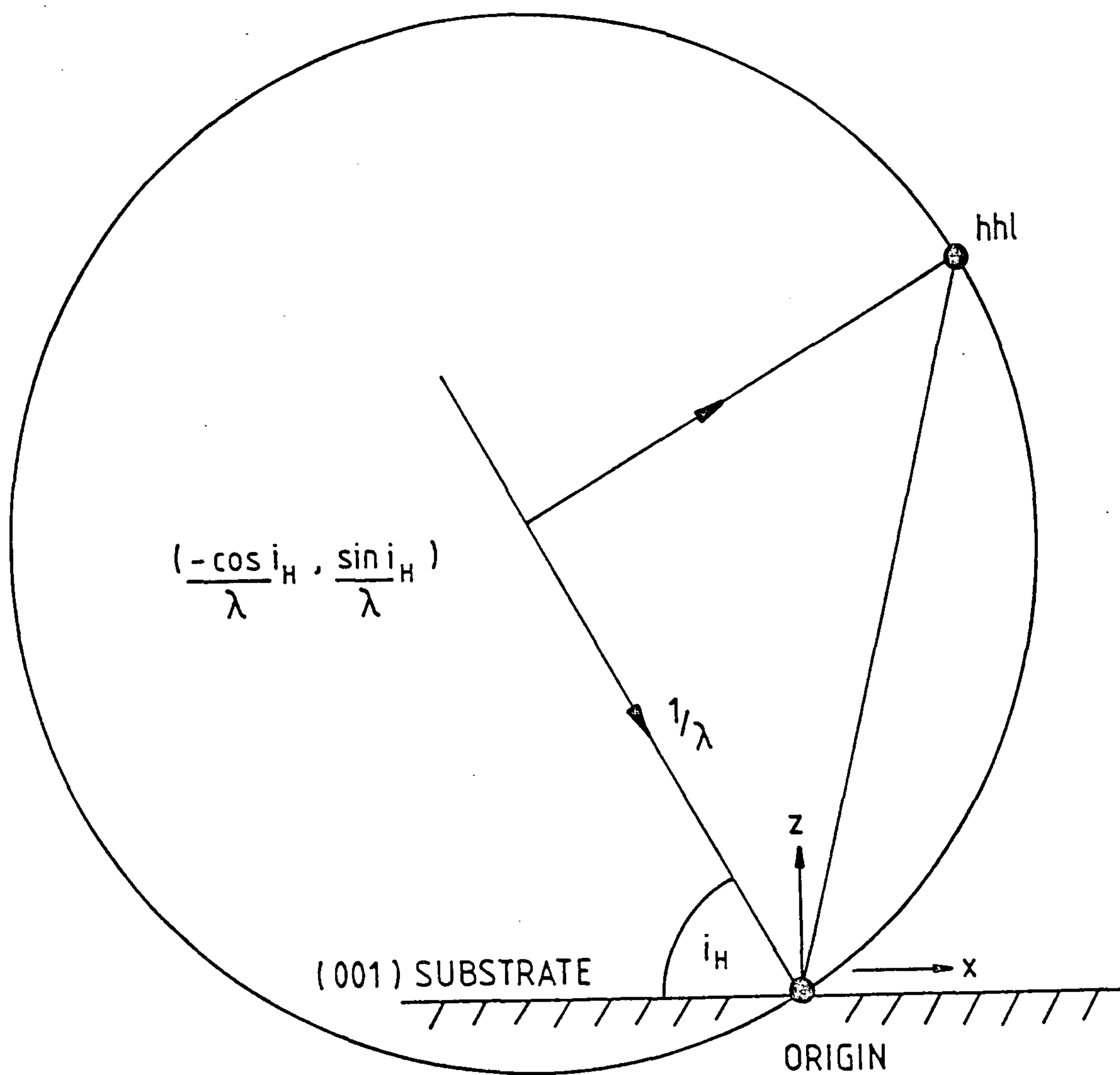

EWALD SPHERE

$$\left(x + \frac{\cos i_H}{\lambda}\right)^2 + \left(z - \frac{\sin i_H}{\lambda}\right)^2 = \frac{1}{\lambda^2}$$

Figure 5.4: The layer reflection reciprocal lattice point. After Halliwell [7]

Equation 5.12 allows substitution for x or z in equations 5.10 or 5.11 leading to an absolute determination of the position of the layer reflection in reciprocal space and from this the dimensions of the layer unit cell can be deduced. Calculation of the degree of tilt between the epitaxial layer and the substrate requires diffractometry data from orthogonal pairs of anti-parallel rocking curves. Hence the minimum data requirement to enable a full description of an asymmetrically relaxed epitaxial layer is a complete set of eight *hhl* reflection rocking curves from a single point on the sample. In practice the experimental error is reduced by employing a surface symmetric 004 reflection to provide an independent determination of the tilt between the epitaxial layer and the substrate and the 'z'parameter. Different asymmetric reflection rocking curves can be recorded to minimise the experimental error.

5.2.3 Asymmetric Relaxation in a Layer of AlAs grown by MBE

In order to investigate the mismatch between AlAs and GaAs and the AlAs Poisson ratio, a series of 1 μm layers of $Al_xGa_{1-x}As$ on 001 GaAs substrates were grown by C. Stanley at Glasgow University using MBE where x=0.1, 0.2, 0.3, 0.5 and 1. The aluminium concentration in each of these layers was measured by reflection high energy electron diffraction [9]. This was compared with the separation between the substrate and epitaxial layer peaks measured on the 004 surface symmetric double crystal rocking curves recorded from these samples. Tanner [5] deduced that a quadratic fit to the diffractometry and composition data would allow determination of the mismatch between AlAs and GaAs and the AlAs Poisson ratio. However diffractometry data from the 1 μm layer of AlAs (x=1) was not consistent with the quadratic fitting function and it was concluded that this layer might have relaxed. Therefore double crystal diffractometry was used in the asymmetric mode to determine the relaxation of this sample.

The AlAs layer in sample GaAs2 is capped by a 1 μm layer of $Al_{0.3}Ga_{0.7}As$ and a 1 μm layer of GaAs. Double crystal rocking curves were recorded in the parallel non-dispersive geometry by employing an 004 reflection from a GaAs crystal at the first axis and removing the $K_{\alpha 2}$ characteristic line component by positioning a set of slits in front of the sample crystal. This geometry facilitates changing between sample reflections without requiring re-alignment of the diffractometer and provides a well conditioned beam with which to probe the sample crystal. A complete set of 115 rocking curves and the 004 rocking curves were recorded and is presented in Figures 5.5 to 5.7 whereas the diffractometry data is presented in Table 5.3

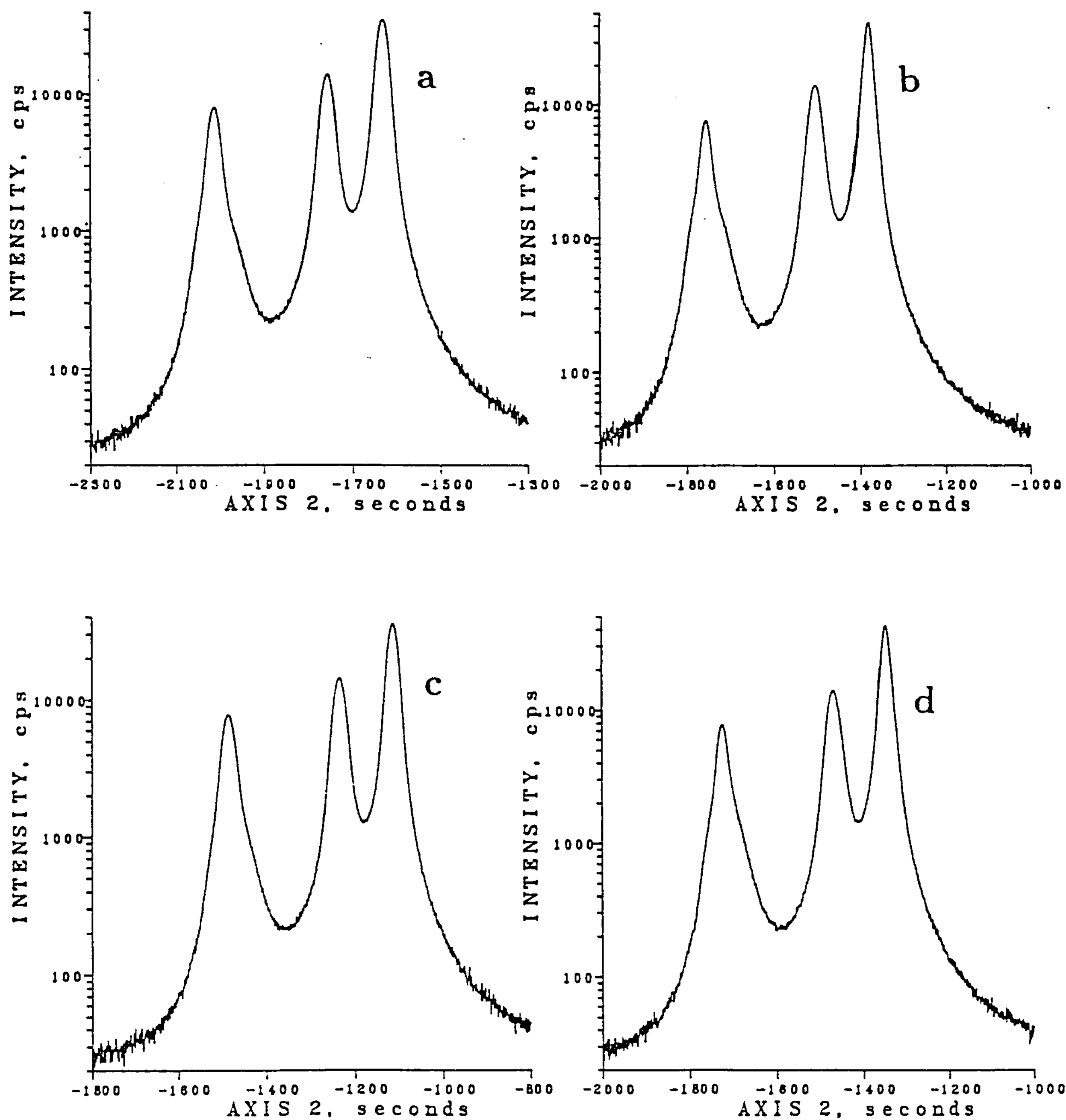

Figure 5.5: 004 experimental rocking curves of sample GaAs2; (a) 0° rotation, (b) 90° rotation, (c) 180° rotation, (d) 270° rotation.

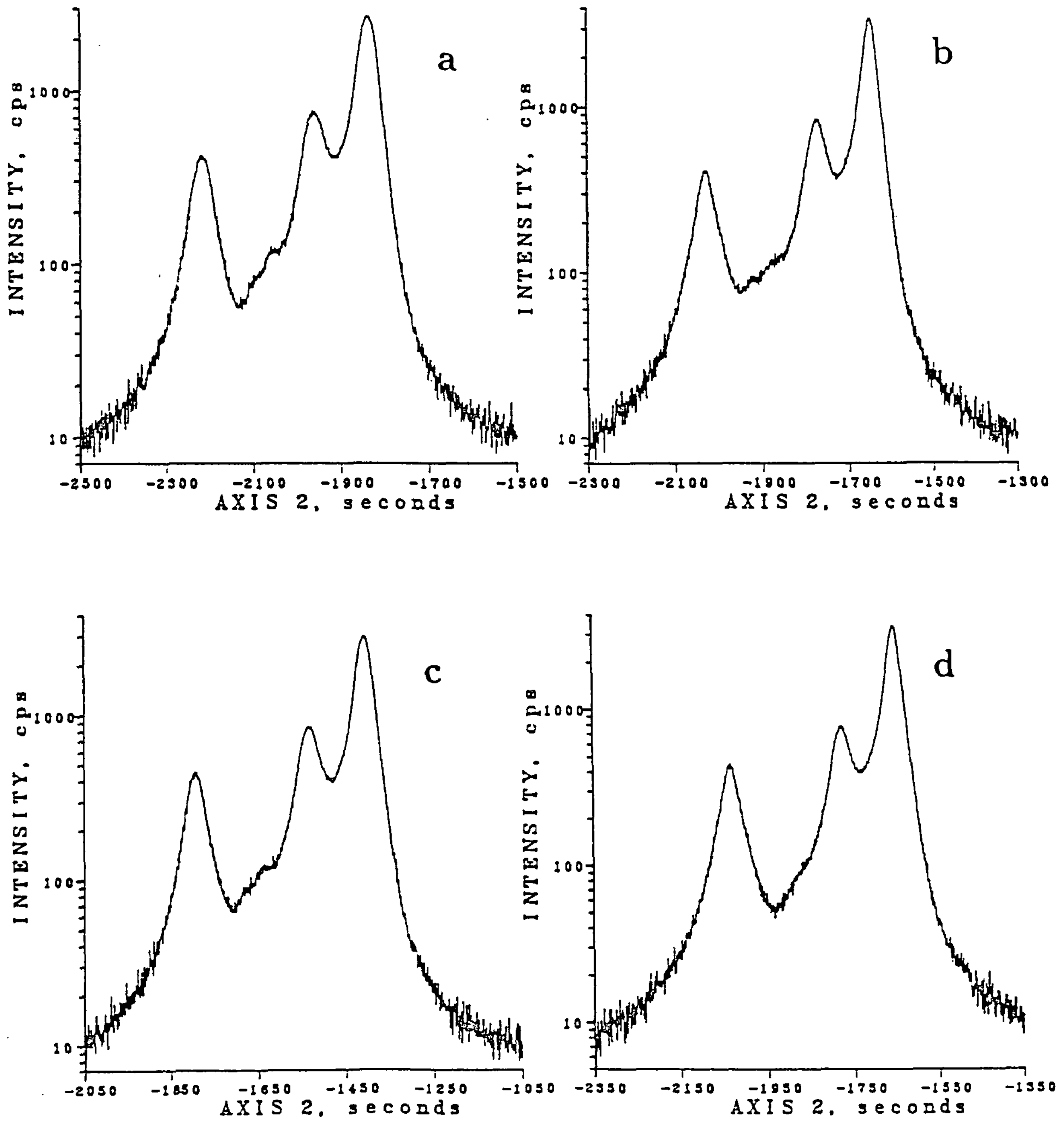

Figure 5.6: 115 high angle of incidence experimental rocking curves of sample GaAs2; (a) 0° rotation, (b) 90° rotation, (c) 180° rotation, (d) 270° rotation.

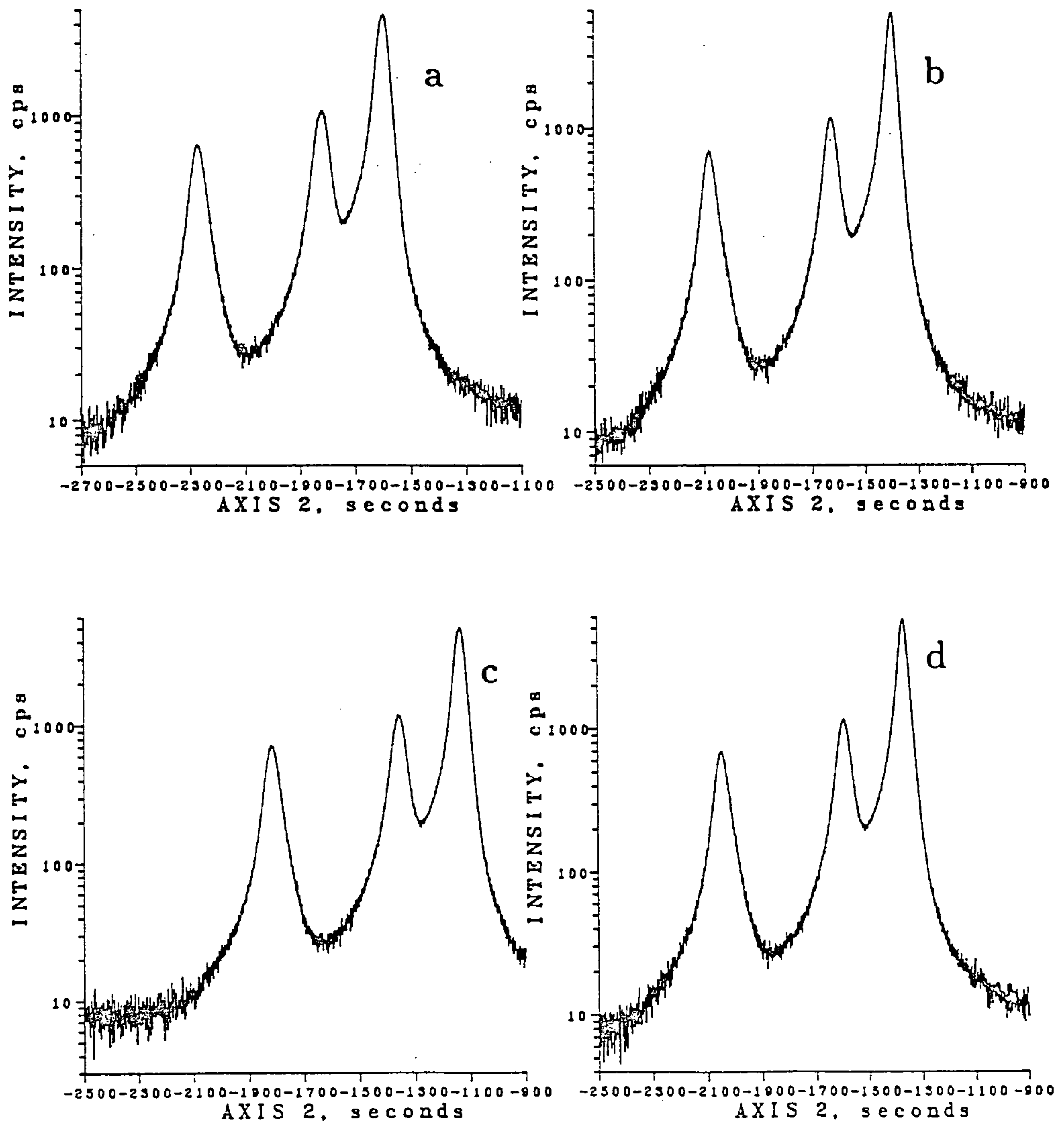

Figure 5.7: 115 low angle of incidence experimental rocking curves of sample GaAs2; (a) 0° rotation, (b) 90° rotation, (c) 180° rotation, (d) 270° rotation.

Table 5.3. 004 and 115 Diffractometry Data From Sample GaAs2

Reflection	Sample Orientation	Mean Peak Separation (Seconds)
004	[110]	-(374.8 ± 0.5)
004	[1$\bar{1}$0]	-(375.1 ± 0.5)
115LOW	[110]	-(675.7 ± 0.5)
115LOW	[1$\bar{1}$0]	-(678.9 ± 0.5)
115HIGH	[110]	-(382.2 ± 0.5)
115HIGH	[1$\bar{1}$0]	-(380.6 ± 0.5)

The Bragg peak separations in Table 5.3 were used to determine the position of the epitaxial layer 115 reflection relative to the substrate 115 reflection in reciprocal space in terms of the coordinate (x,z) for each $\langle 110 \rangle$ direction. The interplanar separation for the 110 and 1$\bar{1}$0 lattice planes, d_l, in the epitaxial layer are determined from the values of 1/x deduced from the separation between the Bragg reflections for the epitaxial layer and the substrate on the 115 rocking curves for the cases where the diffraction plane contains the [110] and [1$\bar{1}$0] directions respectively. The layer lattice parameter perpendicular to the interface, c, is equivalent to $5 \times 1/z$ for each of the sample orientations. These parameters are presented in Table 5.4.

Sample GaAs2 Layer Lattice Parameters Deduced by Diffractometry. Table 5.4

	[110] Orientation	[1$\bar{1}$0] Orientation
c_{004}	5.66956 ± 0.00005 Å	5.66957 ± 0.00005 Å
c_{115}	5.66941 ± 0.00005 Å	5.66945 ± 0.00005 Å
d_l	3.99802 ± 0.00004 Å	3.99787 ± 0.00004 Å

Hence the epitaxial layer relaxation, R, is determined from the interplanar separation of the 110 and 1$\bar{1}$0 planes in the layer as (3.3 ± 0.8)% and (1.0 ± 0.8)% in the [110] and [1$\bar{1}$0] directions respectively. This permitted the observed splittings to be corrected [5]. The quadratic fitting function is given by equation 5.6 (section 5.1.3) and led to values for the mismatch and Poisson ratio of 1600 ± 15 ppm and

0.28 ± 0.01 respectively. For a GaAs lattice parameter of 5.65375 Å (section 5.3), the AlAs lattice parameter is determined as 5.6628 ± 0.0001 Å.

The layer relaxation is clearly asymmetric about the ⟨110⟩ directions and so the 001 face of the layer unit cell is monoclinic. Hence the degree of lattice distortion in the epitaxial layer is also asymmetric about the ⟨110⟩ directions. The exact effect of this asymmetry on the atomic positions within the layer unit cell is not known at this time. However a significant difference in the 005 interplanar spacing (scaled by a factor of 5 to produce c_{115}) and the 004 interplanar spacing (scaled by a factor of 4 to produce c_{004}) is noted in Table 5.4.

In an independant study, Goorsky *et al* [6] examined the composition of a similar series of 1 μm layers of $Al_xGa_{1-x}As$ grown by low pressure MOVPE. The layers were grown on 001 GaAs substrates which were misorientated by 2°. The aluminium concentrations were determined by photoluminescence and microprobe analysis calibrated by a nuclear reaction technique. Goorsky recorded double crystal rocking curves from these samples using Cu $K_{\alpha 1}$ radiation in the parallel non-dispersive geometry on a Bede QC1 diffractometer. In a similar fashion to Tanner, the variation in the separation between the substrate and the epitaxial layer peaks on the 004 rocking curves with aluminium concentration was fitted using a quadratic function. The values for mismatch and Poisson ratio deduced from this analysis are 1580 ± 20 ppm and 0.275 ± 0.015 respectively [6]. These values are in excellant agreement with the values reported by Tanner *et al* [5]. However the 1 μm AlAs layer used by Goorsky appeared to be coherently strained. Goorsky recorded asymmetric reflection rocking curves from this sample and determined the layer relaxation following the analysis developed by Halliwell and discussed in chapter 5. These measurements indicated that the layer relaxation is zero in both ⟨110⟩ directions to within the experimental resolution of this technique. In order to investigate this further, both these layers are examined by topography in chapter7.

5.3 Factors Affecting the Accuracy of the Determination of Layer Relaxation

The accuracy associated with the measurement of the difference between the epitaxial layer lattice parameters and the substrate lattice parameters by diffractometry, which provides a quantitative measure of layer relaxation, is limited by the accuracy to which the Bragg diffraction peaks can be located on the double crystal

rocking curves. Hence this technique cannot be applied easily to very thin epitaxial layers (⟨ 0.1 μm) wherein the layer peak is broadened by dynamical effects, and epitaxial layers which contain compositional grading. However the accuracy associated with the determination of layer relaxation by diffractometry is intrinsically limited by the accuracy associated with the relevant bulk lattice parameters.

The bulk lattice parameters of crystalline solids are sensitive to a wide variety of phenomena [10]. Absolute lattice parameter measurements to a few parts per million are normal whereas the lattice parameter of silicon has been compared to 1 part in 10^9. However at this level of precision measurements are affected by elastic strains within the crystal lattice introduced by variations in temperature, pressure, mechanical stress and electric and magnetic fields. For example, the coefficient of thermal expansion in semiconductor materials ranges from 3 to 30 $\times$ $10^{-6}/°C$ and the bulk compressibility is of the order of $10^{-6}/bar$. Hence the variation in the bulk lattice parameter of a semiconductor with temperature and pressure is 3 to 30 ppm $/°C$ and 0.33 ppm per bar respectively. Elastic strains of this magnitude can also be introduced by stresses arising from poor sample mounting techniques. In addition, the lattice may also contain permanent strains caused by variable concentrations of point defects, phase changes and irradiation damage which have an equivalent effect as deviations from exact stoichiometry.

As an illustration of the variable nature of bulk lattice parameters, consider the range of values quoted in the literature for the lattice parameter of stoichiometrically pure GaAs determined by x-ray methods. Data from a selection of these studies are presented in Table 5.5 and plotted in Figure 5.8. The validity of the lattice parameter data is questioned if one notes that the precision quoted by the authors is less than 5ppm but the total spread of all these values exceeds 130ppm.

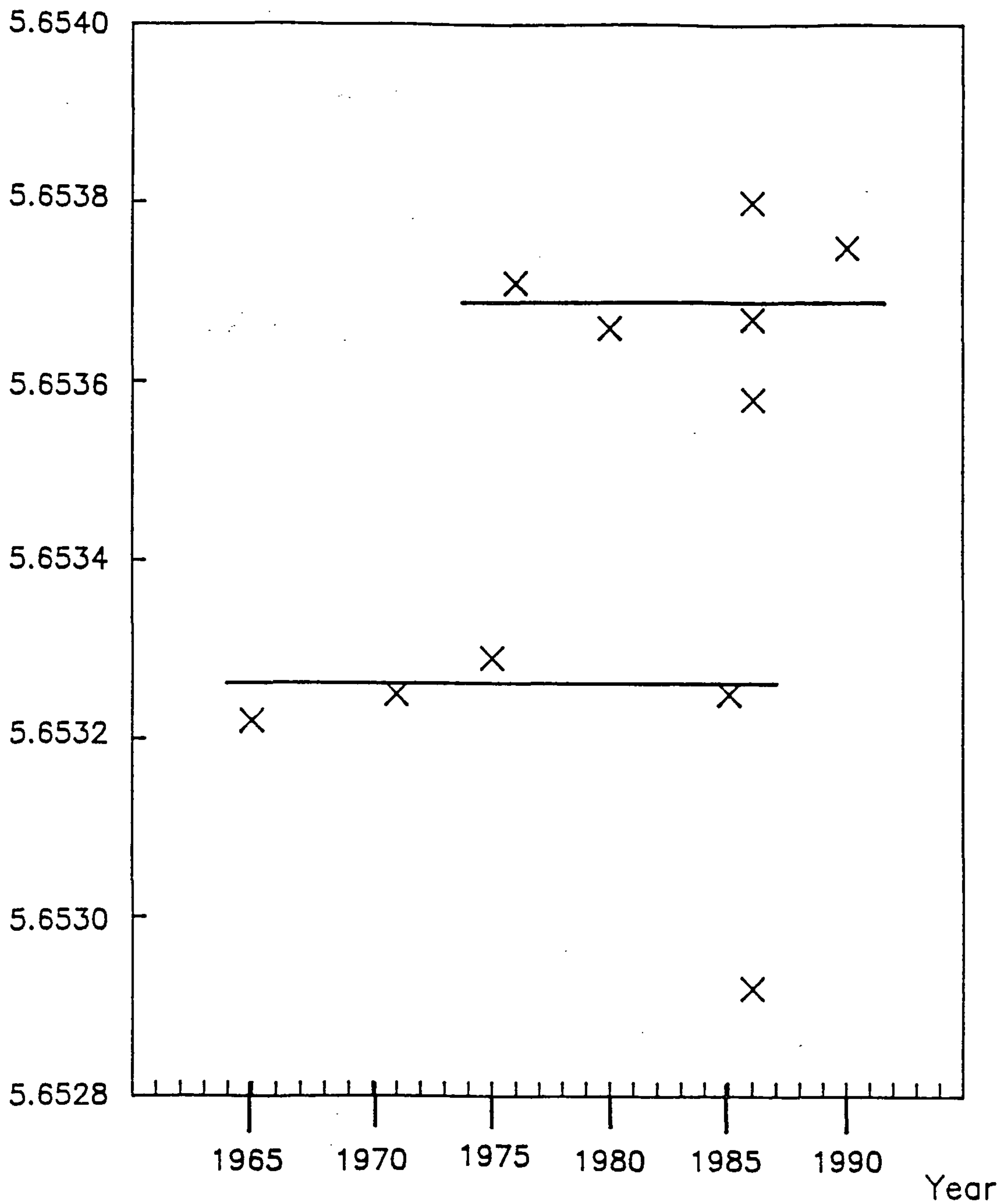

Figure 5.8: Values of GaAs lattice parameter determined by x-ray methods between 1965 and 1990. After several authors.

Table 5.5. The Lattice Parameter of GaAs

Lattice Parameter	Date	Reference
5.65322	1965	[11]
5.65325	1971	[12]
5.65329	1975	[13]
5.65371	1976	[14]
5.65366	1980	[15]
5.65325	1985	[16]
5.65367	1986	[17]
5.65358	1986	[18]
5.65292	1986	[19]
5.65380	1986	[20]
5.65375	1990	[21]

High impurity concentrations may play an important part in the GaAs samples studied in references [11] and [12] since this material was produced in the 1960's and early 1970's before good impurity control was achieved. However the published values of lattice parameter continued to fluctuate during the 1970's and 1980's which suggests that uniform crystal growth conditions between semiconductor materials companies have still not been established. Okada et al [17] measured the lattice parameter of 'stoichiometric' GaAs samples supplied by three manufacturers and found lattice parameter differences of about 12ppm, which he ascribed mainly to differences in impurity concentrations.

The mean of the above data is $(5.6535 \pm 0.0003)\mathring{A}$ but inspection of Table 5.5 and Figure 5.8 shows that this value is not reasonable. With the exception of reference [19], the data set appears to divide into two distinct sets distributed about 5.6537 $\mathring{A}$ and 5.6525 $\mathring{A}$. It is also noted that the majority of the values of GaAs lattice parameter determined after 1975 fall into the data set distributed about 5.6537 $\mathring{A}$. Hence this thesis adopts a GaAs lattice parameter of $(5.65375 \pm 0.00005)\mathring{A}$ which is the mean value determined recently from synchrotron radiation Bond measurements by Useda *et al* [21] and is believed to be the most accurate determination to date.

5.4 Relationship between Layer Relaxation and Misfit Dislocation Density

At low dislocation densities the relief of misfit strain occurs predominantly through the nucleation and propagation of 60° dislocations wherein each dislocation line relieves the epitaxial layer strain by a length $a_0/2\sqrt{2}$ in a $\langle 110 \rangle$ direction normal to the dislocation line. Hence the difference between the average epitaxial layer lattice parameter parallel to the interface and the equivalent substrate lattice parameter can be employed to obtain an estimate of the average dislocation line density near the interface [22]. This analysis has been developed specifically for 001 orientated substrates. If all misfit dislocations near the interface are strain relieving 60° dislocations then the average number of misfit dislocation lines per unit length in a $\langle 110 \rangle$ direction near the interface, N, is related to the epitaxial layer relaxation, R, through equation 5.13

$$N = \frac{2R|d_r - d_0|}{d_0^2} = \frac{2|d_l - d_0|}{d_0^2} \qquad 5.13$$

where d_r and d_0 are the interplanar separations between the $\{110\}$ lattice planes in the bulk epitaxial layer material and the substrate material respectively. In principle, equation 5.13 allows a direct comparison of the linear dislocation line density observed on a double crystal topograph with the linear dislocation line density deduced from double crystal diffractometry. For example, the epitaxial layer relaxation in sample GaAs2 deduced by double crystal diffractometry predicts average misfit dislocation line spacings along the [110] and $[1\bar{1}0]$ directions of $(3.7 \pm 0.8)\mu m$ and $(12.5 \pm 9)\mu m$ respectively and it should be possible to resolve individual dislocation lines on a double crystal topograph of this sample.

5.5 Relationship between Layer Lattice Tilt and Misfit Dislocation Density

During the course of the examination of a number of nominally (001) orientated samples it was noted that double crystal rocking curves recorded from epitaxial layer samples which are coherent across the interface indicate zero tilt, β, between the layer and substrate lattices. In contrast, double crystal rocking curves recorded from nominally (001) orientated samples with non-zero misfit dislocation densities

near the interface measured non-zero values of β. Moreover, the magnitude of β was seen to increase for samples with increased dislocation densities. This is illustrated in Table 5.6.

Table 5.6. Layer Relaxation and Tilt in Samples GaAs1, GaAs2, SLS1 and InP1

Sample GaAs1

	[110]	[1$\bar{1}$0]
Tilt (secs)	0 ± 0.5	0 ± 0.5
Relaxation, R (%)	0	0
Dislocation Density,N	0	0

Sample GaAs2

	[110]	[1$\bar{1}$0]
Tilt (secs)	3.8 ± 0.5	0 ± 0.5
Relaxation, R (%)	3.3 ± 0.8	1.0 ± 0.8
Dislocation Density,N	(2.7 ± 0.6) $\times 10^5 m^{-1}$	(0.8 ± 0.6) $\times 10^5 m^{-1}$

Sample SLS1

	[110]	[1$\bar{1}$0]
Tilt (secs)	6.2 ± 0.5	2.1 ± 0.5
Relaxation (%)	-12.6 ± 2.5	3.0 ± 2
Dislocation Density, N,	(3.0 ± 0.6) $\times 10^5 m^{-1}$	(0.7 ± 0.5) $\times 10^5 m^{-1}$

Sample InP1

	[110]	[1$\bar{1}$0]
Tilt (secs)	28 ± 2	25 ± 2
Relaxation (%)	34.6 ± 0.4	36.0 ± 0.4
Dislocation Density, N,	(6.00 ± 0.07) $\times 10^6 m^{-1}$	(6.46 ± 0.07) $\times 10^6 m^{-1}$

These observations have led to the development of two theoretical models centring on the properties of a 60° dislocation line which are used to examine the relationship between linear dislocation density and epitaxial layer lattice tilt. Although these models are developed for layer growth on nominally 001 orientated substrates, similar models can easily be deduced for other layer growth conditions.

5.5.1 The Edge Component of a Burgers Vector

The 60° dislocation was described in chapter 4 and consists of a dislocation line lying in a $\langle 110 \rangle$ direction with a Burgers vector of length $a_o/\sqrt{2}$ in another $\langle 101 \rangle$ direction. This is illustrated in Figure 4.3 where the Burgers vector of the 60° dislocation is resolved into a screw component and an edge component which are parallel and perpendicular to the dislocation line direction respectively. The screw component of a 60° misfit dislocation line does not relieve misfit strain and has a negligible effect on the lattice orientation of the epitaxial layer.

The total edge component of the Burgers vector of a 60° dislocation line has a magnitude of $a_0\sqrt{3}/2\sqrt{2}$ in a $\langle 112 \rangle$ direction. The projection of the total edge component in the plane of the interface, $E_{\|}$, relieves the misfit strain between the epitaxial layer and the substrate by a length $a_o/2\sqrt{2}$ in a $\langle 110 \rangle$ direction normal to the dislocation line. This phenomenon is regularly discussed in the literature. The projection of the total edge component normal to the (001) plane, $\underline{E_{\perp}}$, has a magnitude of $a_0/2$ and locally tilts the epitaxial layer [001] vector out of alignment with the substrate unit cell [001] vector. The $\underline{E_{\perp}}$ vector is rarely discussed in the literature and its effect on the orientation of the epitaxial layer lattice has been neglected until recently. At this juncture it is important to consider the distribution of Burgers vector directions within a set of 60° dislocation lines.

The sense of $\underline{E_{\|}}$ for a set of [110] 60° dislocation lines is fixed by the size of the epitaxial layer bulk lattice parameter, a_r, with respect to the substrate bulk lattice parameter, a_0. Following the **SF**/*RH* convention developed by Bilby *et al* [23,24], a clockwise Burgers circuit around a [110] dislocation line defines the projection of the closure vector **SF** in the interface, which is equivalent to $\underline{E_{\|}}$ for this dislocation line. For example, if $a_r \langle a_o$ then $\underline{E_{\|}}$ for a 60° dislocation line lying in the [110] direction has a magnitude of $a_o/2\sqrt{2}$ in the $[1\bar{1}0]$ direction. However the existence of a similar selection criterion for the direction of the $\underline{E_{\perp}}$ vector, which may arise from lattice symmetry or crystallographic considerations, is at present unknown. The existence

of this selection criterion would allow a theoretical determination of the relationship between the linear 60° dislocation density in a ⟨110⟩ direction and the lattice tilt along this direction.

The $\underline{E_\perp}$ component of a 60° misfit dislocation line near an 001 interface can have either of two orientations, parallel or anti-parallel to the [001] direction. The two orientations of $\underline{E_\perp}$ contribute to opposite senses of epitaxial layer lattice tilt. On the assumption that adjacent dislocation lines are close enough for their strain fields to overlap significantly, then the $\underline{E_\perp}$ components from adjacent 60° dislocation lines can be added vectorially and the summation can be extended across the interface. In view of this, upper and lower limits on the functional dependence of the variation in epitaxial layer tilt with 60° dislocation line density can be obtained by considering two extreme assumptions, viz. the direction of $\underline{E_\perp}$ for all 60° dislocations in a ⟨110⟩ direction is uniquely defined (Model 1) and the direction distribution of $\underline{E_\perp}$ is random (Model 2).

5.5.2 Model 1

This model is based on the assumption that a specific condition in the epitaxial layer sample selects the direction of $\underline{E_\perp}$ for all 60° dislocation lines near the interface by precluding the formation or propagation of 60° dislocation lines with $\underline{E_\perp}$ in the opposite direction. Hence the region near the interface can be treated as a low angle boundary [25]. Consider a dislocation line density Nm^{-1} in a [110] direction at an interface between an epitaxial layer and a substrate. The net tilt between the epitaxial layer lattice and the substrate lattice, β, is given by equation 5.14

$$\beta \simeq tan\beta = \frac{N\ a_0}{2} \qquad 5.14$$

5.5.3 Model 2

On the assumption that the probabilty that the $\underline{E_\perp}$ vector lies in the [001] direction is equal to a half, then the root mean square epitaxial layer tilt can be obtained from the principle of the random walk which is central to understanding the diffusion of gases. The random walk model is described in most undergraduate texts on the properties of matter [26].

Consider an interface of length d which has a dislocation line density, Nm^{-1}, in the [110] direction and $n = N\ d$. The total number of permutations of the orientation of the $\underline{E_\perp}$ vectors is 2^n whereas the number of permutations, X, resulting in $\sigma\ \underline{E_\perp}$ vectors aligned parallel to [001], referred to as $\underline{E_\perp}$ up, and $(n-\sigma)\ \underline{E_\perp}$ vectors aligned parallel to $[00\bar{1}]$, referred to as $\underline{E_\perp}$ down, is given by equation 5.15

$$X = \frac{n!}{\sigma!(n-\sigma)!} \qquad 5.15$$

Hence the probability, P_{+S}, that the net alignment of the $\underline{E_\perp}$ vectors results in S up (through $\frac{1}{2}(n+S)$ vectors aligned up and $\frac{1}{2}(n-S)$ vectors aligned down) is given by equation 5.16

$$P_{+S} = \frac{n!}{\left(\frac{n+S}{2}\right)!\left(\frac{n-S}{2}\right)!2^n} \qquad 5.16$$

On the assumption that if n is large then there is a great probability that S is small compared to n, and so equation 5.16 can be expanded by applying Stirling's Formula for log $\eta!$, equation 5.17,

$$log\ \eta! = \left(\eta + \frac{1}{2}\right) log\ \eta - \eta + log(2\pi)^{\frac{1}{2}} \qquad 5.17$$

and after some tedious algebra this gives

$$log\ P_{+S} = log\ \left(\frac{2}{\pi n}\right)^{\frac{1}{2}} - \left(\frac{n+S+1}{2}\right) log\ \left(1 + \frac{S}{n}\right) - \left(\frac{n-S+1}{2}\right) log\ \left(1 - \frac{S}{n}\right) \qquad 5.18$$

On the assumption that S/n is small then we can write

$$log\ \left(1 + \frac{S}{n}\right) = \frac{S}{n} - \frac{S^2}{2n^2} + ... \qquad 5.19$$

Then

$$log\ P_{+S} = log\ \left(\frac{2}{\pi n}\right)^{\frac{1}{2}} - \frac{S^2}{2n} \qquad 5.20$$

or

$$P_{+S} = \left(\frac{2}{\pi n}\right)^{\frac{1}{2}} \, exp\left(\frac{-S^2}{2n}\right) \qquad 5.21$$

However $P_{+S} = P_{-S}$ and so $P_{|S|} = 2P_{+S}$. Therefore the mean square magnitude of S, $\overline{S}^2$, is given by equations 5.22

$$\overline{S}^2 = 2 \int_0^{+\infty} S^2 \, P_{+S} \, dS$$

$$\overline{S}^2 = 2\left(\frac{2}{\pi n}\right)^{\frac{1}{2}} \int_0^{+\infty} S^2 \, exp\left(\frac{-S^2}{2n}\right) \, dS \qquad 5.22$$

The integral in equation 5.21 can be solved through a change of variable and translation to polar coordinates or by applying the definite integral given by equation 5.23 [27],

$$\int_0^{+\infty} x^2 \, e^{-r^2 x^2} \, dx = \frac{\sqrt{\pi}}{4\, r^3} \qquad 5.23$$

whence $\overline{S}^2$ is given by

$$\overline{S}^2 = 2\, n \qquad 5.24$$

Hence the distribution of the orientation of the $\underline{E_\perp}$ vectors follows Gaussian statistics with a standard deviation of $\sqrt{2\, n}$; the mean is zero. The standard deviation of the epitaxial layer lattice tilt, β_σ, is related to the average linear dislocation density, N, by equation 5.25 where d is the diameter of the sample wafer.

$$\beta_\sigma = \frac{a_o}{d}\sqrt{\frac{n}{2}} = a_o\sqrt{\frac{N}{2d}} \qquad 5.25$$

The confidence level which determines the statistical relevance of an experimentally determined epitaxial layer tilt is set at $3\beta_\sigma$. Hence the statistical probability of experimentally measuring an epitaxial layer tilt which exceeds $3\beta_\sigma$ is less than 0.0026.

5.5.4 Comparison with Experiment

Table 5.7 compares values of epitaxial layer tilt measured experimentally with the values predicted by model 1 and the values of $3\beta_\sigma$ predicted statistically by model 2. The values of dislocation line density, N, employed in these calculations are obtained from the values of epitaxial layer relaxation deduced by double crystal diffractometry.

Table 5.7 Experimental and Theoretical Values Associated with Epitaxial Layer Tilt

Sample	System	$\beta_{experimental}$ (seconds)	β_{model1} (seconds)	$3\beta_\sigma$ (seconds)
$GaAs1$	AlGaAs/GaAs	0 ± 0.5	0	0
$GaAs2_{[110]}$	AlGaAs/GaAs	3.9 ± 0.7	16 ± 4	0.54 ± 0.12
$GaAs2_{[1\bar{1}0]}$		0.3 ± 0.7	5 ± 3	0.27 ± 0.12
$SLS1_{[110]}$	InGaAs/InP	6.2 ± 0.7	19 ± 4	0.66 ± 0.12
$SLS1_{[1\bar{1}0]}$		2.1 ± 0.7	4.2 ± 0.3	0.30 ± 0.03
$InP1_{[110]}$	InGaAs/InP	28 ± 2	363 ± 6	2.81 ± 0.04
$InP1_{[1\bar{1}0]}$		25 ± 2	390 ± 6	2.94 ± 0.04

The epitaxial layer lattice tilts measured by diffractometry are at least an order of magnitude greater than the values of $3\beta_\sigma$ predicted by model 2, demonstrating conclusively that $\beta_{experimental}$ is not a statistical anomaly. Reasonable agreement between $\beta_{experimental}$ and β_{model1} is observed at low dislocation densities, however the agreement decreases as the dislocation line density deduced by diffractometry increases. This is attributed to an increase in dislocation interactions and dislocation line bunching at high dislocation line densities, both of which serve to decrease the epitaxial layer lattice tilt. The discrepancy between $\beta_{experimental}$ and β_{model1} at low dislocation densities may result from elastic deformation in the epitaxial layer, since the layer thicknesses for the samples examined in Table 5.7 are of the order of 1 μm. Although the epitaxial layers in Table 5.7 were deposited on 001 orientated substrates, the manufacturers of these substrates quote a surface alignment error of the order of a $0.1°$. However from the agreement observed above, it is reasonable

to assume that the effect of substrate misorientation is not significant for misorientations less than 0.1°. However the relationship between epitaxial layer tilt and dislocation line density for growth on substrates misorientated by more than 0.1° has not been investigated.

In conclusion, a lack of tilt between the epitaxial layer and the substrate is a good empirical indication of crystalline perfection near the interface. A quantitative model relating tilt and dislocation density has yet to be developed, though the above analysis demonstrates that the functional form of this relationship is described by equation 5.26

$$\beta = K \ a_0 \ N^x \qquad 5.26$$

where K is a constant and 0.5 ⟨ x ⟨ 1.

Chapter 6

Epitaxial Layers with High Dislocation Densities

6.0 Introduction

In this chapter we examine the correlation between data obtained by double crystal x-ray diffractometry and double crystal synchrotron radiation topography for two epitaxial layer samples containing high densities of misfit dislocations. The results of this study have also been discussed in [1].

6.1 The Samples

Sample InP1 and sample GaAs3 were grown by J. Wilkie and A. K. Chatterjee respectively at the British Telecom Research Laboratories. Sample InP1 consists nominally of a $1\mu m$ layer of $In_xGa_{1-x}As$ deposited on an 001 orientated InP substrate by MOVPE. Sample GaAs3 consists nominally of a $3\mu m$ layer of $GaAs_{1-x}Sb_x$ deposited by LPE on an 001 orientated GaAs substrate.

6.2 Determination of Layer Relaxation by Diffractometry

Double crystal rocking curves were recorded at an x-ray wavelength of 1.54051 Å for the 004 and 115 reflections from samples InP1 and GaAs3 in the parallel geometries, (section 3.1). For each reflection, rocking curves were recorded with the sample rotated through 0°, 90°, 180° and 270° with respect to the [110] direction in order to measure the epitaxial layer tilt, Figures 6.1 to 6.6. These data were used in conjunction with the analysis presented in section 5.2 to determine the epitaxial layer relaxation in the [110] and $[1\bar{1}0]$ directions. The average misfit dislocation line density, N, in each $\langle 110 \rangle$ direction was deduced from the layer lattice parameters using the analysis presented in section 5.4

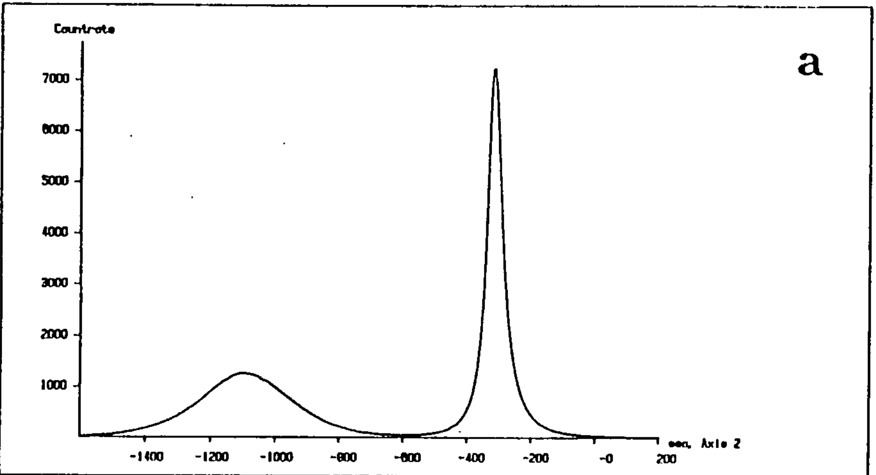

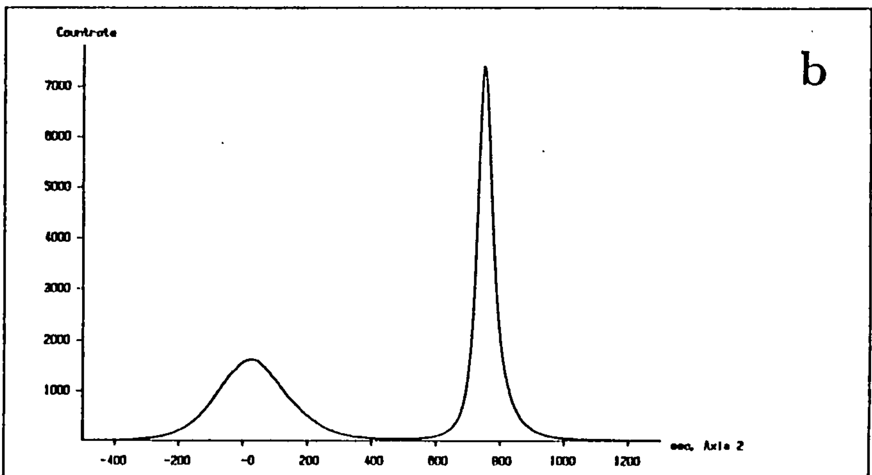

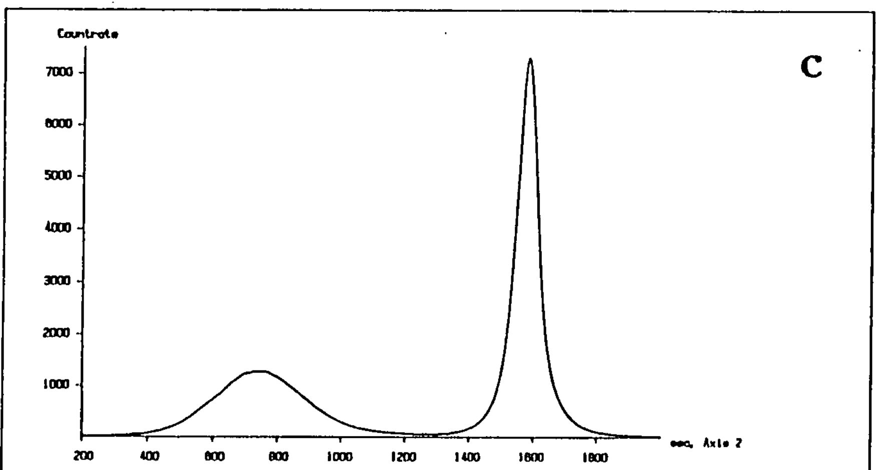

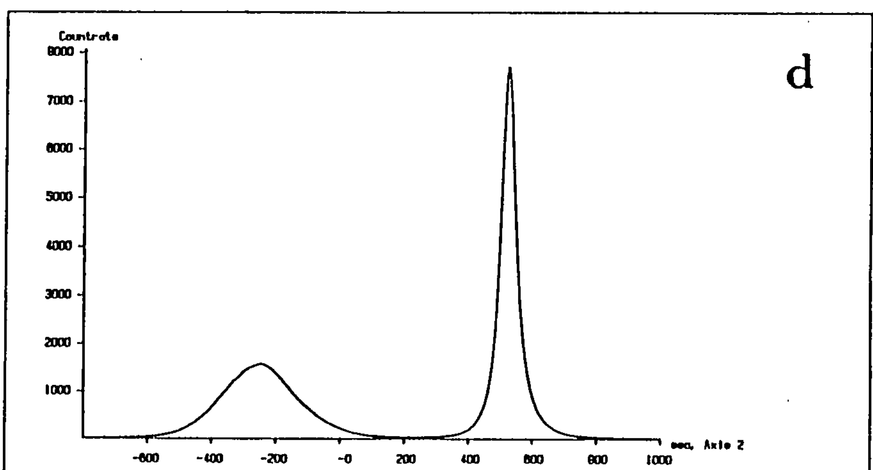

Figure 6.1: 004 experimental rocking curves of InP1; (a) 0° rotation, (b) 90° rotation, (c) 180° rotation, (d) 270° rotation.

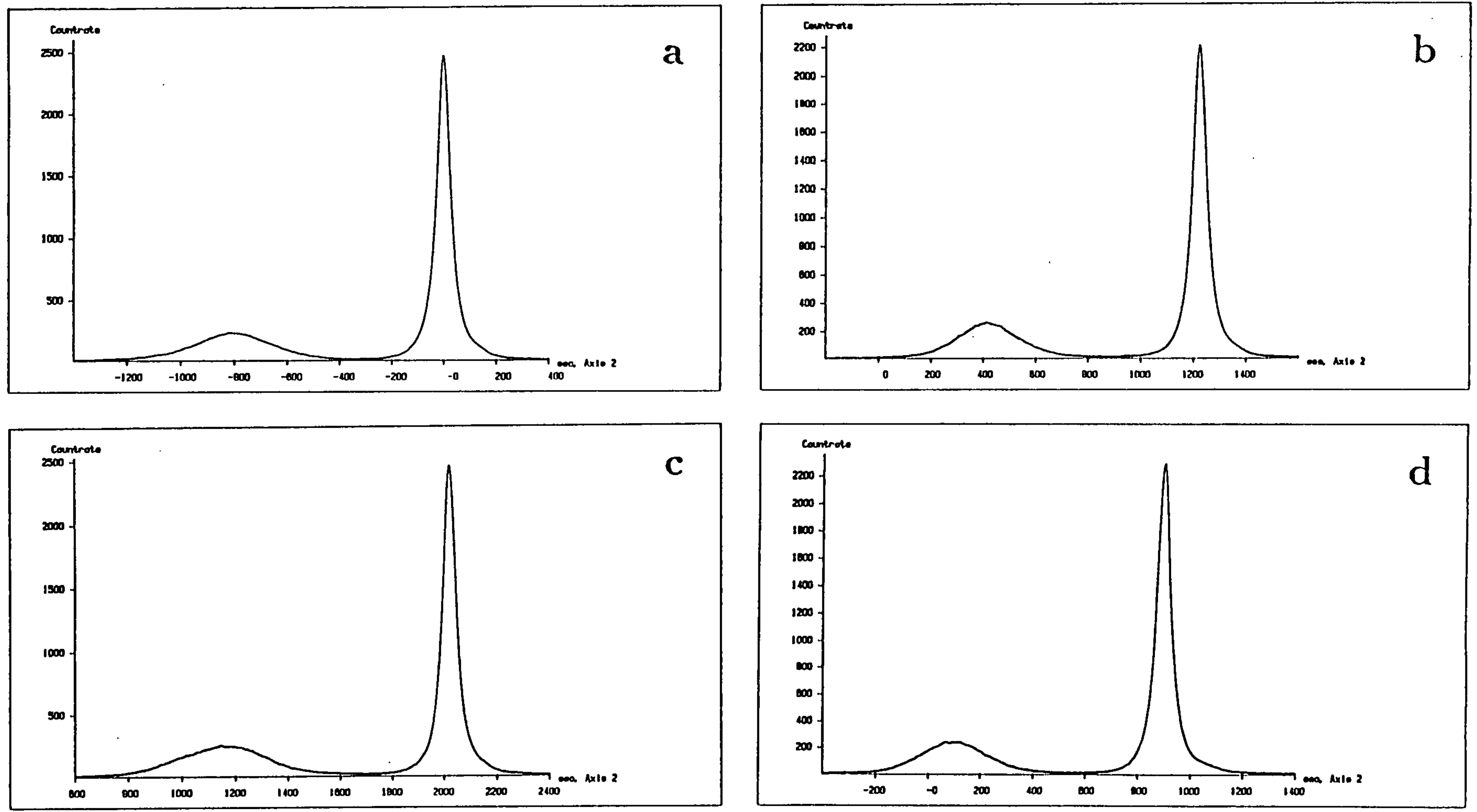

Figure 6.2: 115 high angle of incidence experimental rocking curves of InP1; (a) 0° rotation, (b) 90° rotation, (c) 180° rotation, (d) 270° rotation.

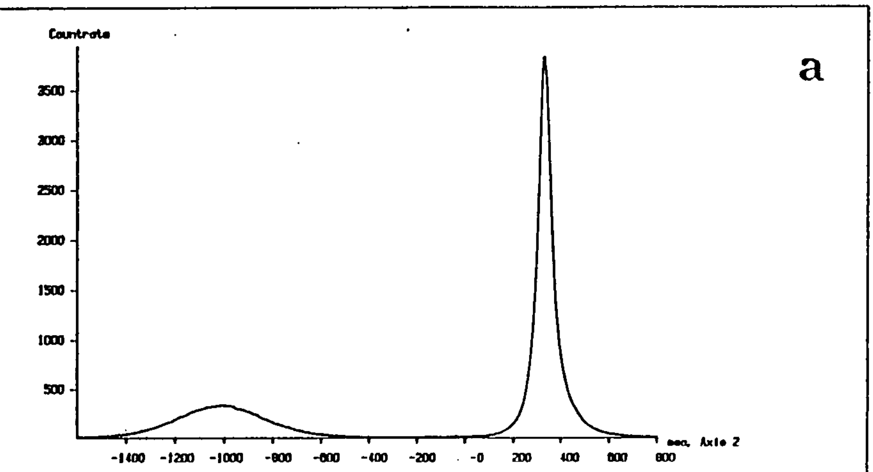

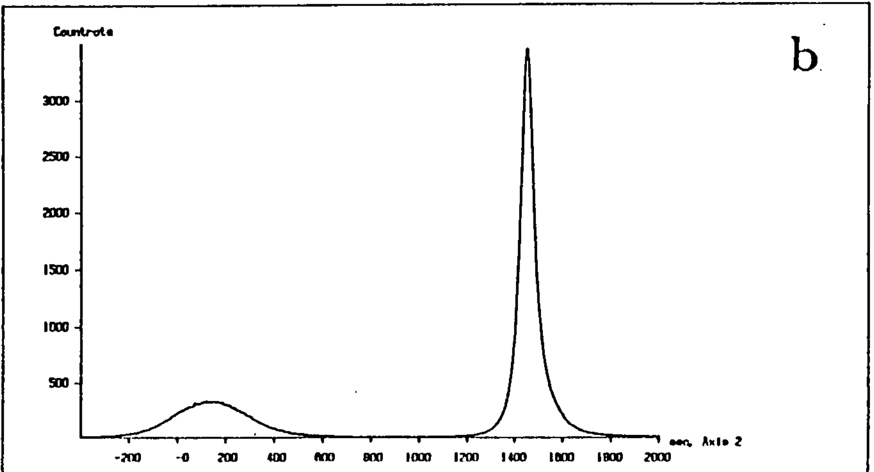

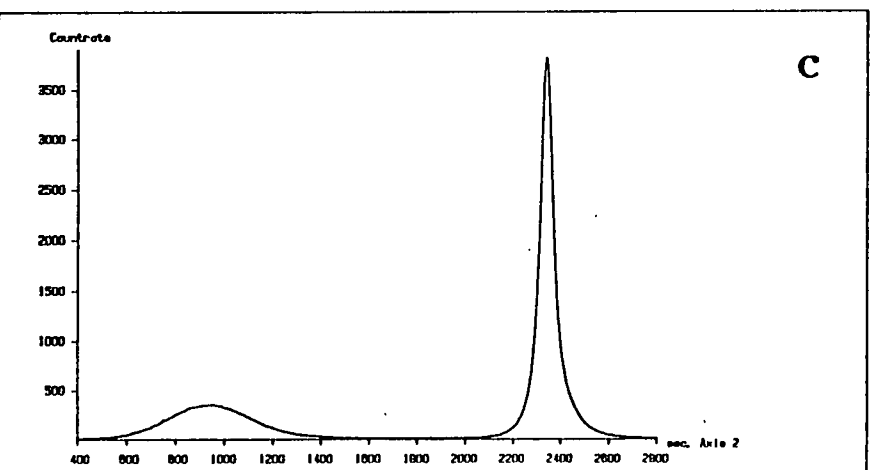

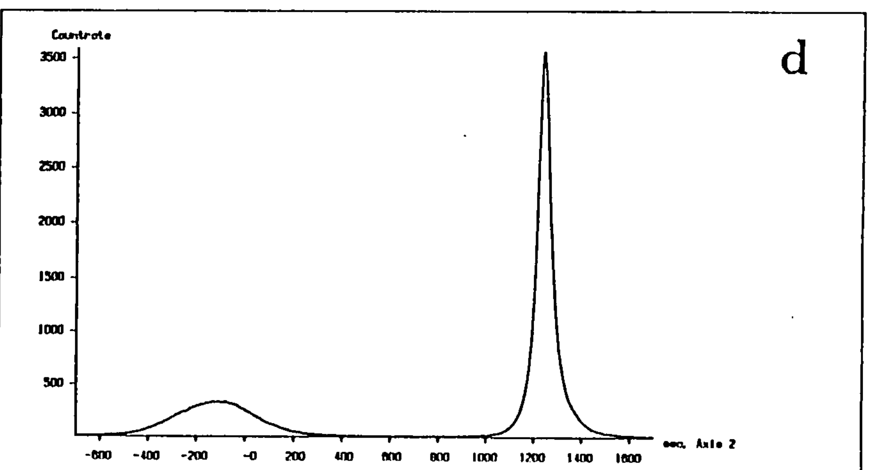

Figure 6.3: 115 low angle of incidence experimental rocking curves of InP1; (a) 0° rotation, (b) 90° rotation, (c) 180° rotation, (d) 270° rotation.

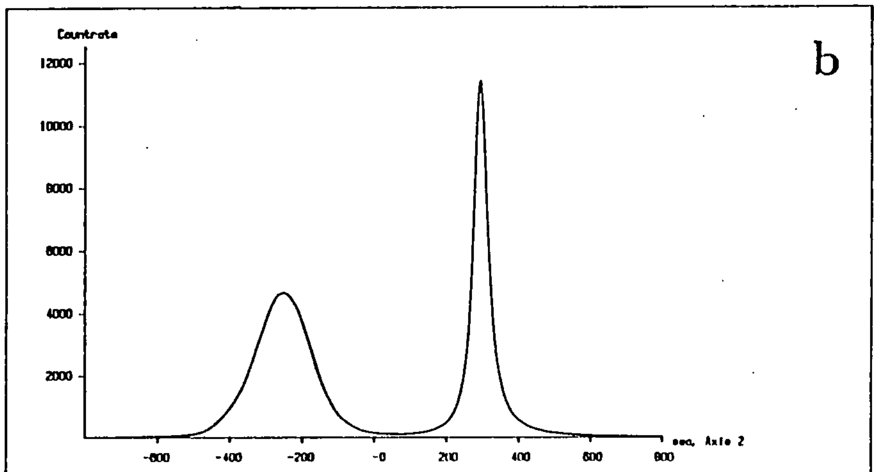

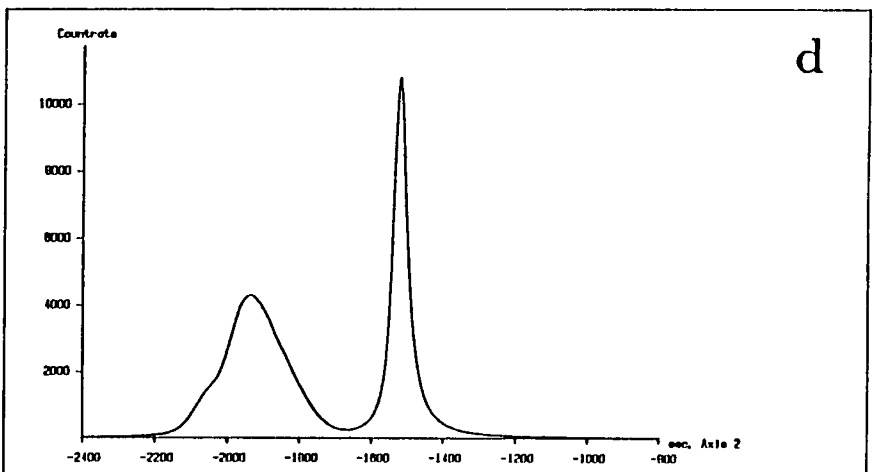

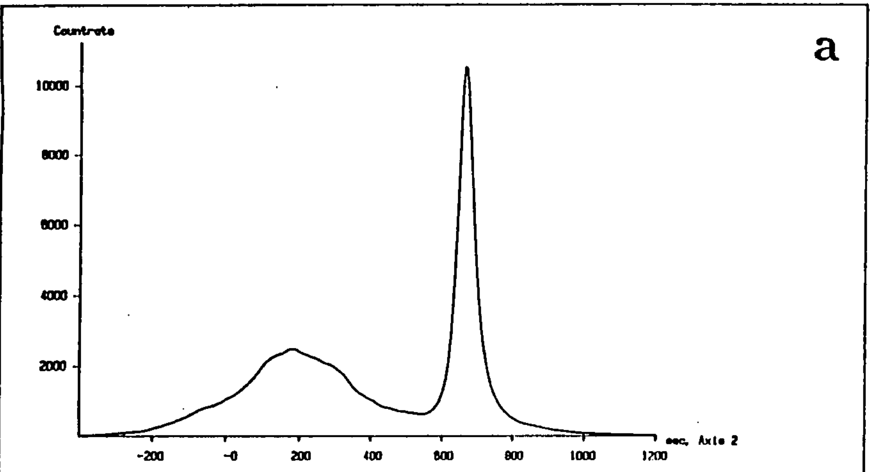

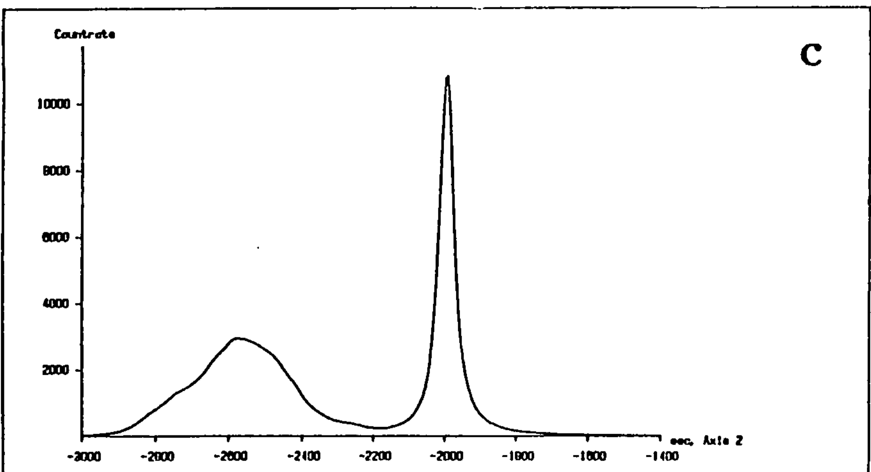

Figure 6.4: 004 experimental rocking curves of GaAs3; (a) 0° rotation (b) 90° rotation, (c) 180° rotation, (d) 270° rotation.

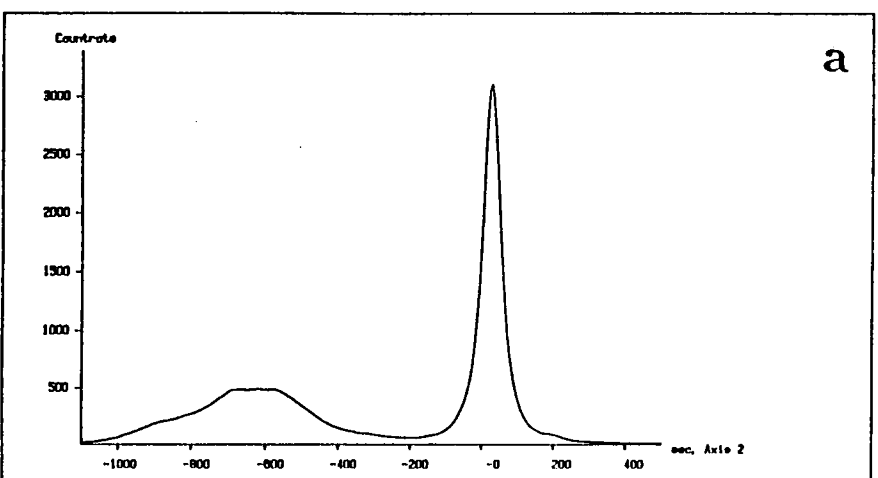

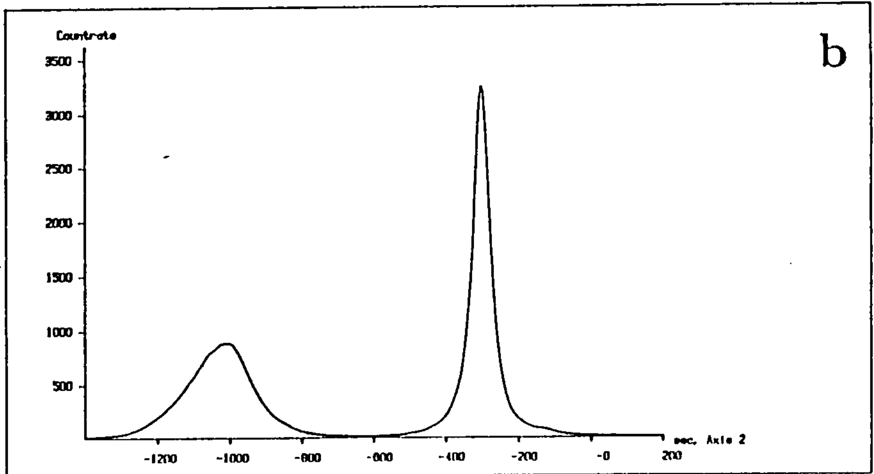

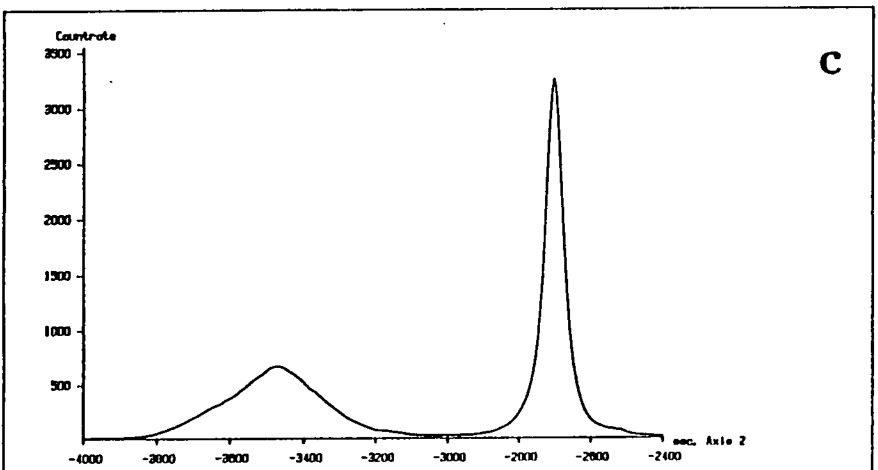

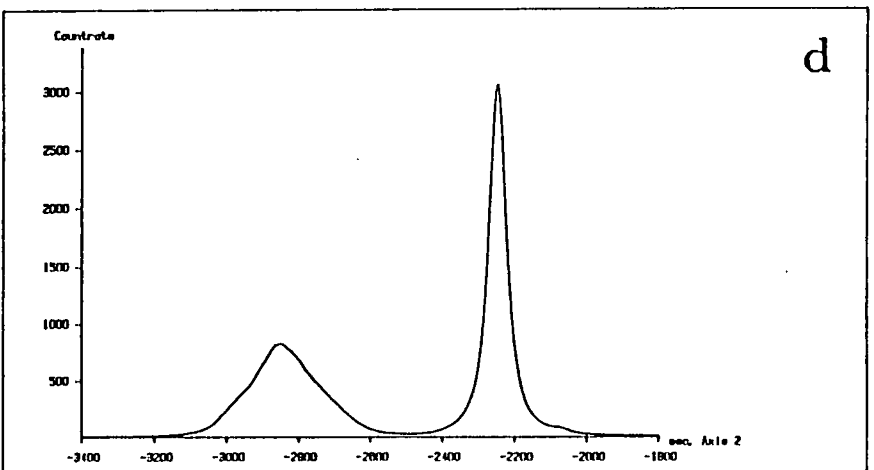

Figure 6.5: 115 high angle of incidence experimental rocking curves of GaAs3; (a) 0° rotation, (b) 90° rotation, (c) 180° rotation, (d) 270° rotation.

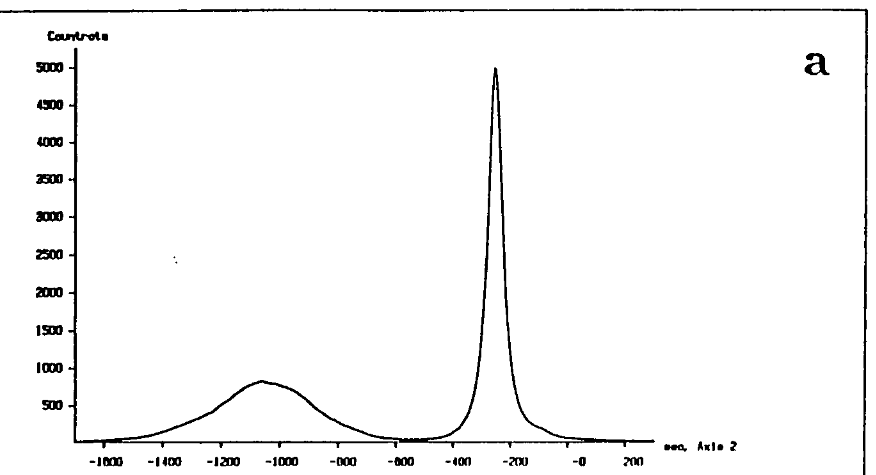

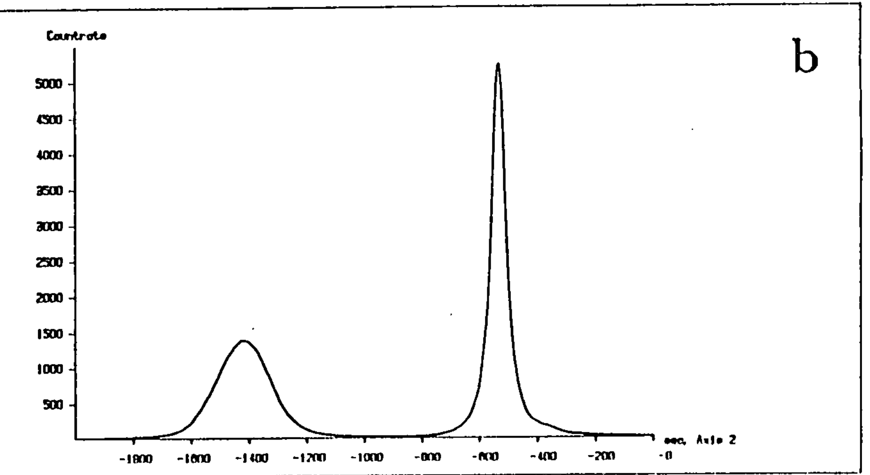

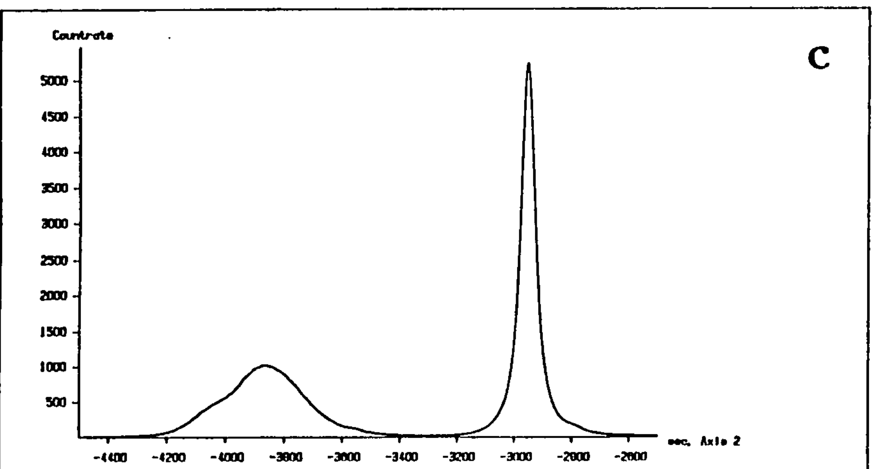

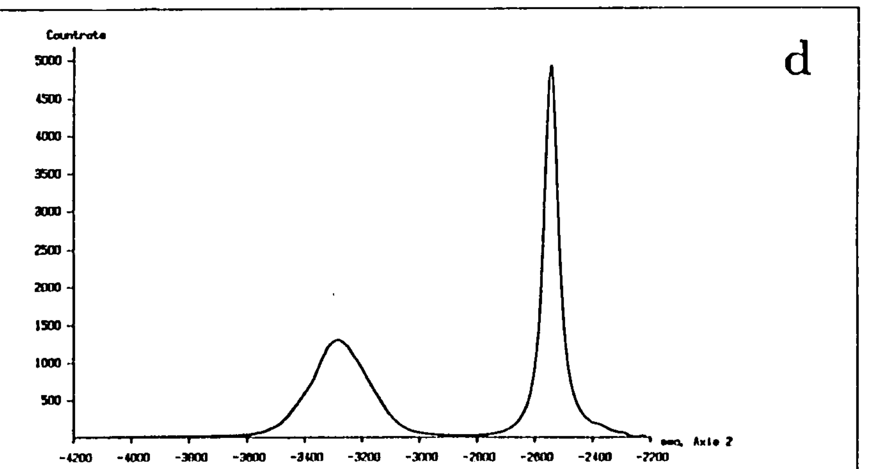

Figure 6.6: 115 low angle of incidence experimental rocking curves of GaAs3; (a) 0° rotation, (b) 90° rotation, (c) 180° rotation, (d) 270° rotation.

6.2.1 Sample InP1

The mean values of the separation between the epitaxial layer and substrate peaks, ψ, for the 004 and 115 reflections, Figures 6.1 to 6.3, and the measurements of relaxation and average misfit dislocation line density deduced from these are presented in Table 6.1. The error associated with ψ is determined from the accuracy to which the peak centroids can be located and is in good agreement with the standard deviation of the epitaxial layer tilts measured in the [110] and [$1\bar{1}0$] directions. The layer mismatch was determined as 3650 $\pm$ 70 ppm which corresponds to a layer composition of $In_{0.58}Ga_{0.42}As$.

Table 6.1. Diffractometry Data for Sample InP1

	[110]	[$1\bar{1}0$]
004 ψ (secs)	-746 $\pm$ 2	-810 $\pm$ 2
115LOW ψ (secs)	-1327 $\pm$ 2	-1364 $\pm$ 2
115HIGH ψ (secs)	-817 $\pm$ 2	-845 $\pm$ 2
Tilt (secs)	28 $\pm$ 2	25 $\pm$ 2
d_l (Å)	4.15496 $\pm$ 0.00005	4.15536 $\pm$ 0.00005
c (Å)	5.90375 $\pm$ 0.00005	5.90479 $\pm$ 0.00005
Relaxation (%)	34.6 $\pm$ 0.4	36.0 $\pm$ 0.4
Dislocation Density, N,	(6.00 $\pm$ 0.06) $\times 10^6 m^{-1}$	(6.46 $\pm$ 0.06) $\times 10^6 m^{-1}$

6.2.2 Sample GaAs3

The reduced diffractometry data measured from Figures 6.4 to 6.6 and the measurements of relaxation and average misfit dislocation line density deduced from them are presented in Table 6.2 where ψ is the mean separation between the epitaxial layer and substrate peaks. The layer mismatch was determined as 3140 $\pm$ 160 ppm which corresponds to a layer composition of $GaAs_{0.96}Sb_{0.04}$.

Table 6.2. Diffractometry Data for Sample GaAs3

	[110]	$[1\bar{1}0]$
004 ψ (secs)	-520 ± 4	-480 ± 10
115LOW ψ (secs)	-855 ± 4	-815 ± 10
115HIGH ψ (secs)	-718 ± 4	-656 ± 10
Tilt (secs)	55 ± 4	63 ± 10
d_l (Å)	4.0081 ± 0.0001	4.0065 ± 0.0002
c (Å)	5.6756 ± 0.0001	5.6743 ± 0.0002
Relaxation (%)	80 ± 1	75 ± 2
Dislocation Density, N,	(12.9 ± 0.3) $\times 10^6 m^{-1}$	(10.9 ± 0.3) $\times 10^6 m^{-1}$

6.2.3 Comment

The epitaxial layer relaxation and average dislocation line density have been measured for these samples. Again, as in sample GaAs3, we have found significant asymmetry in the values of relaxation for the [110] and $[1\bar{1}0]$ directions, though in this case, where the msifit dislocation densities are large, the degree of asymmetry is small. Asymmetric relaxation appears to be a feature of III-V epitaxial layers.

6.3 Double Crystal SRS Topography

Double crystal x-ray topographs were taken on station 7.6 at the Daresbury Laboratory SRS using 25 μm thick Ilford L4 nuclear emulsion plates (section 3.2.4). 004 topographs of samples InP1, Figure 6.7, and GaAs3, Figure 6.8, were recorded at 1.92 Å and 1.4 Å respectively using the substrate reflections. $\underline{X}$ shows the direction of the x-ray beam across the sample. The exposure times were about 5 minutes for a multiple bunch beam with a current of about 190 mA. The maximum dislocation line density which allows resolution of individual dislocation lines on a double crystal topograph is 0.2 μm^{-1} (section 3.2.4).

Figure 6.7: 004 topograph of InP1 at 1.92 Å.

Figure 6.8: 004 topograph of GaAs3 at 1.4 Å.

6.3.1 Sample InP1

The average misfit dislocation line densities deduced by diffractometry for sample InP1, Table 6.1, clearly exceed the maximum dislocation line density which can be resolved by topography. If the misfit dislocations were uniformly distributed near the interface then topographs of these samples would show diffuse contrast across the width of the Bragg diffraction band. Instead, Figure 6.7, distinct images lying along the [110] and $[1\bar{1}0]$ directions are observed on the topographs. It is clear both from the width and the density of these images that the images represent bundles of dislocations and not individual dislocation lines. The distribution in the density of the images on the topographs appears to be asymmetric about the [110] and $[1\bar{1}0]$ directions. However when the geometric scaling factor is taken into account this asymmetry is lost.

The image spacing measured on the 004 topograph of sample InP1 (Figure 6.7) was found to be (17 ± 2) μm in both the [110] and $[1\bar{1}0]$ directions. Hence, on the assumption that the misfit dislocations are 60° dislocations, the average number of dislocations per bundle in this sample is 105 ± 12 and is symmetric in the two $\langle 110 \rangle$ directions. The dislocation images were examined at several points across the Bragg diffraction band and the density of the images was found to be uniform across the wafer.

6.3.2 Sample GaAs3

Again, as in sample InP1, the average dislocation line density deduced by diffractometry in the $\langle 110 \rangle$ directions exceeds the maximum misfit dislocation line density which can be resolved by topography. The spacing of the images on the 004 topograph of sample GaAs3 (Figure 6.8) in the [110] and $[1\bar{1}0]$ directions was measured as (22 ± 3) μm and (17.8 ± 1.3) μm. Hence the average number of misfit dislocations per bundle in the [110] and $[1\bar{1}0]$ directions is 280 ± 40 and 195 ± 14 respectively and is thus clearly asymmetric. The sample was rotated through 90° to check that the image densities in the [110] and $[1\bar{1}0]$ directions are not significantly affected by the asymmetry of the x-ray source size at Daresbury leading to asymmetry in resolution. No systematic variation in image density could be detected. Further confirmation that the asymmetry in resolution was not significant to these measurements was obtained from the region shown in Figure 6.9.

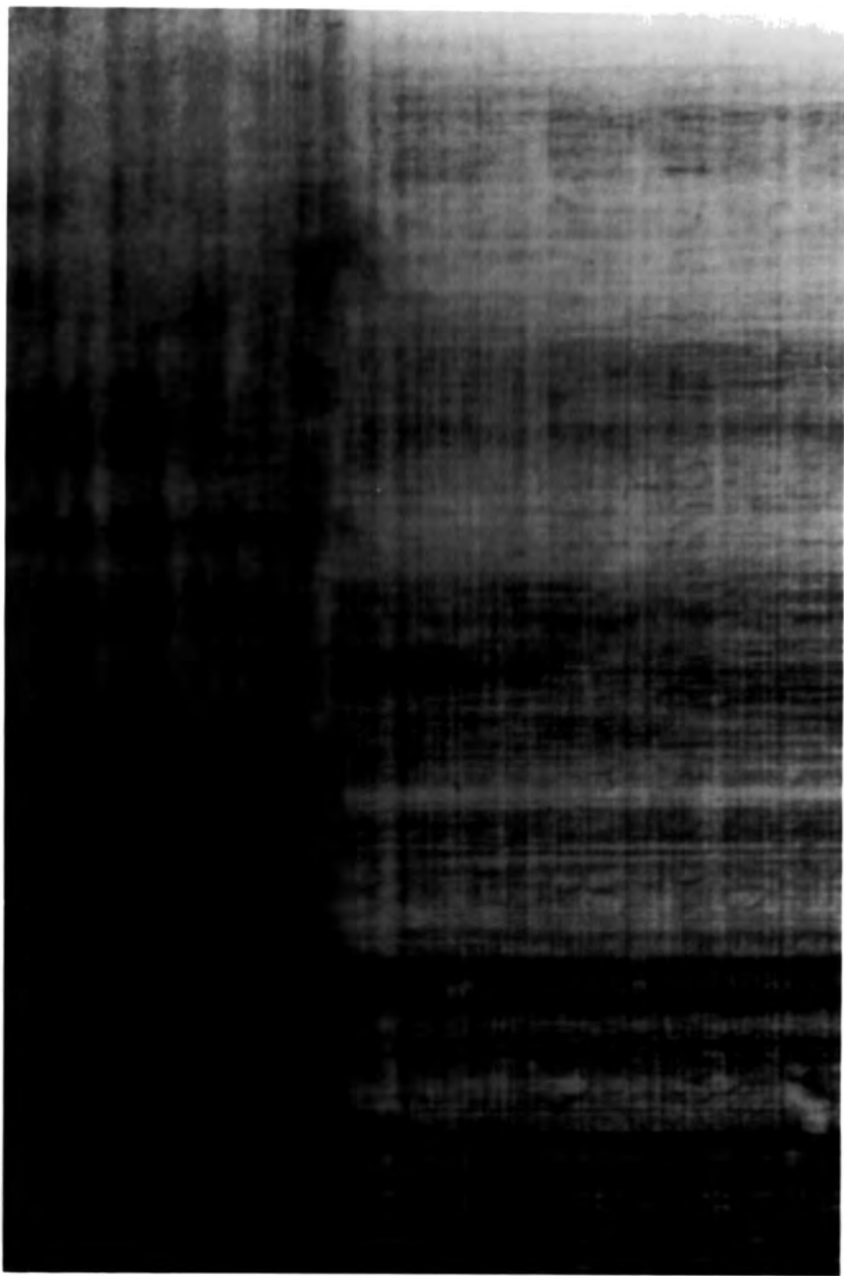

Figure 6.9: 004 topograph at 1.4 Å at the perimeter of the growth area of sample GaAs3.

Examination of the Bragg diffraction band showed that the dislocation density remained uniform across the growth area of this sample, defined by the perimeter of the graphite silo (section 1.3.1). However leakage from the silo resulted in the deposition of a thin epitaxial layer around the edge of the sample. In this region of the Bragg diffraction band, Figure 6.9, a higher density of narrow dislocation images is observed. The image sharpness in the [110] and $[1\bar{1}0]$ directions is almost identical. We do not expect an increase in epitaxial layer relaxation with layer thickness. Hence we conclude that the number of dislocation lines per bundle decreases with decreasing layer relaxation.

6.4 Conclusions

The samples considered in this chapter illustrate that double crystal diffractometry can be used to determine epitaxial layer relaxation for layers with high dislocation densities. Although the individual dislocation lines are not resolved on the topographs, x-ray topography provides a rapid means of investigating the variation in dislocation density across the wafer. From the values of average dislocation line density determined by diffractometry, it is deduced that the dislocation images recorded by x-ray topography represent bundles of misfit dislocations and not individual dislocation lines. The relaxations determined by diffractometry show significant asymmetry in the $\langle 110 \rangle$ directions and in the case of GaAs3 the average number of dislocation lines per dislocation bundle is also asymmetric.

Chapter 7

Epitaxial Layers with Low Dislocation Densities

7.0 Introduction

This chapter examines the application of x-ray diffractometry and x-ray topography to the determination of asymmetric layer relaxation in an ultra thin (17nm) epitaxial layer of InGaAs on GaAs, an InGaAs superlattice on InP and two thick (1 μm) layers of AlAs on GaAs. All the epitaxial layers have low misfit dislocation densities. At low misfit dislocation densities x-ray topography can be expected to resolve individual misfit dislocation lines and hence give a quantitative measure of the asymmetric relaxation. In particular, this is examined for the InGaAs superlattice. However double crystal diffractometry may not have sufficient sensitivity to detect layer relaxation at very low misfit dislocation densities. Results from the data presented in this chapter have also been presented in [1,2,3,4].

7.1 Asymmetric Relaxation in a Thin InGaAs Layer

Sample GaAs4 was grown by M. Enemy at RSRE and consists nominally of a layer of $In_{0.2}Ga_{0.8}As$ deposited by MBE on an 001 orientated semi-insulating GaAs substrate. Additional layers of GaAs were included and the nominal structure of the sample was 800 nm GaAs buffer, 16 nm InGaAs and a 100 nm GaAs cap. This structure, a thin layer sandwiched between two thick layers, is the basis of the high electron mobility transistor. The ternary composition was monitored in situ using the reflection high-energy electron diffraction (RHEED) oscillation technique [5] and an alloy deposition rate of one monolayer per second was employed throughout. This sample was taken from a series of samples of varying thickness around the theoretical value for critical thickness. As the GaAs cap is thick compared to the InGaAs layer, relaxation of the misfit strain in the layer must be accomodated by nucleation of misfit dislocations near the layer/substrate interface and also near the layer/cap interface. In view of this the critical thickness according to the Matthews model

(section 4.4.1), for an $In_{0.2}Ga_{0.8}As$ layer in this structure is found to be about 120 Å (equation 4.1).

A series of double crystal x-ray topographs were taken at station 7.6 of the SRS at Daresbury Laboratory employing the 004, 224 and 404 reflections at 1.4 Å. The 224 reflection allows a 2.1° incidence angle and hence a small extinction distance and photoelectric absorption depth [6]. Both these effects lead to enhanced surface sensitivity. The topographs show a highly anisotropic distribution of misfit dislocation lines; significant length dislocation lines are observed only in the $[1\bar{1}0]$ direction. The topographs reveal that the dislocation line density varies from zero at the edge of the wafer to about 0.12 lines per micron at the wafer centre. Figure 7.1 shows a 224 topograph of a region near the center of the wafer illustrating the highly asymmetric distribution of the dislocation lines and also the cellular distribution of the threading dislocations in the substrate. Because of the high thermal gradients encountered during the growth of GaAs, the density of threading dislocations in commercially available semi insulating GaAs substrates is relatively high (10^4 to $10^5 cm^{-2}$) [7]. Once formed, the dislocations move by a process of glide and climb, arranging themselves into cellular structures [8]. Inspection of the topographs revealed that most of the misfit dislocations have one end terminating at a substrate dislocation or at the cell boundary of the substrate dislocation network. Some of these terminations are observed in Figure 7.1. The substrate dislocations clearly act as nucleation sites for the misfit dislocations. As found previously by Petroff and Sauvage [9] in the AlGaAs/GaAs system, it appears that threading dislocations from the substrate which propagate into the epitaxial layer are caused to bend over near the interface thus creating a misfit dislocation line in the plane of the interface. The threading dislocation propagates to the epitaxial layer surface at the free end of the misfit dislocation line and for some reflections this termination can be identified on the original topograph as a dark contrast spot at the end of each misfit dislocation. The free end of the misfit dislocation occurs predominantly towards the thicker region of the specimen, indicating that the dislocations, once nucleated, propagate preferentially towards the thicker region of the layer.

Single crystal Hirst reflection topographs were also taken of this sample employing Cu $K_{\alpha 1}$ radiation and the 115 low angle of incidence geometry, (section 3.2.1). Although the cellular structure of the threading dislocations in the substrate was clearly imaged, the misfit dislocations were not observed on these topographs. In Hirst topography the range of wavelengths which satisfy the Bragg condition at a point on the sample is limited by the natural width of the $K_{\alpha 1}$ characteristic line. This is sufficient to allow simultaneous Bragg diffraction from regions of per-

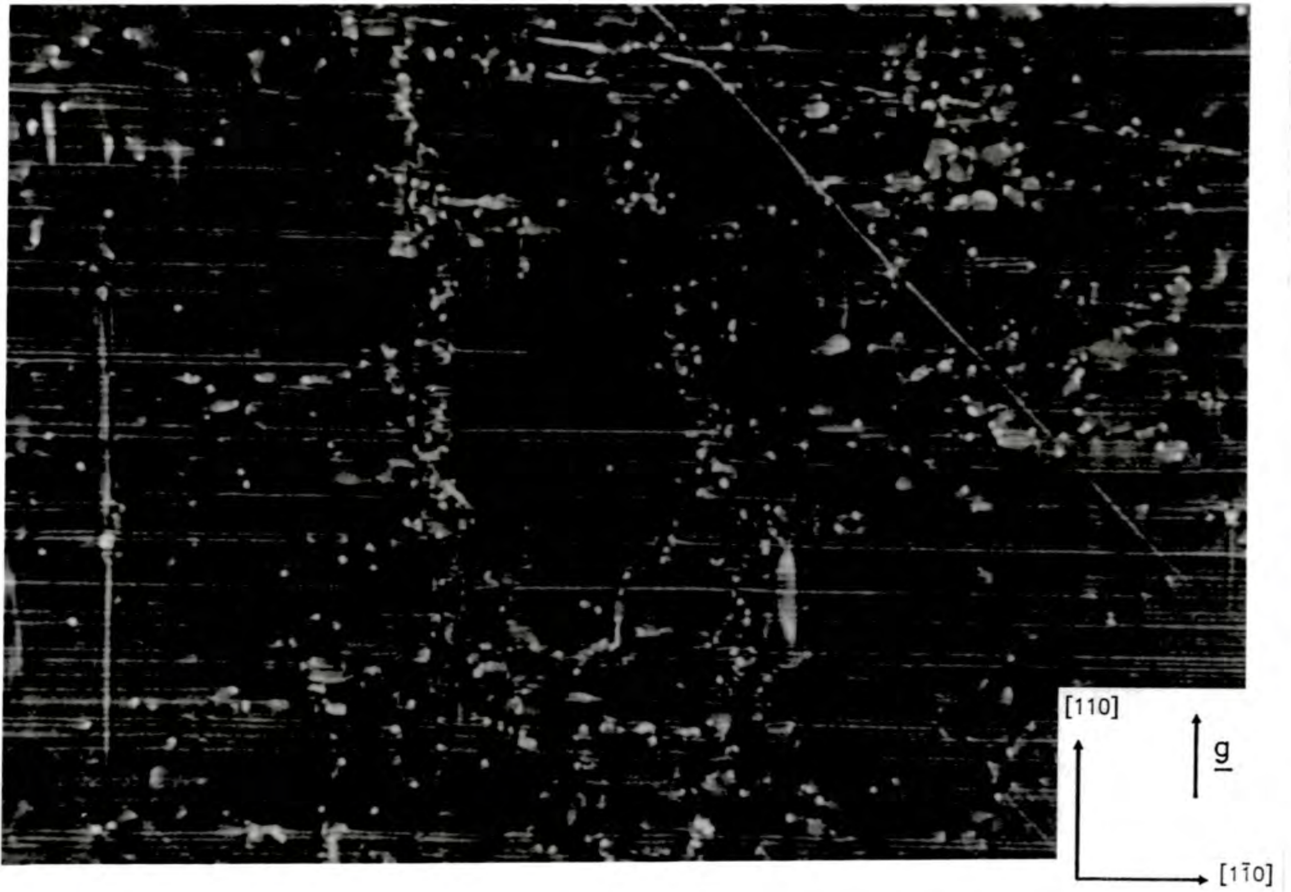

Figure 7.1: 224 topograph of GaAs4 at 1.4 Å of a region near the centre of the wafer

fect crystal and also regions of misorientated crystal surrounding a dislocation core. The intensity of the radiation diffracted by the regions of perfect crystal must be described by the dynamical theory where the scattered intensity is proportional to the structure factor, section 2.3. However the misorientated region surrounding a dislocation core diffracts radiation at different wavelengths and so the intensity of the scattered radiation can be described by the kinematical theory and is proportional to the square of the structure factor, section 2.2. Hence the dislocation is imaged on the topograph as a region of high diffracted intensity. The penetration depth for a 115 reflection using Cu $K_{\alpha 1}$ radiation is about 18 μm [6]. Threading dislocations which extend through the substrate are imaged clearly. However the signal to noise ratio for misfit dislocation lines, which lie along ⟨110⟩ directions near the interface, is too low for these to be imaged on the topographs. This example illustrates that with Hirst reflection topography it is important to select reflections which have a penetration depth close to the depth at which dislocation lines are expected.

Double crystal rocking curves were recorded at an x-ray wavelength of 1.54051 Å employing the 004, 224 and 115 reflections in the parallel non-dispersive geometry. In the 004 reflection the intensity of the layer peak is about 0.035 % that of the substrate peak and has a FWHM of about 1075 seconds. The intensities of the epitaxial layer peaks in the 224 and 115 high angle of incidence reflections were weaker still and these peaks were almost indistinguishable from the background experimental noise. The separation between the substrate and epitaxial layer peaks measured on the 004 reflection is about 200 seconds less than the value predicted from differentiation of Braggs law for the layer compositions determined by comparison of experimental and simulated rocking curves. This is due to interference effects in the thin layer [10] and illustrates the need to simulate experimental data from thin epitaxial layers.

The InGaAs layer in sample GaAs4 is capped by a GaAs layer with a nominal thickness of 100nm. This system behaves like a Bragg case interferometer. The 004 reflection rocking curves show strong interference fringes corresponding to the Pendellösung period for the GaAs cap. Moreover simulations using the Bede Scientific RADS software showed that the position and intensity of the fringes around the substrate peak are extremely sensitive to the exact thickness of the InGaAs layer.

Double crystal 004 rocking curves were taken in the non-dispersive geometry with the sample mounted on a 25mm XY displacement stage. Rocking curves were recorded at five points across the centre of the sample with a separation of 4mm between each position, measured from the edge of the wafer. The rocking curve

data for each position were taken in steps of 4 arc seconds with a counting time of 25 seconds per step. The long counting time reduced the statistical variation of the background noise to less than 1 count in the vicinity of the interference fringes. The experimental rocking curves were compared with simulated rocking curves at each point across the wafer, Figure 7.2.

The mean spacing of the Pendellösung fringes on the rocking curves was measured as 168 $\pm$ 2 seconds and from this the thickness of the GaAs cap is calculated as 0.113 $\pm$ 0.001 μm, from equation 5.12. However the cap thickness deduced from the rocking curve simulations is 0.104 $\pm$ 0.001 μm which would appear to correspond to a Pendellösung fringe period of 182 $\pm$ 2 seconds. The discrepency is again caused by interference effects due to the epitaxial layer and the GaAs capping layer [10] and re-iterates the need to simulate experimental data from thin epitaxial layers.

Careful fitting of the simulated rocking curves allowed the InGaAs layer thickness to be fitted to an accuracy of 1 $\AA$ (i.e. 0.5 %). Similarly, from the position of the layer peak and the effect on the interference fringes, the composition or relaxation can be fitted to 0.5 %. Note that in surface symmetric reflections, the effects of relaxation and composition change on the rocking curve cannot be separated. However the maximum linear dislocation line density measured at the centre of the sample is about 0.12 μm^{-1}. This corresponds to an epitaxial layer relaxation of less than 0.2 % which has a negligible effect on the position and intensity of the interference fringes near the substrate peak on simulated rocking curves. Hence to within the accuracy quoted here, the variations in the position and intensity of the interference fringes can be attributed solely to changes in layer composition and thickness.

The composition and thickness of the InGaAs layer determined at each point across the wafer are presented in Table 7.1. These data are presented graphically in Figure 7.3.

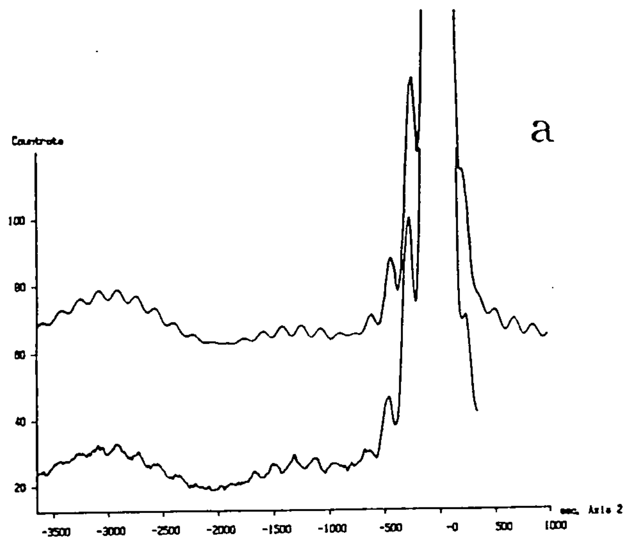

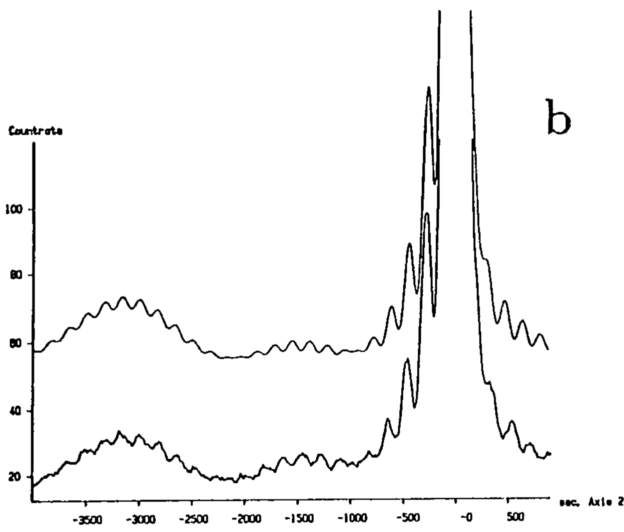

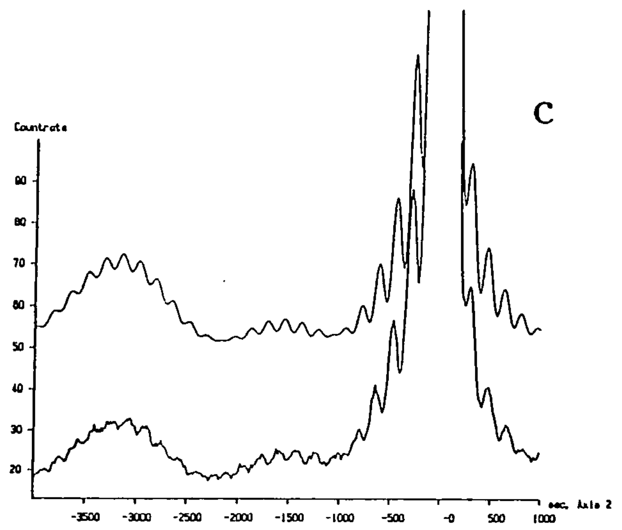

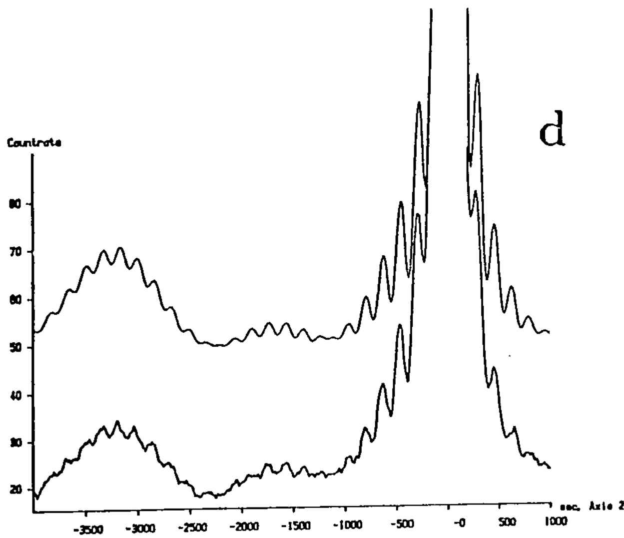

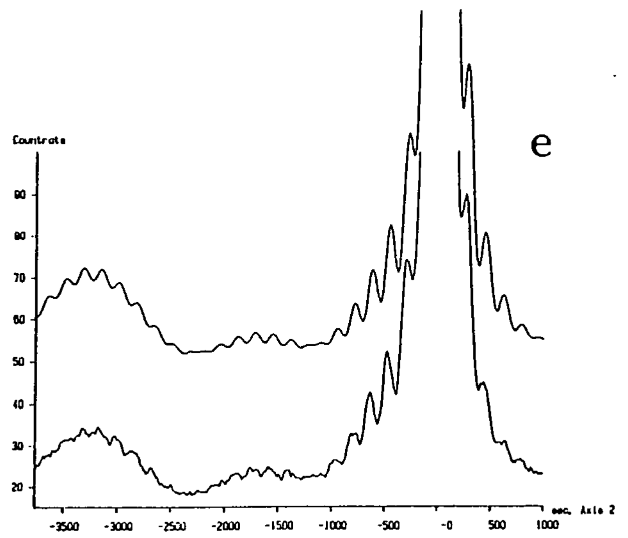

Figure 7.2: 004 experimental rocking curves of GaAs4, with simulated rocking curves displaced above, for five points across the centre of the wafer. The distance from the wafer edge at each position is (a) 6.5mm, (b) 10.5mm, (c) 14.5mm, (d) 18.5mm, (e) 22.5mm.

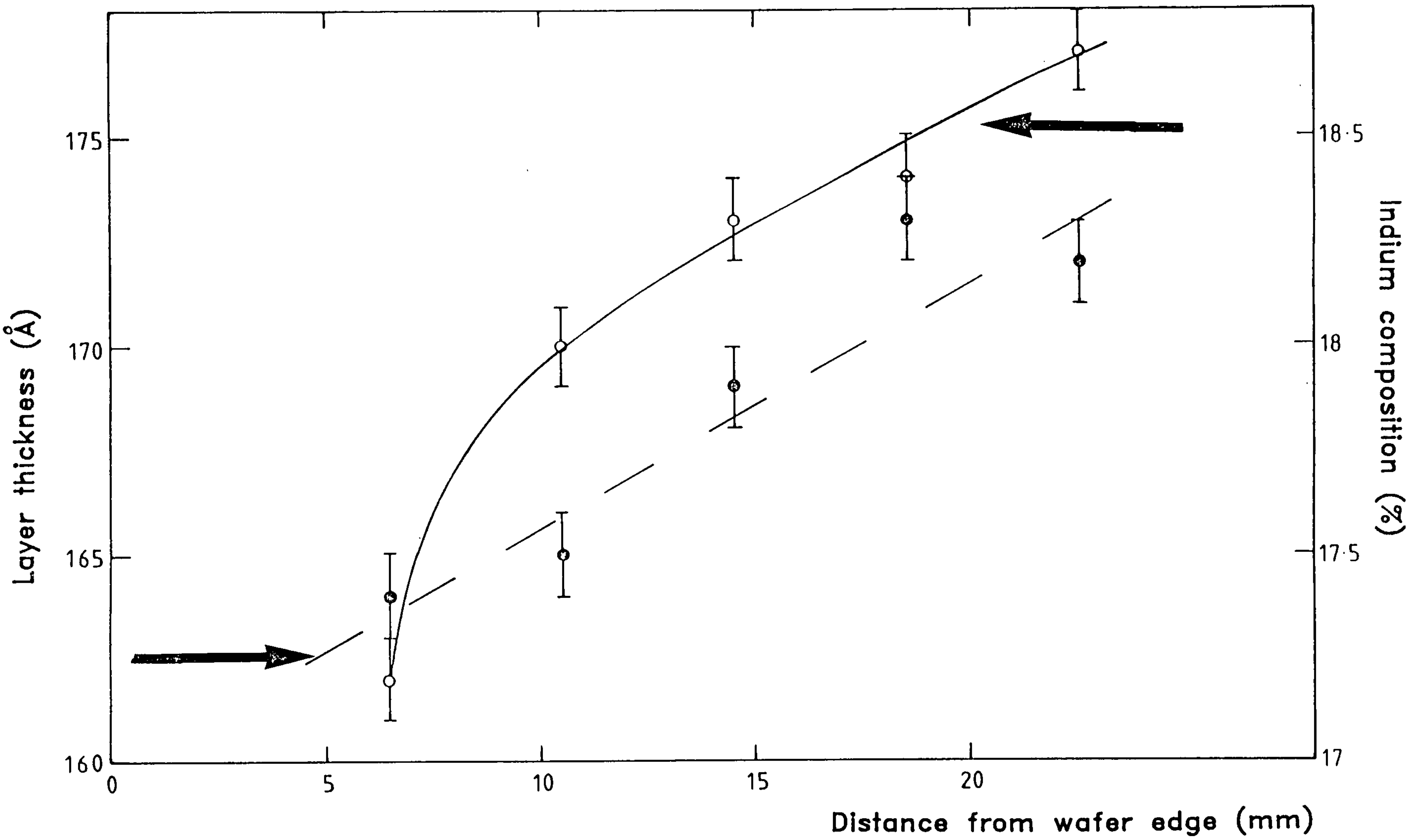

Figure 7.3: Variation in composition and thickness of the InGaAs layer in sample GaAs4 with distance from the edge of the wafer

Table 7.1. Variation in Thickness and Composition of the InGaAs Layer

Distance from wafer edge	Layer Thickness (Å)	Indium Concentration (%)
6.5 mm	164 ± 1	17.2 ± 0.1
10.5 mm	165 ± 1	18.0 ± 0.1
14.5 mm	169 ± 1	18.3 ± 0.1
18.5 mm	174 ± 1	18.4 ± 0.1
22.5 mm	173 ± 1	18.7 ± 0.1

The data clearly show an increase in layer thickness and composition with distance from the edge of the wafer. This is consistent with the increase in dislocation line density towards the centre of the wafer observed by double crystal topography. The first position across the centre of the sample at which misfit dislocation lines are observed by topography was determined as 4.5 ± 0.5 mm from the edge of the wafer. From Figure 7.3 we expect the layer composition and thickness at this position to be 17 ± 0.5 % and 162 ± 2 Å. When relaxation at the layer/substrate and layer/cap interfaces is taken into account, the Matthews model, equation 4.1, predicts a critical thickness of 150 ± 5 Å for the $In_xGa_{1-x}As$ layer where $x = 17 \pm 0.5\%$.

Although topography enables the first dislocations which are nucleated at the critical thickness to be observed, x-ray diffractometry is insensitive to this effect. It is concluded that x-ray diffractometry over estimates the critical epitaxial layer thickness.

7.1.1. Precision of the Strained Layer Thickness Measurement

Variations in layer thickness and composition with radial distance from the wafer centre is characteristic of MBE growth. This effect was discussed in relation to sample GaAs1 (section 5.1) in which the aluminium concentration of an AlGaAs layer deposited by MBE was seen to increase towards the edge of the wafer.

The accuracy of 1 Å associated with the layer thicknesses determined through comparison between simulated and experimental data corresponds to a single mono-

layer. In a similar study Tapfer and Ploog [11] examined thin layers of $Al_xGa_{1-x}As$ and GaAs deposited on GaAs substrates for x=0.33 and x=0.35. They reported an accuracy in layer thickness of 1 nm. A recent theoretical study by Holloway [12] has demonstrated that in the 004 reflection from a GaAs/thin layer/GaAs structure the modulation of the Pendellösung fringes from the GaAs cap undergoes a complete cycle for a change, δd, in the thickness of the thin layer given by

$$\delta d = \frac{a_0}{4m^*} \qquad 7.1$$

where m^* is the effective mismatch and a_0 is the GaAs lattice parameter. We expect to be able to detect a phase change of less than $\pi/16$ by simulation. Hence Holloway predicts the accuracy to which layer thickness can be simulated for thin layers of $In_{0.17}Ga_{0.83}As$ and $Al_{0.33}Ga_{0.67}As$ is less than 1.8Å and 45Å respectively in excellant agreement with the author and Tapfer and Ploog.

Modulation of the Pendellösung fringes has also been observed for thicker layers. Chu and Tanner [13] observed interference fringes on 004 double crystal rocking curves from an AlGaAs laser. The structure consisted nominally of a 0.13 μm active layer of $Al_{0.09}Ga_{0.91}As$ confined between two 1.3 μm layers of $Al_{0.35}Ga_{0.65}As$. The structure was deposited on a 001 GaAs substrate with a 3 μm buffer layer of $Al_{0.16}Ga_{0.84}As$ and capped by a 0.15 μm layer of GaAs. The period of the interference fringes was about 15 arc seconds which, from equation 2.33, corresponds to a layer thickness of about 2.5 μm i.e the confining AlGaAs layers. As the structure is strained to the GaAs substrate, the active layer effective mismatch, m^*, is about 290 ppm. Chu and Tanner observed that the thickness of the active layer could be determined to within 200 Å. This is in good agreement with the accuracy predicted by Holloway of 150 Å.

7.2 Asymmetric Relaxation in a Superlattice

Sample SLS1 was grown by G. Scott at the British Telecom Research Laboratories. It consists of 50 periods of an InGaAs/InP multi quantum well deposited by MBE on an 001 orientated InP substrate. Each quantum well nominally consists of 90 Å InGaAs and 80 Å InP and hence the total superlattice height is 0.85 μm. A complete set of eight 115 double crystal rocking curves was recorded at 1.54051 Å [14]. The mean superlattice unit cell lattice parameters in the [001], [110] and [1$\bar{1}$0] directions were measured from the separation, ψ, between the zero-order superlattice peak and the substrate peak on these reflections, Table 7.2. The percentage relax-

ation in each of the [110] and [1$\bar{1}$0] directions was calculated from these parameters and is clearly asymmetric.

Table 7.2. Diffractometry Data on Sample SLS1

	[110]	[1$\bar{1}$0]
115LOW i_L (secs)	-239.4 ± 0.5	-239.3 ± 0.5
115HIGH i_H (secs)	-122.4 ± 0.5	-129.2 ± 0.5
Tilt (secs)	6.2 ± 0.5	2.1 ± 0.5
d_l ($\AA$)	4.14955 ± 0.00005	4.14986 ± 0.00005
c ($\AA$)	5.87470 ± 0.00005	5.87477 ± 0.00005
Relaxation (%)	-12.6 ± 2.5	3.0 ± 2
Dislocation Density, N,	(3.0 ± 0.6) $\times 10^5 m^{-1}$	(0.7 ± 0.5) $\times 10^5 m^{-1}$

The mean superlattice unit cell mismatch is 502 ± 17 ppm. If all the misfit dislocations formed in the interface then, from equation 5.13, the average dislocation line spacings in the [110] and [1$\bar{1}$0] directions deduced by diffractometry would be (3.3 ± 0.6) μm and (14.9 ± 9) μm respectively, and would be resolved by topography. The sample was examined by Lang topography in the reflection geometry. A 115 reflection was employed in conjunction with Cu $K_{\alpha 1}$ radiation. However the resolution obtained on these topographs was too low to resolve the dislocation images. 004 double crystal topographs were recorded on station 7.6 at the Daresbury Laboratory SRS for an x-ray wavelength of 1.4 $\AA$. Topographs taken with the x-ray beam parallel to the [110] direction show an array of short stubby dislocation images which tend to be aligned along the [1$\bar{1}$0] direction, Figure 7.4. With the x-ray beam parallel to the [1$\bar{1}$0] direction we find specular images with no net axis of alignment. The scaling factor in this geometry is 0.52, equation 3.10. Hence the asymmetry in relaxation measured quantitatively by diffractometry is also observed qualitatively by double crystal synchrotron radiation topography although an estimate of dislocation line spacing on the topographs is not possible.

The dislocation images observed in Figure 7.4 appear to arise from threading dislocations which are forced back upon themselves by the alternating strain fields in the superlattice. This process creates short misfit dislocation segments at each interface within the superlattice. The sense of the strain relief produced by the

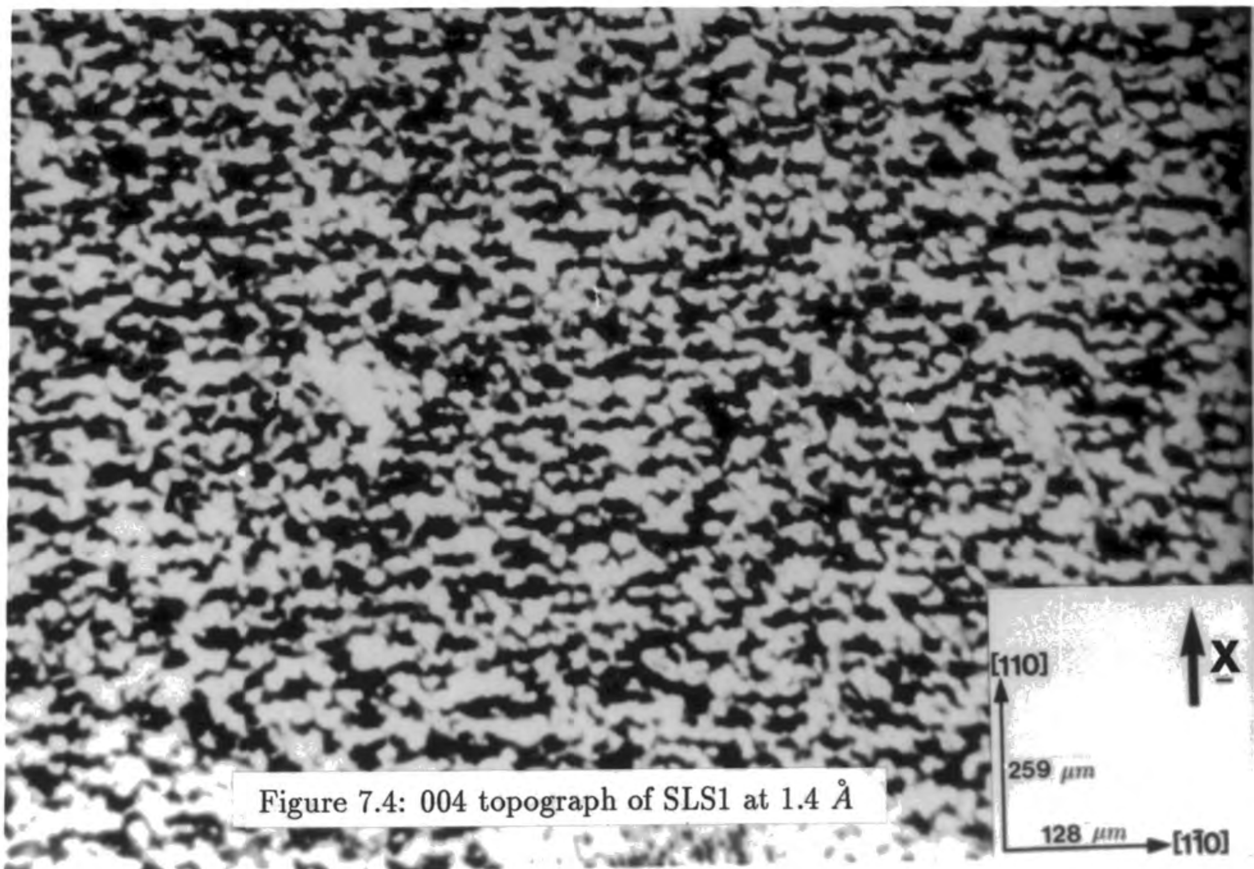

Figure 7.4: 004 topograph of SLS1 at 1.4 Å

misfit dislocation line segments will alternate with the superlattice strain field. This is consistent with transmission electron microscopy studies of $Si/Si_{1-x}Ge_x$ strained layer superlattices [15] Hence threading dislocations produce 'zig-zag' patterns of misfit dislocation lines through the epitaxial layer. 004 reflection topography views these zig-zag patterns 'end-on' and so the images of the misfit dislocation segments are stacked on top of each other.

7.3 Asymmetric Relaxation in Epitaxial Layers of AlAs

In the investigation to establish the mismatch between AlAs and GaAs and the AlAs Poisson ratio [1] it was concluded that the 1 μm layer of AlAs on GaAs grown by MBE, sample GaAs2, had relaxed. This did not appear to be the case for the MOVPE grown AlAs layer used by Goorsky *et al* [16], sample GaAs5. Asymmetric 115 double crystal rocking curves were recorded from sample GaAs2 and the relaxation in each $\langle 110 \rangle$ direction was determined using the analysis developed by Halliwell and discussed in section 5.2.2. These calculations were presented in detail in section 5.2.3 and are briefly summarised here.

As mentioned in section 5.2.3, sample GaAs2 was grown by C. Stanley at Glasgow University and consists of a 1 μm layer of AlAs deposited on an 001 orientated GaAs substrate. The layer is capped by a 1 μm layer of $Al_{0.3}Ga_{0.7}As$ and a 1 μm layer of GaAs. Double crystal rocking curves were recorded for the 004 and 115 reflections in the [110] and $[1\bar{1}0]$ directions giving a total of twelve rocking curves, Figure 5.5 to 5.7. The separations, ψ, between the substrate and epitaxial layer peaks on the 115 rocking curves in the high angle of incidence and low angle of incidence geometries were employed to calculate the epitaxial layer lattice parameters in the [001], [110] and $[1\bar{1}0]$ directions. The layer relaxation and misfit dislocation line density in each $\langle 110 \rangle$ direction were deduced from equations 5.7 and 5.13 and are summarised in Table 7.3.

Table 7.3. Diffractometry Data from Sample GaAs2

	[110]	$[1\bar{1}0]$
Relaxation (%)	3.3 ± 0.8	1.0 ± 0.8
Dislocation Density,N	$(2.7 \pm 0.6) \times 10^5 m^{-1}$	$(0.8 \pm 0.6) \times 10^5 m^{-1}$

The diffractometry data predicts average misfit dislocation line spacings in the [110] and [1$\bar{1}$0] directions of (3.7 ± 0.8) μm and (12.5 ± 9) μm respectively. Hence it should be possible to resolve individual dislocation lines on a double crystal topograph of this sample.

In order to investigate this, double crystal synchrotron topography was performed at the Daresbury Laboratory [section 3.2.3]. 004 topographs recorded at 1.882 Å show a dislocation network which varies in density from zero near the wafer edge to a maximum near the centre. Again, the variation in dislocation density with distance from the centre of the wafer is attributed to radial variations in layer composition and thickness and is characteristic of MBE growth near the critical epitaxial layer thickness. The position on the sample at which the rocking curves were recorded was accurately determined on an 004 topograph and the dislocation network in this region was examined in detail, Figure 7.5. The dislocation image spacings in the [110] and [1$\bar{1}$0] were found to be 11 ± 1 μm and 10 ± 2 μm respectively. In the [1$\bar{1}$0] direction the spacing of the dislocation images measured by topography is in good agreement with the average dislocation line spacing deduced by diffractometry for an array of strain relieving 60° dislocations near the interface. Hence the dislocation images observed on the 004 topograph in the [110] direction do correspond to individual 60° dislocation lines.

In the orthogonal direction the dislocation image spacing is three times larger than the dislocation line density deduced by diffractometry for an array of 60° misfit dislocations. Hence in this direction the dislocation images observed by topography represent bundles of misfit dislocation lines and individual dislocation lines are not resolved.

The topography and diffractometry data in the [110] direction from sample GaAs2 demonstrates that the resolution to which layer relaxation can be measured by these techniques meets. However there does not appear to be a significant overlap in resolution.

Diffractometry measurements were carried out by Goorsky *et al* [16] using the 004 reflection on 1 μm layers of $Al_xGa_{1-x}As$ on GaAs grown by low pressure MOVPE where x ranged from 0 to 1. These indicated that the layers of AlGaAs were coherently strained across the full range of aluminium concentrations. Goorsky also recorded asymmetric reflection rocking curves from the AlAs on GaAs layer, sample GaAs5, and the layer relaxation that he measured from these was found to be zero in both $\langle 110 \rangle$ directions, to within the limit of resolution of this technique.

In order to verify this, double crystal SRS topographs of GaAs5 were taken at

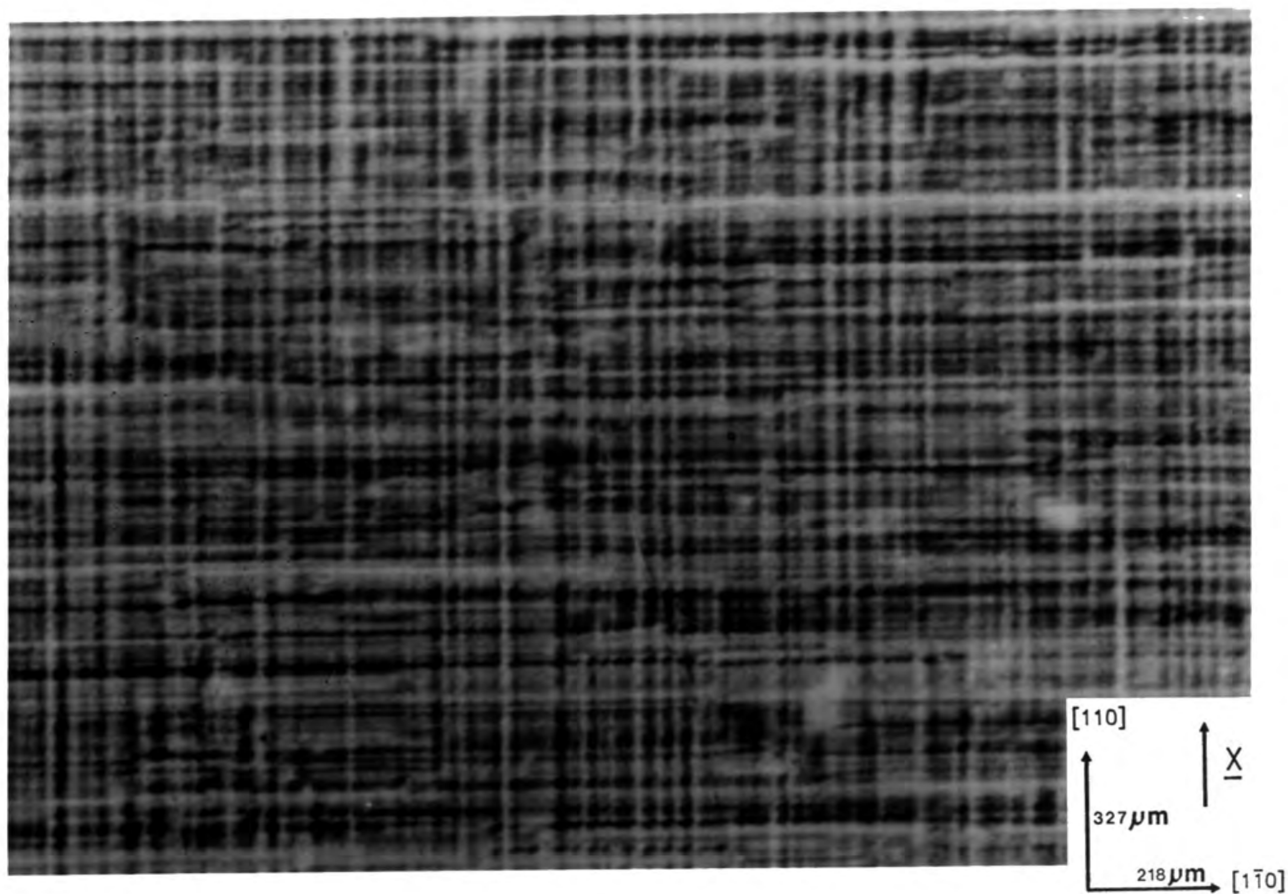

Figure 7.5: 004 topograph of GaAs2 at 1.882 Å

Daresbury Laboratory employing the 004 reflection and an x-ray wavelength of 1.4 Å. The sample was highly curved and so the Bragg band from the substrate reflection on the topographs was narrow. The area of sample imaged on the topographs was further reduced by an inhomogenous layer of photoresist on the sample surface. Large regions of this sample show no dislocation images and confirm the relaxation measurements reported by Goorsky. However near the centre of the wafer a very low density of small segments of misfit dislocation is observed, Figure 7.6. The distribution of the misfit dislocation segments is asymmetric; all segments lie in the [110] direction. A number of these dislocations lines appear to originate at threading dislocations from the substrate whereas other dislocation lines occur far from any images of threading dislocations and so could originate from dislocation line half loops nucleated at the epitaxial layer surface.

Again, as in sample GaAs4, the diffractometry and topography data from sample GaAs5 indicates that x-ray diffractometry is insensitive to the first few misfit dislocations nucleated at the critical epitaxial layer thickness. However these are clearly observed by topography.

The difference in the epitaxial layer relaxation observed in the nominally identical samples GaAs2 and GaAs5 most likely arises from a slight difference in layer thickness between these samples. Sample GaAs2 was grown by MBE whereas sample GaAs5 was grown by low pressure MOVPE. AlAs is almost lattice matched to GaAs at a growth temperature of 630° C [17]; the lattice mismatch of 1600 ± 15 ppm at room temperature arises from the difference in the thermal expansion coefficients. Hence for these samples the rate at which the sample is cooled down after growth in the two deposition techniques may also have a significant effect on epitaxial layer relaxation. It is also noted that the AlAs layer in sample GaAs5 was grown on an 001 GaAs substrate which was off cut by 2° whereas in sample GaAs2 the layer was grown on an orientated 001 GaAs substrate.

In order to further examine the dynamics of the nucleation and propagation of misfit dislocations at the critical epitaxial layer thickness, a joint program between Durham University and RSRE is underway to study the relaxation mechanism *in situ* using x-ray topography at the Daresbury synchrotron radiation source. An MBE chamber fitted with beryllium windows will be installed on the wiggler station 9.4 and images of misfit dislocations will be recorded as they form. This requires the exposure of topographs in quick succession. Although nuclear emulsion plates provide excellent resolution they do not easily lend themselves to producing rapid sequential exposures. The resolution of Kodak technical pan film has been examined

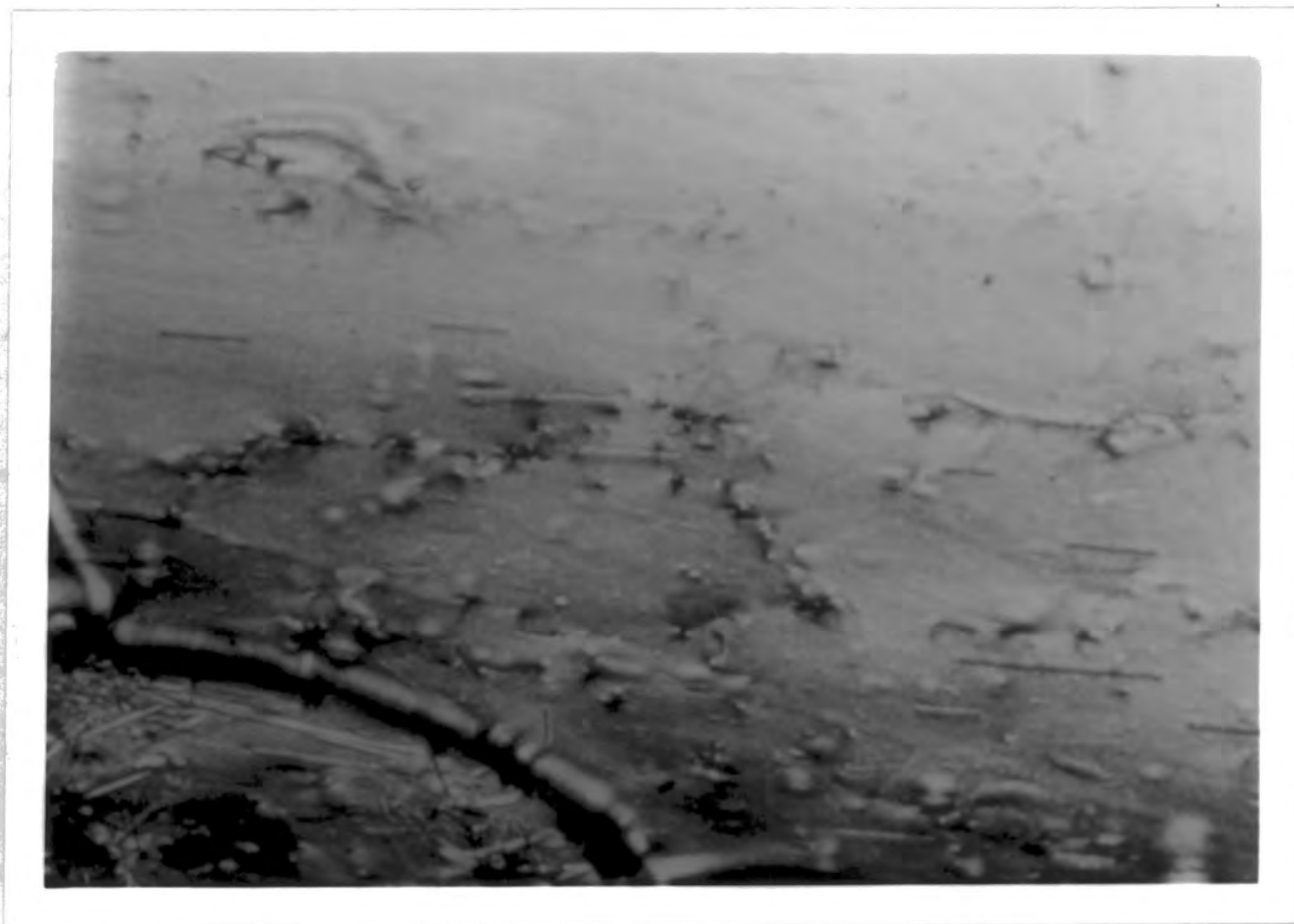

Figure 7.6: 004 topograph of GaAs5 at 1.4 Å recorded on an Ilford L4 nuclear emulsion plate

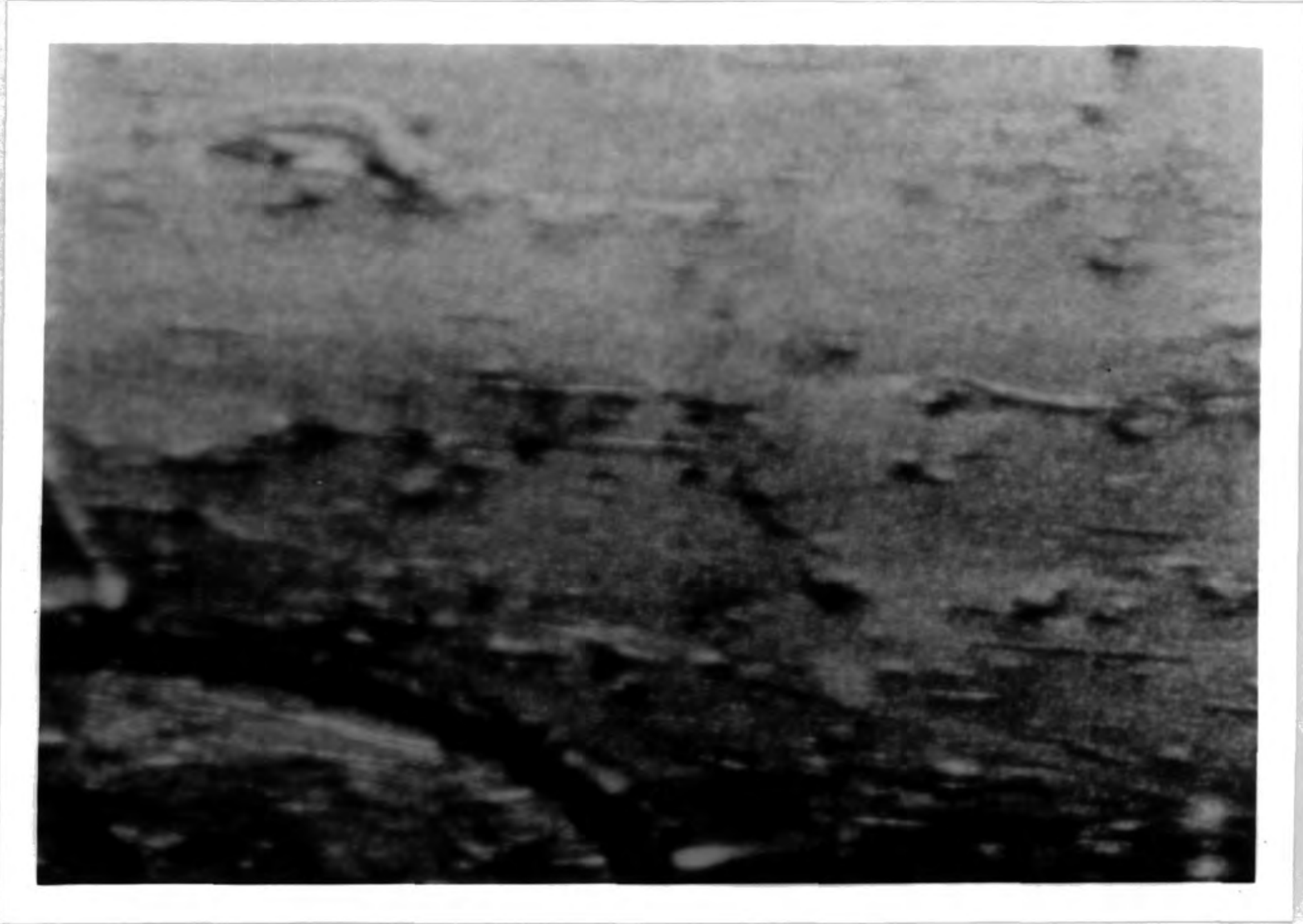

Figure 7.7: 004 topograph of GaAs5 at 1.4 Å recorded using Kodak technical pan film 4415

as this film is available in canisters.

The 004 topograph in Figure 7.6 was recorded on an Ilford L4 nuclear emulsion plate whereas the topograph in Figure 7.7 was recorded using Kodak technical pan film 4415. The exposure time for both these topographs was 5 minutes. Comparison of Figures 7.6 and 7.7 shows that the pan film has a slightly reduced resolution but still images the dislocation lines clearly. As a result of this experiment, the collaborators opted for the use of nuclear emulsion plates !

7.4 Conclusions

Double crystal x-ray diffractometry and x-ray topography have been used to examine the epitaxial layer relaxation in four samples with low dislocation densities; a 17nm layer of InGaAs on a GaAs substrate, an InGaAs superlattice on an InP substrate and two 1 μm layers of AlAs on a GaAs substrate. In all these samples the layer relaxation has been found to be asymmetric about the [110] and $[1\bar{1}0]$ directions.

For ultra thin epitaxial layers the epitaxial layer peak reflection in the high angle of incidence asymmetric rocking curves has a very low intensity and interference effects in the layer reduce the substrate to epitaxial layer peak separation for all reflections. However in sample GaAs4 the 17nm InGaAs layer is sandwiched between a GaAs substrate and a 0.1 μm GaAs cap and this sytem produces strong interference fringes. The period of the fringes is determined by the thickness of the capping layer whereas the position and intensity of the fringes is determined by the composition and thickness of the InGaAs layer. By careful fitting of simulated and experimental rocking curves this phenomenon has been used to determine the layer thickness to within a monolayer and the indium concentration to within 0.5 %.

Double crystal synchrotron radiation topography can resolve individual misfit dislocation lines for epitaxial layer samples with low dislocation densities. In order to image individual misfit dislocations by single crystal reflection topography the penetration depth must be minimised so that the signal to noise ratio for the misfit dislocation images is maximised. Double crystal topography of epitaxial layers deposited on GaAs substrates indicates that the substrates have relatively high densities of threading dislocations which are arranged into cellular structures. The topographs show that in the initial stages of relaxation of InGaAs on GaAs lengths

of misfit dislocation are formed from the bending over of threading dislocations near the interface. Misfit dislocations in the InGaAs superlattice on InP were deduced to be distributed across the interfaces of the superlattice. The images from misfit dislocations above and below each other in the superlattice are integrated on the topograph and hence individual dislocation lines are not resolved. However the asymmetry in relaxation deduced by diffractometry is observed qualitatively by topography.

The asymmetric double crystal rocking curves discussed in this chapter demonstrate that diffractometry can determine the layer relaxation at low dislocation densities for layers which are about 1 μm thick. For these layers the position of the epitaxial layer peak can be accurately determined on the rocking curve. The measurement of misfit dislocation line spacing in the $[1\bar{1}0]$ direction for sample GaAs4 is in excellent agreement with the layer relaxation deduced by diffractometry. This sample illustrates that the maximum dislocation density which allows resolution of individual dislocations by x-ray topography just about corresponds to the minimum relaxation which can be detected by diffractometry. Hence the combination of x-ray diffractometry and x-ray topography enables the investigation of epitaxial layers at all stages of relaxation.

Chapter 8

Characterisation of Misfit Dislocations by Topography

8.0 Introduction

In this chapter we discuss the application of x-ray topography to the analysis of the Burgers vector of misfit dislocation lines. This technique is illustrated for a sample containing several dislocation types where the dislocation line density is sufficiently low for individual dislocations to be resolved by x-ray topography.

8.1 Determination of the Burgers Vector of a Dislocation Line

A double crystal x-ray topograph consists of a photographic record of the diffraction pattern produced when x-rays are scattered from a crystal lattice. Strong diffraction occurs when the Bragg condition is satisfied at a particular set of lattice planes within the sample. The diffracted intensity recorded on the topograph contains information about the uniformity of the diffracting planes in the crystal. Changes in lattice perfection associated with the strain fields surrounding the core of a dislocation line lead to a local variation in the Bragg condition in the vicinity of the dislocation. This produces a corresponding region of varying diffracted intensity on the topograph; the dislocation line image. However if a reflection is chosen from lattice planes in the crystal sample which are not distorted by the strain field associated with a dislocation line then the dislocation line will not be imaged on the topograph. This is the basis of Burger's vector analysis which determines the visibility of dislocation images on x-ray topographs [1].

The strength of the dislocation line contrast on the topograph is a function of C where

$$C = \underline{g}.\underline{u}(\underline{r}) \qquad 8.1$$

and $\underline{u}(\underline{r})$ is the atomic displacement around the dislocation core and $\underline{g}$ is the

diffraction vector. From section 4.1 we recall that the character of a dislocation line is uniquely specified by its Burgers vector, $\underline{b}$, and line direction, $\underline{l}$. The line direction is a unit vector parallel to the core of the dislocation line. The Burgers vector describes the magnitude and direction of the lattice disruption surrounding the dislocation core and is defined by the **SF**/*RH* convention. Equation 8.1 can be represented in terms of $\underline{b}$ and $\underline{l}$, equation 8.2,

$$C = C_1 \underline{g}.\underline{b} + C_2 \underline{g}.\underline{b} \times \underline{l} \qquad 8.2$$

where C_1 and C_2 are constants and C_2 is much smaller than C_1 for all dislocation types [1].

For a pure edge dislocation, $\underline{b}.\underline{l} = 0$. Hence lattice planes can be found which are orthogonal to both $\underline{b}$ and $\underline{r}$ and so are undeformed by the dislocation strain field. The edge dislocation is invisible in x-ray topographs using these reflecting planes. This is illustrated in Figure 8.1. For the pure screw dislocation $\underline{b}$ is parallel to $\underline{l}$ and so the condition for invisibility reduces to $\underline{g}.\underline{b} = 0$. A dislocation containing both screw and edge character is never completely invisible, though the visibility is very much reduced when $\underline{g}.\underline{b} = 0$.

At the exact Bragg diffraction condition the width of a dislocation image depends upon the volume surrounding the dislocation line in which the lattice planes are distorted by more than the width of the Bragg reflection. Hence the image width is proportional to the magnitude of the Burgers vector and inversely proportional to the full width at half maximum intensity of the Bragg reflection. If the wafer is curved then a range of dislocation visibilities will be observed across the Bragg diffraction band. Best dislocation images are obtained in the region corresponding to the flank of the Bragg reflection. Here the dislocation image is asymmetric and the image width is reduced. However the dislocation line width reduces further still as the local mis-orientation of the sample with respect to the exact Bragg condition increases. A dislocation line can appear to go out of contrast if it is imaged by the tail of the Bragg reflection.

8.2 Identification of Screw Dislocations in Strained Layers

Sample InP2 was grown by G. Scott at the British Telecom Research Laboratories and consists of a 4 μm layer of $In_xGa_{1-x}As$ deposited by MBE on an 001

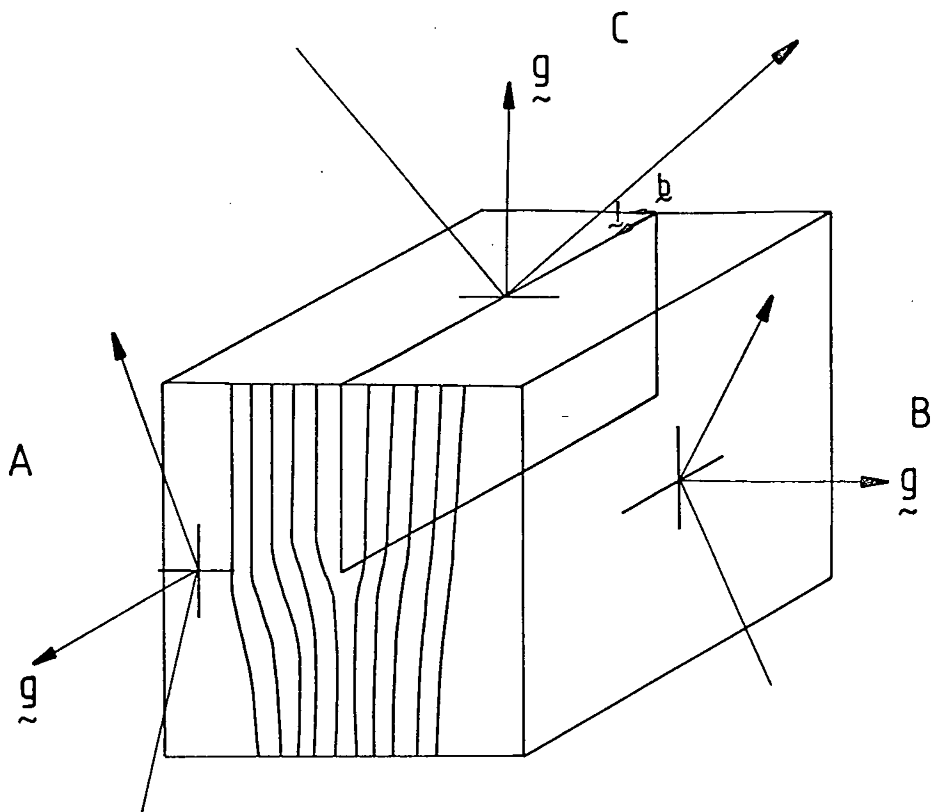

	$\frac{\lvert \underset{\sim}{g} \cdot \underset{\sim}{b} \rvert}{gb}$	$\frac{\lvert \underset{\sim}{g} \cdot \underset{\sim}{b} \wedge \underset{\sim}{l} \rvert}{g\,b\,l}$	CONTRAST
A	0	0	NONE
B	1	0	STRONG
C	0	1	WEAK

Figure 8.1: Burgers vector analysis of an edge dislocation

orientated InP substrate. The mismatch was determined from 004 double crystal rocking curves recorded using Cu $K_{\alpha 1}$ radiation as 883 ± 5 ppm. This corresponds to a indium of 44 ± 0.5 %. Double crystal SRS topographs were recorded at Daresbury Laboratory using the 004, 224 and 404 type reflections at 1.5 Å. Large regions of this sample show no dislocation images on the topographs indicating that the epitaxial layer is coherently strained. However in one corner of the sample an array of long straight dislocation lines was clearly resolved in the 224 reflection. The dislocation lines lie in the [110] direction and are parallel to the diffraction vector, $\underline{g}$, Figure 8.2. In the $2\bar{2}4$ reflection these dislocation lines are observed to go out of contrast, Figure 8.3. Hence from these topographs the Burgers vector of these dislocation lines must lie in a plane perpendicular to the $[2\bar{2}4]$ direction. The white specular images on the topographs arise from surface imperfections and act as useful reference markers. The dislocation lines were not observed on topographs taken using the 004 reflection. Hence the Burgers vector must lie in an 001 plane. Thus we deduce that the Burgers vector is 1/2[110]. The dislocation lines were observed in all the 404 type reflections which confirms the Burgers vector analysis. Since the Burgers vector is parallel to the dislocation line, these are pure screw dislocations. This is an unusual result as an individual screw dislocation cannot relieve misfit strain. A parallel array of screw dislocations of the same sense can relieve misfit strain through twist between the epitaxial layer and the substrate. However this would require a very high density of dislocations and is energetically unfavourable. The screw dislocations are thought to be the the trailing segments of dislocation half-loops gliding on inclined ⟨111⟩ planes [2] and arising from plastic deformation. This deformation could have been induced by substrate handling or thermal gradients present during growth. These defects illustrate vividly that in some cases interfacial dislocations are nucleated which do not contribute to the relaxation process. Hence even at low dislocation densities where studies have demonstrated that the misfit dislocations are 60° dislocations (section 4.1) the dislocation density deduced from rocking curve measurements, equation 5.11, may represent a minimum value.

8.3 Interactions Between 60° Dislocations at Low Dislocation Density

In a separate region towards the centre of sample InP2 another low density array of dislocation lines lying in the $[1\bar{1}0]$ direction was observed in a $2\bar{2}4$ reflection topograph recorded at 1.5 Å. The array was also observed in the 224 and 004 reflections recorded at the same wavelength which indicates that these are not pure

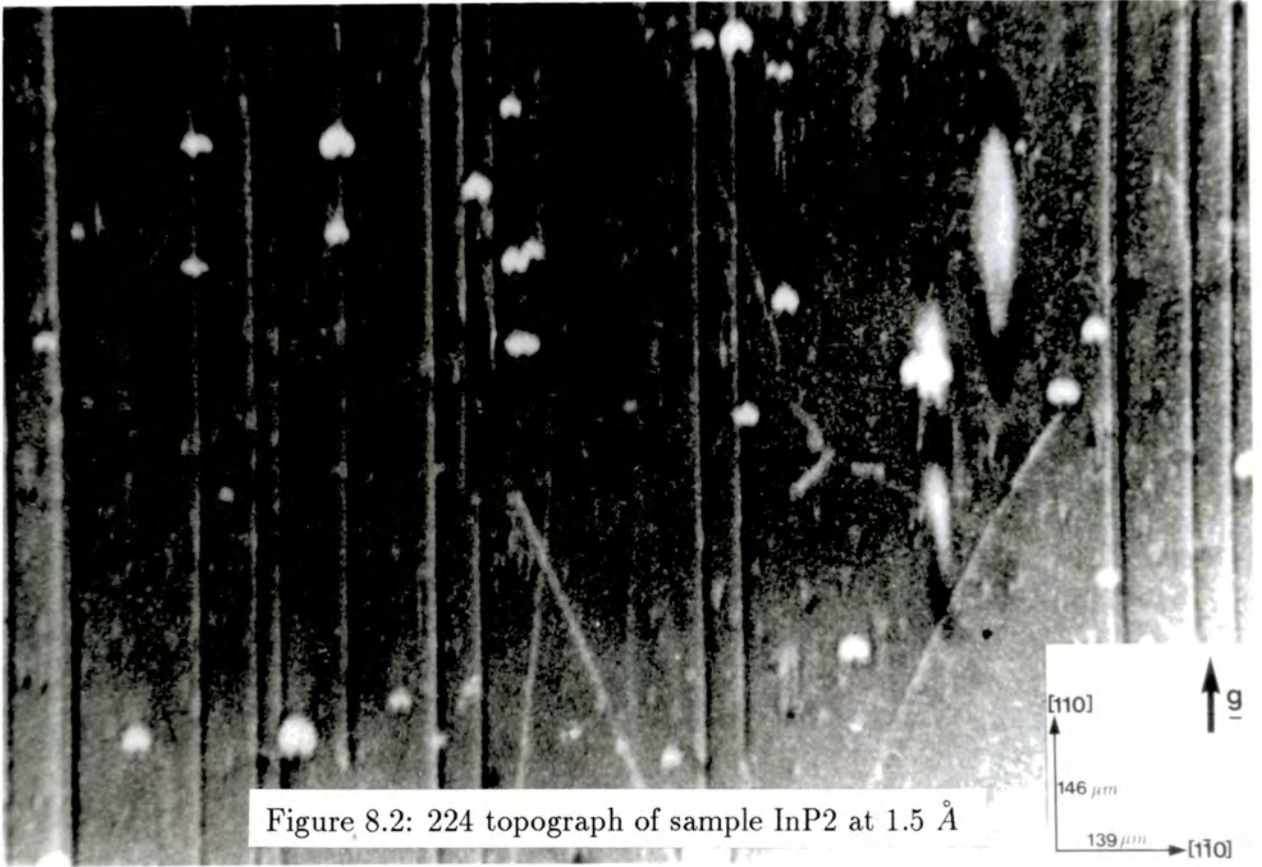

Figure 8.2: 224 topograph of sample InP2 at 1.5 Å

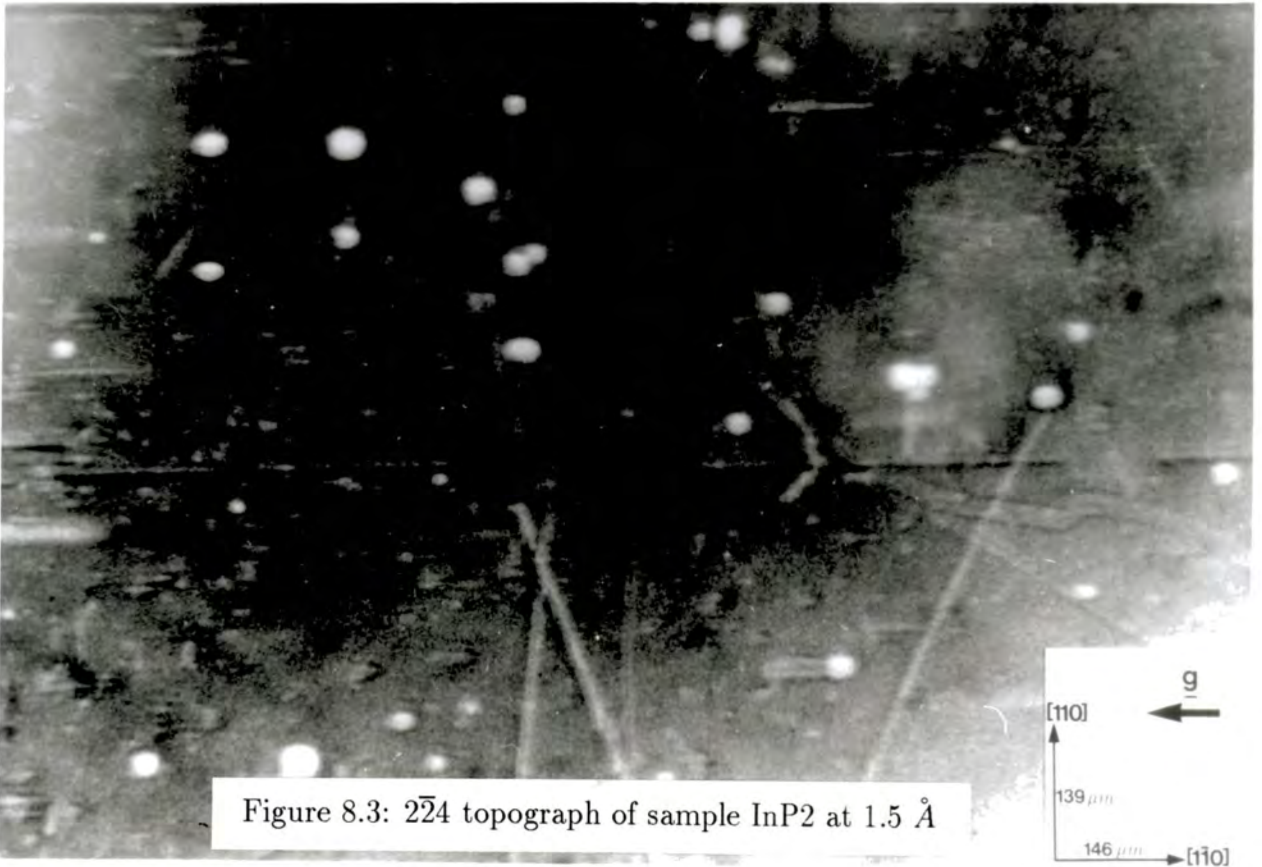

Figure 8.3: $2\bar{2}4$ topograph of sample InP2 at 1.5 Å

screw dislocations. 404 type reflections were also recorded for this sample at an x-ray wavelength of 1.6 Å. Although the 404 type topographs clearly showed the dislocation line array the contrast on the topographs was in general poor and varied considerably with each reflection. This is attributed to problems in experimental stability at the time when these topographs were recorded. Further analysis of the dislocation line Burgers vectors from the 404 type topographs was not possible. However it is reasonable to assume from the 004, 224 and 404 reflections that the isolated dislocation lines are 60° dislocations.

The density of dislocation lines varied considerably across the array. A region of the array imaged by a $2\bar{2}4$ topograph taken at 1.5 Å, Figure 8.4, clearly shows bunching of dislocation lines into a dislocation bundle. A higher number of dislocations appears to be nucleated within the bundle than in surrounding regions. Thus we conclude that dislocations are preferentially nucleated within the bundle. The observation of dislocation bundles at low dislocation densities supports the evidence presented in previous chapters for the bunching of dislocation lines into bundles at high dislocation densities.

In the centre of Figure 8.5, another region of the array imaged by the $2\bar{2}4$ reflection at 1.5 Å, we observe two 60° dislocation lines A, B appear to join a third dislocation line C. The width of the dislocation line C is larger than the widths of dislocation lines A and B. Hence the Burgers vector of dislocation C is also larger than the Burgers vectors of dislocation lines A and B. Thus we conclude that dislocation lines A and B have interacted to form dislocation line C. The dislocation line C is also observed with an enhanced contrast compared to dislocation lines A and B on the 224 reflection, Figure 8.6. Since the energy of a dislocation line is proportional to the square of the Burgers vector [3] then the condition for this interaction to be energetically favourable is that

$$b_A^2 + b_B^2 \leq b_C^2 \qquad 8.3$$

where b_A, b_B and b_C are the Burgers vectors for these dislocations. Dislocations A and B are both 60° misfit dislocations and so their Burgers vectors have the same in plane edge component, $E_{\|}$. This restricts the possible Burgers vectors for these dislocations to the set of four Burgers vectors b_1, b_2, b_3 and b_4 drawn in Figure 8.7. Hence the dislocation interaction observed in Figures 8.5 and 8.6 could arise from

$$(i)..b_1 + b_2 = \frac{a_0}{2}[\bar{1}01] + \frac{a_0}{2}[0\bar{1}1] = \frac{a_0}{2}[\overline{11}2]$$

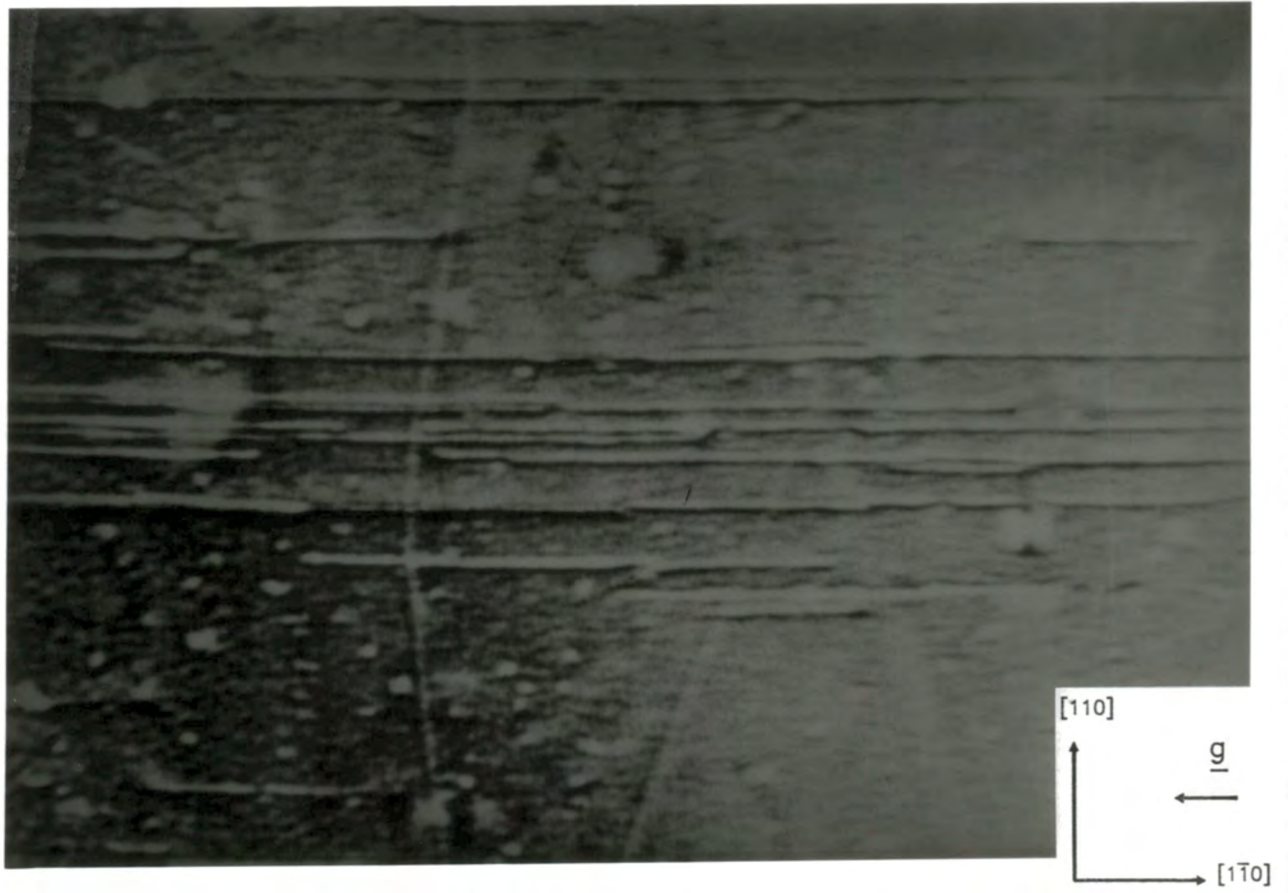

Figure 8.4: $2\bar{2}4$ topograph of sample InP2 at 1.5 $\AA$ showing bunching of misfit dislocation lines into dislocation bundles

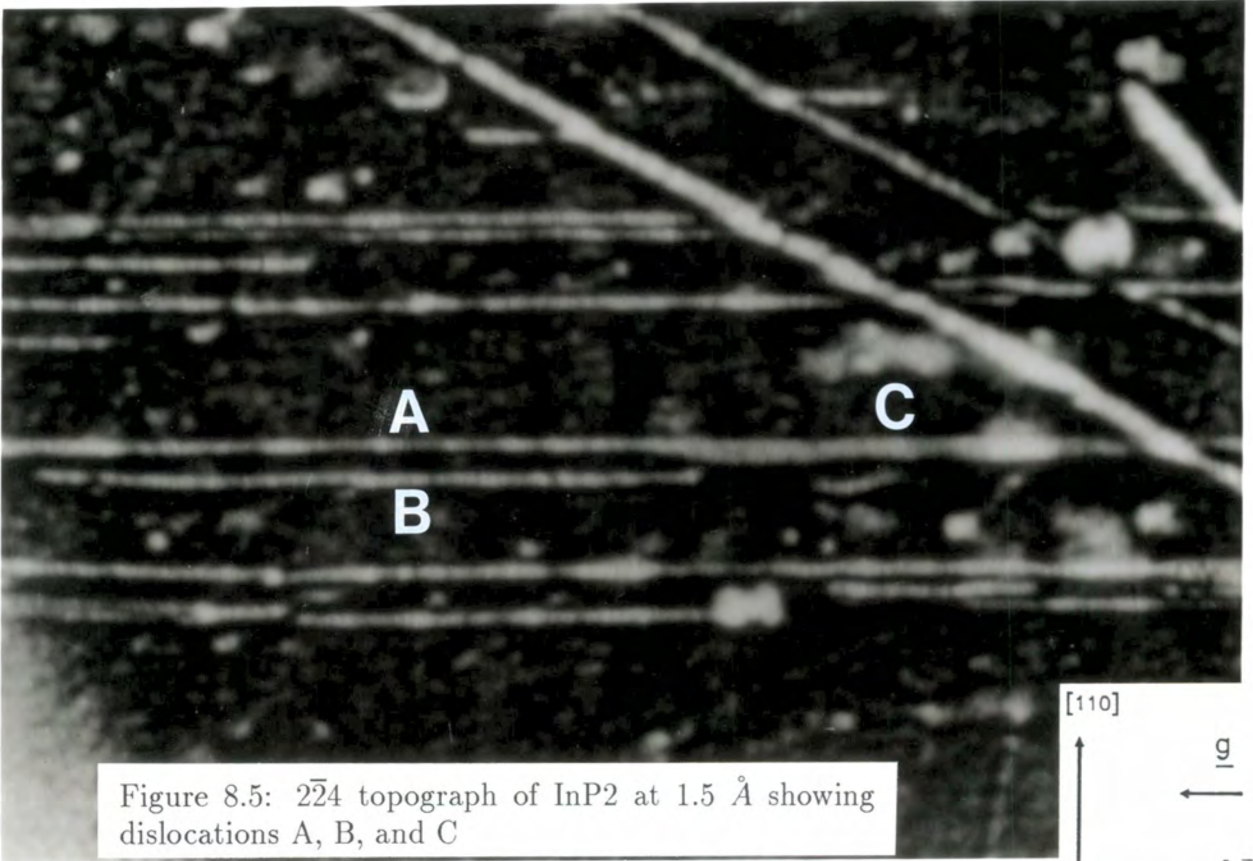

Figure 8.5: $2\bar{2}4$ topograph of InP2 at 1.5 Å showing dislocations A, B, and C

Figure 8.6: 224 topograph of InP2 at 1.5 Å showing dislocations at A, B, and C

$$(ii)..b_1 + b_3 = \frac{a_0}{2}[\bar{1}01] + \frac{a_0}{2}[0\bar{1}\bar{1}] = \frac{a_0}{2}[\bar{1}\bar{1}0]$$

$$(iii)..b_1 + b_4 = \frac{a_0}{2}[0\bar{1}1] + \frac{a_0}{2}[0\bar{1}\bar{1}] = a_0[0\bar{1}0]$$

Interactions (i) and (ii) result in the formation of pure edge dislocations whereas interaction (iii) results in the formation of a mixed dislocation line. Application of equation 8.3 shows that interaction (i) is not energetically favourable and so is unlikely to occur. Also $\underline{g}.\underline{b} = 0$ in the 224 reflection for the dislocation line produced in interaction (i). The 224 topograph shows the dislocation line C in strong contrast and so interaction (i) is not observed here. Although interaction (ii) is the most energetically favourable, $\underline{g}.\underline{b} = 0$ for this edge dislocation in the $2\bar{2}4$ reflection. The mixed dislocation produced by interaction (iii) is visible with equal contrast on both the 224 and $2\bar{2}4$ reflections. This corresponds closely to the contrast of dislocation line C observed in topographs of these reflections, Figures 8.5 and 8.6. We conclude that dislocation line C has a Burgers vector of a_0 [100] and is formed from two 60° dislocation lines which glide on opposite ⟨111⟩ planes. The dislocation line C is formed along the line of intersection between these planes. This dislocation line is observed in strong contrast in the $0\bar{4}4$ reflection and weaker contrast (from the $\underline{g}.\underline{b} \times \underline{l}$ term in equation 8.2) in the $\bar{4}04$ and 004 reflections. The interaction results in a decrease in the overall energy of the dislocation array though no advantage in the relief of misfit strain is obtained.

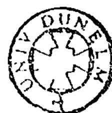

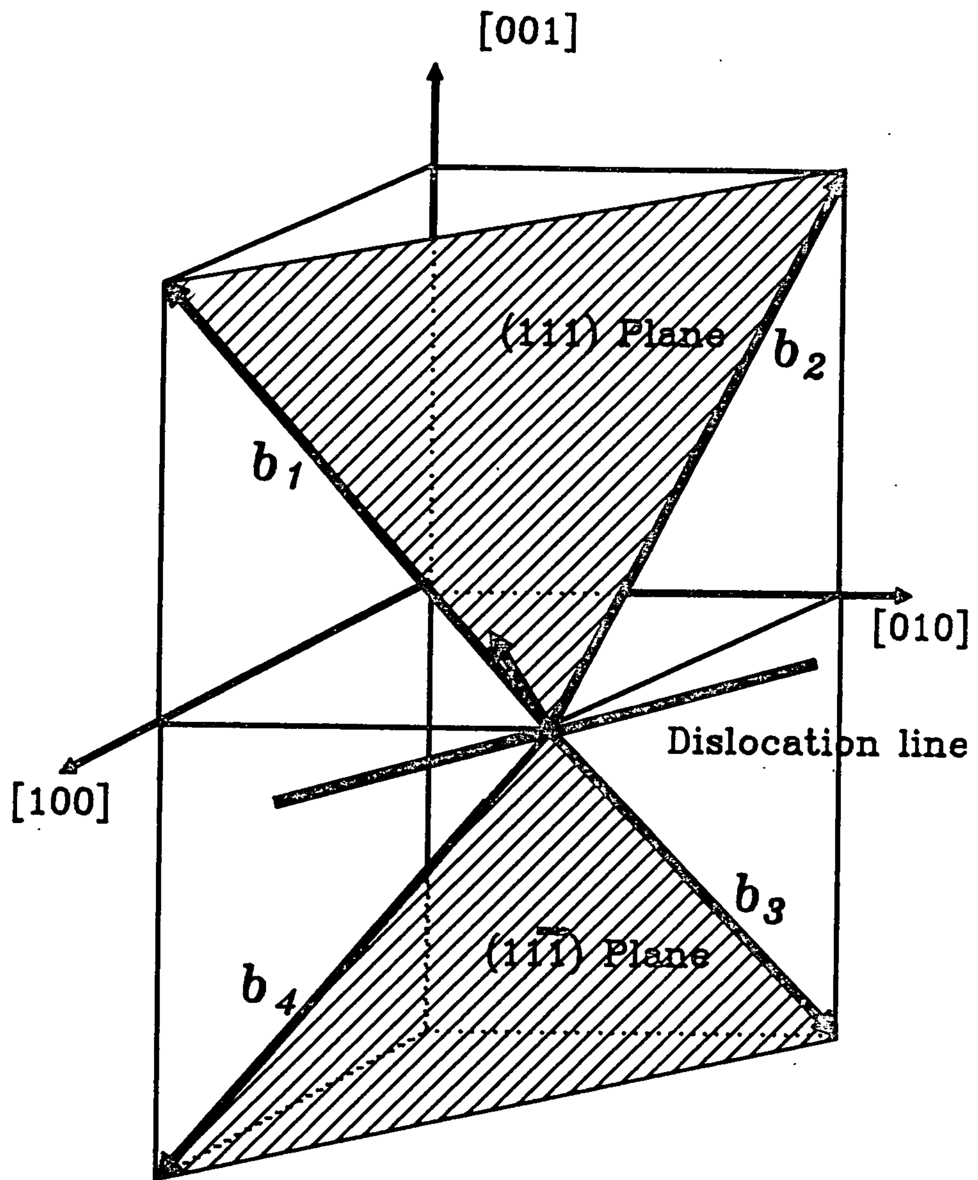

Figure 8.7: Possible Burgers vectors for a 60° dislocation line with an in plane edge component, $\underline{E_{\parallel}}$, of $a_0/(2\sqrt{2})$ $[\bar{1}\bar{1}0]$

8.4 Conclusions

In this chapter we have illustrated that for very low dislocation densities x-ray topography can be used to examine the nature of the Burgers vector for individual dislocation lines. Burgers vector analysis can unambiguously identify pure screw or pure edge dislocations as for these dislocations reflections can be chosen in which the dislocation contrast is zero. Identification of mixed dislocations is more difficult as these dislocations are never completely invisible in a reflection. However a computer program has been developed at Durham which simulates the width of a dislocation line image obtained on a Bragg reflection topograph. The program employs the dynamical theory of x-ray diffraction and is running on a Sun 4/330 Sparcserver. Typically a simulation takes four hours to produce an image with a resolution of about 0.25 μm. The facility to compare simulated and experimental topographic data of dislocations and their interactions will greatly enhance the application of Burgers vector analysis for cases where dislocation invisibilty cannot be obtained in a reflection.

Burgers vector analysis of the topography data presented in this chapter allowed identification of an array of screw dislocations and the formation of a mixed dislocation from two 60° dislocations. The presence of screw dislocations indicates that not all interfacial dislocations are strain relieving misfit dislocations and in conjunction with the identification of dislocation interactions at low dislocation densities indicates that the linear dislocation density deduced by diffractometry is approximate for slightly relaxed epitaxial layers. At high dislocation densities where dislocation interactions will be common the dislocation density deduced by diffractometry should be regarded as a maximum value.

We have clearly observed the bunching of dislocation lines into bundles for a low dislocation density sample and provide evidence for the preferential nucleation of dislocation lines within the bundle. Hence this phenomenon can also be expected at high dislocation densities. This is in agreement with results presented in chapter 6 for high dislocation density samples in which the number of dislocation lines per bundle is seen to increase with dislocation density.

Conclusions and Suggestions for Future Work

The application of double crystal diffractometry and topography to the examination of epitaxial layer relaxation has been compared for a range of dislocation densities and layer thicknesses. We have shown that the information obtained from these techniques is complementary.

Double crystal diffractometry is best suited to the determination of layer relaxation for layer thicknesses of the order of $1\mu m$ where the diffraction peaks for the layer are of high intensity and low FWHM. Here layer relaxations as low as 1 % were deduced from a complete set of asymmetric rocking curves for an AlAs layer on GaAs with a mismatch of 1600 ppm, sample GaAs4. The accuracy associated with the measurement of layer relaxation by diffractometry results from the measurement of the separation between the epitaxial layer and substrate peaks on double crystal rocking curves. Hence we expect to resolve lower relaxations for higher mismatch epitaxial layers and vice versa. This is supported by the epitaxial layer relaxation deduced by diffractometry for an InGaAs superlattice on InP, sample SLS1. Here the mean unit cell mismatch is 502 $\pm$ 17 ppm and the layer relaxation in the $[1\bar{1}0]$ was measured as 3 $\pm$ 2 %. However it must be recognised that for the critical thickness to be of the order of microns, the mismatch must be small. In highly strained systems the critical thickness is small. In these very thin layers the intensity of the layer reflection on the high angle of incidence asymmetric rocking curve is very low and interference effects in the layer reduce the substrate to epitaxial layer peak separation in all reflections. In this case interpretation of the rocking curves may achieved by simulating the experimental data. This was demonstrated for a 17 nm layer of InGaAs sandwiched between a GaAs cap and an 001 GaAs substrate. The system acts as a Bragg case interferometer and produces strong interference fringes. Careful comparison of simulated and experimental data allows determination of the Indium concentration to within 0.5 % and the layer thickness to within a single monolayer.

Layer relaxation in epitaxial layers of III-V compounds deposited on 001 orientated substrates has been found to be asymmetric about the $\langle 110 \rangle$ directions in the interface. Hence the 001 face of the layer unit cell is monoclinic where the [110] and $[1\bar{1}0]$ directions remain perpendicular and the [100] and [010] directions do not. The determination of asymmetric layer relaxation discussed in section 5.2.2 exploits the

above observation by employing asymmetric reflections in the ⟨110⟩ zones to deduce the positions of the hhl and h$\bar{h}$l layer reflections in reciprocal space and hence the 110 and $1\bar{1}0$ interplanar separations in the layer. As layer relaxation is asymmetric about the ⟨110⟩ directions, the strain in the layer unit cell will also be asymmetric. However the shape of the layer unit cell is not known at this time. Once the degree of lattice relaxation in the [110] and [$1\bar{1}0$] directions in the layer unit cell is known then it becomes possible to extend the analysis developed in section 5.2.2 for asymmetric reflections in other diffraction zones. Determination of the positions of these layer reflections in reciprocal space by diffractometry will provide more information on the shape of the layer unit cell.

Epitaxial layer tilt must be taken into account when measuring the substrate to epitaxial layer peak separation on a rocking curve. This is achieved by recording rocking curves with the sample rotated through 0° and 180°. In chapter 5 we demonstrate that for 001 orientated substrates a lack of epitaxial layer tilt is a good indication of crystalline perfection near the interface. The epitaxial layer tilt in the [110] and [$1\bar{1}0$] directions was observed to increase with misfit dislocation line density in these directions. From comparison between theory and experiment we have demonstrated that the values of epitaxial layer tilt measured experimentally are statistically significant and indicate a net alignment of the out of plane edge components $\underline{E_{\perp}}$ of the Burgers vectors of 60° dislocation lines in the [110] and [$1\bar{1}0$] directions. In order to examine the relationship between misfit dislocation density and epitaxial layer tilt further, samples of the same type, e.g. 1 μm InGaAs layers on InP substrates, with different layer relaxations should be investigated. Epitaxial layer samples with substrate misorientations of greater than 0.1° have not been investigated. The variation in epitaxial layer tilt with misfit dislocation line density should be measured by diffractometry for substrate misorientations of up to a few degrees. For low dislocation density layers where double crystal topography can clearly resolve individual dislocation lines, Burgers vector analysis of a complete set of 404 type reflections may allow the orientation of the $\underline{E_{\perp}}$ to be determined for each 60° dislocation line. This would be definitive.

In the determination of layer relaxation by x-ray topography and x-ray diffractometry for the [110] direction in sample GaAs2 we have demonstrated that the resolution of these techniques meets but does not really overlap. X-ray diffractometry has been shown to be insensitive to the first few misfit dislocations nucleated at the initial stages of relaxation where these dislocations are observed by topography. The critical thickness of an $In_xGa_{1-x}As$ layer sandwiched between an 001 GaAs substrate and a GaAs cap where x = 0.17 ± 0.005 has been measured as 162 ±

2 Å. This was achieved by using topography to observe the onset of layer relaxation in sample GaAs4 and diffractometry to determine the layer thickness at this point. Application of these techniques to similar InGaAs on GaAs samples will allow determination of the variation in critical layer thickness with Indium concentration.

X-ray diffractometry has been used to determine the average misfit dislocation line density for epitaxial layers with high dislocation densities, chapter 6. Comparison between these values and the dislocation images recorded by topography indicated that these images represent bundles of dislocations and not individual dislocation lines. Moreover the number of dislocation lines per bundle was seen to decrease with decreasing layer relaxation. A low dislocation density sample where individual misfit dislocation lines are clearly resolved by topography was examined in chapter 8. The bunching of misfit dislocation lines into dislocation bundles was observed and it appears that misfit dislocation lines are preferentially nucleated within the bundles. Dislocation interactions can be characterised by topography using Burgers vector analysis and this allowed the identification of screw dislocations and the characterisation of an interaction between two 60° dislocations to form a mixed dislocation line. However more dislocation reactions at low dislocation densities should be characterised by this method as this may provide information on dislocation multiplication mechanisms as well as dislocation nucleation mechanisms.

References

Chapter 1

[1] Gatos, H. C., and Lavine, M. C., J. Electrochem. Soc. **104** 427 (1960)

[2] Sze, S. M., *Physics of Semiconductor Devices* Wiley Interscience (1981)

[3] Streetman, B. G., *Solid State Electronic Devices* Prentice-Hall (1980)

[4] Zanger, H., *Semiconductor Devices and Circuits* John Wiley & Sons (1984)

[5] Van Vechten, J. A., and Bergstresser, T. K., Phys. Rev. B1, 3361 (1970)

[6] Kao, K. C., and Hockham, G. A., Proc. IEEE **13** 1151 (1961)

[7] Horiguchi, M., and Osanai, H., Electron. Lett., **12** 310 (1976)

[8] Payne, D. N., and Gambling, W. A., Electron. Lett., **11** 176 (1975)

[9] Miya, T., Terunuma, Y., Hosaka, T., and Miyashita, T., Electron. Lett. **15** 106 (1979)

[10] Yamamoto, T., Sakai, K., and Akiba, S., Japan. J. Appl. Phys. **16** 1699 (1977)

[11] Akiba, S., Sakai, K., Matsushima, Y., and Yamamoto, T., Electron. Lett. **15** 606 (1979)

[12] Hiyamizu, S., and Mimura, T., *Japan Annual Reviews in Electronics, Computers and Telecommunications - Semiconductor Technologies* eds. J. Nishizawa and Omasha, P., North Holland, 258 (1982)

[13] Stringfellow, G. B., Semiconductors and Semimetals **22** 209 (1985)

[14] Panish, M. B., Temkin, H., and Sumski, S., J. Vac. Sci Technol. **B3** 657 (1985)

[15] Vogjdani, N., Lamarchand, A., and Paradan, M., J. Phys. Colloq. C5 **43** 339 (1982)

[16] Tokumitsu, E., Kudoo, Y., Konagai, M., and Takabaski, K., J. Appl. Phys. **55** 3163 (1984)

[17] Tsang, W. T., Appl. Phys. Lett. **45** 1234 (1984)

[18] Prakash, H., Prog. Cryst. Growth and Charact. **12** 265 (1986)

[19] Logan, R. A., Prog. Cryst. Growth Charact. **12** 215 (1986)

[20] Agrawal, G. P., and Dutta, N. K., *Long Wavelength Semiconductor Lasers*, Van Nostrand, New York, (1986)

[21] Nagai, H., Prog. Cryst. Growth Charact. **12** 271 (1986)

[22] Takahashi, S., and Nagai, H., J. Cryst. Growth **51** 502 (1981)

[23] Besomi, P., Wilson, R. B., Wagner, W. R., and Nelson, R. J., J. Appl. Phys. **54** 535 (1983)

[24] Nakajima, K., Komiya, S., Akita, K., Yamaoka, T., and Ryuzun, O., J. Electrochem. Soc. **127** 1568 (1980)

[25] Nelson, A. W., Moss, R. H., Spurdens, P. C., Cole, S., and Wong, S., Br. Telecom. Technol. J. **4** 85 (1986)

[26] Günther, K. G., Z. Naturforsch. **13a** 1081 (1958)

[27] Davey, J. E., and Pankey, T., J. Appl. Phys. **39** 1941 (1968)

[28] Cho, A. Y., and Arthur, J. R., Progr. Solid State Chem. **10** 157 (1975)

[29] Chang, L. L., Esaki, L., Howard, W. E., Ludeke, R., J. Vac. Sci. Technol. **10** 11 (1973)

[30] Smith, D. L., Prog. Crystal Growth Charact. **2** 33 (1979)

[31] Davies, G. J., and Andrews, D. A., Br. Telecom. Technol. J. **3** (2) 59 (1985)

[32] Khan, I. H., *Handbook on Thin-Film Technology*, eds. Maissel, L. I., and Glang, R., McGraw-Hill, chapter 10 (1983)

[33] Venables, J. A., Spiller, G. D. T., and Hanbucken, M., Rep. Prog. Phys., **47** 399 (1984)

[34] Davidenkov, N. N., Sov. Phys. Solid State, **2** 2595 (1961)

[35] Chu, S. N. G., Macrander, A. T., Strege, K. E., and Johnston, W. D., J. Appl. Phys. **57** 249 (1985)

[36] Hill, M. J., Ph.D. Thesis, University of Durham (1985)

[37] Hornstra, J., and Bartels, W. J., J. Cryst. Growth, **44** 518 (1978)

[38] Halliwell, M. A. G., Inst. Phys. Conf. Ser., **60** 271 (1981)

[39] Landau, L. D., and Lifshitz, E. M., *Theory of Elasticity* Pergamon Press 52 (1959)

[40] Halliwell, M. A. G., Advances in X-ray Analysis **33** 61 (1990)

[41] Andersson, T. G., Chen, Z. G., Kulakous, V. D., Uddin, A., Vallin, J. T., Appl. Phys. Lett. **51** No 10 (1987)

Chapter 2

[1] Cullity, B. D., *Elements of X-Ray Diffraction* Addison-Wesley, (1969)

[2] Warren, B. E., *X-Ray Diffraction* Addison-Wesley, (1969)

[3] McKie, D., and McKie, C., *Essentials of Crystallography* Blackwell, (1986)

[4] Darwin, C., Phil. Mag. **27** 315 and 675 (1914)

[5] Ewald, P. P., Ann. Physik. **49** 117 (1916)

[6] Von Laue, M., Ergeb. Exakt. Naturw., **10** 133 (1931)

[7] James, R. W., *Solid State Physics* **15** New York Academic Press (1963)

[8] Zachariasen *Theory of X-ray Diffraction in Crystals* John Wiley and Sons, (1945)

[9] Pinsker, Z. G., *Dynamical Scattering of X-rays in Crystals*, Springer-Verlag, Berlin (1978)

[10] Batterman, B. W., and Cole, H., Rev, Mod. Phys. **36** 681 (1964)

[11] Authier, A., In *Advances in Structure Research by Diffraction Methods* eds: Brill and Mason **3** 1 (1970)

[12] Hart, M., In *Characterisation of Crystal Growth Defects by X-ray Methods* eds: Tanner, B. K., and Bowen, D. K., London, Plenum Press, 216 (1980)

[13] Tanner, B. K., X-ray Diffraction Topography, Pergammon Press, (1976)

[14] Bartels, W. J., and Nijman, W., J. Cryst. Growth. **44** 518 (1978)

[15] Segmüller, A., Noyan, I. C., and Speriosu, V. S., Prog. Cryst. Growth and Charact. **18** 21 (1989)

[16] Ryan, T., and Bates, S., Private Communication, November 1990

[17] Petrashen, P. V., Sov. Phys. Solid State **17** 1882 (1976)

[18] Takagi, S., Acta Cryst. **15** 1311 (1962)

[19] Takagi, S., J. Phys. Soc. Jpn. **26** 1239 (1969)

[20] Taupin, D., Bull. Soc. Fr. Mineral. Cristallogr. **87** 469 (1964)

[21] Capano, M. A., Doctoral Thesis, Massachussetts Institute of Technology (1989)

[22] Hill, M. J., Tanner, B. K., Halliwell, M. A. G., and Lyons, M. H., J. Appl. Cryst. **18** 446 (1985)

[23] Fewster, P. F., and Curling, C. J., J. Appl. Phys. **62** 4154 (1987)

[24] Bensoussan, S., Malgrange, C., and Sauvage-Simkin, M., J. Appl. Cryst. **20** 222 (1987)

[25] Miltat, J., Phil. Mag. **57** 79 and 685 (1988)

[26] Barnett, S. J., Brown, G. T., Courtney, S. J., Bass, S. J., and Taylor, L. L., J. Appl. Phys. **64** 1185 (1988)

Chapter 3

[1] Schwarzschild, M. M., Phys. Rev. **32** 162 (1928)

[2] Allison, S. K., and Williams, J. H., Phys. Rev. **35** 1476 (1930)

[3] Allison, S. K., Phys. Rev. **41** 1 (1932)

[4] Compton, A. H., and Allison, S. K., *X-Rays in Theory and Experiment,* Macmillan, (1936)

[5] Compton, A. H., Rev. Sci. Instrum. **2** 7 (1931)

[6] DuMond, J. W. M., and Marlow, D., Rev. Sci. Instrum. **8** 112 (1937)

[7] Hart, M., *Characterisation of Crystal Growth Defects by X-ray Methods* eds. by B. K. Tanner and D. K. Bowen, Plenum Press, 483 (1980)

[8] Longhurst, R. S. *Geometrical and Physical Optics* Longmans, Green and Co., London, Chapter 20 (1957)

[9] Pietsch, U., and Borchard, W., J. Appl. Cryst. **20** 8 (1987)

[10] *International Tables for X-Ray Crystallography* Volume III, Physical and Chemical Constants, Edited by C. H. Macgillavry, G. D. Rieck and K. Lonsdale, 60 (1962)

[11] DuMond, J. W. M., Phys. Rev. **52** 872 (1937)

[12] Yoshimura, J., J. Appl. Cryst. **17** 426 (1984)

[13] Xu, S., and Li, R., J. Appl. Cryst. **21** 213 and 218 (1988)

[14] Fewster, P. F., J. Appl. Cryst. **18** 334 (1985)

[15] Tanner, B. K., X-ray Diffraction Topography, Pergamon Press, (1976)

[16] Armstrong, R. W., *Characterisation of Crystal Growth Defects by X-ray Methods* eds. B. K. Tanner and D. K. Bowen, Plenum Press 349 (1980)

[17] Lang, A. R., *Diffraction and Imaging Techniques in Materials Science* eds. S. Amelinckx, R. Gevers and J. Van Landuyt, North-Holland Publishing Co., Amsterdam, Vol. II 623 (1978)

[18] Loxley, N., Doctoral Thesis, University of Durham, (1988)

[19] Miltat, J., *Characterisation of Crystal Defects by X-ray Methods*, eds. B. K. Tanner and D. K. Bowen, Plenum Press 401 (1980)

[20] Sauvage, M., *Characterisation of Crystal Defects by X-ray Methods*, eds. B. K. Tanner and D. K. Bowen, Plenum Press 433 (1980)

[21] Bowen, D. K., Clark, G. F., Davies, S. T., Nicholson, J. R. S., Roberts, K. J., Sherwood, J. N., and Tanner, B. K. Nuclear Instruments and Methods **195** 277 (1982)

[22] Berg, W. F., Naturwissenschaften **19** 391 (1931)

[23] Barrett, C. S., Trans. AIME **161** 15 (1945)

[24] Wallace, C. A., and Ward, R. C. C., J. Appl. Cryst. **8** 281 (1975)

[25] Born, M., and Wolf, E.,*Principles of Optics*, Pergamon Press, 412 (1965)

[26] Lang, A. R., Acta Met. **5** 358 (1957)

[27] Epelboin, Y., Prog. Cryst. Growth and Charact. **14** 465 (1987)

[28] Vis, R. D., and van Langevelde, F., Nuclear Instruments and Methods in Physics Research **B54** 417 (1991)

[29] Tuomi, T., Naukkarineen, K., and Rabe, P., Phys. Stat. Sol. (a) **25** 93 (1974)

[30] Tanner, B. K., Midgley, D., and Safa, M., J. Appl. Cryst. **10** 281 (1977)

[31] Bond, W. L., Andrus, J., Am. Minerologist **37** 622 (1952)

[32] Bonse, U., Klapper, E., Z. Naturforschung **13a** 348 (1958)

[33] Robert, M. C., Lefaucheux, F., Sauvage, M., J. Cryst. Growth. **52** 976 (1981)

[34] Kikuta, S., Kohra, K., J. Phys. Soc. Jap. **29** 1322 (1970)

[35] Kikuta, S., J. Phys. Soc. Jap. **30** 223 (1971)

[36] Beaumont, J. H., and Hart, M., Journal of Physics E: Scientific Instruments **7** 823 (1974)

[37] Bonse, U., Olthoff-Munter, K., Rumpf, A., J. Appl. Cryst. **16** 524 (1983)

[38] Hart, M., Rodriguies, A. R. D., J. Appl. Cryst. **11** 248 (1978)

[39] Bowen, D. K., and Davis, S. T., Nucl. Instr. Methods **208** 725 (1983)

[40] Barnett, S. J., Doctoral Thesis, University of Durham, (1987)

[41] M. Renninger, Advances in X-ray Analysis **10** 32 (1967)

[42] R. W. James *Solid State Physics* eds. F. Seitz and D. Turnbull New York Academic Press 118 (1948)

[43] Hart, M., and Siddons, D. P., Nucl. Instr. Methods **204** 219 (1982)

[44] Halliwell, M. A. G., Childs, J. B., and O'Hara, S., I. O. P. Symposium on GaAs 99 (1972)

Chapter 4

[1] Hirth, J. P., and Lothe, J., *Theory of Dislocations* McGraw-Hill (1968)

[2] Frank, F. C., Phil. Mag., **42** 809 (1951)

[3] Hull, D., *Introduction to Dislocations* Pergammon Press (1975)

[4] W. A. Lomer Phil. Mag. **41** 1327 (1951)

[5] Nagai, H., J. Appl. Phys., **45** 3789 (1974)

[6] Mader, S., Blakeslee, A. E., and Angilello, J., J. Appl. Phys. **45** 4730 (1974)

[7] Olsen, G. H., J. Cryst. Growth, **31** 223 (1975)

[8] Gourley, P. L., Fritz, I. J., and Dawson, L. R., Appl. Phys. Lett., **52** 377 (1987)

[9] Kavanagh, K. L., Capano, M. A., Hobbs, L. W., Barbour, J. C., Maree, P. M.

J., Schaff, W., Mayer, J. W., Pettit, G. D., Woodall, J. M., Stroscio, J. A., and Feenstra, R. M., J. Appl. Phys., **64** 4843 (1988)

[10] De Cooman, B. C., and Carter, C. B., Acta. Metall. **37** 1765 (1989)

[11] Herbeaux, C., Di Persio, J., and Lefebvre, A., Phil. Mag. Lett. **59** 243 (1989)

[12] Kvam, E. P., Maher, D. M., and Humphreys, C. J., J. Mater. Res. **5** 1900 (1990)

[13] Maree, P. M. J., Barbour, J. C., van der Veen, J. F., Kavanagh, K. L., Bulle-Lieuwma, C. W. T., and Viegers, M. P. A., J. Appl. Phys. **62** 4413 (1987)

[14] Alexander, H., J. Phys. Colloq. **40** C6-1 (1979)

[15] Peierls, R., Proc. Phys. Soc., **52** 34 (1940)

[16] Nabarro, F. R. N., Proc. Phys. Soc., **59** 256 (1947)

[17] Frank, F. C., and van der Merwe, J. H., Proc. Roy. Soc. (London) **A198** 216 (1949)

[18] van der Merwe, J. H., Proc. Phys. Soc., **A63** 616 (1950)

[19] van der Merwe, J. H., J. Appl. Phys., **34** 117 (1963)

[20] van der Merwe, J. H., J. Appl. Phys., **34** 123 (1963)

[21] Matthews, J. W., and Blakeslee, A. E., J. Crystal Growth. **27** 118 (1974)

[22] Matthews, J. W., Blakeslee, A. E., and Mader, S., Thin Solid Films, **33** 253 (1976)

[23] Petroff, J.-F., and Sauvage, M., J. Crystal Growth **43** 628 (1978)

[24] Hagen, W. and Strunk, H. P., Appl. Phys., **17** 86 (1978)

[25] Queisser, H. J., J. Appl. Phys. **32** 1776 (1961)

[26] Matthews, J. W., Phil. Mag., **13** 1207 (1966)

[27] Matthews, J. W., Mader, S., and Light, T. B., J. Appl. Phys., **41** 3800 (1970)

[28] Matthews, J. W., and Blakeslee, A. E., J. Cryst. Growth., **27** 118 (1974)

[29] Matthews, J. W., J. Vac. Sci. Technol. **12** 126 (1975)

[30] Frank, F. C., and van der Merwe, J. H., Proc. Roy. Soc. (A), **198** 205 (1949)

[31] van der Merwe, J. H., Phil. Mag., **7** 1433 (1962)

[32] Bean, J. C., Feldman, L. C., Fiory, A. T., Nakahara, S., and Robinson, I. K., J. Vac. Sci. Technol., **A2** 436 (1984)

[33] People, R., and Bean, J. C., Appl. Phys. Lett., **47** 322 (1985)

[34] Fitzgerald, E. A., Kirchner, P. D., Proano, R., Pettit, G. D., Woodall, J. M., and Ast, D. G., Appl. Phys. Lett. **52** 1496 (1988)

[35] Fitzgerald, E. A., Watson, G. P., Proano, R., Ast, D. G., Kirchner, P. D., Pettit, G. D., and Woodall, J. M., J. Appl. Phys. **65** 2220 (1989)

[36] Nagai, H., J. App. Phys. **43** 4254 (1972)

[37] Rozgonyi, G. A., Petrol, P. M., and Panish, M. B., J. Cryst. Growth **27** 106 (1974)

[38] Turnbull, A. G., Green, G. S., Tanner, B. K., and Halliwell, M. A. G., Mater. Res. Soc. Proc. **202** 513 (1991)

[39] Gatos, H. C., and Lavine, M. C., J. Electrochem. Soc. **104** 427 (1960)

[40] Fox, B. A., and Jesser, W. A., J. Appl. Phys. **68** (6) 2739 (1990)

[41] Erofeeva, S. A., and Osipyan, Y. A., Sov. Phys. Solid State. **15** 538 (1973)

[42] Steinhardt, H. and Haasen, P., Phys. Status Solidi A **49** 93 (1978)

[43] Warren, P. D., Pirouz, P., and Roberts, S. G., Phil. Mag., **50** L23 (1984)

[44] Surowiec, M., and Tanner, B. K., Phil. Mag. A **55** 791 (1987)

Chapter 5

[1] Tanner, B. K., Chu, X, and Bowen, D. K., Mater. Res. Soc. Symp. Proc. **69** 191 (1986)

[2] Tanner, B. K., Miles, S. J., Peterson, G. G., and Sacks, R. N., Mat. Lett. **7** (5,6) 239 (1988)

[3] Miles, S. J., Doctoral Thesis, University of Durham, (1989)

[4] Macrander, A. T., and Swaminathan, V., J. Electrochem. Soc. **134** 1247 (1987)

[5] Tanner, B. K., Turnbull, A. G., Stanley, C. R., Kean, A. H., and McElhinney, M., Appl. Phys. Lett. **59** No. 18 (1991)

[6] Goorsky, M., Kuech, T. F., Tischler, M. A., and Potemski, R. M., Appl. Phys. Lett. **59** 2269 (1991)

[7] Halliwell, M. A. G., Advances in X-Ray Analysis **33**, 61 (1990)

[8] Turnbull, A. G., Green, G. S., Tanner, B. K., and Halliwell, M. A. G., Mater. Res. Soc. Proc. **202** 513 (1991)

[9] Ettenberg, M., and Paff, R. J., J. Appl. Phys. **41** 3926 (1970)

[10] Hart, M., Journal of Crystal Growth **55** 409 (1981)

[11] Straumanis, M. E., Kim, C. D., Acta Cryst. **19** 256 (1965)

[12] Willoughby, A. F. W., Driscoll, C. M. H., Bellamy, B. A., J. Materials. Sci. **6** 1389 (1971)

[13] Driscoll, C. M. H., Willoughby, A. F. W., Mullin, J. B., and Straughan, B. W., Inst. Phys. Conf. Ser. No. 24, chapter 5 (1975)

[14] Baker, J. F. C., Hart, M., Halliwell, M. A. G., and Heckingbottom, R., Solid State Electron. **19** 331 (1976)

[15] Fewster, P. F., and Willoughby, A. F. W., J. Crystal. Growth **50** 648 (1980)

[16] Adachi, S., J. Appl. Phys. **58** R1 (1985)

[17] Okada, Y., Tokumara, Y., *Semi-insulating III-V Materials*, Hakone, 175 (1986)

[18] Nakajima, M., Sato, T., Inada, T., Fukuda, T., Ishida, K., *Semi-insulating III-V Materials*, Hakone, 181 (1986)

[19] Kawamoto, H., Holmes, D. E., J. Appl. Phys. **59** 656 (1986)

[20] JCPDS, Powder Diffraction File, JCPDS International Centre for Diffraction Data, Swarthmore, PA, USA. (1986)

[21] Usuda, K., Yasuami, S., Higashi, Y., Kawata, H., and Ando, M., Japan J. Appl. Phys. **29** L210 (1990)

[22] Abrahams, M. S., Weisberg, L. R., Buiocchi, C. J., Blanc, J., J. Mater. Sci. **4** 223 (1969)

[23] Bilby, R. A., Billough, R., and Smith, E., Proc. Roy. Soc. **A231** 263 (1955)

[24] Hirth, J. P., and Lothe, J., *Theory of Dislocations* McGraw-Hill 21 (1968)

[25] Hull, D., *Introduction to Dislocations* Pergamon Press 34 (1975)

[26] Flowers, B. H., and Mendoza, E., *Properties of Matter* John Wiley and Sons 150 (1970)

[27] Dwight, B. H., *Tables of Integrals and other Mathematical Data* Macmillan 14th Edition 230 (1961)

Chapter 6

[1] Turnbull, A. G., Green, G. S., Tanner, B. K., and Halliwell, M. A. G., Mater. Res. Soc. Proc. **202** 513 (1991)

Chapter 7

[1] Tanner, B. K., Turnbull, A. G., Stanley, C. R., Kean, A. H., and McElhinney, M., Appl. Phys. Lett. **59** 2272 (1991)

[2] Turnbull, A. G., Green, G. S., Tanner, B. K., Halliwell, M. A. G., Mater. Res. Soc. Proc. **202** 513 (1991)

[3] Green, G. S., Tanner, B. K., Turnbull, A. G., Barnett, S. J., Emeny, M., and Whitehouse, C. R., Mater. Res. Soc. Proc. **202** 507 (1991)

[4] Green, G. S., Tanner, B. K., Barnett, S. J., Emeny, M., Pitt, A. D., Whitehouse, C. R., and Clark, G. F., Phil. Mag. Letts. **62** 131 (1990)

[5] Harris, J. J., Joyce, B. A., and Dobson, P. J., Surf. Sci. **103** L90 (1981)

[6] Halliwell, M. A. G., Childs, J. B., and O'Hara, S., I. O. P. Symposium on GaAs **1972** 99

[7] Chen, R. T., Holmes, D. E., J. Cryst. Growth **61** 111 (1983)

[8] Barnett, S. J., Doctoral Thesis, University of Durham (1987)

[9] Petroff, J. F., and Sauvage, M., J. Crystal Growth, **43** 628 (1978)

[10] Fewster, P. F., and Curling, C. J., J. Appl. Phys. **62** 4154 (1987)

[11] Tapfer, L., and Ploog, K., Phys. Rev. B **40** 9802 (1989)

[12] Holloway, H., J. Appl. Phys. **67** 6229 (1990)

[13] Chu, X., and Tanner, B. K., Appl. Phys. Lett. **49** 1773 (1986)

[14] Miles, S. J., Doctoral Thesis, University of Durham (1989)

[15] Halliwell, M. A. G., Lyons, M. H., Davey, S. T., Hockley, M., Tuppen, C. G., and Gibbings, C. J., Semicond. Sci. Technol. **4** 10 (1989)

[16] Goorsky, M., Kuech, T. F., Tischler, M. A., and Potemski, R. M., Appl. Phys. Lett. **59** 2269 (1991)

[17] Ettenberg, M., and Paff, R. J., J. Appl. Phys. **41** 3926 (1970)

Chapter 8

[1] Tanner, B. K., *X-Ray Diffraction Topography*, Pergamon Press (1976)

[2] Surowiec, M. R., and Tanner, B. K., Phil. Mag. A., **55** (6), 791 (1987)

[3] Hull, D., *Introduction to Dislocations*, Pergammon Press (1975)